

# **Thermally Enhanced Forming of Aluminium Sheet**

## **Modelling and Experiments**

Samenstelling van de promotiecommissie:

*voorzitter en secretaris:*

Prof. dr. ir. H.J. Grootenboer      Universiteit Twente

*promotor:*

Prof. dr. ir. J. Huétink      Universiteit Twente

*leden:*

Prof. dr. ir. M.G.D. Geers      Technische Universiteit Eindhoven

Prof. dr. ir. F.J.A.M. van Houten      Universiteit Twente

Prof. dr. ir. P. van Houtte      Katholieke Universiteit Leuven

Prof. dr. ir. H. Tijdeman      Universiteit Twente

Dr. ir. H. Vegter      Corus Research, Development and Technology

ISBN 90-365-1815-6

1st Printing November 2002

Keywords: plasticity, material models, warm forming, aluminium

This thesis was prepared with  $\text{\LaTeX}$  by the author and printed by Ponsen & Looijen, Wageningen, from an electronic document.

Copyright © 2002 by A.H. van den Boogaard, Hengelo, The Netherlands

All rights reserved. No part of this publication may be reproduced, stored in a retrieval system, or transmitted in any form or by any means, electronic, mechanical, photocopying, recording or otherwise, without prior written permission of the copyright holder.

THERMALLY ENHANCED FORMING OF ALUMINIUM SHEET  
MODELLING AND EXPERIMENTS

PROEFSCHRIFT

ter verkrijging van  
de graad van doctor aan de Universiteit Twente,  
op gezag van de rector magnificus,  
prof. dr. F.A. van Vught,  
volgens besluit van het College voor Promoties  
in het openbaar te verdedigen  
op vrijdag 6 december 2002 te 15.00 uur.

door

Antonius Henricus van den Boogaard

geboren op 28 mei 1961  
te Haarlem

Dit proefschrift is goedgekeurd door de promotor:

Prof. dr. ir. J. Huétink

# Contents

<b>Summary</b>	<b>ix</b>
<b>Samenvatting</b>	<b>xi</b>
<b>Preface</b>	<b>xiii</b>
<b>Nomenclature</b>	<b>xv</b>
<b>1 Introduction</b>	<b>1</b>
1.1 The Significance of Weight Reduction . . . . .	1
1.2 Formability of Aluminium Sheet . . . . .	2
1.3 Objective of this Thesis . . . . .	3
1.4 Terminology and Notation . . . . .	4
1.5 Outline . . . . .	5
<b>2 Experimental Observations</b>	<b>7</b>
2.1 Material Characteristics . . . . .	7
2.2 Uniaxial Tensile Tests . . . . .	10
2.2.1 Constant Temperature and Strain Rate Tests . . . . .	10
2.2.2 Strain Rate Jumps . . . . .	15
2.3 Biaxial Tests . . . . .	17
2.4 Conclusion . . . . .	19
<b>3 Material Models</b>	<b>21</b>
3.1 Classical Rate Independent Plasticity . . . . .	21
3.1.1 The Yield Surface . . . . .	21
3.1.2 Normal and Planar Anisotropy . . . . .	23
3.2 Polycrystal Plasticity . . . . .	25
3.2.1 Single Crystal Model . . . . .	25
3.2.2 Homogenisation . . . . .	29
3.2.3 Determination of the Yield Locus . . . . .	29
3.3 Explicit Yield Functions . . . . .	31
3.3.1 Hill '48 Yield Function . . . . .	31
3.3.2 Tresca Yield Function . . . . .	35
3.3.3 Vegter Yield Function . . . . .	36

3.4	Flow Stress and Hardening . . . . .	38
3.4.1	Phenomenological Models . . . . .	39
3.4.2	Physically Based Models . . . . .	44
3.5	Discussion . . . . .	50
<b>4</b>	<b>Large Deformations</b>	<b>53</b>
4.1	Continuum Mechanics . . . . .	53
4.2	Plastic Spin and Texture Evolution . . . . .	60
4.3	Proportional Deformation and Simple Shear . . . . .	68
4.4	Closure . . . . .	71
<b>5</b>	<b>Tensile Instabilities and Forming Limits</b>	<b>73</b>
5.1	Preliminaries . . . . .	73
5.2	Diffuse Necking . . . . .	75
5.3	Localised Necking . . . . .	78
5.3.1	Localisation in the Drawing Region . . . . .	78
5.3.2	Localisation in the Stretching Region . . . . .	80
5.4	Forming Limit Curves . . . . .	83
5.5	Finite Element Analysis . . . . .	87
5.5.1	Grooved Plate . . . . .	87
5.5.2	Plane Strain Test . . . . .	89
5.6	Conclusion . . . . .	91
<b>6</b>	<b>Efficient Finite Element Simulations</b>	<b>93</b>
6.1	Problem Definition . . . . .	93
6.1.1	Time Integration Methods . . . . .	95
6.2	Elements . . . . .	97
6.2.1	Continuum Elements . . . . .	98
6.2.2	Shell Elements . . . . .	98
6.2.3	Contact Elements . . . . .	101
6.3	Comparison Between Implicit and Explicit Methods . . . . .	101
6.3.1	Implicit Methods . . . . .	102
6.3.2	Explicit Methods . . . . .	103
6.3.3	An Efficient Strategy for Implicit Methods . . . . .	104
6.4	Linear Equation Solvers . . . . .	105
6.4.1	Direct Solvers . . . . .	105
6.4.2	Iterative Solvers . . . . .	105
6.4.3	Convergence Criterion . . . . .	106
6.4.4	Examples . . . . .	108
6.5	Stabilisation by Dynamics Contributions . . . . .	111
6.5.1	Deep Drawing of a Rectangular Product . . . . .	111
6.5.2	Front Door Panel . . . . .	114
6.6	Conclusion . . . . .	116

<b>7 Applications</b>	<b>117</b>
7.1 Tensile Test . . . . .	117
7.1.1 Influence of Element Size . . . . .	118
7.1.2 Influence of Temperature and Strain Rate . . . . .	121
7.2 Cylindrical Cup Deep Drawing . . . . .	122
7.2.1 Experiments . . . . .	122
7.2.2 Axisymmetric Simulations . . . . .	124
7.2.3 Shell Element Simulations . . . . .	128
7.3 Conclusion . . . . .	134
<b>8 Conclusions and Recommendations</b>	<b>135</b>
<b>A Selected Topics from Tensor Algebra</b>	<b>139</b>
A.1 Functions of a 2nd Order Tensor . . . . .	139
A.2 2D Polar Decomposition . . . . .	141
A.3 Simple Shear . . . . .	142
<b>B Proportional Deformation</b>	<b>145</b>
B.1 Proportionality Factors . . . . .	145
B.2 Hardening Relations . . . . .	146
B.3 Diffuse Necking with the Hill '48 Yield Locus and Nadai Hardening model	147
<b>C Yield Locus Parameters</b>	<b>149</b>
<b>Bibliography</b>	<b>151</b>
<b>Curriculum Vitae</b>	<b>161</b>
<b>Index</b>	<b>163</b>





# Summary

One of the ways to reduce the weight of vehicles is by substitution of traditional mild steel parts by aluminium. The formability of aluminium, however, is less than that of mild steel. To improve the formability of an aluminium sheet, the local flow behaviour can be controlled by applying elevated temperatures and temperature gradients. Experiments with Al–Mg sheet show that in this way the limiting drawing ratio can be increased up to the same level as that of mild steel.

At room temperature, the mechanical behaviour of Al–Mg sheet is almost independent of the strain rate. Increasing the temperature up to 100 °C does not change the stress–strain response either. Above 125 °C, the ultimate tensile strength decreases and the strain rate sensitivity increases. The initial yield stress, however, hardly changes until a temperature of 175 °C. Above 175 °C, the initial yield stress also drops.

In this thesis a numerical model is developed to simulate the warm forming of Al–Mg sheet. An important part of the numerical model is the modelling of the material behaviour. Both the hardening behaviour, including temperature and strain rate effects, and the biaxial stress–strain response of the sheet are considered. Two hardening models are compared: a phenomenological model in which the parameters of a Ludwik–Nadai hardening model and a power law strain rate relation are made temperature dependent, and a physically-based model according to Bergström. The latter model incorporates the influence of the temperature on the flow stress and on the hardening rate based on dynamic recovery. For deformations at constant temperature and strain rate, the Bergström model reduces to the well known Voce hardening model. The Ludwik–Nadai and Bergström–Voce models can be fitted quite well to the results of monotonic tensile tests of an AA 5754-O alloy. At large strains, the Bergström–Voce model gives a better prediction than the Nadai model. Large differences appear, however, if strain rate jumps are applied. After a strain rate jump, the experimental stress–strain curve gradually reaches the curve that is obtained from a test at the corresponding constant strain rate. The Bergström model grossly overestimates the strain increment that is needed to reach the corresponding constant strain rate curve.

The biaxial stress–strain response of the material is experimentally determined by uni-axial stress, plane strain, simple shear and equi-biaxial stress tests. The results are compared with, and partly supplemented by, crystal plasticity analyses. It is demonstrated that the widely used Hill '48 yield locus is inappropriate for simulation of deformation in aluminium. The low  $R$ -values for aluminium lead to a significant underestimation of the equi-biaxial yield stress. In the simulation of the deep drawing of a cylindrical cup this results in a much too thin bottom of the cup. The Vegter yield criterion is sufficiently flexible to accurately represent the shape of the yield locus and the anisotropy .

In forming processes, large deformations occur. Most plasticity formulations are based on strain rates or on small strain theory. For large deformations proper strain measures or objective rates must be chosen. The results from a simple shear test are particularly sensitive to the chosen objective rates. With considerations from crystal plasticity theory it is demonstrated that, for materials with only a weak texture, the choice of objective rate is of the same significance as the update of the shape of the yield locus during deformation. This means that, if the changing locus is not considered in an analysis, the choice of a particular objective rate is irrelevant for the overall accuracy.

The formability of sheet material is to a large degree determined by necking. This is a geometric instability, in which the work hardening is no longer able to compensate for the reduction in sheet thickness. The strain at which this instability occurs can be determined from a Marciniak–Kuczynski analysis. The accuracy of this method is determined by the accuracy of the material model. The accuracy of the material model is much more critical for the determination of necking than *e.g.* for the calculation of the tool forces and general thickness distribution. A finite element model with shell elements can predict necking in the same way as an M–K analysis. In a finite element model the boundary conditions are better represented than in an M–K analysis. If accurate material models are used necking can be predicted without comparison with forming limit curves.

To simulate industrial sheet forming processes, explicit time integration methods are often used. Implicit time integration methods are potentially more accurate, but the solution of a set of equations requires too much time for large systems. Iterative solvers are known to perform badly for shell element models, due to the poor condition of the stiffness matrix. By not ignoring the dynamic contribution—as is usually done—the condition of the matrix can be improved. Using the same mass scaling as is customary in explicit methods, large scale simulations can be performed with an implicit method, using an iterative solver, in a fraction of the time needed with a direct solver. The implicit integration method is now a serious alternative for explicit methods.

# Samenvatting

Eén van de manieren om het gewicht van voertuigen te verminderen, is het vervangen van staal door aluminium. De vervormbaarheid van aluminium is echter minder dan van het gebruikelijke vervormingsstaal. De vervormbaarheid kan worden verbeterd door gebruik te maken van verhoogde temperaturen en temperatuurverschillen. Experimenten met Al–Mg plaat tonen aan dat de dieptrek-verhouding hiermee kan worden verhoogd tot hetzelfde niveau als voor vervormingsstaal.

Bij kamertemperatuur is het mechanisch gedrag van Al–Mg plaat vrijwel onafhankelijk van de reksnelheid. Ook een verhoging van de temperatuur tot 100 °C heeft bijna geen invloed op de spannings–rek-relatie. Boven de 125 °C neemt de treksterkte af en neemt de reksnelheidsafhankelijkheid toe. De initiële vloeispanning verandert echter weinig tot aan 175 °C. Boven 175 °C neemt ook de initiële vloeispanning af.

Er is een numeriek model ontwikkeld om het warm vervormen van Al–Mg plaat te simuleren. Een belangrijk aspect van het numerieke model is de modellering van het materiaalgedrag. Zowel de versteviging, inclusief temperatuur- en reksnelheidsinvloed, als de spannings–rek relatie onder meerassige belasting moet worden beschouwd. Er worden twee verstevigingsmodellen met elkaar vergeleken: een fenomenologisch model, waarbij de parameters van een Ludwik–Nadai model en een machtsrelatie voor de reksnelheidsafhankelijkheid afhankelijk zijn gemaakt van de temperatuur en een model op fysische grondslag, zoals voorgesteld door Bergström. Dit laatste model bevat temperatuur- en reksnelheidsafhankelijkheid van de vloeispanning en versteviging, gebaseerd op dynamisch herstel. Voor rek bij een constante temperatuur en reksnelheid reduceert het Bergström model tot het bekende Voce verstevigingsmodel. De Ludwik–Nadai en de Bergström–Voce modellen kunnen beide redelijk goed aangepast worden aan de resultaten van monotone trekproeven. Voor grote rekken geeft het Bergström–Voce model een betere voorspelling dan het Nadai model. Grote verschillen ontstaan echter als de reksnelheid ineens wordt veranderd. Na een reksnelheidssprong bereikt de experimentele spannings–rek-kromme met enige vertraging de kromme die hoort bij een test met de corresponderende constante reksnelheid. Het Bergström model overschat het rek-increment dat nodig is om een spanning te bereiken die correspondeert met de nieuwe reksnelheid sterk.

Van het gebruikte materiaal zijn biaxiale spannings–rek relaties bepaald door middel van éénassige, vlak-vervormings, afschuivings en equi-biaxiale experimenten. De resultaten hiervan zijn vergeleken, en aangevuld, met berekeningen op basis van kristal-plasticiteit. Hiermee kan worden aangetoond dat het veelgebruikte Hill '48 vloeï-oppervlak niet geschikt is voor de simulatie van de vervorming van aluminium. De lage *R*-waarden voor aluminium leiden tot een aanzienlijke onderschatting van de equi-biaxiale vloeispanning. In de

simulatie van het dieptrekken van een cilindrisch bakje resulteert dit in een veel te dunne bodem. Het Vegter vloeicriterium is flexibel genoeg om de vorm van het vloeiooppervlak en de anisotropie nauwkeurig vast te leggen.

In plastische vormgevingsprocessen treden grote vervormingen op. De meeste beschrijvingen van plastische deformatie gaan uit van reksnelheden of van kleine vervormingen. Voor grote vervormingen moeten geschikte rekdefinities of objectieve afgeleiden worden gebruikt. De resultaten van de afschuivingsproef zijn in het bijzonder gevoelig voor de keuze van de objectieve afgeleide. Voor materialen met slechts een lichte textuur kan op basis van kristal-plasticiteit aannemelijk worden gemaakt dat de invloed van de keuze voor een bepaalde objectieve afgeleide van dezelfde orde is als de verandering van het vloeiooppervlak als gevolg van deformatie. Dit betekent dat, als in een berekening het vloeiooppervlak niet wordt aangepast, de keuze voor een specifieke objectieve afgeleide geen relevante verbetering geeft van de resultaten.

De vervormbaarheid van plaatmateriaal wordt in belangrijke mate bepaald door het optreden van insnoering. Dit is een geometrische instabiliteit, waarbij de versteviging van het materiaal de afname van de plaatdikte niet meer kan compenseren. De rek waarbij deze instabiliteit optreedt kan worden bepaald met een Marciniak–Kuczynski analyse. De nauwkeurigheid van deze methode wordt bepaald door de nauwkeurigheid van het materiaalmodel. De nauwkeurigheid van het materiaalmodel is hierbij veel kritischer dan bijvoorbeeld bij het bepalen van de gereedschapskrachten of de algemene dikteverdeling. Een eindige-elementenberekening met schaalementen kan insnoering modelleren op dezelfde manier als een M–K analyse. In een eindige-elementen model worden de randvoorwaarden beter gerepresenteerd dan in een M–K analyse. Als nauwkeurige materiaalmodellen worden gebruikt kan het optreden van insnoering worden voorspeld, zonder gebruik te maken van een vergelijking met grens-vervormingsdiagrammen.

Voor de simulatie van industriële plaatvervormingsprocessen worden vaak expliciete berekeningsmethoden gebruikt. Impliciete methoden zijn in principe nauwkeuriger, maar de oplossing van een stelsel vergelijkingen kost voor grote modellen teveel tijd. Iteratieve oplossingsmethoden voor lineaire stelsels, staan erom bekend dat ze slecht presteren voor modellen met schaalementen omdat de stijfheidsmatrix slecht geconditioneerd is. Door de bijdrage van massa-traagheid niet te verwaarlozen—wat meestal wel gedaan wordt—kan het conditiegetal van de matrix worden verbeterd. Het gebruik van iteratieve methoden kan in dat geval de rekentijd bij impliciete berekeningsmethoden met factoren reduceren ten opzichte van het gebruik van directe methoden. Als gebruik wordt gemaakt van massaschaling, zoals gebruikelijk is bij expliciete methoden, kan de impliciete methode wedijveren met expliciete methoden.

# Preface

In 1998, a project on the forming of light metals was started within the framework of the Netherlands Institute for Metals Research.<sup>1</sup> The NIMR is a research organisation funded by the Dutch government and the Dutch metals industry, based at four Dutch universities and the Netherlands Organisation for Applied Scientific Research (TNO). The main subject of this project was the warm forming of aluminium sheet. This particular project was atypical in the sense that it was performed by permanent staff from TNO and the University of Twente and it was, at first, not the intention that it would result in a thesis. The project consisted of an experimental part and a numerical part. The experiments were the main responsibility of TNO and the numerical simulations were the main responsibility of the University of Twente *viz.* the author of this thesis.

The project was finished at the end of 2001, but as the work progressed, it was suggested that the results would form a sound basis for a doctoral thesis if extended with a more theoretical background on the material models. This extension is elaborated in the sections on polycrystal plasticity and stability of deformation. Large-scale analysis of sheet forming processes required the use of iterative solvers, which were investigated by the author back in 1997. An important step forward was reached in 2000–2001 with the introduction of dynamic terms in the finite element equations. The method is described in this thesis because it is applied to the presented applications, but is much more generally applicable than in the analysis of warm forming of aluminium only.

## Acknowledgements

With an organisation of the presented work as described above, it is obvious that many people contributed to the final result. In an attempt to thank all people involved, I will follow a more or less chronological order.

After my graduation in 1988, I learned a lot about computational mechanics and finite element programming from my former colleagues at TNO Building and Construction Research. My knowledge of nonlinear solution strategies and the application of iterative solvers was founded there.

I thank Henk Tjeldeman and Han Huétink for offering me a position at the University of Twente in 1995. In retrospect, it is hard to believe that I hesitated to take this opportunity at first and I still do not regret that I finally did. It is a pleasure to work in the section for Applied Mechanics and Polymers, thanks to all past and present colleagues—permanent staff, Ph.D. students and graduate students alike. With respect to this thesis, I specially

---

<sup>1</sup>Project ME 97033b of the Netherlands Institute for Metals Research ([www.nimr.nl](http://www.nimr.nl)).

acknowledge the encouragement of Han Huétink to continue this research, the co-operation with Timo Meinders on the dynamic regularisation for sheet forming simulations and the patient explanations from Jenö Beyer regarding the physics of plastic deformation.

The longstanding co-operation between the ‘Simulation of Forming Processes’ group in Twente and Corus Research Development and Technology manifests itself in regular meetings, specially with the Product Application Centre. These meetings form a response group, in which academic ideas can be tested against industrial relevance and applicability. I appreciate the contribution from all members in these meetings. Henk Vegter and Peter van Liempt deserve special reference for their elucidation on physically based material models.

Pieter Jan Bolt from TNO is acknowledged for initiating the NIMR project on light metals. He and Robert Werkhoven performed the TNO part of the project and our regular discussions have had a significant influence on the results. The extended Nadai model and the MSC.MARC calculations, mentioned in this thesis, are due to Robert. Joop Brinkman, Loes van Haaren and Erik van de Ven from the University of Twente, Marco van Hout, Jaco van Leeuwen en Peter de Maat from TNO and Louisa Elliot from Corus RD&T performed the mechanical experiments. Uniaxial tensile tests and deep drawing experiments were performed by TNO. The equi-biaxial yield curve, the grain size and the chemical composition were determined by Corus RD&T. The plane strain tension and simple shear tests and the uniaxial tensile tests with strain rate jumps were performed at the University of Twente.

Prof. Van Houtte and Dr. Saiyi Li from the Catholic University of Leuven are acknowledged for the determination of the orientation distribution function for the used material and the determination of discrete sets of orientations that were used in the polycrystal analyses.

Finally, the text of this thesis improved considerably from the comments of Han Huétink, Timo Meinders, Kasper Valkering, Jenö Beyer, Loes van Haaren, Marcel Brekelmans and Katrina Emmett who read the complete or parts of the manuscript.

Other people have supported me, but cannot be placed in the above chronology. Friends and relatives took care that my mind was not always on mechanics and material models. Family, former house-mates, college friends, climbers, I enjoy your company and cherish our friendship. A special word of thanks goes to my parents, who always stimulated me to achieve the goals that I had set for myself, even if the route was difficult and dangerous. The last word of thanks is reserved for Hester, from whom I borrowed so much time in order to finish this thesis.

Ton van den Boogaard  
Hengelo, October 2002

# Nomenclature

## Roman symbols

<b>B</b>	element strain–displacement matrix
<i>b</i>	magnitude of the Burgers vector
<b>C</b>	capacity and damping matrix
<b>D</b>	rate of deformation
<b>d</b>	degrees of freedom vector in a discretised system
<i>E</i>	Young’s modulus
<b>F</b>	deformation gradient
<b>f</b>	force vector in a discretised system
<i>f<sub>(.)</sub></i>	yield stress ratio with respect to the uniaxial yield stress
<b>G</b>	shear modulus
<b>K</b>	stiffness matrix
<i>k</i>	Boltzmann’s constant ( $1.3807 \cdot 10^{-23}$ J/K)
<b>L</b>	velocity gradient
<b>M</b>	mass matrix
<b>m</b>	slip plane normal
<b>N</b>	element interpolation matrix
<b>P</b>	symmetric part of the Schmid tensor <b>T</b>
<b>Q</b>	skew-symmetric part of the Schmid tensor <b>T</b>
<b>q</b>	heat flux vector

<b>R</b>	rotation tensor
<i>R</i>	Lankford <i>R</i> -value, ratio between width and thickness strain
<i>R</i>	universal gas constant (8.3144J/(mol K))
<b>r</b>	residual force vector in a discretised system
<b>s</b>	slip direction
<b>T</b>	Schmid tensor <b>sm</b>
<i>T</i>	temperature
<b>U</b>	right stretch tensor
<i>U</i>	dislocation storage parameter in Bergström model
<b>u</b>	material displacement vector
<b>v</b>	material velocity vector
<b>W</b>	spin tensor
<b>w, w</b>	weighting functions
<i>w</i>	work
<b>Z</b>	Zener–Hollomon parameter

### **Greek symbols**

<b><math>\alpha</math></b>	back-stress tensor
$\alpha$	stress ratio $\sigma_2/\sigma_1$
$\beta$	parameter in the Newmark scheme
$\beta$	strain ratio $\varepsilon_2/\varepsilon_1$
$\Gamma$	equivalent slip value
$\Gamma$	boundary of analysis domain
$\gamma$	parameter in the Newmark scheme
$\gamma$	shear strain (tangent of shear angle)
$\dot{\gamma}$	slip rate
<b><math>\epsilon</math></b>	infinitesimal strain tensor
$\epsilon_{\text{eq}}$	equivalent plastic strain



$\theta$	hardening rate
$\Lambda_{\text{prop}}$	global proportionality factor
$\lambda$	material conductivity tensor
$\lambda$	stretch factor (eigenvalues of $\mathbf{U}$ )
$\lambda_{\text{prop}}$	current proportionality factor
$\rho$	dislocation density
$\rho$	mass density
$\sigma$	Cauchy stress tensor
$\sigma_{\text{eq}}$	equivalent stress
$\sigma_{\text{f}}$	flow stress
$\tau$	(resolved) shear stress
$\tau^{\text{c}}$	critical resolved shear stress
$\phi$	yield function
$\Omega$	rate of rotation $\dot{\mathbf{R}} \cdot \mathbf{R}^{\text{T}}$
$\Omega$	recovery parameter in Bergström model
$\Omega$	analysis domain

### General subscripts and superscripts

$(\cdot)_{1,2,3}$	principal values
$(\cdot)_{\text{bi}}$	equi-biaxial
$(\cdot)^{\text{e}}$	elastic part
$(\cdot)^{\text{L}}$	lattice part
$(\cdot)^{\text{P}}$	plastic part
$(\cdot)_{\text{ps}}$	plane strain
$(\cdot)_{\text{sh}}$	pure shear
$(\cdot)_{\text{un}}$	uniaxial
$(\cdot)_{\alpha}$	reference to slip system $\alpha$
$(\cdot)_{\theta}$	angle between tensile and rolling direction

### **Operators**

- [.] components of a tensor in matrix form
- $\dot{x}$  material time derivative of  $x$
- $\mathbf{a} \cdot \mathbf{b}$  single tensor contraction:  $a_i b_i$
- $\mathbf{A} : \mathbf{B}$  double tensor contraction:  $A_{kl} B_{kl}$
- $\|\cdot\|$  Euclidean norm
- $\nabla x$  gradient of  $x$

### **Abbreviations**

- b.c.c. body centred cubic
- d.o.f. degree(s) of freedom
- f.c.c. face centred cubic
- FEM finite element method
- FLC forming limit curve
- FLD forming limit diagram
- M–K Marciniak–Kuczynski (analysis)
- ND normal direction
- RD rolling direction
- TD transverse direction

# 1. Introduction

## 1.1 The Significance of Weight Reduction

In the world around us, we can see many metals. In an industrial environment, in transportation, and also in domestic applications large amounts of steel, aluminium, copper and other metals are used. Metals are used in these applications mainly because of their stiffness, strength, resistance to low and high temperatures and good formability. Another legitimate reason is that engineers have experience in working with these materials. The combination of these and other factors, like the price, makes the application of metals economical.

In the transport industry the need for weight reduction is unquestionable, for aerospace structures as well as for railway and road vehicles. Current and future government regulations require a reduction in exhaust emissions for cars and trucks. There is a general consensus that this cannot be reached by engine improvements alone. It is estimated that a 10% reduction in vehicle weight improves the fuel efficiency by 5.5% (Miller *et al.*, 2000). Exhaust emissions will be proportionally lower. Also in other areas, *e.g.* all kinds of portable equipment, a low weight is a desirable attribute.

The weight of a structure is determined in the design process, in which the shape and type of material for a particular product are selected, based on the functions to be performed. Often one of the functions is of a structural kind. In order to obtain a low weight, the ratio of strength or stiffness to mass density of the material should be high. Compared to traditional steel products weight reduction can be reached by using *e.g.* plastics, composites, light metals or high strength steels (HSLA). In Table 1.1 the density,  $\rho$ , specific stiffness,  $E/\rho$ , and specific strength,  $\sigma_{0.2}/\rho$ , are given for a number of materials. It can be seen that the specific stiffness for metals does not differ much. For the specific strength a typical alloy for the material class is chosen. The strength of plastic and fibre reinforced plastic is a rough estimate, because the materials show significant creep and a yield stress cannot be given.

The specific stiffness and strength, as presented in Table 1.1, are not the only relevant parameters for materials selection. Corrosion resistance, thermal stability, fatigue behaviour, formability, weldability and last but not least the price also have a strong influence.

Plain plastic is often used in relatively small parts with low structural and thermal loads, *e.g.* the housing of portable electronic equipment. These parts can be produced cheaply and at large volumes by injection moulding. For heavily loaded lightweight structures, fibre reinforced plastics can be used. Fibre reinforced plastics have a high specific strength, but the thermal stability is limited and production times are long, hence costly.

Castings of aluminium and magnesium are already quite common in *e.g.* engine blocks and wheel rims. Recent developments of full aluminium car bodies demonstrate the use

Table 1.1: A comparison of weight related parameters for a range of materials (Stiomak/tht, 1978).

material	$\rho$ ( $10^3 \text{ kg/m}^3$ )	$E/\rho$ ( $10^6 \text{ N m/kg}$ )	$\sigma_{0.2}/\rho$ ( $10^3 \text{ N m/kg}$ )
FeP04 (mild steel)	7.85	25	28
A 607 gr.50 (HSLA steel)	7.85	25	42
AlMg5 (aluminium)	2.63	27	42
MgAl3Zn (magnesium)	1.78	25	100
TiAl6V4 (titanium)	4.43	26	233
polystyrene	1.1	1–3	10–20
glass fibre/EP	1.5–2	10–20	> 60

of extruded aluminium tubes in space frame structures and aluminium sheet for inner and outer panels, and in a more conventional design for the body structure. Weight reductions of 50% for the ‘body in white’ have been achieved by the substitution of steel by aluminium (Carle and Blount, 1999; Miller *et al.*, 2000). The numbers in Table 1.1 indicate that HSLA steel is also a good candidate to achieve weight reduction, but the formability is considered less than aluminium, which is already less deformable than mild steel (Wilson, 1988). Magnesium sheet is definitely less deformable than aluminium and is therefore not considered an alternative at the moment. Based on the specific strength, titanium would be a good choice, but for most applications this material is much too expensive.

The application of light metals or high strength steel is hampered by higher costs and lower formability of the materials, compared to mild steel. Lower formability can be expressed in higher production costs. The materials in Table 1.1 that would seem most promising from a technical point of view are rejected because of higher material or production costs. High strength steel and aluminium alloys are economically feasible alternatives for mild steel sheet in automotive applications. Of these two, aluminium is more easily deformable than high strength steel. The formability of aluminium sheet is, however, not as good as mild steel. To enlarge the application of aluminium sheet, the formability can be improved by increasing the temperature during the forming process. The numerical simulation of such a process is the subject of this thesis.

## 1.2 Formability of Aluminium Sheet

Typical sheet metal forming processes are bending, deep drawing and stretching. Bending is used if only a single curvature must be created. The minimum bending radius is limited by the maximum attainable strain in uniaxial loading. If a doubly curved product must be made from a metal sheet, the deep drawing process or the stretching process is used. The deep drawing process can reach production cycles of less than 10 seconds, and is hence a suitable process for mass production.

In deep drawing and stretching the stresses normal to the sheet are usually very small compared to the in-plane stresses and are therefore neglected. Hence, a biaxial stress state

is considered. Two important failure modes limit the applicability of the deep drawing and stretching process: necking and wrinkling. Both are closely related to the material properties and the local biaxial stress state. On top of that, wrinkling also depends on the sheet thickness and the local curvature of the sheet (Hutchinson and Neale, 1985; Selman *et al.*, 2002). Therefore, the formability of a material, without reference to the product geometry, only considers the necking failure.

The formability of aluminium sheet is, under normal processing conditions, lower than for a typical mild steel. This means that the maximum attainable strain in one process step is less than that for mild steel along the same deformation path. Hence press operations are often more critical for aluminium than for mild steel. The formability is affected by the composition of the aluminium alloy. Aluminium-magnesium alloys (the AA 5xxx series) have a relatively good formability. A disadvantage is that these alloys suffer from stretcher lines, which gives an uneven surface after deformation. In automotive applications, therefore, these alloys are mostly used for inner panels. For outer panels, aluminium-magnesium-silicon alloys (the AA 6xxx series) are often used. The lower formability is less important here.

The mechanical properties of aluminium alloys can be influenced by varying the temperature. This can be exploited to improve press operations. A paper by Takuda *et al.* (2002) contains references to publications, relating to this subject, dating back to 1946 and the early 1950s. After some publications in the 1970s and 1980s by Shehata *et al.* (1978); Wilson (1988); Schmoeckel and Heller (1988) the research accelerated in the last decade (Schmoeckel *et al.*, 1995a,b; Naka and Yoshida, 1999; Bolt *et al.*, 2000, 2001; Moon *et al.*, 2001). It was demonstrated that the formability improves by a uniform temperature increase, but the best results are obtained by applying temperature gradients. In deep drawing experiments with AA 5754-O, the limiting drawing ratio could be increased from 2.1 to 2.6 by heating the flange up to 250 °C and by cooling the punch to room temperature (Van den Boogaard *et al.*, 2001b). This leads to an increase in maximum attainable cup height by 70%. The resulting cups are presented in Figure 1.1. An extra benefit of warm forming is that the stretcher lines that develop when Al-Mg alloys are deformed at room temperature do not appear at elevated temperatures.

### 1.3 Objective of this Thesis

Controlling the temperature distribution in a workpiece can enhance the formability of aluminium. This expands the process window for a feasible stamping process. However, experience with temperature controlled stamping is lacking and it would be beneficial if the process could be optimised by numerical simulations instead of trial and error in the workshop. The objective of this thesis is to show how deep drawing of Al-Mg alloys at elevated temperatures can be simulated. Of particular interest is the prediction of thickness distributions in the final product and the onset of necking, because these have an impact on the product performance and determine the limits of formability.

In order to be able to simulate the forming process, the most important requirement is to have a proper material model. This model should describe the relation between strain, strain rate, temperature and stress. With a material model, a prediction of formability can be made by plastic stability analysis. This should give the strain at the onset of necking for



Figure 1.1: Maximum cup heights achieved at 20 °C (left) and with the flange at 250 °C (right) (courtesy TNO Industrial Technology).

different deformation paths. If the model is not too complex, it can be used in a large scale finite element analysis. FE simulations of deep drawing are performed on a regular basis nowadays, but only very few simulations of thermo-mechanical analysis of sheet forming have been published (Keum *et al.*, 2001; Van den Boogaard *et al.*, 2001a,b; Takuda *et al.*, 2002).

The finite element solution procedure must include a calculation of the temperature in the workpiece, depending on a prescribed temperature in the tools. For large scale sheet forming simulations, an efficient analysis requires the use of shell elements. In the case of warm forming, these elements must be equipped with thermal degrees of freedom. The contact conditions between tool and workpiece must include the heat transfer. In order to be useful for optimisation of the process, it should be feasible to perform an analysis ‘overnight’, also for relatively large models. This puts constraints on the allowable computation time for the material model and requires efficient solution of the resulting global sets of equations.

In broad outline, the modelling of the material behaviour is discussed in the first part of this thesis. The finite element method and its application to warm forming processes is the subject of the remaining part.

## 1.4 Terminology and Notation

The simulation of forming processes involves research areas such as manufacturing technology, computational mechanics, materials science, numerical mathematics and software engineering. In this thesis, the terminology and symbols that are widely used in these fields are adopted as much as possible. However, sometimes conflicts arise because, in the literature, the same symbol is used for different phenomena, or the same phenomena are given different symbols. In these cases the terminology of the computational mechanics community is followed. It can occur sometimes, that the same symbol has different meanings

in different parts of the thesis. An overview is given in the *Nomenclature* at the beginning of the thesis.

## Metals, Alloys and Material Models

Multidisciplinary research, as that presented here, can give rise to confusion of tongues. The research presented in this thesis was performed by a mechanical engineer with a specialisation in computational mechanics. For the modelling of the material behaviour an appeal was made to materials scientists. Materials scientists, reading this thesis, should be aware of the following differences in terminology.

In this thesis the engineering sense of the word *metals* is used, which include all metallic materials, such as alloys. This as opposed to materials science, where a distinction is made between (pure) metals and alloys.

During the research for this thesis, it was found that the term ‘material modelling’ could lead to confusion. In this work, material modelling is restricted to the mechanical behaviour of materials: relating stresses and strains, given a prescribed deformation path including the influence of strain rate and temperature. The model should describe the mechanical behaviour of the material that is used in the forming process. The parameters that are used in the model are commonly determined by experiments on that particular material. This is somewhat different from materials science, where ‘material models’ serve to predict mechanical and other behaviour, based on the composition of the metal (alloy) and the thermo-mechanical history that determines the grain size, texture and micro-structure.

## Tensor Notation

Regarding tensors, the notation often used in physics was adopted, in which a dyadic product is implied without a symbol. Hence  $\mathbf{ab}$  is the dyadic product of the vectors  $\mathbf{a}$  and  $\mathbf{b}$ . In mathematical texts this is often presented as  $\mathbf{a} \otimes \mathbf{b}$ . On the other hand, for a contraction of first or higher order tensors a dot is used, or a colon for a double contraction. In mathematical texts contractions are often implied without a symbol. The definition of the single and double contraction is implied by giving the equivalent index notation:  $\mathbf{C} = \mathbf{A} \cdot \mathbf{B}$  is represented by  $C_{ij} = A_{ik} B_{kj}$  and  $c = \mathbf{A} : \mathbf{B}$  is represented by  $c = A_{ij} B_{ij}$ , applying the summation convention over repeated indices.

In general, non-bold letters are scalars, bold lower-case letters are vectors (1st order tensors) and bold upper-case letters are 2nd or higher order tensors. The upper and lower case distinction does not apply to Greek letters, or to other cases where the use of a particular symbol is customary, e.g.  $\sigma$  for the 2nd order stress tensor. Note that in this thesis, upper or lower case symbols do *not* imply the reference to an initial, intermediate or current configuration. In Appendix A some topics of tensor algebra are presented.

## 1.5 Outline

The simulation of deep drawing of aluminium at different temperatures and strain rates requires a model for the mechanical behaviour of the material. In Chapter 2 experimental

observations on an AA 5754-O alloy are described, including uniaxial tensile tests at different temperatures and strain rates, and biaxial tests at room temperature. This is followed by a chapter on material models. To describe the multiaxial behaviour of the material, several yield functions are considered. For comparison, also a polycrystal based model is described. To model the work hardening, some phenomenological and physically based hardening laws are considered.

Because large deformations are involved, the experiments and material models are described in terms of so-called true stress and true strain. These measures are valid for proportional deformation. Although not all experiments are completely proportional, the complications that arise in large deformation mechanics are not discussed until Chapter 4. Numerous strain measures can be defined in large deformation mechanics. With the help of the polycrystal model some light can be shed on this matter.

With the description of the material model and large deformations we are ready to consider the necking problem in Chapter 5. Necking is an unstable type of deformation in which further loading leads to localised deformation and, finally, to fracture. Without considering a complete forming process, the Marciniak–Kuczynski analysis is used to clarify the phenomena that influence the maximum allowable strain. The results are compared with finite element simulations of some simple geometries, in order to see whether a finite element analysis is able to predict the onset of necking.

In Chapter 6 the finite element discretisation and an efficient solution method for sheet forming simulations are considered as a precursor to Chapter 7 in which two applications are presented. First a tensile test is simulated, including the non-uniform part of the clamping area. The second application concerns the warm forming of a cylindrical cup. Two and three-dimensional simulations are performed. The results are extensively compared with experiments. Finally, in Chapter 8, the conclusions from this research are summarised and directions for future work are given.



## 2. Experimental Observations

The goal of the research described in this thesis is to simulate the warm forming of Al–Mg sheet at temperatures of up to 250 °C. In order to obtain accurate results, an appropriate model for the mechanical behaviour of the material is required. The selection of a proper material model and the determination of parameters for the model should be based on experimental observations.

In this chapter, results of a number of experiments are described. The alloy AA 5754-O was used as a representative example of Al–Mg alloys. Sheet material with a thickness of 1.2 mm from one batch was used for the deep-drawing experiments described in Chapter 7 and the material tests described here.

In Section 2.1 some characteristics of this material are presented. Samples were prepared for uniaxial testing at several temperatures and strain rates, and for biaxial testing at room temperature. The uniaxial tests described in Section 2.2 are used to describe the hardening behaviour. The biaxial tests used to describe the shape of a yield locus are presented in Section 2.3.

### 2.1 Material Characteristics

In this section the material used in the experiments is characterised. The mechanical behaviour of an alloy is mainly determined by its chemical composition, grain size, texture and micro-structure. The composition, grain size and initial texture were determined for this particular Al–Mg sheet. The micro-structure develops during deformation and heat treatments. Phenomena that may be relevant for warm forming of Al–Mg alloys are discussed, based on the literature.

#### Composition, Grain Size, Texture

The chemical composition of the alloy was given by the manufacturer and is presented in Table 2.1. The main alloying element is magnesium, which is—in this amount—mostly in solid solution. It has a strengthening effect on the aluminium.

The average grain size of the alloy is 20–25  $\mu\text{m}$ . With X-ray diffraction, the texture was determined in the mid-plane of the sheet. In Figure 2.1, the orientation distribution function is presented. A weak cube texture can be observed, with the density of the cube orientation about four times that of a random texture.

Table 2.1: Chemical composition of the investigated AA 5754-O alloy.

%Mg	%Si	%Cu	%Mn	%Ti	%Al
3.356	0.130	0.010	0.320	0.009	rem.

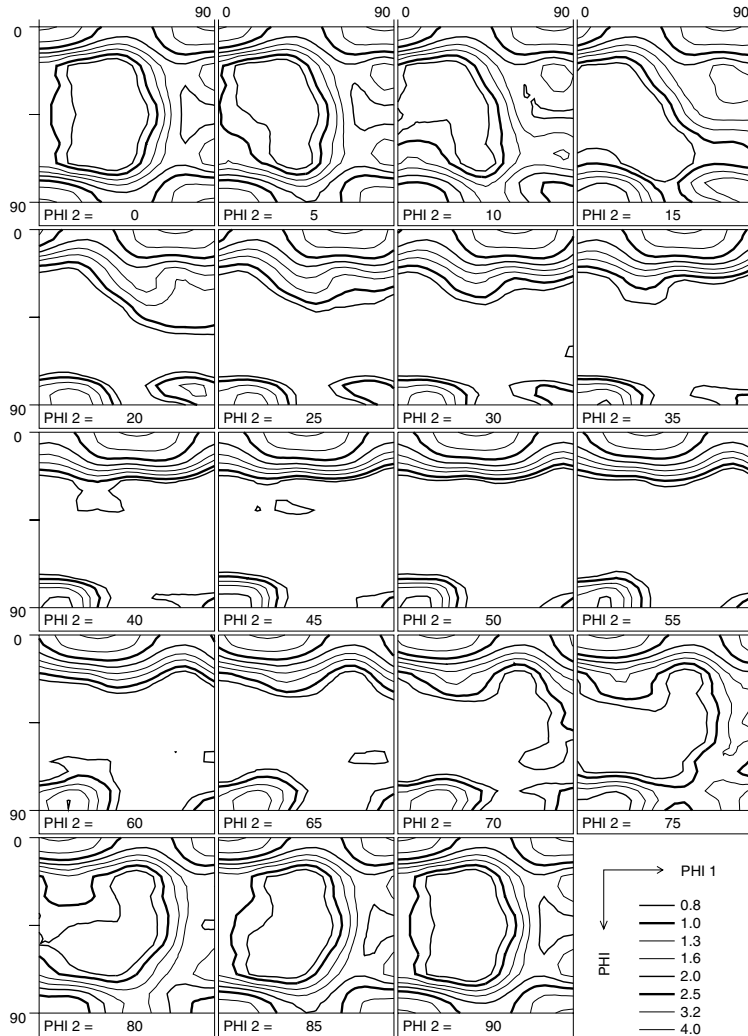


Figure 2.1: Orientation Distribution Function for the investigated AA 5754-O sheet.

## Dynamic Strain Ageing

In a tensile test at room temperature, Al–Mg alloys show serrated flow curves. This behaviour is known as the Portevin–Le Chatelier effect, which is attributed to dynamic strain ageing (see *e.g.* Hähner, 1996a,b; Wagenhofer *et al.*, 1999; Lebyodkin *et al.*, 2000). In a forming process, this effect can lead to so-called *stretcher lines* in a product and is therefore detrimental for visible parts.

A physical explanation for dynamic strain ageing is found in the interaction between dislocations and solute atoms. The dislocation movement is hampered by the solute magnesium atoms, leading to a higher initial yield stress. If dislocations move slowly (at low strain rates), the solute atoms can migrate to the dislocations while they are arrested at other obstacles or solutes. This further hampers the dislocation movement. The *solute drag* increases the flow stress repeatedly. On a macroscopic scale the behaviour of single dislocations cannot be observed and a continuous increase of the flow stress is found. This hardening effect is called *dynamic strain ageing*.

At higher strain rates the solutes cannot catch up with the dislocations and a lower flow stress is found. Macroscopically this appears as a negative strain rate sensitivity. The negative strain rate sensitivity can lead to instabilities. Locally, the strain rate can differ from the macroscopic strain rate, leading to stress variations that show as the Portevin–Le Chatelier effect. At elevated temperatures, the mobility of the solutes increases and the serrations disappear. Correspondingly, in forming processes, no stretcher lines develop at elevated temperatures.

## Heat Treatments

The AA 5754 alloy is generally classified as a *non-heat-treatable* alloy. This reflects that no precipitation hardening takes place. However, heat treatments such as annealing are very well possible. On deformation, the micro-structure of a metal changes, and most notably the dislocation density increases. This reveals itself as work hardening. By increasing the temperature sufficiently during a certain period, the dislocation density decreases, at least locally, and the material softens. The lowest temperature at which this occurs is the recovery regime (Verdier *et al.*, 1999). During recovery dislocations rearrange to a configuration of minimum energy, *e.g.* by forming wall structures, and the dislocation density decreases locally, but the material does not recrystallise. For Al–Mg alloys, recovery can start already at temperatures as low as 95–120 °C (Van Horn, 1967). Only after recrystallisation is the mechanical effect of deformation completely cancelled. This happens in Al–Mg alloys only above 250 °C. Recrystallisation requires higher temperatures or longer times than recovery and is not expected to happen in the experiments described in this thesis. The material is initially in the ‘O’ condition, which means that it is fully annealed. Therefore, the time that a specimen is held at elevated temperatures before deformation starts does not influence the results. Only after the first deformation some effect of recovery may be present. Since the duration of the experiments is less than one minute, not much influence is expected.

## Thermo-Mechanical Interactions

The melting temperature of Al–Mg alloys is of the order of 640 °C. With temperatures between 25 °C and 250 °C, the *homologous* temperature<sup>1</sup> is between 0.33 and 0.57. In this interval the physics of plastic deformation changes, *e.g.* the contribution of cross slip increases at higher temperatures. The influence of the temperature on the yield stress and hardening are dealt with in the following sections. The elastic parameters are not very sensitive to the exact composition of the material and are taken from the literature. In the next chapter, about material models, thermo-mechanical interactions will be discussed in greater detail.

## 2.2 Uniaxial Tensile Tests

In this section, the results of two types of uniaxial tensile tests are presented. First, tests at constant temperature and constant strain rate are described in Section 2.2.1. Secondly, tests at constant temperature with strain rate jumps are described in Section 2.2.2.

### 2.2.1 Constant Temperature and Strain Rate Tests

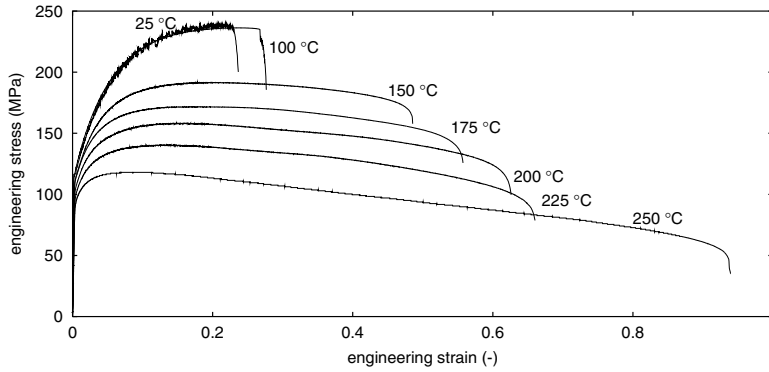
Tests at constant temperature and with constant strain rate were performed on a mechanical testing machine (Zwick) where the specimen and clamps were placed in a furnace with a maximum temperature of 250 °C. The specimen was made according to EN-10002, with a test section of 12.5 mm width and 75 mm length. The displacement was measured directly on the specimen over an initial gauge length of 50 mm. The temperature of the air in the vicinity of the specimen was controlled by a PID controller to within 1 °C. The specimen was clamped first on one side, and when it had reached the test temperature, the other side was clamped. To actuate the clamps, the furnace had to be opened. The test was initiated after the temperature had stabilised. Depending on the test temperature the procedure took 1 to 3 minutes.

Uniaxial tensile tests were performed at temperatures between 25 °C and 250 °C at strain rates of 0.002, 0.02 and 0.1 s<sup>-1</sup>. In all the tests described in this section, the tensile direction was perpendicular to the rolling direction in order to eliminate influence of the loading direction. For every combination of temperature and strain rate, 2 to 5 tests were performed, in some cases with a one year interval. The reproducibility of the ultimate tensile strength was typically better than 3 MPa and always better than 7.5 MPa. No systematic difference was found between the first test series and the series made one year later. For every combination of temperature and strain rate one representative stress–strain curve is shown in Figure 2.2.

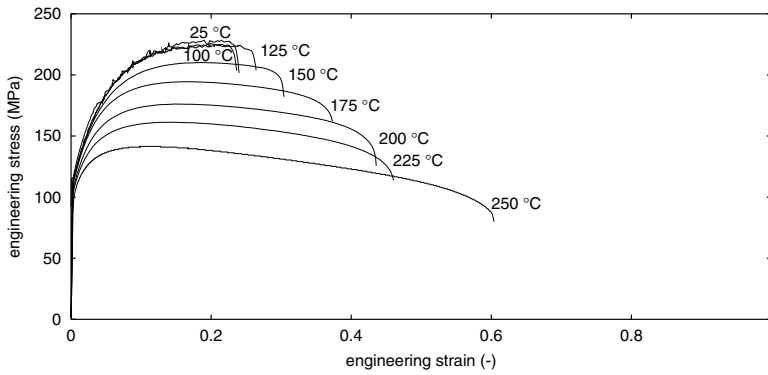
It is observed that, for all strain rates, the difference between the stress–strain curves at room temperature and at 100 °C is marginal. Above 125 °C, the ultimate tensile strength decreases with increasing temperature, and the stress–strain curves become strain rate dependent. With increasing strain rate the stress becomes higher and the ultimate strain decreases.

---

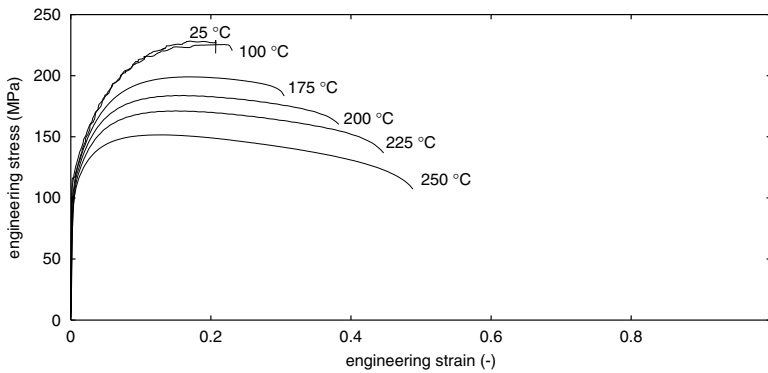
<sup>1</sup>The homologous temperature  $T_h$  is the absolute temperature divided by the absolute melting temperature.



(a)  $\dot{\epsilon} = 0.002 \text{ s}^{-1}$



(b)  $\dot{\epsilon} = 0.02 \text{ s}^{-1}$



(c)  $\dot{\epsilon} = 0.1 \text{ s}^{-1}$

Figure 2.2: Measured engineering stress–strain curves.

The *uniform strain* is defined as the strain where the engineering stress is at a maximum. In a well prepared test specimen, it is assumed that below the uniform strain, the deformation in the specimen is macroscopically homogeneous. In Figure 2.2 it is seen that the uniform strain decreases with decreasing ultimate tensile strength. In the absence of strain rate sensitivity, the uniform strain marks the onset of plastic instability resulting in severe local necking and rapid failure of the specimen. Therefore, at 25 °C and 100 °C, the uniform strain and the ultimate strain almost coincide. At higher temperatures, however, the uniform strain decreases, whereas the ultimate strain increases. Here, the strain rate sensitivity stabilises the plastic deformation and a diffuse neck develops.

The stress–strain curves at relatively low temperatures show the typical serrations of the Portevin–Le Chatelier effect, that result in stretcher lines on a product. The serrations do not appear in tests with a temperature of 150 °C and above.

In the investigated temperature range, the initial yield stress changes much less than the ultimate tensile strength. This indicates that the observed temperature dependence should be attributed mainly to the effect on hardening. In Figure 2.3 the initial part of the stress strain curves is plotted. It can clearly be seen that the Young's modulus depends on the temperature. However, the tests were focused on large deformations and no accurate determination of the Young's modulus was performed. If needed, the temperature dependent Young's modulus is taken from literature.

The initial yield stress is commonly defined as the stress after 0.2 % plastic strain. Taking the elastic deformation into account, Figure 2.3 shows that after 0.2 % plastic strain a reasonably smooth part of the stress–strain curve is reached.

The initial yield stress at 175 °C is almost equal to the yield stress at room temperature. At 100 °C and 125 °C it may be a little higher. Between 175 °C and 250 °C, the initial yield stress decreases by 10–20 MPa. The most significant decrease is at the lowest strain rate.

## **True Stress and Strain**

The engineering stress–strain curves presented in Figure 2.2 show the combined influence of the current stress in the material and the change in geometry of the specimen. The *true stress*, defined as the tensile force divided by the current cross section area, keeps increasing up to large strains, but because the cross section area is reduced, the total force reaches a maximum and decreases after that point. For plastically deforming materials the constitutive behaviour is a relation between strain rate and stress. The engineering strain rate, however, depends on the initial gauge length. A strain measure that relates strain rates to the current gauge length is the logarithmic strain, also known as *true strain*. As a link to material models, therefore, the uniaxial tensile test is usually presented in the form of true stress–strain curves, as presented in Figure 2.4. In the transformation between engineering and true strain and stress, volumetric incompressibility of plastic deformation is used and the elastic deformation is neglected.

Formally, only for a strain below the uniform strain, it can be assumed that the deformation in the specimen is uniform. Above the uniform strain, the strain localises. For the temperatures at which the material behaviour is strain rate dependent it was observed that the localisation was very diffuse. Therefore the true stress and strain in Figure 2.4 are calculated as if a uniform state existed within the gauge length. Up to the presented strain of

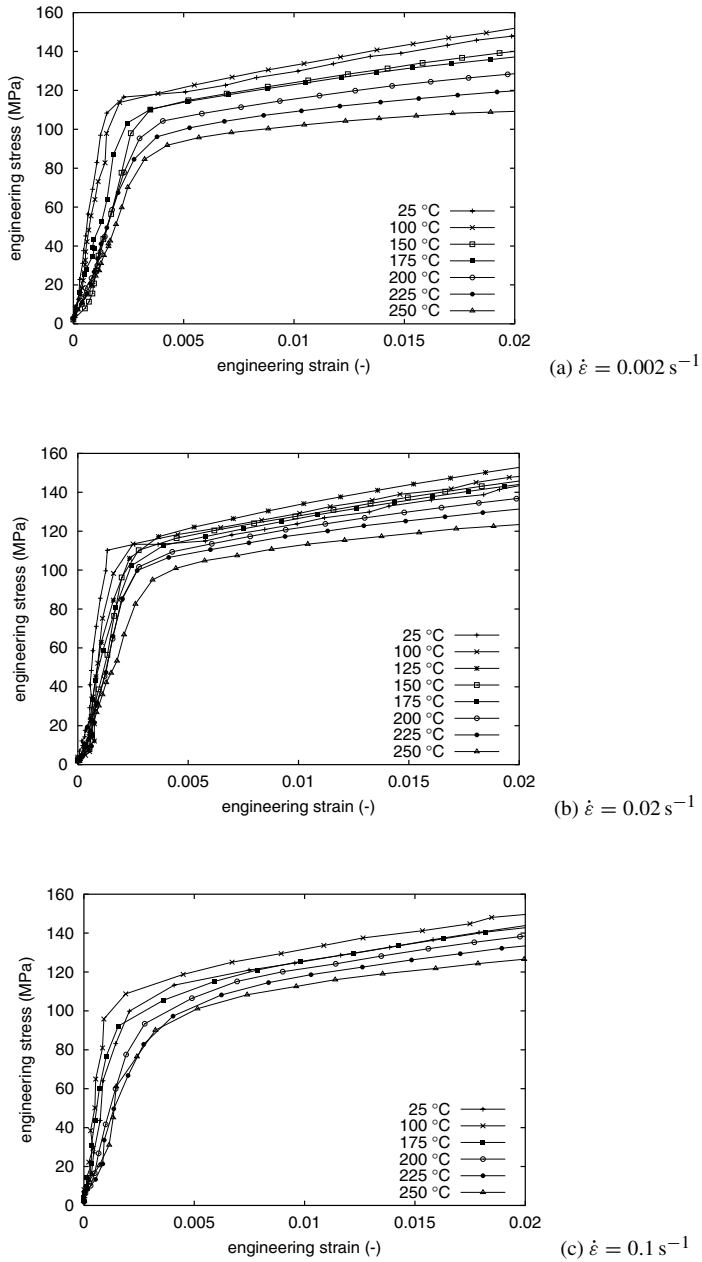
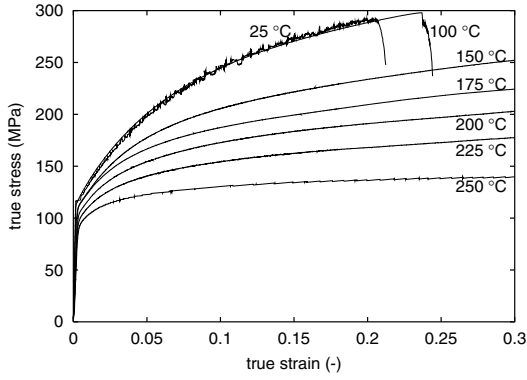
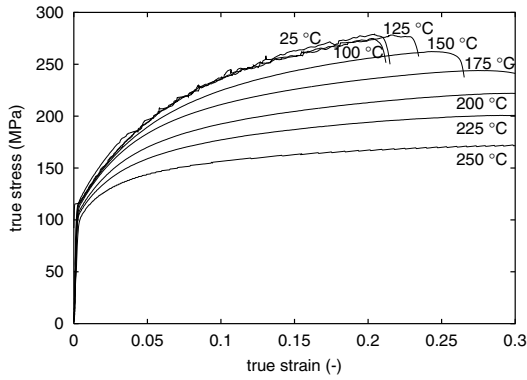


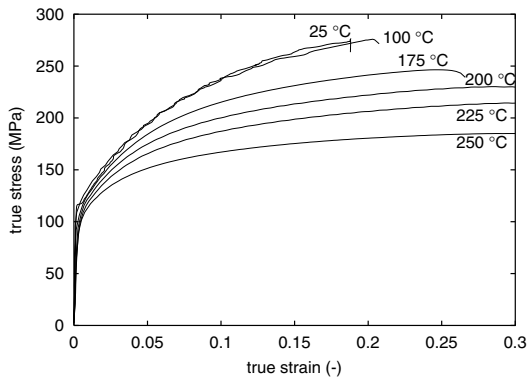
Figure 2.3: Initial part of stress–strain curves.



(a)  $\dot{\epsilon} = 0.002 \text{ s}^{-1}$



(b)  $\dot{\epsilon} = 0.02 \text{ s}^{-1}$



(c)  $\dot{\epsilon} = 0.1 \text{ s}^{-1}$

Figure 2.4: Temperature influence on true stress–strain curves.



0.3 this seems a reasonable assumption, but it cannot be extended to the ultimate strain.<sup>2</sup> It should be remembered that, also in Figure 2.2, the shape of the curves beyond the uniform strain depends on the actual size of the specimen.

### Strain Rate Effects

Another cross-view through the experimental results is given in Figure 2.5. Here the influence of the strain rate is visible. It can be seen that the strain rate sensitivity increases at higher temperatures. At 25 °C (not presented) and at 100 °C the lowest strain rate yields the highest stresses. Although the difference is not very large and some combinations of experiments could be drawn from the set of all experiments where the curves overlap, the general trend shows this phenomenon. This observation is often presented as a negative strain rate sensitivity of aluminium alloys and is attributed to dynamic strain ageing as described in Section 2.1.

At higher temperatures other effects dominate, such as remobilisation or annihilation of dislocations. At 175 °C *e.g.*, the more common situation is observed that the flow stress increases with increasing strain rate. The difference between the flow stress at a strain rate of 0.02 s<sup>-1</sup> and at 0.1 s<sup>-1</sup> is still quite small. At 250 °C the difference is more clear and the hardening at low strain rate becomes very small.

#### 2.2.2 Strain Rate Jumps

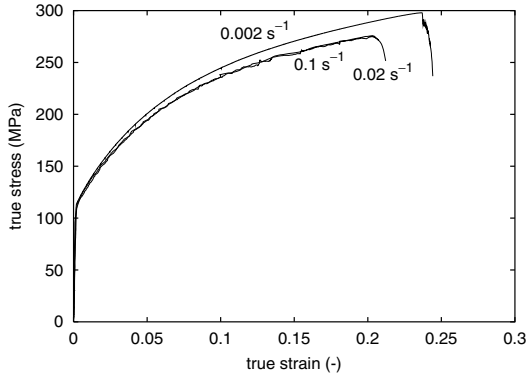
The uniaxial tests in the previous section showed a small influence of temperature on the initial yield stress and a large influence on the ultimate tensile strength. This led to the conclusion that the temperature mainly influenced the hardening behaviour and not the flow stress directly.

Each curve in Figures 2.2–2.5 was obtained at constant temperature and constant strain rate. If the temperature or strain rate is changed during deformation, it is not obvious that the stress will immediately adapt to the new situation. The evolution of the micro-structure during deformation may depend on the strain rate. At an instantaneous increase in strain rate, the micro-structure at that moment still represents the lower strain rate. If the test was performed at a constantly high strain rate, at the same strain the micro-structure would have been different. In general a distinction can be made between instantaneous strain rate sensitivity and total strain rate sensitivity (Yao and Zajac, 2000).

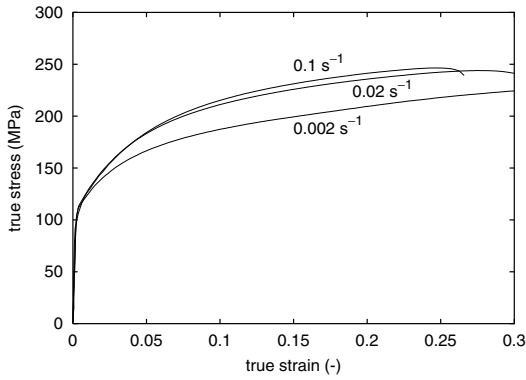
To investigate the behaviour of the material under non-constant strain rates, tests at constant temperature with strain rate jumps were performed on an Instron servo-hydraulic testing machine. In these tests, an oven is placed around the specimen and heated to the required temperature. The temperature of the specimen is measured with a thermocouple. The engineering strain is determined from the displacement of the clamps. An analysis of the results showed that the strain rate ‘jump’ was performed within 0.1 s, representing a strain increment of 0.0015. In Figure 2.6, the results of 4 tests at 175 °C and 4 tests at 250 °C are presented with strain rates of 0.002 s<sup>-1</sup> and 0.02 s<sup>-1</sup> and jumps from the lower to the higher strain rate and from the higher to the lower strain rate at a strain of 0.05.

---

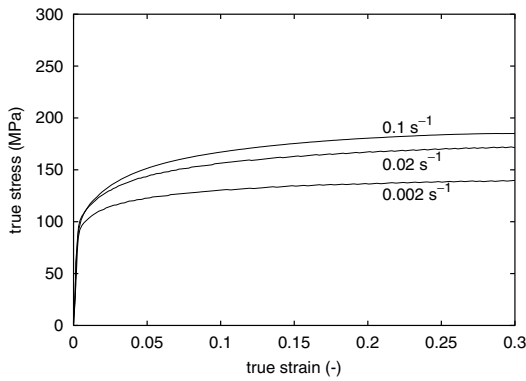
<sup>2</sup>Note that a true strain of 0.3 is equivalent to an engineering strain of 0.35.



(a)  $T=100^\circ\text{C}$



(b)  $T=175^\circ\text{C}$



(c)  $T=250^\circ\text{C}$

Figure 2.5: Strain rate influence on true stress–strain curves.

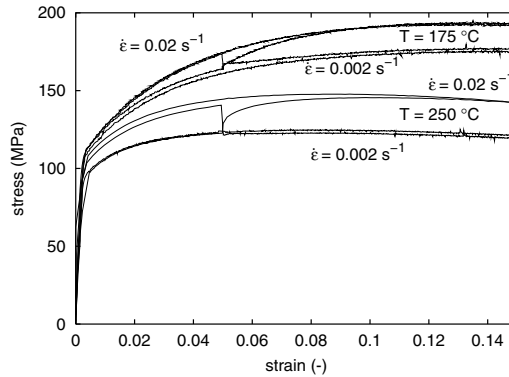


Figure 2.6: Measured engineering stress–strain curves with strain rate jump.

First of all it can be seen that the curve for a constant strain rate and the curve for a strain rate jump do not always overlap, even before the jump. This is attributed to a not completely reproducible temperature distribution in the specimen. Due to convection, the temperature at the bottom of the specimen was approximately  $20\text{ }^{\circ}\text{C}$  lower than in the centre and at the top of the specimen. It can be observed that the stress increased very rapidly after increasing the strain rate from  $0.002\text{ s}^{-1}$  to  $0.02\text{ s}^{-1}$  and then increased further at a lower rate until the curve was reached that represents the test with a constant strain rate of  $0.02\text{ s}^{-1}$ . The direct influence seems to be larger for the  $250\text{ }^{\circ}\text{C}$  experiment than for the  $175\text{ }^{\circ}\text{C}$  experiment. For a decreasing strain rate, the direct influence on the stress was much larger. Especially for the  $250\text{ }^{\circ}\text{C}$  experiment, the stress dropped immediately to the lower strain rate curve and no transient phenomenon was observed.

## 2.3 Biaxial Tests

The tests presented in Section 2.2 concentrated on the hardening in a uniaxial stress state, at several temperatures and strain rates. In sheet forming processes, the stress state is mainly biaxial. The stresses normal to the sheet are small compared to the in-plane stresses and are usually ignored, but both principal in-plane stresses can be non-zero. An infinite number of stress states can be defined, on top of an infinite number of strain paths to reach such a state. The principal stress directions are in general not equal to the principal axes of anisotropy of the material, nor do they remain constant during the deformation. To determine the material behaviour in multiaxial stress states only a limited number of stress or strain states are experimentally investigated. The data from these tests is supplemented by theoretical considerations, as described in the next chapter.

In addition to the uniaxial tests, normal compression tests, plane strain tests and simple shear tests were performed. The normal compression test is equivalent to an equi-biaxial tensile test, assuming that the plastic deformation is independent of the hydrostatic stress. A stack of sheet specimens was prepared with nominal dimensions of  $10 \times 10 \times 10\text{ mm}^3$ . The stack is loaded in the normal direction, and lubricated with oiled PTFE film. The

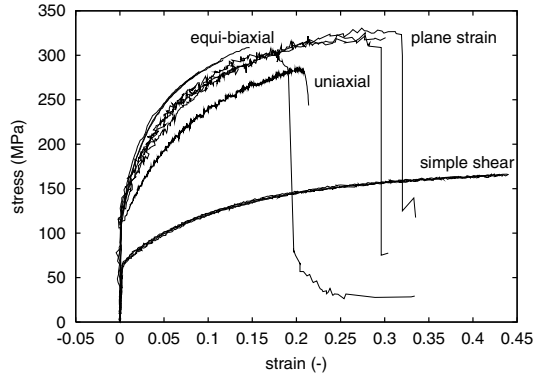


Figure 2.7: Stress–strain curves for different types of loading at room temperature.

displacements in the rolling and transverse directions are recorded as functions of the normal force. Three normal compression tests were performed.

The plane strain and simple shear tests were performed in a biaxial loading frame, as described by Pijlman (2001). In this loading frame a sheet area of  $45 \times 3 \text{ mm}^2$  can be deformed in plane strain tension or simple shear, or any combination of these simultaneously. The deformation in the plane strain and simple shear experiments is determined by recording the displacements of 4 dots on the specimen with a digital camera and subsequent image processing. The 4 dots are initially placed on the corners of a  $2 \times 2 \text{ mm}^2$  square in the middle of the deformation zone. With this equipment, no elevated temperature tests can be executed.

Plane strain tests were performed with the loading direction perpendicular to the rolling direction and at  $45^\circ$  to the rolling direction. Simple shear tests were performed with the shear direction at  $-45^\circ$ ,  $90^\circ$  and  $45^\circ$  to the rolling direction. For each direction two samples were tested. The stress–strain curves are presented in Figure 2.7 together with one uniaxial curve for comparison. For the uniaxial, plane strain and equi-biaxial tests, the true stress and strain in the loading direction are presented. For the simple shear test, the shear stress and the shear angle  $\gamma$  are used. In the normal compression test, the ratio between the true strain in the transverse and rolling directions was 1.17. This is a measure for planar anisotropy, additional to the  $R$ -values.

The irregularities on the uniaxial stress–strain curve are accurately measured serrations, due to dynamic strain ageing. The irregularities on the shear curve and especially the plane strain curve are due to the limited accuracy of the optical strain measurement in the horizontal direction and to serrations in the vertical direction.

It can be seen that the simple shear curves all fall on one common curve with a shear stress of approximately half the main stress in a uniaxial experiment. In the simple shear test, no thinning of the specimen takes place and therefore there is no geometric instability. The maximum attainable strain is larger than for tensile loading.

The plane strain curves also follow the same trend, but the measuring error and serrations are larger. The difference between the curves is larger than for the simple shear test. A systematic influence of the loading direction with respect to the rolling direction could not

be observed. The flow stress is systematically higher than the uniaxial stress. One of the specimens failed by fracture in the clamping area.

Usually, the maximum strain in a plane strain test would be lower than in a uniaxial test. However, in Figure 2.7 the limit strain for the plane strain test is larger. This is an artefact of the test. It was observed that in the middle of the plane strain specimen localisation starts. At both edges of the specimen, where we have a uniaxial stress state, the material integrity is maintained for a longer time. Since the strain is measured in the localised area, the large strain that is presented in Figure 2.7 does not represent a uniform state.

## 2.4 Conclusion

In this chapter some characteristics of Al–Mg alloys were presented that are relevant for the warm forming process. In general, the initial yield stress is hardly influenced by a change of temperature within the investigated temperature range. The hardening rate, however, reduces for increasing temperatures. This leads to a lower ultimate tensile strength and a reduced uniform strain. At temperatures above 125 °C the flow stress becomes strain rate dependent. At high strain rates, higher stresses are obtained than at low strain rates. Due to the strain rate sensitivity the fracture strain increases significantly, compared to tests at lower temperatures. A small negative strain rate sensitivity was observed at temperatures of 25 °C and 100 °C: the stress at a low strain is higher than at a high strain rate. For the investigated alloy this dynamic strain ageing effect is rather small.

With a proper material model, it should be possible to unite all observations. In the next chapter, existing material models are evaluated in an attempt to describe the mechanical behaviour of the material under different temperatures, strain rates and deformation histories.



## 3. Material Models

In the previous chapter, material experiments were presented showing the mechanical behaviour of a particular Al–Mg alloy. For process simulations, the experimentally observed behaviour must be cast into a material model. In this chapter, a number of material models are presented and their predictive capabilities with respect to warm forming of Al–Mg alloys are examined. Material models for plastic deformation that are used in process simulations commonly apply a separation of the model in a yield surface and an evolution of the yield stress (hardening). The yield surface determines the plastic flow in a multiaxial stress state, while a hardening law determines the evolution of the yield surface. The same approach is used here. In Section 3.1, a short repetition of classical continuum plasticity theory is presented. Special attention is paid to non-isotropic plastic behaviour in a plane stress condition. Then, in Section 3.2, a physical background is presented based on polycrystal plasticity. The polycrystal model will be used in Chapter 4 to predict the evolution of deformation texture and its effect on the yield locus. In Section 3.3, several yield functions are described that are suitable for use in finite element simulations. In Section 3.4 the work hardening and the influence of the temperature and strain rate are considered. The yield functions and hardening models will be used in the warm forming simulations in Chapter 7. The chapter ends with a short discussion.

### 3.1 Classical Rate Independent Plasticity

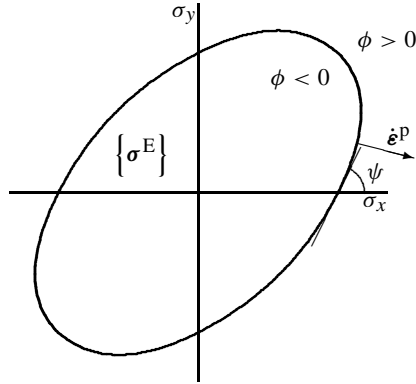
#### 3.1.1 The Yield Surface

When testing metals, often a uniaxial stress is exerted on a test-piece. The lowest stress which shows a permanent strain is called the yield stress. Below this stress the deformation is purely elastic. For metals, the elastic deformation is almost linear with respect to the stress. The generalised Hooke's law gives the relation between the stress tensor  $\sigma$  and the elastic strain tensor  $\epsilon^e$ :

$$\sigma = \mathbf{E} : \epsilon^e \quad (3.1)$$

where  $\mathbf{E}$  is a 4th order tensor with elastic moduli. In metal forming processes, the elastic strain is usually a very small part of the total strain. Nevertheless, if *elastic springback* is considered, the elastic strain cannot be neglected.

To describe plastic deformation under multiaxial loading, the concept of a yield surface is used. The yield surface is a hyper-surface in the 6-dimensional stress-space which is the closure of an elastic region. A 2-dimensional cross section through the yield surface shows a yield locus. For sheet forming simulations, the  $\sigma_x$ – $\sigma_y$ -plane is the commonly used cross

Figure 3.1: Typical yield locus for the  $\sigma_x$ - $\sigma_y$ -plane.

section to present a yield locus, where  $x$  and  $y$  denote two orthogonal axes in the sheet plane. A typical example is shown in Figure 3.1.

The yield surface bounds the elastic region  $\{\sigma^E\}$ . For numerical computations, a yield function  $\phi = \phi(\sigma, \dots)$  can be defined. The yield function depends on the stress tensor and additional variables, *e.g.* determined by the deformation history. The equation  $\phi = 0$  represents the yield surface. If  $\phi < 0$  the material behaves elastically. Stress states where  $\phi > 0$  are not feasible in an elastoplastic theory. If the stress state is on the yield surface, plastic deformation can occur. Following Drucker's postulate, the plastic strain rate  $\dot{\epsilon}^P$  is perpendicular to the yield surface,

$$\dot{\epsilon}^P = \dot{\lambda} \frac{\partial \phi}{\partial \sigma} \quad (3.2)$$

where  $\dot{\lambda}$  is a consistency parameter.<sup>1</sup> As a consequence of Drucker's postulate, the yield surface must be convex.

The yield surface can change size, position and shape, due to *e.g.* plastic deformation or a temperature change. A change of size, while the centre of the yield surface and the shape remain constant, can be modelled with isotropic hardening or softening. This is the most commonly used hardening model. With this model, a reversal of the load will cause plastic flow exactly at the same absolute values of stress as in monotonic loading. For isotropic hardening only one history parameter needs to be stored, usually the equivalent plastic strain.

A change in position of the yield surface in the stress-space can be modelled with kinematic hardening. With kinematic hardening, the size and shape of the yield surface remain constant. Computationally this is achieved by using an effective stress  $(\sigma - \alpha)$  in the yield function instead of  $\sigma$ . The tensor  $\alpha$  is called the *back-stress*. An evolution equation for the back-stress must be defined. For kinematic hardening, a (symmetric and deviatoric) second order tensor is used as history parameter. The simulation of cyclic loading improves

<sup>1</sup>The plastic strain rate,  $\dot{\epsilon}^P$ , and the plastic rate of deformation,  $\mathbf{D}^P$ , are equivalent, although in a large strain analysis  $\dot{\epsilon}^P$  is not really the time derivative of a specific strain tensor.



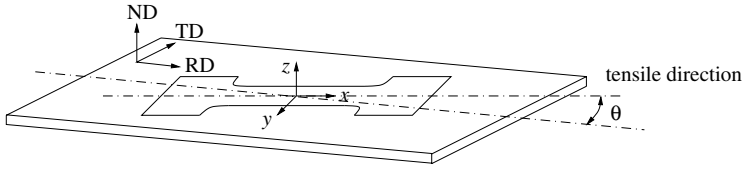


Figure 3.2: A tensile test specimen inclined at an angle  $\theta$  to the rolling direction.

when, besides isotropic hardening, kinematic hardening is also used. The use of kinematic hardening for non-proportional deformation, however, is disputed (Kocks, 1998).

Although a change in shape of the yield surface is probably realistic, continuum models that actually take this into account are currently considered ‘exotic’. A change of shape can be measured for small deformations after a pre-deformation. However, the results depend very much on the applied threshold value to define plastic deformation. If a large threshold is used, the effect of the pre-deformation rapidly diminishes (Kuwabara *et al.*, 2000). In most of this thesis isotropic hardening will be used, but for the prediction of necking, in Chapter 5, the influence of kinematic hardening is also considered.

In an incremental analysis the stress at the end of an increment is usually determined by an elastic prediction and a return mapping algorithm. Details of computational procedures are described among others by Bathe (1982); Crisfield (1991); Simo and Hughes (1998); Zienkiewicz and Taylor (2000b).

### 3.1.2 Normal and Planar Anisotropy

In simulations of sheet metal forming, the out-of-plane stresses  $\sigma_z$ ,  $\tau_{yz}$  and  $\tau_{zx}$  are neglected. For rolled material, three orthogonal axes can be defined, *viz.* the rolling direction (RD), the transverse direction (TD) and the normal direction (ND). A tensile specimen can be taken from the sheet in any orientation. The angle  $\theta$  between the loading direction and the rolling direction is used to define the specimen’s  $xyz$ -coordinate system (see Figure 3.2).

The rolling process will introduce a deformation texture in the sheet. After possible recrystallisation, the texture will not vanish, but a typical recrystallisation texture can evolve. The texture is symmetric along the rolling, transverse and normal directions. Usually, texture will result in anisotropic mechanical behaviour. Anisotropy in sheet metal can have a significant influence on the limiting drawing ratio. A technological parameter for the anisotropy in sheet metal is the Lankford strain ratio  $R$ . The  $R_\theta$ -value is defined as the ratio of the width to the thickness strains in a uniaxial tensile test with specimen orientation  $\theta$ :

$$R_\theta = \frac{\varepsilon_y}{\varepsilon_z} \quad (3.3)$$

where:  $\varepsilon_y = \ln(w/w_0)$  and  $\varepsilon_z = \ln(t/t_0)$ , the true strain in the width and thickness directions respectively. Since the thickness strain is difficult to measure, the volume constraint

Table 3.1:  $R$ -values for the AA 5754-O alloy investigated here.

$R_0$	$R_{45}$	$R_{90}$	$\bar{R}$	$\Delta R$
0.85	0.67	0.70	0.72	0.11

is invoked and the strain ratio can be calculated as

$$R_\theta = \frac{\varepsilon_y}{-(\varepsilon_x + \varepsilon_y)} \quad (3.4)$$

These relations can also be written in a differential or rate formulation.

For isotropic behaviour the  $R$ -value is equal to 1 for any value of  $\theta$ . An  $R$ -value not equal to 1 indicates *normal anisotropy*: the magnitude of the strain in the thickness direction is smaller ( $R > 1$ ) or larger ( $R < 1$ ) than would be the case for an isotropic material. If  $R$  is independent of the orientation  $\theta$ , the material is called *planar isotropic*. The material behaves isotropically in the plane, but can still be normal anisotropic. If the measured  $R$ -values depend on  $\theta$ , the material is called *planar anisotropic*.

If the yield locus is represented graphically, as in Figure 3.1, the uniaxial stress experiment determines the intersection of the yield locus with the  $\sigma_x$ -axis. The inclination  $\psi$  of the yield locus at the intersection with the  $\sigma_x$ -axis can, using Equations (3.2) and (3.4), be expressed in terms of the  $R$ -value:

$$\tan \psi = \frac{d\sigma_y}{d\sigma_x} = -\frac{\frac{\partial \phi}{\partial \sigma_x}}{\frac{\partial \phi}{\partial \sigma_y}} = -\frac{d\varepsilon_x}{d\varepsilon_y} = \frac{1 + R_\theta}{R_\theta} \quad (3.5)$$

Because of planar anisotropy, a cylindrical cup drawn from a circular blank is not equally high in the circumferential direction. This phenomenon is called *earing*. The sensitivity to earing can be represented by  $\Delta R$ :

$$\Delta R = \frac{R_0 - 2R_{45} + R_{90}}{2} \quad (3.6)$$

A high  $R$ -value means that the material has a high resistance to thinning and thickening. Therefore in high  $R$ -directions the cup will be higher than in low  $R$ -directions.

For computational convenience it is sometimes assumed that the  $R$ -value is constant with respect to  $\theta$ . The anisotropy in this model is characterised by the single value  $R$ . Often, sheet material that is actually planar anisotropic, is characterised by a single  $R$ -value determined by

$$\bar{R} = \frac{R_0 + 2R_{45} + R_{90}}{4} \quad (3.7)$$

This weighted average takes into account the fact that the  $+45^\circ$  and  $-45^\circ$  directions are symmetric.

The  $R$ -values for the AA 5754-O alloy used in this research were measured in three directions and are presented in Table 3.1.

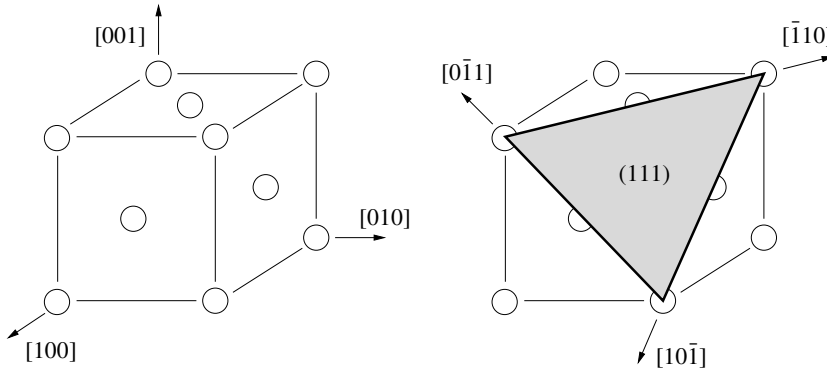


Figure 3.3: Face centred cubic unit cell and the (111) slip plane with three slip directions.

## 3.2 Polycrystal Plasticity

In this section, we descend one level below the abstraction level of continuum mechanics. At this level the material is no longer considered to be homogeneous, but separate grains with different lattice orientations are distinguished. In a simple homogenisation method, the mechanical response of crystallites and the grain orientations are used to predict the behaviour of an aggregate of grains. The polycrystal model will be used in the following sections and chapters to justify certain assumptions in phenomenological models and to do some, geometrically simple, simulations.

### 3.2.1 Single Crystal Model

#### Deformation Mechanism

Dislocation glide (slip) is by far the most prominent mechanism for plastic deformation in forming processes. In a crystal lattice only a pre-determined set of planes can serve as slip planes and within these planes only a limited number of directions can serve as slip directions. A combination of one slip plane with one slip direction in that plane is called a slip system. For f.c.c. metals<sup>2</sup>—such as aluminium—only the four closed packed planes and within each plane the three closed packed directions are considered as potential slip systems. One slip plane with the three corresponding slip directions is depicted in Figure 3.3. The 12 slip systems are designated by the Miller-indices  $\{111\}\langle 110\rangle$ .

A slip plane is identified by its normal  $\mathbf{m}_\alpha$  and a slip direction by  $\mathbf{s}_\alpha$ , where  $\alpha$  indicates the particular slip system and ranges from 1 to 12 for f.c.c. metals. Slip on a number of parallel planes in the same direction will, on average, produce shear deformation (see Figure 3.4). On a length scale where the individual slip planes cannot be distinguished, a locally homogeneous velocity gradient can be defined. The velocity gradient due to the slip

<sup>2</sup>face centred cubic crystallographic arrangement

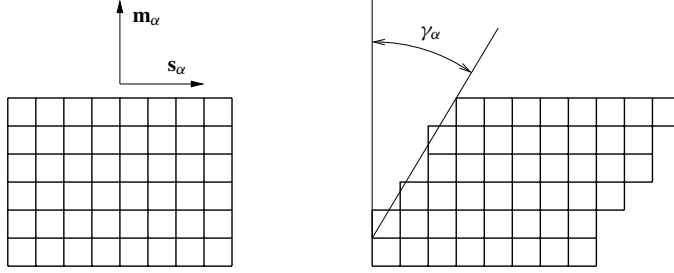


Figure 3.4: Shear deformation by averaged dislocation glide on one slip system  $\alpha$ .

rate  $\dot{\gamma}_\alpha$  is

$$\frac{\partial \mathbf{v}_\alpha}{\partial \mathbf{x}} = \dot{\gamma}_\alpha \mathbf{s}_\alpha \mathbf{m}_\alpha \quad (3.8)$$

For brevity of notation, it is useful to define the Schmid tensor  $\mathbf{T}_\alpha$ , the symmetric part of the Schmid tensor  $\mathbf{P}_\alpha$ , and the skew-symmetric part of the Schmid tensor  $\mathbf{Q}_\alpha$ :

$$\mathbf{T}_\alpha = \mathbf{s}_\alpha \mathbf{m}_\alpha \quad (3.9a)$$

$$\mathbf{P}_\alpha = \frac{1}{2} (\mathbf{s}_\alpha \mathbf{m}_\alpha + \mathbf{m}_\alpha \mathbf{s}_\alpha) \quad (3.9b)$$

$$\mathbf{Q}_\alpha = \frac{1}{2} (\mathbf{s}_\alpha \mathbf{m}_\alpha - \mathbf{m}_\alpha \mathbf{s}_\alpha) \quad (3.9c)$$

The total plastic velocity gradient  $\mathbf{L}^P$  is composed of the deformation of all slip systems and follows from Equations (3.8) and (3.9a):

$$\mathbf{L}^P = \sum_{\alpha=1}^{12} \dot{\gamma}_\alpha \mathbf{T}_\alpha \quad (3.10)$$

The rate of plastic deformation  $\mathbf{D}^P$  and the plastic spin  $\mathbf{W}^P$  are the symmetric and skew-symmetric parts of the plastic velocity gradient respectively:

$$\mathbf{D}^P = \sum_{\alpha=1}^{12} \dot{\gamma}_\alpha \mathbf{P}_\alpha \quad (3.11)$$

$$\mathbf{W}^P = \sum_{\alpha=1}^{12} \dot{\gamma}_\alpha \mathbf{Q}_\alpha \quad (3.12)$$

The total spin is composed of the plastic spin and the lattice spin. The lattice spin represents the change of orientation of the crystal lattice. It results in texture evolution and will be considered in the next chapter.

It is clear that, based on dislocation glide, plastic deformation does not change the volume of the material. With a combination of slip rates on the 12 slip systems, any isochoric rate of deformation can be obtained. In fact, 5 independent slip systems would be

enough. Therefore, even if  $\mathbf{D}^p$  is prescribed, the average slip on each slip system cannot be determined from kinematic relations alone. Constitutive relations must be used in order to obtain unique solutions for all shear rates.

### Constitutive Models

It is assumed that the slip rate of a particular slip system depends only on the shear stress that is acting on that slip system. The shear stress on a plane normal to  $\mathbf{m}_\alpha$  in the direction of  $\mathbf{s}_\alpha$  is called the resolved shear stress  $\tau_\alpha$ . The resolved shear stress can easily be derived from the definition of the stress tensor:  $\tau_\alpha = \mathbf{m}_\alpha \cdot \boldsymbol{\sigma} \cdot \mathbf{s}_\alpha$ . This can also be written as  $\tau_\alpha = \mathbf{s}_\alpha \cdot (\mathbf{m}_\alpha \cdot \boldsymbol{\sigma})$  or, with (3.9a), (3.9b) and the symmetry of  $\boldsymbol{\sigma}$  as

$$\tau_\alpha = \mathbf{T}_\alpha : \boldsymbol{\sigma} = \mathbf{P}_\alpha : \boldsymbol{\sigma} \quad (3.13)$$

The constitutive models for the mechanical behaviour of a single crystallite can be classified, based on two criteria. Firstly, the model can include or neglect elastic deformation of the lattice. Secondly, the inelastic deformation can be considered purely plastic or viscoplastic. The choice for an elasto-(visco)-plastic or rigid-(visco)-plastic model should be made with the goal of the analysis in mind. If elastic deformation can be ignored, *e.g.* in the determination of a yield locus or the evolution of texture, a rigid-(visco)-plastic model can be used. Including elastic deformations can, in some cases, give more accurate results, but usually at higher computational costs. In an incremental analysis, including elastic deformations will typically reduce the critical time step above which no convergence is reached.

The choice for a purely plastic or viscoplastic model results in completely different algorithms. In a purely plastic model, no slip is assumed if the resolved shear stress is below a critical value: the critical resolved shear stress  $\tau_\alpha^c$ . The resolved shear stress cannot become larger than  $\tau_\alpha^c$ , but the critical resolved shear stress can increase due to hardening. The algorithm must maintain the consistency between evolution of the critical resolved shear stress and the maximum stress on the slip systems. A major problem is that the same rate of deformation can be reached by different combinations of slip rates on the 12 slip systems. The choice of active slip systems influences the evolution of the critical resolved shear stress. Additional relations are required to define unique slip rates on each slip system. The task to determine which slip systems are active in a finite time increment is not trivial. Some algorithms to solve this problem are given by Knockaert *et al.* (2000); Miehe and Schröder (2001).

In a viscoplastic approach, the selection of active slip systems is completely avoided. It is assumed that the slip rate  $\dot{\gamma}_\alpha$  is related to the resolved shear stress  $\tau_\alpha$  as (Asaro and Needleman, 1985)

$$\dot{\gamma}_\alpha = \dot{\gamma}_0 \left| \frac{\tau_\alpha}{\hat{\tau}_\alpha} \right|^{1/m} \text{sgn}(\tau_\alpha) \quad (3.14)$$

where  $\hat{\tau}_\alpha$  is a reference value. With a small value for the strain rate parameter  $m$ , *e.g.* less than 0.01,  $\dot{\gamma}_\alpha$  reduces to almost zero for  $\tau < \hat{\tau}_\alpha$  and becomes very large for  $\tau > \hat{\tau}_\alpha$ . In this case the model reduces to a purely plastic model, and  $\hat{\tau}_\alpha$  can be interpreted as the critical resolved shear stress  $\tau_\alpha^c$ .

It can be argued that above a temperature of 0 K dislocation glide is thermally activated, and strain rate sensitivity is a physical reality. Hence, a viscoplastic model should be used. However, for very low strain rate sensitivities,  $1/m$  becomes very large and can result in numerical difficulties. Typically, the rate of convergence can be very low. Nevertheless, the conceptual simplicity of the algorithm itself is appealing and the viscoplastic model is therefore widely used.

The implementation of a rigid-viscoplastic model is straightforward and is partly described by Beaudoin *et al.* (1994). Large strain increments are possible with this approach and this model will be used for the analysis of yield loci and texture evolution in this thesis.

**Evolution of the critical resolved shear stress** The critical resolved shear stress on a particular slip system is related to the dislocation structure. The dislocation structure, in its turn, is a result of the previous deformation. Therefore, the critical resolved shear stress is often formulated by an evolution equation, starting with equal values for all slip systems:

$$\dot{\tau}_\alpha^c = \sum_{\beta=1}^{12} h_{\alpha\beta} |\dot{\gamma}_\beta| \quad (3.15a)$$

$$\tau_\alpha^c(t_0) = \tau_0 \quad (3.15b)$$

With the hardening matrix  $h_{\alpha\beta}$ , the interaction between different slip systems can be chosen freely. *E.g.*, a phenomenon such as *latent hardening* is modelled by letting slip in other slip planes have a larger influence on the critical resolved shear stress than slip in the same slip plane. Physically, this phenomenon is explained by the resistance to dislocation glide, stemming from forest dislocations in other slip planes. It is modelled by defining

$$h_{\alpha\beta} = q_{\alpha\beta} h_\beta \quad (\text{no sum on } \beta) \quad (3.16)$$

where  $q$  is often given a value 1.0 if  $\alpha$  and  $\beta$  refer to the same slip plane and a value of 1.4 otherwise (Asaro and Needleman, 1985; Wu *et al.*, 1996).

Many hardening functions  $h_\beta$  can be found in the literature. One of the simplest is a power law

$$h_\beta = h_0 \left( 1 - \frac{\tau_\beta^c}{\tau^{\text{sat}}} \right)^a \quad (3.17)$$

where  $\tau^{\text{sat}}$  is a saturation stress. With  $q_{\alpha\beta} \equiv 1$  this leads to isotropic hardening, where  $\tau_\beta^c = \tau^c$  for all  $\beta$ . Then, the critical resolved shear stress can be evaluated analytically:

$$\tau^c = \begin{cases} \tau^{\text{sat}} - (\tau^{\text{sat}} - \tau_0) \exp\left(-\frac{h_0}{\tau^{\text{sat}}} \Gamma\right) & \text{if } a = 1 \\ \tau^{\text{sat}} \left\{ 1 - \left[ \left(1 - \frac{\tau_0}{\tau^{\text{sat}}}\right)^{1-a} - (1-a) \frac{h_0 \Gamma}{\tau^{\text{sat}}} \right]^{\frac{1}{1-a}} \right\} & \text{if } a \neq 1 \end{cases} \quad (3.18)$$

where

$$\Gamma(t_1) = \int_0^{t_1} \left( \sum_{\alpha=1}^{12} |\dot{\gamma}_\alpha(t)| \right) dt \quad (3.19)$$

is an equivalent slip value. For  $a = 1$  this equation is similar to the well known Voce relation, where the equivalent stress is substituted by  $\tau^c$  and the equivalent strain by  $\Gamma$ . This relation makes it easy to compare results from the polycrystal model and phenomenological models.

### 3.2.2 Homogenisation

In a polycrystal material model the mechanical response of a material is calculated based on the response of a large number of single crystallites. An important ingredient in a polycrystal theory is the assumption that is made to relate the macroscopic strains and stresses to the local strains and stresses in the crystallites. Many such theories exist, ranging from a micro-scale finite element analysis to the full constraints Taylor model (Taylor, 1938).

In a micro-scale finite element analysis, every grain in a 3D polycrystalline aggregate is modelled by a number of elements. The relation between local and global strains and stresses follows from the finite element discretisation and the weighted equilibrium equations. At the other end of the spectrum, the full constraints Taylor model assumes that the deformation in every crystallite is equal to the macroscopic deformation and the macroscopic stress is assumed to be the average of all crystallites. In this model, the equilibrium equations are clearly violated. A comparison of several models is given by Van Houtte *et al.* (2002).

In this study the polycrystal model is used to guide some decisions that have to be made for the phenomenological models and to validate their influence on yield behaviour and necking conditions. For this purpose, the full constraints Taylor model is sufficient, because it gives a reasonable first-order approximation of texture evolution and stress–strain response for single-phase materials (Bronkhorst *et al.*, 1992).

### 3.2.3 Determination of the Yield Locus

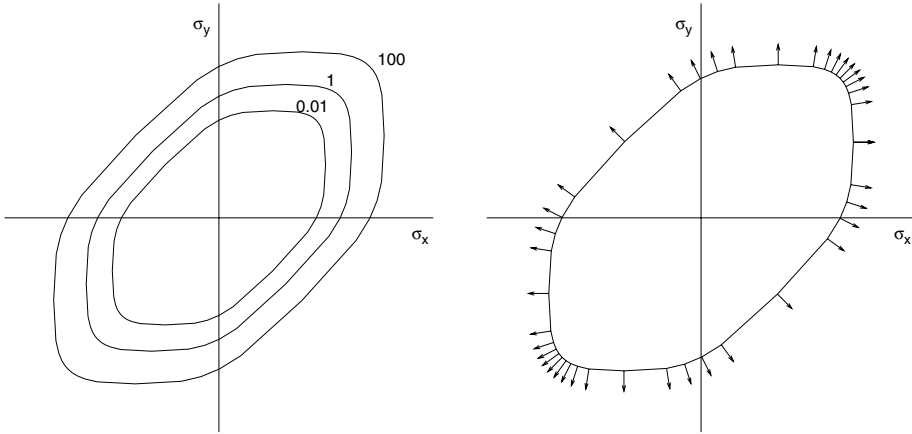
Using the polycrystal model, a yield locus can be determined when the single crystal behaviour and the distribution of grain orientations are known. In this work, the rigid-viscoplastic model is used for this purpose. Within the rigid-viscoplastic model there is no elastic deformation and no arbitrary offset strain to determine plastic flow (*e.g.* 0.2% permanent strain). On the other hand, in a viscoplastic model there is, strictly speaking, no yield locus but only a flow potential. With a sufficiently low rate parameter, say  $m < 0.01$ , the difference between an equi-potential surface and the yield surface vanishes. The shape of the yield surface is hardly influenced when  $m$  is increased to 0.05 (Kocks, 1998) and this value is used for computational efficiency.

The flow potential is given by the rate of plastic work

$$\dot{w}^P = \boldsymbol{\sigma} : \mathbf{D}^P \quad (3.20)$$

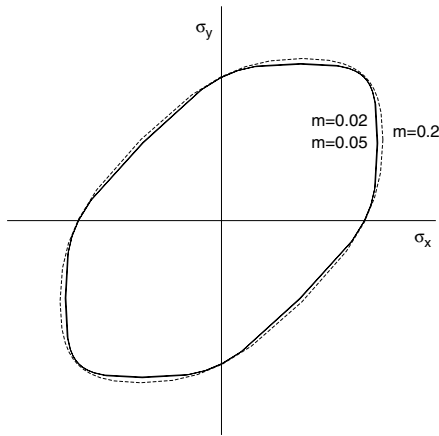
To obtain a ‘yield stress’ related to a certain plastic strain rate direction, the strain rate is imposed on a numerical polycrystal. The magnitude of this strain rate is irrelevant for the rate insensitive limit ( $m \rightarrow 0$ ). For rate sensitive behaviour, the magnitude should be such that  $\dot{w}^P$  has the same value independent of the strain rate direction. By definition:  $\frac{\partial \dot{w}^P}{\partial \boldsymbol{\sigma}} = \mathbf{D}^P$ , hence the prescribed rate of deformation determines the normal to the yield surface.

To determine a plane stress yield locus the two in-plane normal strain rates  $\dot{\epsilon}_x$  and  $\dot{\epsilon}_y$  are prescribed in order to determine the yield stress in different deformation directions. For



(a) at 3 different  $\dot{w}^P$  values,  $m = 0.05$

(b) scaled to the same uniaxial value,  $m = 0.05$



(c) scaled to the same uniaxial value, at 3 different  $m$  values

Figure 3.5: Calculated flow potentials with 2000 randomly oriented grains.

every direction, the other components of  $\mathbf{D}^P$  are iteratively changed, such that  $\sigma_z$ ,  $\tau_{xy}$ ,  $\tau_{yz}$  and  $\tau_{zx}$  are zero.

In Figure 3.5 the direction of deformation is varied over  $180^\circ$  in 20 equal steps. The assumption that for every slip system a reversed shear stress will give a reversed slip rate of



the same magnitude leads to a perfect symmetry with respect to the origin. This determines the yield locus for the remaining 180°. In Figure 3.5(a), 3 contour lines are plotted for plastic dissipation rates of 0.01, 1 and 100 W/mm<sup>3</sup>. The contours differ quite a lot, but if they are scaled to the same uniaxial stress (Figure 3.5(b)) all contours coincide. Therefore, the visco-plastic approach does not yield a quantitative prediction of the yield locus, but the shape of the equi-flow-potential contour can be used as shape of the yield locus, independent of the rate of dissipation.

In Figure 3.5(b) the plastic flow directions are also plotted. As can be seen, the equally spaced deformation directions do not imply that the resulting stress points on the yield locus are also equally spaced. The typical yield locus for f.c.c. metals is found, and it appears to develop vertices when compared with the ellipse of the Von Mises yield locus. In Figure 3.5(c) the influence of the value of  $m$  is examined. The difference between  $m = 0.05$  and  $m = 0.02$  can hardly be seen at this scale, but a too high value ( $m = 0.2$ ) results in a yield locus that is too smooth. This suggests that the shape of the yield surface can, indeed, be determined with a non-physically high value of 0.05. Characteristic yield locus values for a random texture and for the AA 5754-O sheet under consideration are given in Appendix C. It will be shown in subsequent chapters that the shape of the yield function plays an important role in the stability of a deformation path (necking) and the strain distribution in deep drawing.

### 3.3 Explicit Yield Functions

The polycrystal analysis in the previous section predicts the relation between macroscopic stress and plastic deformation. The analysis, however, is computationally expensive. Process simulations would last prohibitively long and faster methods are required. The usual way to achieve faster solutions is to define an explicit yield function. The yield locus that was constructed in the polycrystal case is then readily available, and the direction of the plastic flow can be calculated from the derivative of the yield function to the stress. A disadvantage is that, in this approach, texture evolution and latent hardening are difficult to incorporate.

From the plastic deformation mechanism described in Section 3.2.1, it follows that for metals the hydrostatic pressure does not influence plastic deformations. Hence, any isotropic or anisotropic yield function for metal plasticity should be independent of the hydrostatic pressure. In continuum mechanics it is customary to derive yield functions for general 3-dimensional situations (6 independent stress components). For sheet metal forming, however, it is generally assumed that the normal stress and shear stresses acting on the plane of the sheet are negligible. Therefore only 3 independent stress components remain:  $\sigma_x$ ,  $\sigma_y$  and  $\tau_{xy}$ . In this section, three explicit yield functions will be given. Two are first described in the general stress space and then reduced to the plane stress situation. The third is directly formulated in the plane stress space.

#### 3.3.1 Hill '48 Yield Function

A widely used anisotropic yield function is the quadratic yield function postulated by Hill (1948, 1950), also known as Hill '48 to distinguish it from later models. In this yield

function three orthogonal planes of symmetry are presumed, leading to three principal axes of anisotropy. In sheet metal, the principal directions coincide with the rolling, transverse and thickness directions of the sheet.

The Hill yield function can be written as

$$\phi = F(\sigma_y - \sigma_z)^2 + G(\sigma_z - \sigma_x)^2 + H(\sigma_x - \sigma_y)^2 + 2L\tau_{yz}^2 + 2M\tau_{zx}^2 + 2N\tau_{xy}^2 - x^2 \quad (3.21)$$

where  $F$ ,  $G$  and  $H$  may be expressed in terms of the yield stresses in tension and  $L$ ,  $M$  and  $N$  in terms of the yield stresses in simple shear.

The value of  $x$  can be scaled with the orthotropy parameters  $F$ ,  $G$ ,  $H$ ,  $L$ ,  $M$  and  $N$  and was taken equal to 1 in the original formulation of Hill. In that case, the orthotropy parameters are not dimensionless and must all be adapted in the case of hardening. Currently therefore,  $x$  is often given the dimension of stress. In this work,  $x$  is taken equal to  $\sigma_f \sqrt{G + H}$ . By this choice the ‘flow stress’  $\sigma_f$  equals the stress  $\sigma_x$  during plastic deformation, for a uniaxial tensile test in the  $x$ -direction.

It should be noted that for large deformations, the evolution of texture will influence the values of the orthotropy parameters. This is usually ignored. By taking  $F$ ,  $G$  and  $H$  equal to 1 and  $L$ ,  $M$  and  $N$  equal to 3, the quadratic Hill yield function degenerates to the isotropic Von Mises yield function.

In (3.21), there is no difference between the tensile and compressive yield stresses in a particular stress direction, hence the Bauschinger effect cannot be described. If the stress  $\boldsymbol{\sigma}$  is substituted by the effective stress  $\boldsymbol{\sigma} - \boldsymbol{\alpha}$ , where  $\boldsymbol{\alpha}$  is the back-stress, the Bauschinger effect can be described by a kinematic hardening model.

It is computationally convenient to write the yield function in a tensor expression and use a homogeneous function of first degree<sup>3</sup> (De Borst and Feenstra, 1990). The yield surface as described by (3.21), extended with kinematic hardening can now be defined as

$$\phi(\boldsymbol{\sigma} - \boldsymbol{\alpha}, \varepsilon_{\text{eq}}) = \sqrt{(\boldsymbol{\sigma} - \boldsymbol{\alpha}) : \mathbf{P} : (\boldsymbol{\sigma} - \boldsymbol{\alpha})} - \sigma_f(\varepsilon_{\text{eq}}) = 0 \quad (3.22)$$

where  $\varepsilon_{\text{eq}}$  is an equivalent strain that determines the isotropic hardening, formally defined in Section 3.4.1. The fourth-order tensor  $\mathbf{P}$  contains the orthotropy parameters and is symmetric. The derivative of  $\phi$  with respect to  $\boldsymbol{\sigma}$  can now be written explicitly as

$$\frac{\partial \phi}{\partial \boldsymbol{\sigma}} = \frac{\mathbf{P} : (\boldsymbol{\sigma} - \boldsymbol{\alpha})}{\sqrt{(\boldsymbol{\sigma} - \boldsymbol{\alpha}) : \mathbf{P} : (\boldsymbol{\sigma} - \boldsymbol{\alpha})}} = \frac{1}{\sigma_f} \mathbf{P} : (\boldsymbol{\sigma} - \boldsymbol{\alpha}) \quad (3.23)$$

The plastic strain rate is given, according to Drucker’s postulate, by

$$\dot{\boldsymbol{\varepsilon}}^{\text{P}} = \dot{\lambda} \frac{\partial \phi}{\partial \boldsymbol{\sigma}} = \frac{\dot{\lambda}}{\sigma_f} \mathbf{P} : (\boldsymbol{\sigma} - \boldsymbol{\alpha}) \quad (3.24)$$

The flow stress  $\sigma_f$  defines the isotropic hardening and is a function of the equivalent plastic strain  $\varepsilon_{\text{eq}}$ . In rate form this gives

$$\dot{\sigma}_f = h_{\text{iso}} \dot{\varepsilon}_{\text{eq}} \quad (3.25)$$

The chosen format of the yield function  $\phi$  results in  $\dot{\varepsilon}_{\text{eq}} = \dot{\lambda}$  and in the case of a uniaxial tensile test  $\dot{\varepsilon}_{\text{eq}} = \dot{\varepsilon}_x^{\text{P}}$ .

<sup>3</sup>In a homogeneous function of degree  $k$ :  $\phi(\alpha\boldsymbol{\sigma}) = \alpha^k \phi(\boldsymbol{\sigma})$ .

With kinematic hardening according to Prager, the back-stress evolution takes place in the direction normal to the yield surface, co-directional with the plastic strain rate:

$$\dot{\boldsymbol{\alpha}} = c_{\text{kin}} \dot{\boldsymbol{\epsilon}}^{\text{P}} = c_{\text{kin}} \dot{\lambda} \frac{\partial \phi}{\partial \boldsymbol{\sigma}} \quad (3.26)$$

To derive the relation between kinematic hardening and the strain increments in a uniaxial tensile test, we note that all stress components apart from the tensile stress are zero and remain zero. Only  $\sigma_x \neq 0$  and  $d\sigma_x \neq 0$ . The stress point must remain on the yield surface, hence in the absence of isotropic hardening

$$\begin{aligned} d\sqrt{(\boldsymbol{\sigma} - \boldsymbol{\alpha}) : \mathbf{P} : (\boldsymbol{\sigma} - \boldsymbol{\alpha})} &= \frac{1}{\sigma_f} (\boldsymbol{\sigma} - \boldsymbol{\alpha}) : \mathbf{P} : d(\boldsymbol{\sigma} - \boldsymbol{\alpha}) \\ &= \frac{1}{\sigma_f} (\boldsymbol{\sigma} - \boldsymbol{\alpha}) : \mathbf{P} : \left\{ d\boldsymbol{\sigma} - \frac{d\lambda c_{\text{kin}}}{\sigma_f} \mathbf{P} : (\boldsymbol{\sigma} - \boldsymbol{\alpha}) \right\} = 0 \end{aligned} \quad (3.27)$$

with, in components

$$[d\boldsymbol{\sigma}] = \begin{bmatrix} d\sigma_x & 0 & 0 \\ 0 & 0 & 0 \\ 0 & 0 & 0 \end{bmatrix} \quad (3.28)$$

If the loading direction is parallel to the material  $x$ -direction, there is no coupling between the normal and shear components in  $\mathbf{P}$ . Initially,  $\boldsymbol{\alpha} = \mathbf{0}$  and  $(\boldsymbol{\sigma} - \boldsymbol{\alpha})$  is equal to  $\sigma_f$  normal to the  $x$ -direction and 0 in all other directions. With the components of  $\mathbf{P}$  as *e.g.* given by Carleer (1997), we can derive

$$d\sigma_x = \left( 1 + \frac{G^2 + H^2}{(G + H)^2} \right) c_{\text{kin}} d\varepsilon_{\text{eq}} = h_{\text{kin}} d\varepsilon_{\text{eq}} \quad (3.29)$$

For an isotropic material,  $G = H = 1$  and this results in the often described ratio  $c_{\text{kin}} = \frac{2}{3} h_{\text{kin}}$  (see *e.g.* Chaboche, 1986). However, the ratio is different for anisotropic material and changes upon deformation when  $\boldsymbol{\alpha} \neq \mathbf{0}$ .

### Plane Stress Condition

If a plane stress situation is assumed, the Hill '48 yield function can be simplified. Setting  $\sigma_z = \sigma_{yz} = \sigma_{zx} = 0$ , Equation (3.21) reduces to

$$\phi = (G + H)\sigma_x^2 - 2H\sigma_x\sigma_y + (F + H)\sigma_y^2 + 2N\tau_{xy}^2 - 2\sigma_f^2 = 0 \quad (3.30)$$

If we perform a tensile test in the rolling and in the transverse directions, we can determine  $R_0$  and  $R_{90}$ . From the quadratic Hill yield function we would derive values that follow from (3.4) in rate form and the derivatives of (3.30):

$$R_0 = \frac{-\frac{\partial \phi}{\partial \sigma_y}}{\frac{\partial \phi}{\partial \sigma_y} + \frac{\partial \phi}{\partial \sigma_x}} (\sigma_y = 0) = \frac{H}{G} \quad (3.31)$$

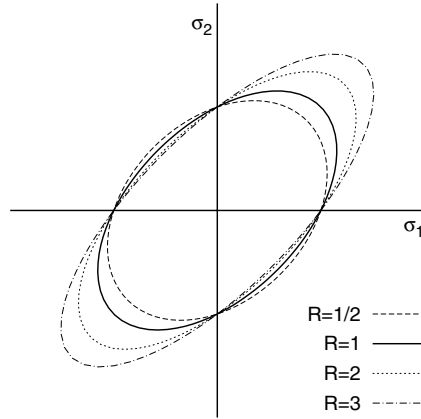


Figure 3.6: The yield locus for the planar isotropic quadratic Hill function.

$$R_{90} = \frac{-\frac{\partial \phi}{\partial \sigma_x}}{\frac{\partial \phi}{\partial \sigma_x} + \frac{\partial \phi}{\partial \sigma_y}} (\sigma_x = 0) = \frac{H}{F} \quad (3.32)$$

If planar isotropic behaviour is assumed, the response of the material is independent of the loading direction in the plane. It is then useful to write the yield surface in terms of the principal stresses. The quadratic Hill yield function for plane stress (3.30), can now be simplified further. From (3.31) and (3.32) it follows that  $F = G$ . With a formulation in the principal directions, the shear stress disappears. The value of  $\sigma_f$  depends on the scaling of  $F$ ,  $G$  and  $H$ . Defining the uniaxial yield stress  $\sigma_{un}$  by  $\sigma_{un}^2 = 2\sigma_f^2/(G + H)$ , gives

$$\sigma_1^2 + \sigma_2^2 - \frac{2R}{R+1}\sigma_1\sigma_2 = \sigma_{un}^2 \quad (3.33)$$

where  $\sigma_{un}$  is the uniaxial in-plane yield stress.

The planar isotropic quadratic Hill function is graphically represented in Figure 3.6. Three special stress states, apart from the uniaxial stress state, are the equi-biaxial stress state ( $\sigma_1 = \sigma_2$ ), the pure shear stress state ( $\sigma_2 = -\sigma_1$ ), and the plane strain state ( $d\varepsilon_2 = 0$ ). We now determine the yield values for these stress states, compared to the uniaxial yield stress as functions of the  $R$ -value. The results are used in the following sections.

**Equi-biaxial stress** If  $\sigma_1 = \sigma_2 = \sigma_{bi}$  is substituted into (3.33) it is found that

$$\left(\frac{\sigma_{bi}}{\sigma_{un}}\right)^2 = \frac{1+R}{2} \quad (3.34)$$

The biaxial yield stress clearly increases, compared to the uniaxial yield stress, with increasing  $R$ -value.

**Pure shear stress** If  $\sigma_2 = -\sigma_1 = \sigma_{sh}$  is substituted into (3.33) it is found that:

$$\left(\frac{\sigma_{sh}}{\sigma_{un}}\right)^2 = \frac{1+R}{4R+2} \quad (3.35)$$

The shear yield stress equals  $\frac{1}{2}(\sigma_1 - \sigma_2) = \sigma_{sh}$  and decreases with increasing  $R$ -value, compared to the uniaxial yield stress.

**Plane strain** Finally, to determine the plane strain yield stress, the point on the yield locus with a vertical tangent must be determined. In this case the normal to the yield locus must have a vanishing component in the  $\sigma_2$ -direction:

$$\begin{aligned} \frac{d\varepsilon_1}{d\varepsilon_2} &= \frac{\frac{\partial\phi}{\partial\sigma_1}}{\frac{\partial\phi}{\partial\sigma_2}} \rightarrow \infty \\ \Rightarrow \frac{\partial\phi}{\partial\sigma_2} &= 2\sigma_2 - \frac{2R}{R+1}\sigma_1 \rightarrow 0 \end{aligned} \quad (3.36)$$

Representing the stress ratio  $\sigma_2/\sigma_1 = \alpha$  yields

$$\alpha = \frac{R}{R+1} \quad (3.37)$$

for the plane strain situation. Substituting  $\sigma_2 = \frac{R}{R+1}\sigma_1$  and  $\sigma_1 = \sigma_{ps}$  in (3.33) we find that for plane strain

$$\left(\frac{\sigma_{ps}}{\sigma_{un}}\right)^2 = \frac{(1+R)^2}{2R+1} \quad (3.38)$$

### 3.3.2 Tresca Yield Function

In crystal plasticity, only shear stresses on slip systems are considered to induce plastic deformation. A straightforward generalisation to continuum plasticity would be to assume that a maximum allowable shear stress is a valid yield criterion. The maximum shear stress in an infinitesimal material element can be found by calculating the principal stresses:  $\sigma_1 \geq \sigma_2 \geq \sigma_3$ . The maximum shear stress is half of the difference between the lowest and highest principal stress. With this criterion, the maximum allowable shear stress would be half the allowable uniaxial stress. A yield function can therefore be defined as

$$\phi(\sigma, \varepsilon_{eq}) = (\sigma_1 - \sigma_3) - \sigma_f(\varepsilon_{eq}) = 0 \quad (3.39)$$

This criterion is known as the Tresca yield function. It is not continuously differentiable in the 'real' stress-space. This is made clear by creating the yield locus for a plane stress situation and  $\sigma_{xy} = 0$ . With only  $\sigma_x$  and  $\sigma_y$  non-zero, the yield locus is described by

$$\begin{cases} |\sigma_x| = \sigma_f & \text{if } |\sigma_x| \geq |\sigma_y| \text{ and } |\sigma_x| \geq |\sigma_x - \sigma_y| \\ |\sigma_y| = \sigma_f & \text{if } |\sigma_y| \geq |\sigma_x| \text{ and } |\sigma_y| \geq |\sigma_x - \sigma_y| \\ |\sigma_x - \sigma_y| = \sigma_f & \text{if } |\sigma_x - \sigma_y| \geq |\sigma_x| \text{ and } |\sigma_x - \sigma_y| \geq |\sigma_y| \end{cases} \quad (3.40)$$

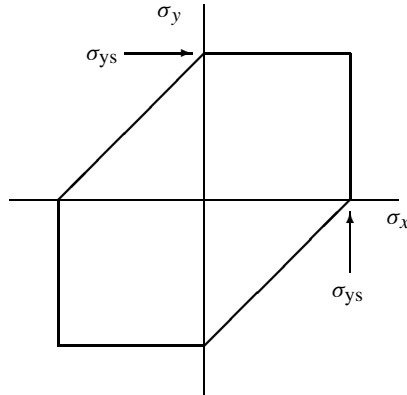


Figure 3.7: Yield locus for plane stress Tresca criterion.

The corners in the yield locus form a computational complication, because at those points, the strain rate direction is not completely determined by the yield function. A solution is found by considering the Tresca yield condition as a set of six, smooth, yield functions  $\phi_\alpha$ . The flow condition  $\phi_\alpha \leq 0$  must be satisfied for all  $\alpha$ . In a corner, the plastic strain rate can be found as a contribution from both yield functions (Koiter, 1953). An algorithm presented by De Borst (1987) and Simo *et al.* (1988) is used in this work. It will be shown in Chapter 5 that the corners in the Tresca yield locus have a strong effect on the prediction of necking.

If the plane stress yield loci of Figures 3.6 and 3.7 are compared with the polycrystal prediction of Figure 3.5 it can be seen that the polycrystal prediction is somewhere between the Hill and Tresca models. It should be remarked here that the Tresca yield criterion is isotropic. The shape of the yield locus is independent of the orientation of the material. In Figure 3.6 this is only the case for  $R = 1$ , which represents the Von Mises yield locus.

### 3.3.3 Vegter Yield Function

The Vegter yield criterion (Vegter *et al.*, 1995, 1998; Pijlman, 2001) defines a yield function for plane stress situations, directly based on experimental measurements on sheet material. The yield function is defined in the principal stress space. For planar anisotropic material, therefore, the yield function depends on the angle between the principal axes and the rolling direction. For a particular loading direction with respect to the rolling direction, four experiments are necessary to determine the model parameters. These are a pure shear test, a uniaxial tensile test, a plane strain tensile test and an equi-biaxial tensile test, see Figure 3.8. Between the measured stress points a Bezier curve is used to describe the yield locus. These four stress states are exactly the same as those derived in the previous section for the planar isotropic Hill criterion. In the Hill criterion these points were fully determined by the measured  $R$ -value. In the Vegter criterion these points can be used independent of the  $R$ -values.

For the initial yield stress in pure shear, a simple shear test can be used rotated over  $45^\circ$ .

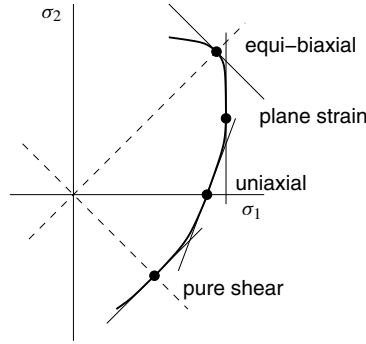


Figure 3.8: Basic stress points and tangents to the Vegter yield locus.

Instead of the equi-biaxial tensile test, a compression in the normal direction can be used, assuming that the hydrostatic stress has no effect on the plastic deformation. The experiments indicated in Figure 3.8 result in a set of 4 reference stress points with  $\sigma_x > \sigma_y$ . For the situations where  $\sigma_y > \sigma_x$ , the same experiments can be performed with the specimen rotated by  $90^\circ$ . The part of the yield locus where  $\sigma_x + \sigma_y < 0$  is usually not measured experimentally, but is determined by the assumption that the initial yield stress in compression is equal to that in tension. Both assumptions, invariance of hydrostatic stress and initial equivalence of tensile and compressive flow stress, are supported by the polycrystal theory.

At yielding, not only the yield stress, but also the direction of plastic strain is determined. Based on Drucker's postulate, the normal to the yield locus has the same direction as the plastic strain rate. If the stress points and the yield locus directions are known, a set of Bezier curves can be constructed such that the ensuing yield locus is  $C^1$  continuous. In the two-dimensional principal stress space, a stress point is represented by the vector

$$\vec{\sigma} = \begin{Bmatrix} \sigma_x \\ \sigma_y \end{Bmatrix} \quad (3.41)$$

Every plane stress situation can now be represented by the principal stresses  $\vec{\sigma}$  and the angle  $\theta$  between the 1st principal axis and the rolling direction.

For every part of the yield locus between two reference stress points,  $\vec{\sigma}_i$  and  $\vec{\sigma}_j$ , a second order Bezier function is defined. The Bezier function is determined by the two reference stress points and the direction of the yield locus at the reference points. The two tangents at the reference points define the hinge point  $\vec{\sigma}_h$ , see Figure 3.9. The yield locus between two reference stress points is defined by

$$\vec{\sigma}_{\text{locus}} = \vec{\sigma}_i + 2\mu (\vec{\sigma}_h - \vec{\sigma}_i) + \mu^2 (\vec{\sigma}_i + \vec{\sigma}_j - 2\vec{\sigma}_h) \quad \mu \in [0, 1] \quad (3.42)$$

A yield function in the sense of Section 3.1.1 is constructed by defining an equivalent stress  $\sigma_{\text{eq}}$ , that can be determined for any plane stress state by the relation

$$\vec{\sigma} = \frac{\sigma_{\text{eq}}}{\sigma_f} \left[ \vec{\sigma}_i + 2\mu (\vec{\sigma}_h - \vec{\sigma}_i) + \mu^2 (\vec{\sigma}_i + \vec{\sigma}_j - 2\vec{\sigma}_h) \right] \quad \mu \in [0, 1] \quad (3.43)$$

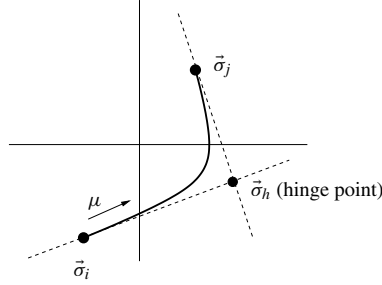


Figure 3.9: Second order Bezier curve between two reference stress points.

A yield function  $\phi$  that is defined as

$$\phi(\boldsymbol{\sigma}, \varepsilon_{\text{eq}}) = \sigma_{\text{eq}}(\boldsymbol{\sigma}) - \sigma_f(\varepsilon_{\text{eq}}) \quad (3.44)$$

fulfils the condition that  $\phi = 0$  on the yield locus and  $\phi < 0$  in the elastic regime. The direction of the plastic strain rate can be calculated from the derivative of  $\phi$  to the stress  $\boldsymbol{\sigma}$ . Since  $\phi$  is continuously differentiable, the plastic strain rate direction is continuous.

Planar anisotropic behaviour can be modelled by letting all reference and hinge stress points depend on the angle  $\theta$  between the first principal stress and the rolling direction. For common rolled materials, that develop four ears in deep drawing of a cylindrical cup, experiments are performed for the  $0^\circ$ ,  $45^\circ$  and  $90^\circ$  directions with respect to the rolling direction. The reference and hinge stress points for intermediate directions are, in this model, defined by an interpolation, based on harmonic functions:

$$\vec{\sigma}_k(\theta) = \sum_{j=0}^n \vec{\zeta}_{kj} \cos(2j\theta) \quad (3.45)$$

$$\left( \frac{\partial \phi}{\partial \vec{\sigma}} \right)_k(\theta) = \sum_{j=0}^n \vec{\varphi}_{kj} \cos(2j\theta) \quad (3.46)$$

A value  $n = 2$  is used for the earlier mentioned materials with four ears. A complete yield locus for one specific angle  $\theta$  is presented in Figure 3.10, including all reference and hinge points and the tangents. For implementation details see Pijlman (2001).

Not all reference and hinge points are determined experimentally. The stress  $\sigma_y$  in a plane strain test in the  $x$ -direction cannot be measured easily and the slope of the yield locus in the pure shear point is not measured accurately. For those points, data derived from a polycrystal analysis is used.

### 3.4 Flow Stress and Hardening

The flow stress  $\sigma_f$  is a measure for the resistance to (further) plastic deformation of a material. It is usually defined as the true yield stress in a uniaxial tensile test. In the temperature



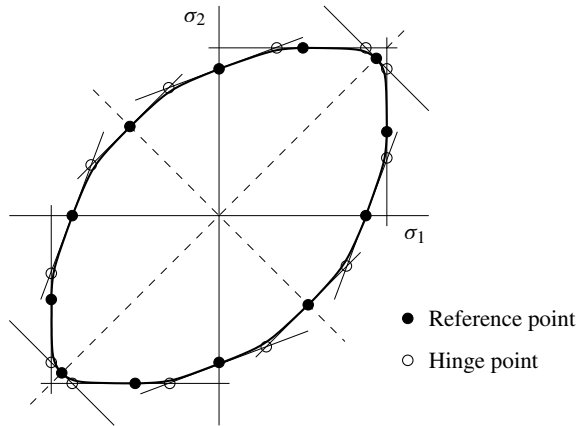


Figure 3.10: A complete Vegter yield locus, and tangents in the reference points.

interval that is of interest for warm forming of aluminium, the flow stress increases upon plastic deformation. This is known as *work hardening* or *strain hardening*. For uniaxial stress states this is illustrated by the stress–strain diagrams of Figure 2.2. The experiments described in Section 2.2 showed that the work hardening in Al–Mg alloys depends on the deformation, temperature and strain rate.

For numerical analysis, a description of this work hardening is needed. The classical approach is to fit macroscopic mechanical measurements to a convenient mathematical function. These *phenomenological* models dominate the current simulation software. Two well-known hardening functions are described in Section 3.4.1. The validity of phenomenological models is limited to situations that are comparable to the range of experiments on which they are based. Interpolation between measured data may be allowable, but extrapolation is certainly not. Models that are based on the physics of plastic deformation may have a wider applicability. However, completely physical models based on composition and micro-structure are not yet accurate enough, and some parameters are difficult to measure. The combination in which the type of function is based on physics, but where some of the parameters are based on macroscopic experiments, are called *physically based* or *physically motivated* material models. Some examples of physically based models are given in Section 3.4.2.

Throughout this section hardening models are fitted to the experimental data from Section 2.2. For this fitting procedure, only the stress–strain values up to the uniform strain (maximum engineering stress) were used.

### 3.4.1 Phenomenological Models

For polycrystalline metals, the hardening rate  $\theta = d\sigma_f/d\varepsilon$ , decreases continuously from an initially high value to zero, apart from yield point elongation such as in low carbon steel. The limit of no-hardening is not interesting for sheet metal, since the deformation will localise before that point.

### Nadai Model

A good approximation of a large part of the true stress–strain curve can be obtained with a power law, *e.g.* the Ludwik–Nadai or Nadai relation<sup>4</sup>

$$\sigma_f = C\varepsilon^n \quad (3.47)$$

Here  $\varepsilon$  should formally be the plastic strain in the tensile direction, but for large deformations the elastic part is usually neglected. If the material is pre-strained the relation can be updated to give<sup>5</sup>

$$\sigma_f = C(\varepsilon + \varepsilon_0)^n \quad (3.48)$$

### Voce Model

If the hardening rate is plotted as a function of the stress, often a linearly decreasing relation can be observed. This part of the hardening curve is often denoted as *Stage III* hardening. A relation that represents this behaviour is as follows:

$$\theta = \frac{d\sigma_f}{d\varepsilon} = \theta_0 \left(1 - \frac{\sigma}{\sigma^{\text{sat}}}\right) \quad (3.49)$$

This equation is equivalent to Equation (3.17) for  $a = 1$ , *i.e.* for the critical resolved shear stress in the crystal plasticity model. The resulting flow stress as a function of the strain is written as

$$\sigma_f = \sigma_{y0} + \Delta\sigma \left[1 - \exp\left(-\frac{\varepsilon}{\varepsilon_0}\right)\right] \quad (3.50)$$

where  $\Delta\sigma = \sigma^{\text{sat}} - \sigma_{y0}$  and  $\varepsilon_0 = \tau^{\text{sat}}/\theta_0$ . This model was first described by Voce (1948).

### Equivalent Stress and Strain

The hardening relations described above are derived from one-dimensional experiments. For the analysis of sheet metal forming, the relations should be extended, at least, to two-dimensional deformations. The common way to achieve this is to determine equivalent stress and equivalent plastic strain values for arbitrary stress states. The equivalent stress then depends on the equivalent plastic strain in the same way as the uniaxial stress depends on the uniaxial plastic strain in a uniaxial tensile test.

A numerically straightforward approach is to use the Euclidean norm of the stress and plastic strain rate tensors as equivalent values. The equivalent plastic strain is obtained by integration of the equivalent plastic strain rate. Since the hydrostatic stress does not affect the plastic flow, only the deviatoric part of the stress tensor is used. Furthermore, in order to obtain equivalent stress and strain values for a uniaxial stress state that are equal to the uniaxial stress and strain, the norms are scaled as follows:

$$\sigma_{\text{eq}} = \sqrt{\frac{3}{2}\boldsymbol{\sigma}^{\text{dev}} : \boldsymbol{\sigma}^{\text{dev}}} \quad \text{and} \quad \dot{\varepsilon}_{\text{eq}} = \sqrt{\frac{2}{3}\dot{\boldsymbol{\varepsilon}}^{\text{P}} : \dot{\boldsymbol{\varepsilon}}^{\text{P}}} \quad (3.51)$$

<sup>4</sup>Also called the ‘Hollomon’ relation.

<sup>5</sup>Also called the ‘Swift’ relation.

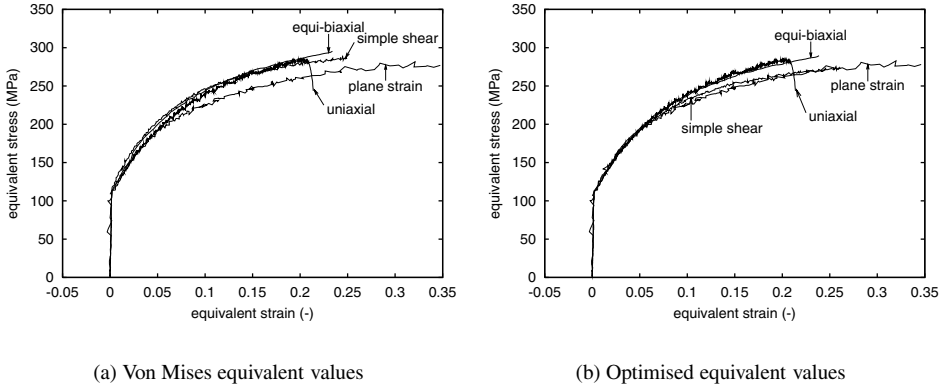


Figure 3.11: Equivalent stress–strain curves.

These values are consistent with the Von Mises yield surface and are therefore called Von Mises equivalent values. Figure 3.11(a) shows the Von Mises equivalent stresses and strains, which are calculated from the measured stress and strain curves according to Figure 2.7. It can be seen that the curves do not completely coincide, suggesting that the Von Mises yield function does not fully apply.

To make the equivalent stress consistent with a selected yield function, that particular yield function can be used as a definition. Usually, the yield surface can be written in the format

$$\phi(\boldsymbol{\sigma}, \varepsilon_{\text{eq}}, \dots) = \varphi(\boldsymbol{\sigma}) - \sigma_f(\varepsilon_{\text{eq}}, \dots) \quad (3.52)$$

It is natural to define the part  $\varphi$  that depends only on the stress, as the equivalent stress.

The equivalent strain could still be chosen according to the Von Mises definition, but it is often assumed that the equivalent stress and strain pair should be energetically conjugate. The rate of plastic work per unit volume is then described by

$$\dot{w}^{\text{P}} = \sigma_{\text{eq}} \dot{\varepsilon}_{\text{eq}} = \boldsymbol{\sigma} : \dot{\boldsymbol{\varepsilon}}^{\text{P}} \quad (3.53)$$

which leads to a definition of the equivalent strain rate:

$$\dot{\varepsilon}_{\text{eq}} = \frac{\boldsymbol{\sigma} : \dot{\boldsymbol{\varepsilon}}^{\text{P}}}{\sigma_{\text{eq}}} \quad (3.54)$$

A strong argument for taking energetically conjugate pairs is found in crystal plasticity. Combining (3.11), (3.13) and (3.53) yields

$$\dot{w}^{\text{P}} = \boldsymbol{\sigma} : \mathbf{D}^{\text{P}} = \boldsymbol{\sigma} : \sum_{\alpha=1}^{12} \dot{\gamma}_{\alpha} \mathbf{P}_{\alpha} = \sum_{\alpha=1}^{12} \dot{\gamma}_{\alpha} \boldsymbol{\sigma} : \mathbf{P}_{\alpha} = \sum_{\alpha=1}^{12} \dot{\gamma}_{\alpha} \tau_{\alpha} \quad (3.55)$$

For isotropic hardening, each resolved shear stress on an active slip system ( $\dot{\gamma}_\alpha \neq 0$ ) is equal to the critical resolved shear stress  $\tau^c$ . The sign of  $\tau_\alpha$  is equal to  $\dot{\gamma}_\alpha$ , hence, with (3.19):

$$\dot{w}^p = \tau^c \sum_{\alpha=1}^{12} |\dot{\gamma}_\alpha| = \tau^c \dot{\Gamma} \quad (3.56)$$

The equivalent slip rate  $\dot{\Gamma}$  represents the total amount of dislocation movement. The dislocation movements, their interactions and subsequent immobilisation is considered to be the main source for work hardening. Therefore, an energetically conjugate  $\varepsilon_{\text{eq}}$  seems to be an appropriate measure of plastic deformation.

An improved equivalent stress and strain measure was determined by fitting the initial 5% strain of the experimental stress–strain curves in uniaxial, equi-biaxial, plane-strain and simple shear states to each other. With the constraint that the equivalent stress and strain are equal to the true stress and strain in the uniaxial case and that the equivalent stress and strain measures are energetically conjugate, we can define equi-biaxial, plane strain and shear factors  $f_{\text{bi}}$ ,  $f_{\text{ps}}$  and  $f_{\text{sh}}$  such that

$$\sigma_{\text{eq}} = \sigma_{\text{un}} \quad \varepsilon_{\text{eq}} = \varepsilon_{\text{un}} \quad (3.57\text{a})$$

$$\sigma_{\text{eq}} = \frac{1}{f_{\text{bi}}} \sigma_{\text{bi}} \quad \varepsilon_{\text{eq}} = f_{\text{bi}} \varepsilon_{\text{bi}} \quad (3.57\text{b})$$

$$\sigma_{\text{eq}} = \frac{1}{f_{\text{ps}}} \sigma_{\text{ps}} \quad \varepsilon_{\text{eq}} = f_{\text{ps}} \varepsilon_{\text{ps}} \quad (3.57\text{c})$$

$$\sigma_{\text{eq}} = \frac{1}{f_{\text{sh}}} \tau_{\text{sh}} \quad \varepsilon_{\text{eq}} = f_{\text{sh}} \gamma_{\text{sh}} \quad (3.57\text{d})$$

The equi-biaxial, plane strain and shear factors derived from the fitting of the initial part of the curve are given in Table 3.2. Note that these experimentally determined values can be used directly in the Vegter yield function. The values that follow theoretically from the Von Mises yield function, the quadratic Hill yield function and a polycrystal analysis are given for comparison. For the Hill function, a planar isotropic model, based on  $\bar{R} = 0.72$ , is used. Based on this  $R$ -value, the equi-biaxial yield stress for the Hill model is much too low. For the polycrystal analysis, the stress factors were calculated based on a Taylor model and a discretised orientation set of the material. The range of values for the  $-45^\circ$ ,  $0^\circ$ ,  $45^\circ$  and  $90^\circ$  orientations are presented in the table (see also Appendix C).

The resulting stress–strain curves are presented in Figure 3.11(b). It can be seen that the plane strain and shear curves are almost equal for the complete strain interval. The uniaxial and equi-biaxial curves deviate from the other two after approximately 6% strain. Apparently, the concept of equivalent stress and strain values is not valid for large strains. This may be due to texture or other micro-structural developments during the deformation. The role of texture evolution will be considered in the next chapter.

### Effects of Temperature and Strain Rate

The Nadai and Voce hardening function described above only consider work hardening. It was shown in Section 2.2 that for warm forming of aluminium, the strain rate and temperature

Table 3.2: Equi-biaxial, plane strain and shear factors.

	experimental	Von Mises	Hill '48	Taylor theory
$f_{bi}$	1.02	1.000	0.927	0.94–1.00
$f_{ps}$	1.15	1.155	1.101	1.05–1.10
$f_{sh}$	0.605	0.577	0.594	0.56–0.60

have a significant influence on the flow stress. It is attempted to adapt the hardening functions in order to take changing temperatures and strain rates into account.

The strain rate sensitivity of the flow stress is often described by the technological parameter  $m$ , which is the slope of the curve in a  $\log \sigma$ – $\log \dot{\varepsilon}$  plot. Combining, *e.g.* the Nadai work hardening function with this strain rate relation, we obtain

$$\sigma = C(\varepsilon + \varepsilon_0)^n \left( \frac{\dot{\varepsilon}}{\dot{\varepsilon}_0} \right)^m \quad (3.58)$$

where  $\dot{\varepsilon}_0$  is a reference strain rate.

The physics of dislocation movement suggests a thermally activated process. The relation between strain rate and temperature can then be derived from statistical mechanics (Meyers, 1999). This approach is the basis of the Zener–Hollomon parameter (Zener and Hollomon, 1944) defined as

$$Z = \dot{\varepsilon} \exp \left( \frac{U}{kT} \right) \quad (3.59)$$

where  $U$  is an activation energy  $k$  is Boltzmann's constant and  $T$  is the absolute temperature.<sup>6</sup> This parameter can be used to describe the combined effects of strain rate and temperature. In Equation (3.58), the strain rate  $\dot{\varepsilon}$  must be replaced by  $Z$  to account for variable temperatures.

This approach may be legitimate for small strain rate and temperature variations. However, from the experimental data given in Section 2.2 it is immediately clear that the rate sensitivity parameter  $m$  itself is temperature dependent. At low temperatures the behaviour is almost rate independent, and at high temperatures the rate sensitivity is significant. In (3.58) combined with (3.59), the influence of work hardening, strain rate and temperature are multiplied together. Many other phenomenological models described by Meyers (1999) share this property. An influence of the temperature on the strain rate sensitivity cannot be modelled in this way and therefore these models are inappropriate for the simulation of warm forming of aluminium.

A more advanced, but still completely phenomenological, adaptation is reached by allowing  $C$ ,  $n$  and  $m$  in (3.58) to depend on the temperature. The stress–strain curves can be fitted separately to the tests at different temperatures. This leads to sets of parameters  $C$ ,

<sup>6</sup>In this thesis, the temperature is mostly given in degrees Celsius, but in the material models the absolute temperature in Kelvin must be used.

Table 3.3: Parameters for the extended Nadai model.

$T_m$	800 K	$a_1$	134.2 MPa	$n_0$	0.3117
$\varepsilon_0$	0.004118	$a_2$	3.669	$m_0$	0.001236
$\dot{\varepsilon}_0$	$0.002 \text{ s}^{-1}$	$b_1$	0.2086	$c$	12.42
$C_0$	491.7 MPa	$b_2$	1.698		

$n$  and  $m$ . The results suggested to use the following functions:

$$C(T) = C_0 + a_1 \left[ 1 - \exp \left( a_2 \frac{T - 273}{T_m} \right) \right] \quad (3.60a)$$

$$n(T) = n_0 + b_1 \left[ 1 - \exp \left( b_2 \frac{T - 273}{T_m} \right) \right] \quad (3.60b)$$

$$m(T) = m_0 \exp \left( c \frac{T - 273}{T_m} \right) \quad (3.60c)$$

where  $T$  is the absolute temperature.  $T_m$  is used to make that part of the formulas dimensionless and can be chosen arbitrarily. The remaining 9 parameters were fitted simultaneously to 8 uniaxial tensile tests, representing temperatures of 25 °C, 100 °C, 175 °C and 250 °C at strain rates of  $0.002 \text{ s}^{-1}$  and  $0.02 \text{ s}^{-1}$ . The data set was reduced to 166 points. This resulted in the values presented in Table 3.3 and stress–strain curves as presented in Figure 3.13. The RMS stress error for this fit is 6.77. This *extended Nadai* model is used in some of the process simulations in Chapter 7.

### 3.4.2 Physically Based Models

In physically based models, the evolution of the flow stress is predicted by considering the physical mechanisms of plastic deformation. Ideally, the influence of work hardening, strain rate and temperature, and their interactions, are included. In reality, the models do not predict all phenomena as accurately as hoped for, but the approach is certainly more appealing than adding another fit function for every new phenomenon.

#### The Basis

Plastic deformation in f.c.c. and b.c.c. metals is mainly the result of dislocation movement on the active slip systems. Hence, the resistance to dislocation movement determines the flow stress. The basis of most physically based models is the Orowan equation in rate form:

$$\dot{\gamma} = \rho_m b v \quad (3.61)$$

where  $\dot{\gamma}$  is the average shear rate on a slip system,  $\rho_m$  the mobile dislocation density,  $b$  the magnitude of the Burgers vector and  $v$  is the mean velocity of dislocations that contribute to  $\dot{\gamma}$ . The mean dislocation velocity can be related to the resolved shear stress and the current micro-structure.

The physically based model used here starts with a decomposition of the flow stress into a strain and strain rate independent stress  $\sigma_0$ , a dynamic stress  $\sigma^*$  that depends on the strain rate and temperature and a term  $\sigma_w$  that incorporates the work hardening:

$$\sigma_f = \sigma_0(T) + \sigma^*(\dot{\epsilon}, T) + \sigma_w(\rho, T) \quad (3.62)$$

This decomposition is used, *e.g.* by Bergström (1969, 1983); Van Liempt (1994); Nes (1998). The implementation in the current work was originally used for the simulation of hot deformation of steel by Rietman (1999).

### Dynamic Stress

The dynamic stress  $\sigma^*$  is the driving force that is required to move dislocations through the atomic lattice at a certain velocity. The velocity of a dislocation depends on the rate at which atoms change position in the atomic lattice. This rate is described with a probabilistic approach in statistical thermodynamics (Krausz and Krausz, 1996, Ch.8). Nes (1998) elaborates this to

$$v = bB\nu_D \exp\left(-\frac{U}{kT}\right) 2 \sinh\left(\frac{\tau^*V}{kT}\right) \quad (3.63)$$

where  $B$  is a constant,  $\nu_D$  the Debeye frequency,  $U$  an activation energy,  $V$  an activation volume related to obstacles to dislocation glide and  $\tau^*$  the dynamic shear stress or friction stress. Substitution of this velocity in the Orowan equation (3.61) gives

$$2 \sinh\left(\frac{\tau^*V}{kT}\right) = (b^2\rho_m B)^{-1} \left(\frac{\dot{\gamma}}{\nu_D}\right) \exp\left(\frac{U}{kT}\right) \quad (3.64)$$

At a specified slip rate  $\dot{\gamma}$  and temperature  $T$  the friction stress  $\tau^*$  can be solved from this equation. For large values of  $x$ ,  $\sinh(x)$  can be approximated by  $0.5 \exp(x)$ . Using this in (3.64) yields for the low temperature range

$$\tau^* \approx \frac{U}{V} + \frac{kT}{V} \ln\left(\frac{\dot{\gamma}}{b^2\nu_D\rho_m B}\right) \quad (3.65)$$

With values suggested by Nes (1998) for solute pinning, a rough estimation is made for the 5754-O alloy. The results of (3.64), and (3.65) are presented in Figure 3.12. The curves intersect at a temperature of 0 K.

In simulation programs, the dynamic stress  $\sigma^*$  is often defined by a relation attributed to Krabiell and Dahl (1981):

$$\sigma^*(\dot{\epsilon}, T) = \begin{cases} 0 & \text{if } \dot{\epsilon} < \dot{\epsilon}_0 \exp(-\Delta G_0/kT) \\ \sigma_0^* \left(1 + \frac{kT}{\Delta G_0} \ln \frac{\dot{\epsilon}}{\dot{\epsilon}_0}\right)^p & \text{if } \dot{\epsilon}_0 \exp(-\Delta G_0/kT) < \dot{\epsilon} < \dot{\epsilon}_0 \\ \sigma_0^* & \text{if } \dot{\epsilon} > \dot{\epsilon}_0 \end{cases} \quad (3.66)$$

This relation is clearly based on (3.65), but adapted with a power  $p$  and a maximum value  $\sigma_0^*$ . The preceding discussion suggests that  $p$  should not differ too much from 1 and the non-physical discontinuity at  $\dot{\epsilon} = \dot{\epsilon}_0$  is explained by Figure 3.12.

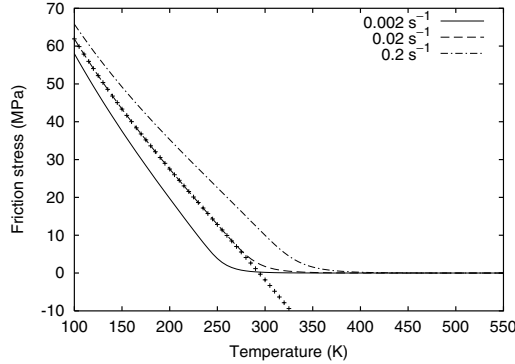


Figure 3.12: Friction stress as function of temperature and strain rate, according to Eq. (3.64). The markers indicate the approximate solution (3.65) for  $\dot{\gamma} = 0.02 \text{ s}^{-1}$ .

The dynamic stress causes a translation of the stress–strain curves. For the experimental determination of the dynamic stress it is convenient to consider the initial yield stress, in order to eliminate rate dependent hardening effects. In the experimental stress–strain curves (Figure 2.3), it is observed that the influence of the strain rate on the initial yield stress is small between 300 K and 450 K and increases rapidly between 450 K and 525 K. In the whole temperature range, Equation (3.65) and also the solution of (3.64) show a large strain rate influence at low temperatures that vanishes at high temperatures. This is in contradiction with the observations and we therefore conclude that the change in initial yield stress cannot be explained by the dynamic stress and  $\sigma^*$  is neglected altogether. This means that the complete influence of the temperature on the flow stress is introduced indirectly by the influence on the hardening rate. For f.c.c. alloys, this behaviour is also noted in the literature *e.g.* Yao and Zajac (2000). Notice that in the extended Nadai model the strain rate and temperature act directly on the flow stress and not on the hardening rate.

### Work Hardening

The work hardening part of the model,  $\sigma_w$ , takes the evolution of the micro-structure into account. A relatively simple one-parameter model is used, where the evolution of the dislocation density  $\rho$  is responsible for the hardening. The relation between the dislocation density and  $\sigma_w$  is given by the Taylor equation (see *e.g.* Estrin, 1996; Meyers, 1999):

$$\sigma_w = \alpha G(T) b \sqrt{\rho} \quad (3.67)$$

where  $\alpha$  is a scaling parameter of order 1. This equation is supported by a dimensional analysis and numerous experiments and is used in a large number of physically based models.

The essential part in these models is the evolution of the dislocation density  $\rho$ . The creation and storage of dislocations is taken to be proportional to the mean free path, while dynamic recovery is taken to be proportional to the dislocation density itself. This leads to



the basic equation for the Bergström model as well as the family of Kocks–Mecking models (Bergström, 1969; Kocks, 1976; Mecking and Kocks, 1981):

$$\frac{d\rho}{d\varepsilon} = c_1 \frac{1}{L} - c_2 \rho \quad (3.68)$$

where the recovery parameter  $c_2$  depends on temperature and strain rate. This will lead to a temperature and strain rate influence on the *hardening*, whereas  $\sigma^*$  influences the *flow stress*. The interpretation of the processes that give a foundation for the parameter  $c_2$  is slightly different for the Bergström model and Kocks–Mecking model. Kocks and Mecking consider only annihilation of dislocations, while Bergström also considers remobilisation. The interpretation and notation of Bergström is used here.

**Bergström model** In the original Bergström model, the mean free path  $L$  was considered to be constant. The formation of dislocation walls and the principle of similitude led Vetter and van den Beukel (1977), to a storage factor that is proportional to the square root of the dislocation density. The dynamic recovery term is considered to be due to annihilation and remobilisation of immobile dislocations. The remobilisation is a thermally activated process, based on vacancy climb (Bergström, 1983). The evolution of dislocation density is now reformulated as

$$\frac{d\rho}{d\varepsilon} = U(\rho) - \Omega(\dot{\varepsilon}, T)\rho \quad (3.69a)$$

with

$$U = U_0 \sqrt{\rho} \quad (3.69b)$$

$$\Omega = \Omega_0 + C \exp\left(-\frac{mQ_v}{RT}\right) \dot{\varepsilon}^{-m} = \Omega_0 + CZ^{-m} \quad (3.69c)$$

The function  $U$  represents storage of mobile dislocations (immobilisation), and  $\Omega$  represents dynamic recovery by remobilisation and annihilation. The functions  $U$  and especially  $\Omega$  determine the shape of the hardening curve at different temperatures and strain rates.  $Z$  is the Zener–Hollomon parameter according to (3.59). In the original model,  $m$  was fixed at  $1/3$ , but here it is used as a fitting parameter.  $Q_v$  is an activation energy for vacancy migration.

Equation (3.69a) can be integrated analytically for constant  $U_0$  and  $\Omega$  (Van Liempt, 1994; Estrin, 1996). For an incremental algorithm the dislocation density  $\rho_{i+1}$  at time  $t_{i+1}$  can be calculated from

$$\rho_{i+1} = \left[ \frac{U_0}{\Omega} \left( \exp\left(\frac{1}{2}\Omega\Delta\varepsilon\right) - 1 \right) + \sqrt{\rho_i} \right]^2 \exp(-\Omega\Delta\varepsilon) \quad (3.70)$$

where  $U_0$  and  $\Omega$  are assumed to be constant during the time increment. This gives a contribution to the flow stress of  $\sigma_{i+1}^w = \alpha Gb \sqrt{\rho_{i+1}}$ , leading to

$$\sigma_{i+1}^w = \alpha Gb \left[ \sqrt{\rho_i} + \left( \frac{U_0}{\Omega} - \sqrt{\rho_i} \right) \left( 1 - \exp\left(-\frac{1}{2}\Omega\Delta\varepsilon\right) \right) \right] \quad (3.71)$$

If we write  $\sigma_0 = \alpha Gb\sqrt{\rho_0}$ ,  $\sigma_{\text{sat}} = \alpha GbU_0/\Omega$ ,  $\Delta\sigma = \sigma_{\text{sat}} - \sigma_0$  and  $\varepsilon_0 = 2/\Omega$  we find for a constant temperature and strain rate exactly the Voce hardening relation (3.50). The Bergström model gives a physical foundation for the Voce parameters, and an extension for deformation paths with non-constant strain rates or non-constant temperatures. Note that introducing strain rate and temperature dependent parameters in (3.50) will not yield the same result as integrating the Bergström relation with the same strain rate and temperature dependent parameters. The Voce relation will result in an immediate stress change on a strain rate or temperature change, while the Bergström model is actually an evolution equation and, accordingly, the stress will only change gradually.

### Strain Rate Independent Stress

Finally the strain rate independent stress  $\sigma_0(T)$  from Equation (3.62) must be determined. It is assumed that this stress is related to stresses in the atomic lattice. Hence, the temperature dependence of the shear modulus  $G(T)$  is also used for  $\sigma_0$  (Rietman, 1999). The flow stress is now evaluated by

$$\sigma_f = g(T) (\sigma_0 + \alpha G_{\text{ref}} b \sqrt{\rho}) \quad (3.72)$$

where  $g(T)$  is the shear modulus divided by the reference value  $G_{\text{ref}}$ . The temperature dependence is numerically represented in this work by the empirical relation

$$g(T) = 1 - C_T \exp\left(-\frac{T_1}{T}\right) \quad (3.73)$$

where  $C_T$  and  $T_1$  are fitting parameters.

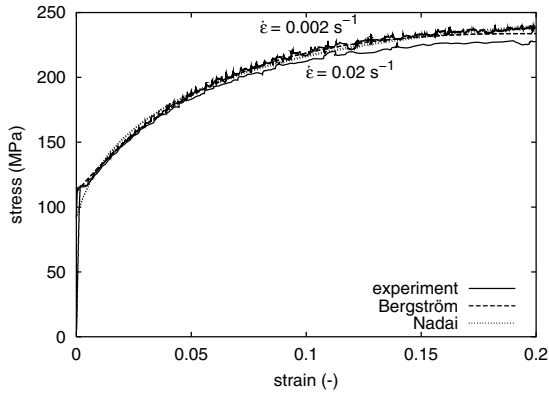
### Comparison with Experiments

Some of the parameters in the Bergström model can be selected beforehand. The rest is determined by a least squares approximation of experimental results, described in Section 2.2.

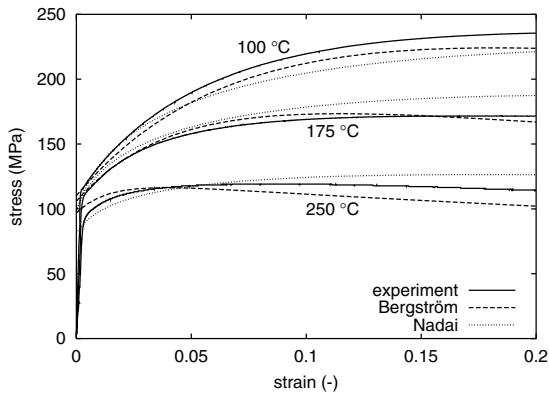
The initial dislocation density  $\rho_0$  was chosen to be  $10^{11} \text{ m}^{-2}$ , which seems to be a reasonable value for annealed aluminium. A ten times lower or higher value only had a small influence on the initial stages of plastic deformation. The magnitude of the Burgers vector  $b$  and the shear modulus at room temperature  $G_{\text{ref}}$  were taken from the literature and a value of  $\alpha = 1.0$  was chosen. The parameters  $C_T$  and  $T_1$  could have been fitted to experimental values of the shear modulus, but better results were obtained by fitting them to the hardening curves, simultaneously with the other parameters.

The 8 remaining parameters were fitted to the same 8 tensile tests as used to fit the extended Nadai model. It resulted in the values presented in Table 3.4. The RMS stress error for this fit is 4.30, which is significantly smaller than the 6.77 for the extended Nadai model.

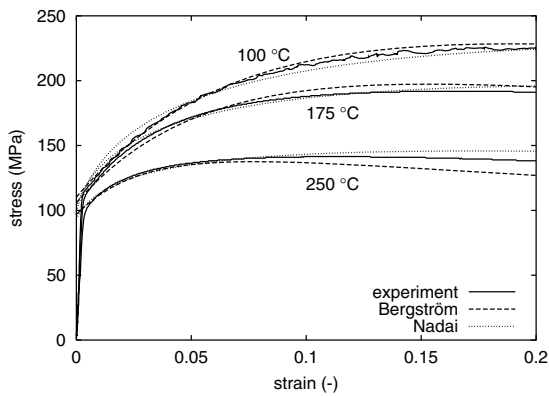
In Figure 3.13 the simulated engineering stress–strain curves are plotted for the extended Nadai model and the Bergström model, together with the experimental data. It can be seen that both models are more or less capable of describing the experiments. It should be noted that the comparison is only valid for a uniform strain, which means up to the maximum engineering stress.



(a)  $T = 25 \text{ }^\circ\text{C}$



(b)  $\dot{\epsilon} = 0.002 \text{ s}^{-1}$



(c)  $\dot{\epsilon} = 0.02 \text{ s}^{-1}$

Figure 3.13: Engineering stress–strain curves — experiments and models.

Table 3.4: Parameters for the Bergström model.

$\sigma_0$	109.3 MPa	$m$	0.422	$\rho_0$	$10^{11} \text{ m}^{-2}$
$\alpha$	1.0	$U_0$	$6.093 \cdot 10^8 \text{ m}^{-1}$	$G_{\text{ref}}$	26354 MPa
$b$	$2.857 \cdot 10^{-10} \text{ m}$	$\Omega_0$	23.63	$C_T$	38.45
$C$	$3.3422 \cdot 10^5$	$Q_V$	$1.0917 \cdot 10^5 \text{ J/mol}$	$T_1$	2975 K

The room temperature curves are plotted separately in Figure 3.13(a) for two strain rates. At this temperature, the models are almost completely independent of the strain rate, although the experiments show a slightly smaller stress at the higher strain rate. This is attributed to dynamic strain ageing, which is not included in the models.

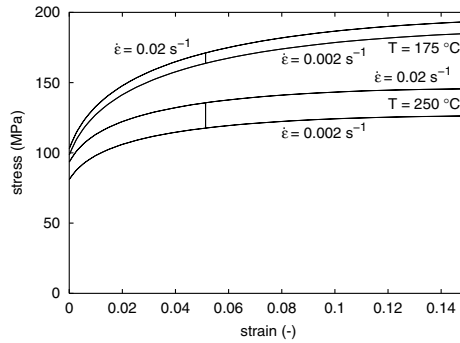
The stress–strain curves for temperatures of 100 °C, 175 °C and 250 °C are plotted in Figure 3.13(b) for a strain rate of 0.002 s<sup>-1</sup> and in Figure 3.13(c) for a strain rate of 0.02 s<sup>-1</sup>. For the higher strain rate, both models perform quite well, specially for the strains below the stress maximum that were used in the parameter fitting. For the lower strain rate the differences are larger. The large stress drop between 100 °C and 175 °C is not very well represented by the extended Nadai model. For the extended Nadai model the flow stress at 100 °C is already too low, while the stress is still too high at 175 °C. The Bergström model does not perform very well if the initial yield stress is overestimated as in the low strain rate case at 250 °C.

Although the models yield more or less similar stress–strain curves for constant strain rate simulations, the predictions are completely different if a jump in the strain rate is simulated. In Figure 3.14 the stress–strain curves are plotted for deformation at 175 °C and 250 °C and for strain rates of 0.002 s<sup>-1</sup> and 0.02 s<sup>-1</sup>. If strain rate changes from 0.002 s<sup>-1</sup> to 0.02 s<sup>-1</sup> or from 0.02 s<sup>-1</sup> to 0.002 s<sup>-1</sup> are applied after a strain of 5 %, the Nadai model immediately follows the curve corresponding to a constant strain rate. With the Bergström model the constant strain rate curve is only slowly approached after continuous straining. These predictions should be compared with the experiments as presented in Figure 2.6. It shows that real material behaviour is somewhere in between and should be investigated more thoroughly.

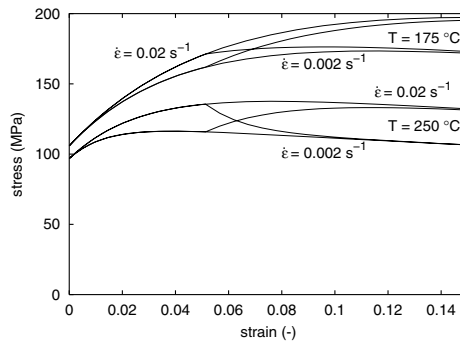
### 3.5 Discussion

In this chapter, the material models were introduced that will be used in the subsequent chapters. The basics of polycrystal plasticity were outlined. Some choices that were made in the phenomenological models were founded on polycrystal plasticity theory. The choice for symmetry in tension and compression and for isotropic hardening, *e.g.*, were related to crystal plasticity models. Moreover, for the Vegter yield function, some necessary parameters could not be measured experimentally and polycrystal models can be used to determine their values. The polycrystal model will be used in a simple necking analysis in Chapter 5. It will not be used in the finite element simulations, because of the computational restrictions.

The phenomenological yield functions are relatively easy to use in finite element simula-



(a) extended Nadai



(b) Bergström

Figure 3.14: Engineering stress–strain curves with and without strain rate jumps at 250 °C.

tions. The Hill '48 model is widely used, but by comparison with the polycrystal model it is shown that it is not well suited for aluminium—or in general for f.c.c. metals. Technological parameters such as the  $R$ -value are often given a meaning based on their relation with the Hill '48 criterion. For  $R$ -values less than 1, *e.g.* Equation (3.34) predicts an equi-biaxial yield stress lower than the uniaxial yield stress. However, experiments by Woodthorpe and Pearce (1970) on aluminium showed a larger equi-biaxial yield stress than the uniaxial yield stress, with  $R$ -values lower than 0.65. They named this *the anomalous behaviour of aluminium sheet*.

Good deep drawability is often related to high  $R$ -values, but the completely different shape of yield loci for f.c.c. metals compared to the yield loci for b.c.c. metals does not permit a direct comparison of  $R$ -values between the two classes of metals. The ratios between equi-biaxial, plane strain, uniaxial and pure shear yield stresses, as presented in Section 3.3.1,

are relevant technological parameters for deep drawing and stretching (Vegter, 1991), but for f.c.c. metals they should not be based on  $R$ -value measurements and the Hill '48 yield function. The Vegter yield function can give a better representation of the yield surface of aluminium because the relevant stress states are used directly. The differences between the Hill '48 and Vegter yield functions will show significant effects on the necking analysis in Chapter 5 and the process analyses in Chapter 7.

The work hardening at different temperatures and strain rates was modelled by adapting the parameters of a Nadai model and with a physically based model. It was shown that the physically based Bergström model equals the phenomenological Voce model if the temperature and strain rate are constant. The temperature and strain rate sensitivity enters the Bergström model through a relatively simple modelling of dynamic recovery. It can predict stress–strain curves at constant strain rate very well, but the response on strain rate jumps is too slow. More recent physically based models are extensions of the one-parameter models. Estrin (1996) adapted the Kocks–Mecking model with a separate evolution of mobile and immobile dislocations. Results show a reasonable result for strain rate jumps, but at higher temperatures than used in this thesis. Nes (1998); Roters *et al.* (2000); Goerdeler and Gottstein (2001) distinguish dislocation densities in cell walls and in cell interiors. The presented results are impressive, but the experimental validation seems to be focused on rolling of aluminium at higher temperatures than in warm forming. These advanced models are not considered in this thesis but it seems justified to investigate their applicability to warm forming in the near future.

## 4. Large Deformations

In the previous two chapters, the logarithmic (or true) strain was used to account for large deformations. For simple, proportional deformations, the time derivative of the true strain is exactly the rate of deformation. For a general description of large plastic deformations, however, the true strain is no longer applicable. The extension of rate constitutive equations to general large deformations requires the use of objective formulations.

Large rotations must be accounted for by rotating the stress tensor. For anisotropic material behaviour, not only the stresses, but also the relation between stress rate and strain rate must be updated. In this case it is easier to use a co-rotating reference frame and apply the constitutive relations on a strain measure that is neutralised for rigid body rotations.

For general large deformations, the determination of the ‘rotation’ of the material is not as straightforward as one would expect at first sight. The choice for a specific rotation or rotation rate will influence the results of a simulation. This also applies to the simple shear test, which was presented in Chapter 2. The choice of a specific rotation is intimately related to the concept of *plastic spin*.

In Section 4.1 the kinematics of large deformations for a continuum is shortly reviewed. This *continuum mechanics* level is usually the level that is directly applied to finite element calculations. It can also be applied to polycrystal models, where each crystallite is considered as a continuum, although the complete polycrystal is not. This is worked out in Section 4.2, where it is used to numerically investigate some effects of large deformations on the plastic behaviour of metals. Plastic spin, texture evolution and the influence on the yield locus and on flow curves are considered. Special attention is given to the simple shear deformation in Section 4.3 because of the relevance for the performed experiments.

### 4.1 Continuum Mechanics

In a continuum mechanics setting, the analysis of large deformations is primarily concerned with proper stress and strain definitions and the constitutive behaviour. Plastic deformation is commonly modelled with a yield function and a hardening rule. Usually, it is assumed that the shape of the yield locus does not change, but in the case of an anisotropic yield function or kinematic hardening, rotation of the yield function or back-stress must be included. The continuum approach is used in the finite element calculations presented in Chapter 7. In this section the fundamental equations and the consequences of particular choices are reviewed. A more complete overview can be found in many textbooks *e.g.* Malvern (1969); Becker and Bürger (1975); Chadwick (1976); Betten (1993).

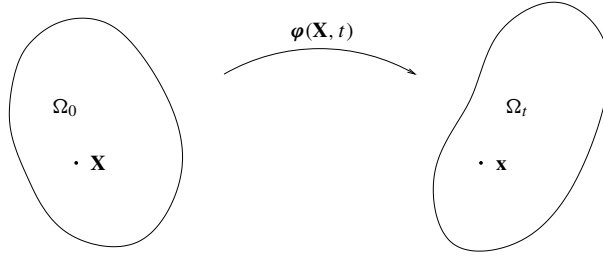


Figure 4.1: Deformation of body  $\Omega_0$  in the reference configuration to the current configuration  $\Omega_t$ .

### Total Formulation

The deformation from a reference configuration  $\Omega_0 \subset \mathbb{R}^3$  to a current configuration at time  $t$ , as depicted in Figure 4.1, can be described by the mapping

$$\varphi : \Omega_0 \longrightarrow \Omega_t \subset \mathbb{R}^3 \quad (4.1)$$

A material point  $\mathbf{X} \in \Omega_0$  in the reference configuration is related to the point  $\mathbf{x} \in \Omega_t$  in the current configuration by

$$\mathbf{x} = \varphi(\mathbf{X}, t) \quad (4.2)$$

The deformation of an infinitesimal environment in  $\Omega_0$  can be described by the *deformation gradient*  $\mathbf{F}$ :

$$\mathbf{F}(\mathbf{X}, t) = \frac{\partial \varphi(\mathbf{X}, t)}{\partial \mathbf{X}} \quad (4.3)$$

The determinant of the deformation gradient represents the volume ratio of the current configuration with respect to the reference configuration, hence:  $\det \mathbf{F} > 0$ . If this condition is satisfied, a multiplicative decomposition into a proper orthogonal tensor and a symmetric tensor can be performed. The proper orthogonal tensor represents a rotation and the symmetric tensor represents a deformation, such that

$$\mathbf{F} = \mathbf{R} \cdot \mathbf{U} = \mathbf{V} \cdot \mathbf{R} \quad (4.4)$$

where  $\mathbf{R}$  is the rotation tensor and  $\mathbf{U}$  and  $\mathbf{V}$  are the right and left stretch tensors respectively.

### Rate Formulation

Models of plastic deformation usually consider the plastic strain rate in the current configuration (see *e.g.* Section 3.2.1). For this purpose we need material velocities rather than displacements. The velocity  $\mathbf{v}$  of material point  $\mathbf{X}$  is given by the material time derivative of  $\mathbf{x}$ :

$$\mathbf{v} = \dot{\mathbf{x}} = \frac{\partial \varphi(\mathbf{X}, t)}{\partial t} \quad (4.5)$$

The local change of current configuration (deformation and rotation) in rate form is given by the *velocity gradient*  $\mathbf{L}$ . The relation between the deformation gradient and the velocity



gradient is given by

$$\mathbf{L} = \frac{\partial \mathbf{v}}{\partial \mathbf{x}} = \dot{\mathbf{F}} \cdot \mathbf{F}^{-1} \quad (4.6)$$

The velocity gradient can be decomposed in the rate of deformation tensor  $\mathbf{D}$  and the spin tensor  $\mathbf{W}$ :

$$\mathbf{L} = \mathbf{D} + \mathbf{W} \quad (4.7)$$

where  $\mathbf{D}$  is the symmetric part and  $\mathbf{W}$  the skew-symmetric part of  $\mathbf{L}$ . In elastoplastic analysis of metals, the rate of deformation is commonly decomposed in an elastic and a plastic part

$$\mathbf{D} = \mathbf{D}^e + \mathbf{D}^p \quad (4.8)$$

An ambiguity in the ‘rotation update’ becomes evident by considering the relation between the polar decomposition of the deformation gradient and the rate of deformation and spin tensors. This relation is found by substitution of (4.4) into (4.6). For the right stretch tensor this yields—with  $\mathbf{R}^{-1} = \mathbf{R}^T$

$$\mathbf{L} = \dot{\mathbf{R}} \cdot \mathbf{R}^T + \mathbf{R} \cdot \dot{\mathbf{U}} \cdot \mathbf{U}^{-1} \cdot \mathbf{R}^T \quad (4.9)$$

The first term on the right-hand side is skew-symmetric and will contribute to the spin tensor  $\mathbf{W}$ . It is referred to as the rate of rotation with reference to the current configuration  $\mathbf{\Omega} = \dot{\mathbf{R}} \cdot \mathbf{R}^T$ . The second term on the right-hand side is only symmetric if  $\dot{\mathbf{U}}$  and  $\mathbf{U}^{-1}$  commute.<sup>1</sup> In all other cases, a change in the right stretch tensor  $\dot{\mathbf{U}}$  will result in a non-symmetric contribution  $\mathbf{R} \cdot \dot{\mathbf{U}} \cdot \mathbf{U}^{-1} \cdot \mathbf{R}^T$  and hence, in a contribution to the rate of deformation  $\mathbf{D}$  and to the spin tensor  $\mathbf{W}$ . The other way around, this means that a spin tensor  $\mathbf{W} = \mathbf{0}$  does *not* imply that  $\dot{\mathbf{R}}$  is also zero. Only if  $\dot{\mathbf{U}}$  and  $\mathbf{U}$  have the same principal directions, do both tensors commute. In that case, the spin tensor  $\mathbf{W}$  is equal to the rate of rotation  $\mathbf{\Omega}$ .

### Rotation of Material Axes

For anisotropic materials, the constitutive equations depend on the direction of deformation and thus on the chosen reference frame. If the displacements are large, the axes of anisotropy will, in general, rotate. In a fixed reference frame, the constitutive equations must then be updated. To avoid updating of the constitutive equations, it is convenient to choose a co-rotating reference frame. The stress and strain increments are always related to this reference frame when the constitutive equations are applied. If, locally, a velocity field represents a rigid rotation, then the rotation of the reference frame should obviously be equal to this rigid rotation. Or, more generally, regarding the results of the previous section: if  $\dot{\mathbf{U}}$  and  $\mathbf{U}$  commute continuously (and therefore  $\mathbf{W}$  equals  $\dot{\mathbf{R}} \cdot \mathbf{R}^T$ ) the rotation of the reference frame follows the rotation  $\mathbf{R}$ . The material axes in this case are chosen to coincide with the principal deformation axes. This situation is depicted in Figure 4.2(a).

If non-commuting deformations take place, the update of the material axes is not trivial. For an elastically deforming material usually a total deformation description is used, which makes  $\mathbf{R}$  a logical candidate to describe material rotation. For a plastically deforming material, however, the current rate of deformation is more important; then the spin  $\mathbf{W}$

<sup>1</sup>Tensors  $\mathbf{A}$  and  $\mathbf{B}$  commute if  $\mathbf{A} \cdot \mathbf{B} = \mathbf{B} \cdot \mathbf{A}$ .

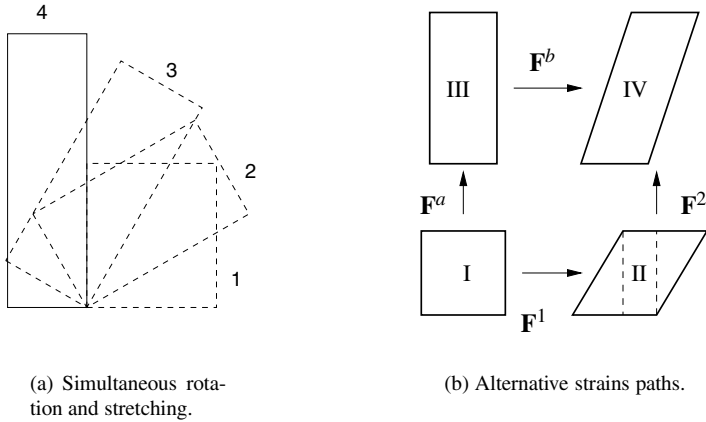


Figure 4.2: Two large deformation tests.

would be a logical choice. To make this more clear, consider two deformation paths from configuration I to IV, shown in Figure 4.2(b). In path 1–2, simple shear is followed by uniaxial tension, whereas in path a–b uniaxial tension is followed by simple shear. Two algorithms are constructed, both based on the polar decomposition of a deformation gradient. One is based on the decomposition of the total deformation gradient, the other on the decomposition of the incremental deformation gradient. Index 0 refers to the start-of-increment values and index 1 to the end-of-increment values. The material rotation tensor  $\mathbf{R}_m$  is used to formulate the stress–strain behaviour in a co-rotating reference frame and the logarithm of the stretch tensor,  $\ln \mathbf{U}$ , is used as a strain measure (the Hencky strain). The integration of the plastic rate of deformation is always based on strain increments.

**Total Algorithm** If the polar decomposition is performed on the total deformation gradient, the rotation tensor directly determines the rotation of the material. The deformation part, however, must be given in an incremental way, in order to follow the strain path. A total algorithm can be based on the following equations:

$$\mathbf{F}_1 = \mathbf{R}_1 \cdot \mathbf{U}_1 \tag{4.10a}$$

$$\mathbf{F}_0 = \mathbf{R}_0 \cdot \mathbf{U}_0 \tag{4.10b}$$

$$\mathbf{R}_{m1} = \mathbf{R}_1 \tag{4.10c}$$

$$\Delta \boldsymbol{\varepsilon} = \ln \mathbf{U}_1 - \ln \mathbf{U}_0 \tag{4.10d}$$

**Incremental Algorithm** If the polar decomposition is performed on the incremental deformation gradient  $\mathbf{F}_0^1$ , the material rotation  $\mathbf{R}_m$  must be updated at every increment. The incremental deformation gradient is the deformation gradient at the end of the increment with respect to the configuration at the start of the increment. The strain increment is now only determined by the change of the current configuration. An incremental algorithm can

be based on the following equations:

$$\mathbf{F}_1 = \mathbf{F}_0^1 \cdot \mathbf{F}_0 \quad (4.11a)$$

$$\mathbf{F}_0^1 = \mathbf{R}_0^1 \cdot \mathbf{U}_0^1 \quad (4.11b)$$

$$\mathbf{R}_{m1} = \mathbf{R}_0^1 \cdot \mathbf{R}_{m0} \quad (4.11c)$$

$$\Delta \boldsymbol{\varepsilon} = \ln \mathbf{U}_0^1 \quad (4.11d)$$

With both formulations, the uniaxial deformation with a superposed rigid rotation as in Figure 4.2(a) will give the same result as the deformation without the rotation (in the material coordinate system) because, for proportional deformation,  $\ln \mathbf{U}_0^1 = \ln \mathbf{U}_1 - \ln \mathbf{U}_0$ . If the deformation is non-proportional<sup>2</sup>, the total rotation, as found from the polar decomposition of the total deformation gradient, Equation (4.10c), depends on the previous stretching. This situation is indicated in Figure 4.2(b). The deformations from I to III and from II to IV do not impose any continuum spin, but clearly deformation  $\mathbf{F}^2$  changes the total rotation in situation IV. It is however not evident that the total deformation determines the material axes. In *e.g.* a crystal plasticity analysis, the rotation of a crystallite depends on the current lattice orientation and the velocity gradient and *not* on the initial orientation. It can be argued that if a new tensile test specimen were machined from the part within the dashed lines, the ‘knowledge’ of the previous stretch cannot be incorporated in the material model, and using the incremental values of  $\mathbf{R}$  and  $\mathbf{U}$  would be consistent with the assumption of an orthotropic material model. At the end of this section and in the next section, when the Mandel spin and the plastic spin are introduced, this discussion will be continued.

### Objective Rates

The presented total and incremental algorithms have clear relations with two generally applied objective rates, the Green–Naghdi rate and the Jaumann rate. These relations are discussed below.

By defining the constitutive equations in a reference frame that rotates with  $\mathbf{R}_m$ , a co-rotating stress  $\hat{\boldsymbol{\sigma}}$  can be defined. The stress in a fixed reference frame then becomes

$$\boldsymbol{\sigma} = \mathbf{R}_m \cdot \hat{\boldsymbol{\sigma}} \cdot \mathbf{R}_m^T \quad (4.12)$$

The rate of change of  $\boldsymbol{\sigma}$  can be written as (using  $\mathbf{R}_m \cdot \mathbf{R}_m^T = \mathbf{1}$ )

$$\begin{aligned} \dot{\boldsymbol{\sigma}} &= \dot{\mathbf{R}}_m \cdot \hat{\boldsymbol{\sigma}} \cdot \mathbf{R}_m^T + \mathbf{R}_m \cdot \dot{\hat{\boldsymbol{\sigma}}} \cdot \mathbf{R}_m^T + \mathbf{R}_m \cdot \hat{\boldsymbol{\sigma}} \cdot \dot{\mathbf{R}}_m^T \\ &= \dot{\mathbf{R}}_m \cdot \mathbf{R}_m^T \cdot \mathbf{R}_m \cdot \hat{\boldsymbol{\sigma}} \cdot \mathbf{R}_m^T + \mathbf{R}_m \cdot \dot{\hat{\boldsymbol{\sigma}}} \cdot \mathbf{R}_m^T + \mathbf{R}_m \cdot \hat{\boldsymbol{\sigma}} \cdot \mathbf{R}_m^T \cdot \mathbf{R}_m \cdot \dot{\mathbf{R}}_m^T \\ &= \dot{\mathbf{R}}_m \cdot \mathbf{R}_m^T \cdot \boldsymbol{\sigma} + \mathbf{R}_m \cdot \dot{\hat{\boldsymbol{\sigma}}} \cdot \mathbf{R}_m^T + \boldsymbol{\sigma} \cdot (\dot{\mathbf{R}}_m \cdot \mathbf{R}_m^T)^T \end{aligned} \quad (4.13)$$

Since  $\hat{\boldsymbol{\sigma}}$  is invariant and  $\mathbf{R}_m$  represents rigid body rotation exactly, the second term on the right-hand side is an objective stress rate. The choice of  $\mathbf{R}_m$  determines the type of objective stress rate. If the total algorithm is applied,  $\mathbf{R}_m = \mathbf{R}$ , then the Green–Naghdi rate<sup>3</sup> (Green

<sup>2</sup>Or actually if  $\dot{\mathbf{U}} \cdot \mathbf{U}^{-1}$  is non-symmetric.

<sup>3</sup>Also called the Green–McInnis rate, Green–McInnis–Naghdi rate or Dienes rate.

and Naghdi, 1965) is obtained:

$$\overset{\diamond}{\sigma} = \dot{\sigma} - \mathbf{\Omega} \cdot \sigma - \sigma \cdot \mathbf{\Omega}^T \quad (4.14)$$

If the incremental algorithm is applied then  $\dot{\mathbf{R}}_m \cdot \mathbf{R}_m^T = \dot{\mathbf{R}}_0^1 \cdot (\mathbf{R}_0^1)^T$ . For infinitesimally small time steps we can write

$$\lim_{\Delta t \downarrow 0} \mathbf{R}_0^1 = \mathbf{1} \quad \text{and} \quad \lim_{\Delta t \downarrow 0} \mathbf{U}_0^1 = \mathbf{1} \quad (4.15)$$

Comparison of (4.7) and (4.9) and using (4.15) makes clear that for infinitesimal increments  $\dot{\mathbf{R}}_m \cdot \mathbf{R}_m^T = \mathbf{W}$ . This leads to the Jaumann rate<sup>4</sup>

$$\overset{\nabla}{\sigma} = \dot{\sigma} - \mathbf{W} \cdot \sigma - \sigma \cdot \mathbf{W}^T \quad (4.16)$$

If the Green–Naghdi or Jaumann rate is selected for analysis, the arguments can also be reversed. The rotation of material axes in a finite element analysis can now be determined as given in the total or incremental algorithm, without the need to integrate the rate equations.

Objective time derivatives have been heavily investigated in relation to kinematic hardening. When using the Jaumann rate, spurious stress oscillations can be observed in the simulation of a simple shear test for large shear angles (Dienes, 1979; Nagtegaal and de Jong, 1981). With the above considerations, it is clear that this stems from the fact that the constant spin  $\mathbf{W}$  determines a constant rate of rotation of the material axes  $\dot{\mathbf{R}}_m \cdot \mathbf{R}_m$ . Use of the Jaumann rate would also lead to a non-vanishing rotation of the axes of anisotropy of a material.

For simple shear, the polar decomposition of the total deformation gradient results in a rotation of the reference frame  $\alpha$  for which  $\tan \alpha = \gamma/2$  (see (A.23) and (A.27)). Since the Green–Naghdi rate is based on the polar decomposition of the total deformation gradient, a maximum rotation of 90° is reached asymptotically. Here no oscillations appear. Usually, the rate of deformation is still obtained from the incremental displacements, mixing the rotation from the total algorithm (4.10c) with the deformation from the incremental algorithm (4.11d). The total algorithm compares well with the results for rigid–plastic material as given by Schieck and Stumpf (1995). In this case, however, the current rate of deformation depends on the total deformation by (4.10d). This is in contradiction with the commonly accepted physical models of plastic deformation.

Instead of  $\mathbf{\Omega}$  and  $\mathbf{W}$ , other rotation rates can be used. Mandel (1973) defines an *isoclinic* configuration. The rotation of the *directors* of this configuration determine in rate formulation the *Mandel spin*. This concept is also used when the mean rotation of crystal lattices is considered to determine the *sub-structural* spin. Rotation of the crystal lattice is considered in Section 4.2. It will be shown there that lattice rotations depend on the direction of the deformation, and therefore the sub-structural spin depends on the current texture and the direction of the rate of deformation. In an isotropic material, the sub-structural spin equals the continuum spin  $\mathbf{W}$ , which is initially equal to the rate of rotation  $\mathbf{\Omega}$ .

For small deformations—but possibly large rotations—all objective rates are similar. The differences between several objective rates appear at large strains. For metals, the deviation from the continuum spin  $\mathbf{W}$  is due to the rotation of individual crystallites. However,

<sup>4</sup>Also called the Jaumann–Zaremba rate.

this also leads to a change in texture. In Section 4.2 it is demonstrated on the basis of polycrystal calculations, that large deformations change the shape of the yield locus. As long as the shape of the yield locus is not changed in an analysis, the choice of the Jaumann rate is as good as any other, unless the material is strongly non-isotropic. This is supported by Peeters *et al.* (2001), who found that, if the texture is not updated, the Mandel spin is better than the rigid body spin only for some specific initial textures.

This conclusion is especially important for finite element models in which shell elements are used. In shell elements, typically, a local coordinate system attached to the element is applied. The out-of-plane rotation is then followed naturally. The in-plane update of the material axes can be performed on an incremental basis. If the presented incremental algorithm is used, no explicit use is made of a total deformation gradient. This can be considered an advantage, because the deformation gradient is generally not calculated for shell elements. It was shown that for the limit  $\Delta t \downarrow 0$ , the algorithm is equivalent to the use of the Jaumann rate. This method is used in the finite element calculations presented in Chapter 7.

### Multiplicative Decomposition

Above, the additive split of the rate of deformation into an elastic part and a plastic part was considered. Alternatively, the deformation gradient can be split into an elastic and a plastic part using multiplicative decomposition:

$$\mathbf{F} = \mathbf{F}^e \cdot \mathbf{F}^p \quad (4.17)$$

attributed to Lee (1969). The computational framework was elaborated by Simo and Ortiz (1985); Simo (1988b,a). It is presented here for completeness and because it is a basis for the plastic spin analysis in the following section.

A physical interpretation of the multiplicative decomposition is that a deformed, stressed configuration can be relaxed, at least locally, to a stress-free state. The mapping from the undeformed configuration to the intermediate stress-free state is described by the plastic deformation gradient  $\mathbf{F}^p$ . The mapping from the intermediate state to the current configuration is described by the elastic deformation gradient  $\mathbf{F}^e$ . Work on the multiplicative decomposition was partly motivated by the large influence of the choice of objective rate in the rate formulation.

Relations between the multiplicative decomposition and rate formulations are given by Eterovic and Bathe (1990); Gabriel and Bathe (1995); Schieck and Stumpf (1995). Especially for small elastic strains, the relations are straightforward. It should be noted that the multiplicative decomposition is not unique. Any rotation tensor  $\tilde{\mathbf{R}}$  can be used to transform (4.17) to

$$\mathbf{F} = \mathbf{F}^e \cdot \mathbf{F}^p = (\mathbf{F}^e \cdot \tilde{\mathbf{R}}) \cdot (\tilde{\mathbf{R}}^T \cdot \mathbf{F}^p) = \tilde{\mathbf{F}}^e \cdot \tilde{\mathbf{F}}^p \quad (4.18)$$

This indeterminacy has the same origin as described with the choice of spin of material axes. Therefore, like in the rate formulation, additional ‘constitutive’ relations are necessary to completely determine the decomposition.

## 4.2 Plastic Spin and Texture Evolution

In Section 3.2 a crystal plasticity model was presented. In that model, the plastic strain rate for a single crystallite was defined as a function of stress and lattice orientation. If the deformations are large, the lattice orientation can change considerably. In a polycrystal, the orientation of each crystallite rotates differently, but not in a random way. The individual rotation of all crystallites causes the evolution of texture. With the large deformation analysis presented here, the texture evolution due to deformation can be determined, within the limitations of the full constraints Taylor theory.

### Calculation of the Lattice Rotation

In crystal plasticity theory, a polycrystal is no longer regarded as a continuum. One abstraction level deeper, however, a single crystallite is considered as a continuum. Therefore, the equations that were derived in the previous section can be applied to a single crystallite. Within one crystallite an orthogonal basis can be defined fixed to the lattice orientation, and its rotation as a result of deformation can be determined. The concept of plastic spin evolves naturally from this.

The deformation gradient is split into a plastic component  $\mathbf{F}^P$  and a non-plastic component  $\mathbf{F}^*$ :

$$\mathbf{F} = \mathbf{F}^* \cdot \mathbf{F}^P \quad (4.19)$$

The ambiguity in (4.17) is resolved by the definition that  $\mathbf{F}^P$  is the result of dislocation glide only. The non-plastic part  $\mathbf{F}^*$  is due to elastic deformation and lattice rotation. In metals, the elastic deformation is very small and can be neglected for the determination of texture evolution. Therefore, only a rigid viscoplastic crystal plasticity model will be considered.

In a rigid viscoplastic material model, the non-plastic deformation in (4.19) represents the lattice rotation  $\mathbf{R}^*$  only:

$$\mathbf{F} = \mathbf{R}^* \cdot \mathbf{F}^P \quad (4.20)$$

The lattice rotation  $\mathbf{R}^*$  is not equal to the rotation tensor  $\mathbf{R}$  from the polar decomposition of  $\mathbf{F}$  in (4.4), since the plastic deformation gradient  $\mathbf{F}^P$  also contains a rotational part. Using (4.6) and (4.20), the velocity gradient for the crystallite becomes

$$\begin{aligned} \mathbf{L} &= \dot{\mathbf{F}} \cdot \mathbf{F}^{-1} \\ &= (\dot{\mathbf{R}}^* \cdot \mathbf{F}^P + \mathbf{R}^* \cdot \dot{\mathbf{F}}^P) \cdot (\mathbf{F}^P)^{-1} \cdot \mathbf{R}^{*T} \\ &= \dot{\mathbf{R}}^* \cdot \mathbf{R}^{*T} + \mathbf{R}^* \cdot \dot{\mathbf{F}}^P \cdot (\mathbf{F}^P)^{-1} \cdot \mathbf{R}^{*T} \end{aligned} \quad (4.21)$$

where the first component on the right-hand side represents the lattice spin  $\mathbf{W}^L$ , and the second component the plastic velocity gradient  $\mathbf{L}^P$ . The decomposition of the plastic velocity gradient into a symmetric and a skew-symmetric part, representing plastic deformation and plastic spin, finally results in

$$\mathbf{L} = \mathbf{W}^L + \mathbf{W}^P + \mathbf{D}^P \quad (4.22)$$

$\mathbf{D}^P$  and  $\mathbf{W}^P$  were already defined in (3.11) and (3.12) for the single crystal model. The total spin of a crystallite now becomes

$$\mathbf{W} = \mathbf{W}^L + \mathbf{W}^P = \dot{\mathbf{R}}^* \cdot \mathbf{R}^{*T} + \mathbf{W}^P \quad (4.23)$$

The relation between the rate of the rotation tensor  $\dot{\mathbf{R}}^*$  and the lattice spin is then given by

$$\dot{\mathbf{R}}^* = \mathbf{W}^L \cdot \mathbf{R}^* \quad (4.24)$$

For an increment from  $i$  to  $i + 1$  this is often integrated, using (A.10), to

$$\mathbf{R}_{i+1}^* \approx \exp(\mathbf{W}^L \Delta t) \cdot \mathbf{R}_i^* \quad (4.25)$$

where the integration of (4.24) is only approximate, since  $\mathbf{W}^L$  is not a constant but depends on  $\mathbf{R}^*$  also.

Kok *et al.* (2001) recently introduced a more accurate algorithm by recognising that  $\dot{\mathbf{F}}^P \cdot (\mathbf{F}^P)^{-1}$  is the plastic velocity gradient in the non-rotated lattice reference system  $\mathbf{L}_0^P$ . The velocity gradient is then written as

$$\mathbf{L} = \dot{\mathbf{R}}^* \cdot \mathbf{R}^{*T} + \mathbf{R}^* \cdot \mathbf{L}_0^P \cdot \mathbf{R}^{*T} \quad (4.26)$$

and the spin as

$$\mathbf{W} = \dot{\mathbf{R}}^* \cdot \mathbf{R}^{*T} + \mathbf{R}^* \cdot \mathbf{W}_0^P \cdot \mathbf{R}^{*T} \quad (4.27)$$

The lattice rate of rotation can now be solved from

$$\dot{\mathbf{R}}^* = \mathbf{W} \cdot \mathbf{R}^* - \mathbf{R}^* \cdot \mathbf{W}_0^P \quad (4.28)$$

If  $\mathbf{W}$  and  $\mathbf{W}_0^P$  are considered constant within the time increment this can be integrated exactly, using (A.11), resulting in

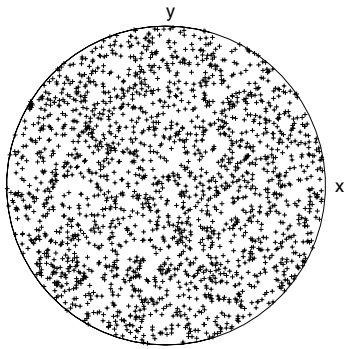
$$\mathbf{R}_{i+1}^* = \exp(\mathbf{W} \Delta t) \cdot \mathbf{R}_i^* \cdot \exp(-\mathbf{W}_0^P \Delta t) \quad (4.29)$$

It was demonstrated by Kok *et al.* (2001, 2002) that this indeed yields a more accurate rotation than (4.25), especially for large deformation increments.

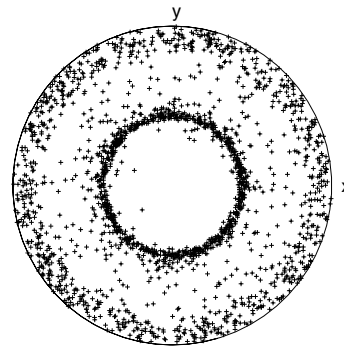
## Texture Evolution

The plastic rate of deformation and the plastic spin follow from the constitutive equations for the crystallite (3.11), (3.12) and (3.14) that were already determined for small deformation analysis. Since  $\mathbf{W}^P$  depends on the orientation of the crystallite, each crystallite in a polycrystal rotates differently. Depending on the imposed deformation, crystallites will rotate to preferred orientations. The rotations of all the crystallites together cause a deformation texture for the polycrystal. Pole figures can be used to represent lattice orientations graphically. In Figure 4.3, the  $\langle 111 \rangle$  pole figures are presented for an initial random texture of 500 grains and 5 calculated deformation textures. An equal area or ‘Lambert’ projection is used to indicate each  $\langle 111 \rangle$  direction for all crystallites in the polycrystal (see *e.g.* Vadon, 1986).

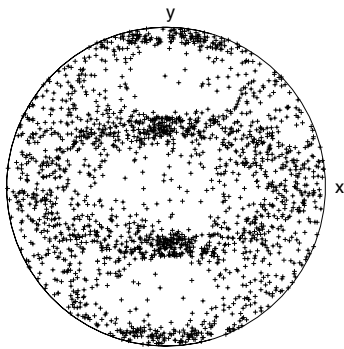
Figures 4.3(b)–4.3(e) represent calculated pole figures, after proportional deformation up to a maximum true strain of  $\varepsilon_y = 0.5$ . Note that these deformations are high compared to the deformations that can be obtained in a real sheet. All pole figures show a clear deformation texture. The texture after equi-biaxial deformation, Figure 4.3(b), is especially sharp. The deformation of  $\varepsilon_x = \varepsilon_y = 0.5$  can also be represented by a uniaxial compressive



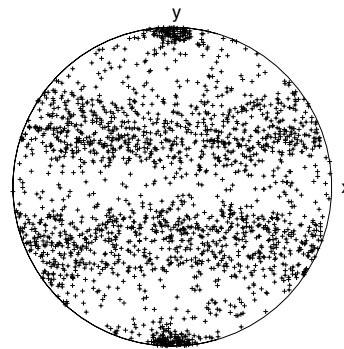
(a) initial, random texture



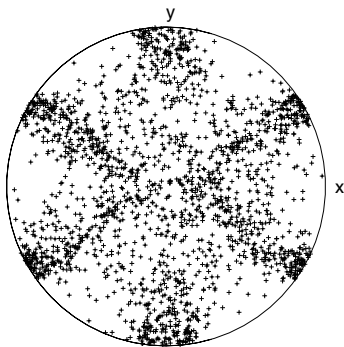
(b) equi-biaxial  $\varepsilon_x = \varepsilon_y = 0.5$



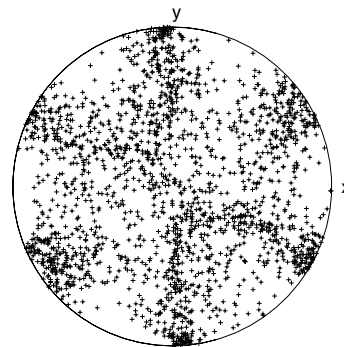
(c) plane strain  $\varepsilon_x = 0, \varepsilon_y = 0.5$



(d) uniaxial  $\sigma_x = \sigma_z = 0, \varepsilon_y = 0.5$



(e) pure shear,  $\varepsilon_y = -\varepsilon_x = 0.5$



(f) simple shear,  $\gamma_{xy} = 1.042$

Figure 4.3: Calculated  $\langle 111 \rangle$  equal area pole figures for 500 crystallites.



deformation of  $\varepsilon_z = -1$ , which is twice as large as the uniaxial tensile deformation in Figure 4.3(d). This explains the sharper texture.

The rotation of crystal lattices is reversed if the deformation is reversed. This means that, even if compression and tension initially show an equivalent flow curve, after some deformation differences will appear. If we interpret Figure 4.3(d) as the top view of a sphere, and rotate it by  $90^\circ$  around the  $x$ -axis, the deformation represents equi-biaxial compression. Compared to Figure 4.3(b), representing equi-biaxial tension, it is seen that for tension, the  $\langle 111 \rangle$  directions rotate away from the centre, while for compression they rotate towards the centre. In other words, the areas with high and low densities of orientations will invert, for a reverse deformation.

The plane strain tensile deformation of Figure 4.3(c) is comparable with a rolling texture. With  $\varepsilon_x = 0$ , tension in the  $y$ -direction and compression in the  $z$ -direction are equivalent. Compression in the  $z$ -direction with  $\varepsilon_x = 0$  is typical for rolling in the  $y$ -direction. There is a clear difference between plane strain and uniaxial tension, represented by Figure 4.3(c) and Figure 4.3(d) respectively. The resulting difference in yield locus can be viewed in Figure 4.4 and is discussed in the next section.

The texture for pure shear deformation is represented by Figure 4.3(e). This deformation can be interpreted as a combination of uniaxial tension in the  $y$ -direction and uniaxial compression in the  $x$ -direction. As stated above, for uniaxial compression Figure 4.3(d) inverts, *i.e.* the dark areas become light and the light areas become dark. Indeed, Figure 4.3(e) can be considered as a combination of Figure 4.3(d) for tension in the  $y$ -direction and the inversion of the same figure, rotated by  $90^\circ$  for compression in the  $x$ -direction.

In Figure 4.3(f), the texture after a simple shear deformation of  $\gamma_{xy} = 1.042$  ( $\frac{\partial u}{\partial y} = \gamma_{xy}$  and  $\frac{\partial v}{\partial x} = 0$ ), is presented. It is demonstrated in Appendix A.3 that, for a simple shear deformation  $\gamma$ , the principal stretch  $\lambda$  is related to the shear angle  $\arctan(\gamma)$  by

$$\gamma = \lambda - \frac{1}{\lambda} \quad (4.30)$$

Hence, the principal stretches for the pure shear and the simple shear deformations in Figures 4.3(e) and 4.3(f) are chosen equal. For small deformations, the pure shear deformation and the simple shear deformation are equivalent, but rotated by  $45^\circ$  with respect to each other. In Figure 4.3(f), the  $x = y$  direction represents the tensile direction of the pure shear deformation. For large deformations, however, the principal directions rotate in the simple shear case and remain constant for the pure shear case. The simple  $45^\circ$  rotation rule does not then apply. Nevertheless, it can be seen that pure shear and simple shear produce, also for relatively large strains, similar orientation changes. Differences and similarities between pure and simple shear deformation are further discussed in Section 4.3.

The predicted pole figures can be compared with experimentally obtained pole figures. It is observed that the full constraints Taylor model will generally produce textures that are too sharp. In reality, the interaction between grains will result in smoother distributions. This should be kept in mind when the influence of texture evolution on yield locus and flow curves is determined, based on the full constraints Taylor model.

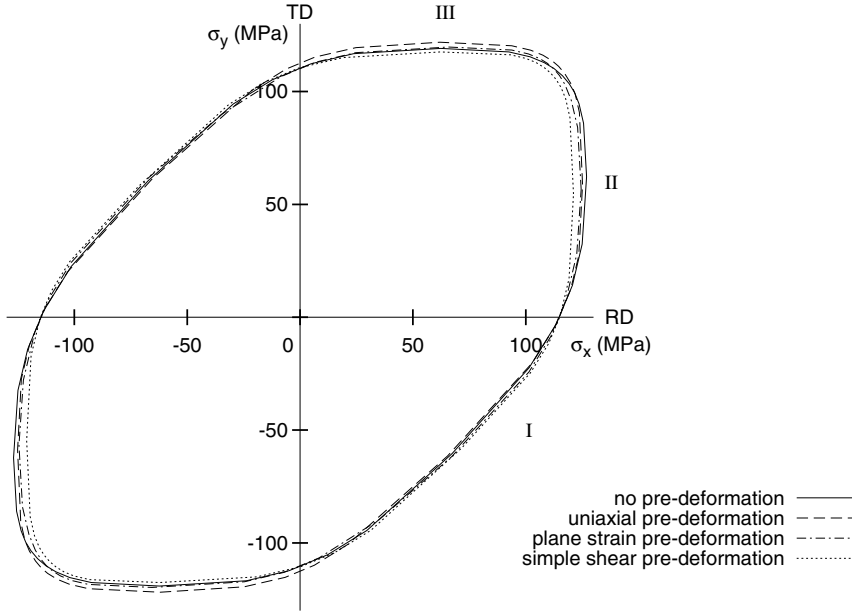


Figure 4.4: Calculated yield loci after several pre-deformations for the applied Al–Mg alloy.

### Influence of Texture Evolution on the Yield Locus

Yield loci can be calculated as explained in Section 3.2.3 on the basis of a polycrystal model. By first calculating the lattice rotations due to a prescribed deformation and then determining the yield locus, the influence of the deformation texture on the yield locus can be predicted. In Figure 4.4, four calculated yield loci are presented. The lattice orientations in the undeformed configuration are based on the experimentally obtained orientation distribution function (ODF) for the Al–Mg sheet used in this research (see Figure 2.1). The ODF was discretised with 2000 orientations, according to the statistical discretisation method of Tóth and van Houtte (1992). The strain rate sensitivity used in the analysis was  $m = 0.05$ .

The yield locus is presented for the ‘as-received’ material, after a uniaxial stress and after plane strain deformation, each up to  $\varepsilon_y = 0.5$ , and after simple shear deformation up to  $\gamma_{xy} = 1.042$ . This is equivalent with the deformations that were used to create Figure 4.3. The  $x$ -direction coincides with the rolling direction and the  $y$ -direction with the transverse direction. All yield loci were scaled, such that the uniaxial flow stress in the rolling direction is equal to 115 MPa, representing the yield strength of the investigated AA 5754 alloy.

It can be seen that uniaxial tension in the transverse direction increases the flow stress in the same direction (indicated as region III in Figure 4.4) and reduces it a little perpendicular to the tensile direction (region II). A plane strain deformation hardly increases the flow stress in the tensile direction (region III), but it does decrease the flow stress in the perpendicular direction (region II). The difference between uniaxial stress and plane strain deformation is mainly observed in the equi-biaxial area and the tensile direction. In the area between

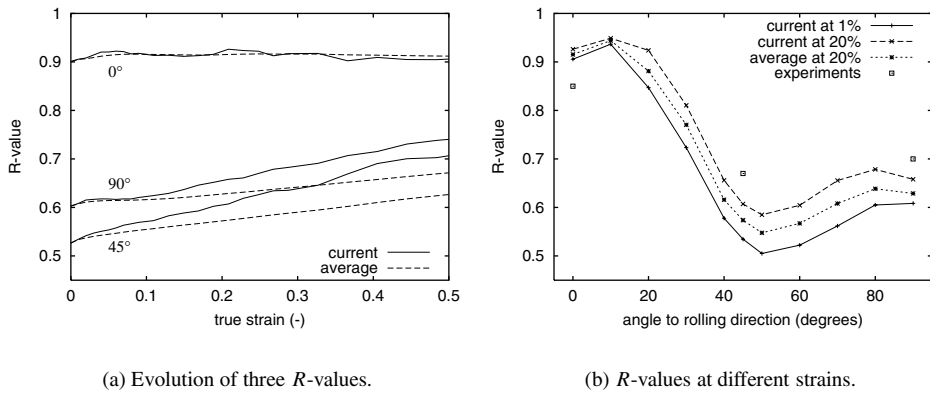


Figure 4.5: Calculated  $R$ -values for the applied Al-Mg alloy.

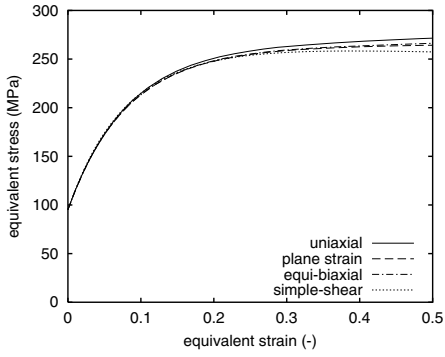
pure shear and uniaxial tension in the rolling direction (region I), a plane strain deformation increases the flow stress somewhat, while uniaxial tension hardly shows any influence in this region. The simple shear pre-deformation mainly decreases the flow stress in the area between equi-biaxial tension and uniaxial tension in the shear direction (region II).

Note, again, that especially the uniaxial and plane strain deformations are larger than what would be expected in sheet forming processes. The magnitude of simple shear may be reached in some areas of a blank, although probably in combination with pure shear. The change in yield locus may have some effect on the global deformation prediction. For a necking analysis, as presented in Chapter 5, the small change of shape in the area between equi-biaxial and plane strain can have a large influence on the predicted limit strain.

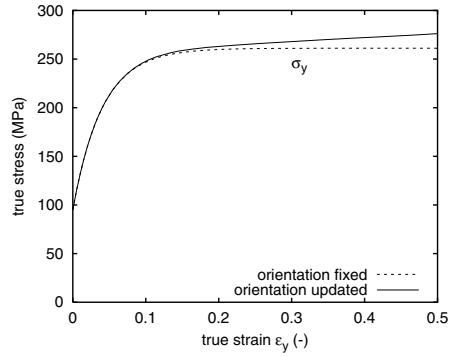
The change of angle between the yield locus and the TD-axis, while stretching in the TD-direction, suggests that the  $R$ -value changes during deformation. In Figure 4.5(a) the calculated current and average  $R$ -values are plotted for tensile tests in the 0°, 45° and 90° directions. The average values are determined from the true strain, using Equation (3.3). The 'current' values are determined from the same equation, but using the strain rate instead of the true strain. The influence of the strain is clear, notably for  $R_{45}$  and  $R_{90}$ .  $R_0$  does not change much. In Figure 4.5(b), the calculated values are shown in the 0° to 90° range. A determination of  $R$ -values, based on the first 1 % strain gives the lowest value for all angles. For most angles the instantaneous  $R$ -values at 20 % strain are significantly higher.  $R$ -values that are based on the total width and thickness strain at 20 % uniaxial strain are in between the two. The global shape of the  $R$ -value distribution is not influenced by the strain range that is used for its determination. It is noted that the predicted variation in  $R$ -values is much larger than that measured experimentally.

### Influence of Texture Evolution on Flow Curves

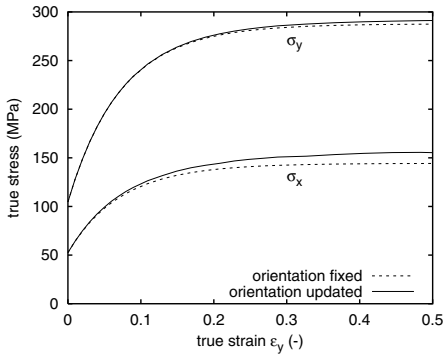
We now consider the influence of the texture evolution on the flow curves. In Figure 4.6 the true stress–strain curves are plotted, as calculated by a full constraints Taylor model



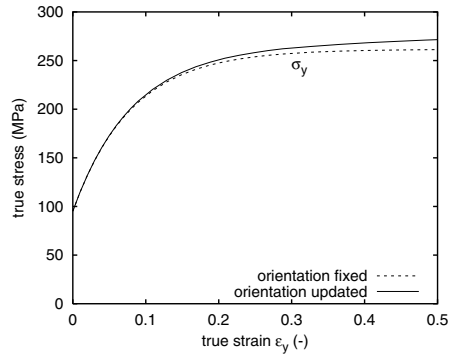
(a) equivalent stress–strain curves



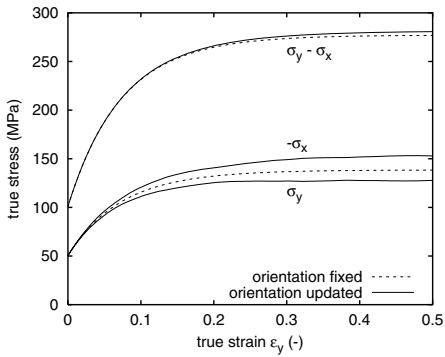
(b) equi-biaxial  $\varepsilon_x = \varepsilon_y$



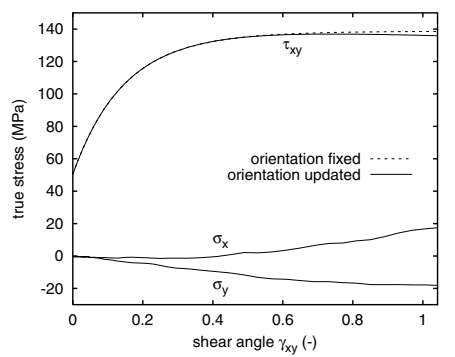
(c) plane strain  $\varepsilon_x = 0$



(d) uniaxial  $\sigma_x = \sigma_z = 0$



(e) pure shear,  $\varepsilon_y = -\varepsilon_x$



(f) simple shear

Figure 4.6: Calculated flow curves for 2000 random crystallites.

with an initial random texture and 2000 crystallites. The deformations are equal to that for the pole figure calculation in Figure 4.3, but more crystallites are used in order to better represent an isotropic initial condition. The hardening parameters are chosen such that the experimental, uniaxial tensile test for 5754-O alloy is well represented. Calculations based on the measured texture for the 5754-O alloy show the same trends, but an isotropic random texture was used here in order to avoid dependence on the loading direction.

Equivalent stress and strain values were calculated as described in Section 3.4. In Figure 4.6(a), the predicted equivalent stress–strain curves are presented for the experiments that were shown in Sections 2.3 and 3.4. Note that without orientation update, all the curves would coincide. In Figure 3.11(b) it was shown that in the experiments, the equivalent stress for the uniaxial and equi-biaxial case increased more than for the plane strain and simple shear case. In Figure 4.6(a), the equivalent stress for the uniaxial test also increases more than that for the plane strain test and especially more than that for the simple shear test. However, the equivalent stress for the plane strain and equi-biaxial tests almost coincide. Comparing Figure 3.11(b) and Figure 4.6(a), it is clear that the difference which is apparent experimentally at an equivalent strain of 0.2 cannot be explained by texture evolution alone.

For the individual deformation types, stress–strain curves are presented with and without orientation update. It can be seen that for equi-biaxial stress, plane strain and uniaxial stress (Figures 4.6(b–d)), the texture update yields some additional hardening. For the plane strain case, the difference is small in the tensile direction, but the transverse stress is influenced more. This can be explained by the fact that, in Figure 3.5(b), the transverse stress is determined by the horizontal position of the point where the tangent to the yield locus is horizontal. A small change in texture typically has a larger effect on  $\sigma_x$  than on  $\sigma_y$ . For an isotropic material with a pressure independent strictly convex yield surface it is required that  $\sigma_x = \frac{1}{2}\sigma_y$ .

The pure shear deformation presented in Figure 4.6(e) shows a large influence of the orientation update on  $\sigma_x$  and  $\sigma_y$ . Note that  $-\sigma_x$  is plotted, to see the difference in evolution clearly. The difference between the largest and the smallest principal stresses  $\sigma_y - \sigma_x$  is not much influenced by the orientation update. This can be visualised as a Mohr circle of which the radius is not influenced by the orientation update, whereas the centre shifts to the compression direction due to the orientation update.

Finally, the simple shear deformation is presented in Figure 4.6(f). For small deformations, the shear stress  $\tau_{xy}$  can be compared with  $\frac{1}{2}(\sigma_y - \sigma_x)$  for the pure shear case. Without orientation update this relation holds, but with orientation update, the pure shear flow stress increases, whereas the simple shear flow stress decreases. The differences are, however, not very large. For large simple shear deformation also normal stresses  $\sigma_x$  and  $\sigma_y$  develop. Further comparisons between pure and simple shear can be found in the next section.

To conclude this section, we recall that the calculated flow curves are based on isotropic hardening of the critical resolved shear stress and an orientation update based on a full constraints Taylor model with an initial random texture. This means that the true influence of orientation update will probably be less than shown here. Moreover, the evolution of micro-structure is only accounted for by a scalar hardening parameter. In reality the micro-structure will also introduce directional dependence. This is totally ignored here and in the rest of this thesis.

### 4.3 Proportional Deformation and Simple Shear

The concept of proportional deformation is often used when rate-type constitutive equations are integrated analytically. Standard forming limit diagrams, described in Chapter 5, also presuppose proportional loading. In the previous section it was noted that a pure shear deformation is proportional, but a simple shear deformation is not. In this section, first three measures for proportionality are defined. These proportionality factors can be used to compare the non-proportionality of a simple shear test with obvious non-proportional deformation such as pure shear followed by plane strain deformation. Implemented in a finite element code, the proportionality factors can give a quick indication of the proportionality of the deformation path for every integration point. Finally, pure and simple shear are compared.

#### Proportional Deformation

For small deformations, proportional deformation means that the rate of deformation is constant, up to a scalar multiplication factor:

$$\mathbf{D}(t) = \alpha(t)\mathbf{D}^* \quad \forall t \quad (4.31)$$

In the case of rigid-plastic behaviour, this means that the stress state is always represented by the same point on the yield locus. With isotropic hardening, this will give a constant ratio between the current uniaxial flow stress and the actual stress state.

If the deformations are large, rigid body rotations should be excluded from these considerations. In other words: proportional deformation of a material remains proportional if a rigid body rotation is added to the deformation, although with respect to a fixed reference frame the rate of deformation at different points in time are not coaxial. The condition is that in a reference frame that rotates with the rigid body, the co-rotating rate of deformation must be coaxial. The right stretch tensor is independent of rigid body rotation and can therefore be used to meet this condition. The co-rotational rate of deformation  $\hat{\mathbf{D}} = \mathbf{R}^T \cdot \mathbf{D} \cdot \mathbf{R}$  is equal to the material time derivative of the logarithmic strain tensor (see Appendix A.1, equation A.18):

$$\hat{\mathbf{D}} = \frac{d \ln \mathbf{U}}{dt}, \quad \text{if the principal directions are constant} \quad (4.32)$$

Proportionality can therefore be defined by the condition

$$\ln \mathbf{U}(t) = \alpha(t) \ln \mathbf{U}^* \quad \forall t \quad (4.33)$$

Note that proportionality is a stronger condition than the requirement that the tensors  $\mathbf{U}^{-1}$  and  $\dot{\mathbf{U}}$  commute. In the last case, all deformations  $\dot{\mathbf{U}}$  must have the same principal directions only. For proportionality, the ratio of eigenvalues  $U_1 : U_2 : U_3$  must also be constant.

In Appendix B, three proportionality factors are defined for a deformation path that is

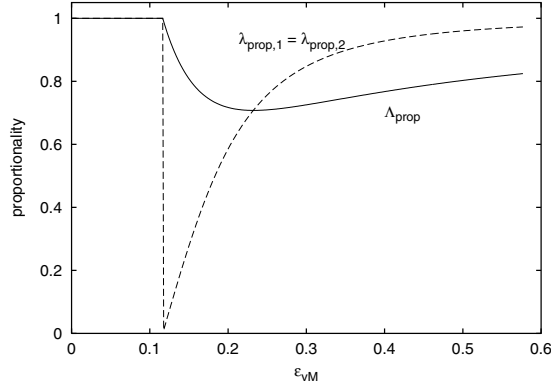


Figure 4.7: Proportionality factors for pure shear, followed by plane strain.

followed incrementally:

$$\Lambda_{\text{prop}} = \frac{\|\ln \mathbf{U}\|}{\sum_{i=1}^n \|\Delta \ln \mathbf{U}_i\|} \quad (4.34)$$

$$\lambda_{\text{prop},1} = \cos(\Delta \ln \mathbf{U}, \ln \mathbf{U}) = \frac{\Delta \ln \mathbf{U} : \ln \mathbf{U}}{\|\Delta \ln \mathbf{U}\| \|\ln \mathbf{U}\|} \quad (4.35)$$

$$\lambda_{\text{prop},2} = \cos(\hat{\mathbf{D}}, \ln \mathbf{U}) = \frac{\hat{\mathbf{D}} : \ln \mathbf{U}}{\|\hat{\mathbf{D}}\| \|\ln \mathbf{U}\|} \quad (4.36)$$

The factor  $\Lambda_{\text{prop}}$  is a measure for the proportionality of a complete deformation path, while  $\lambda_{\text{prop},1}$  and  $\lambda_{\text{prop},2}$  measure the current deformation direction with respect to the total deformation up to the current configuration. All three measures can readily be implemented in a finite element code, in order to spot areas with mainly proportional or highly non-proportional deformation.

In Figure 4.7 the proportionality factors for a pure shear deformation at  $45^\circ$  to the  $x$ - and  $y$ -axes, followed by plane strain deformation ( $\varepsilon_y = 0$ ) are presented. The pure shear deformation is stopped at a maximum of  $\varepsilon_1 = -\varepsilon_2 = 0.1$ . The proportionality factors are plotted as a function of the Von Mises equivalent strain. It can be seen that pure shear is a proportional deformation and plane strain deformation is perpendicular to this pre-deformation ( $\lambda_{\text{prop},1} = \lambda_{\text{prop},2} = 0$  directly after the strain path change).

After a plane strain deformation of the same (equivalent) amount as the preceding pure shear deformation, the total proportionality  $\Lambda_{\text{prop}}$  again increases to 1, since now the plane strain part of the deformation path is dominant. The lowest value of  $\Lambda_{\text{prop}}$  is  $1/\sqrt{2}$ .

### Simple Shear

The relation between simple shear and pure shear is of practical interest, since we adopted a simple shear test to determine the pure shear point of the yield locus. For small deformations, *e.g.* for a determination of the initial yield stress, the relation is straightforward. In order

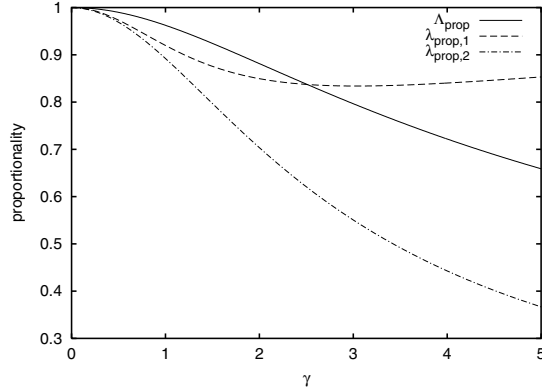


Figure 4.8: Simple shear proportionality factors.

to determine the complete flow curve, however, the rotation of the principal deformation directions in simple shear must be considered carefully.

In Figure 4.8 the proportionality factors are presented for a simple shear test. It can be seen that this type of deformation is not proportional. Although the rate of deformation is constant with reference to the fixed coordinate axes, the principal axes of deformation rotate.  $\Lambda_{\text{prop}}$  and  $\lambda_{\text{prop},2}$  keep decreasing (within this extremely large strain range), whereas  $\lambda_{\text{prop},1}$  reaches a minimum and then increases again. Apparently the change in  $\ln \mathbf{U}$  approaches the direction of  $\ln \mathbf{U}$  more and more. Up to reasonable shear angles ( $\gamma < 1$ ), the values of the proportionality factors are relatively high compared to the values presented in Figure 4.7. This suggests that the non-proportionality of a simple shear deformation is not very severe.

In Section A.3 it is shown that the principal stretches  $\lambda_1$  and  $\lambda_2$  are related by  $\lambda_2 = 1/\lambda_1$  and therefore

$$\ln \lambda_2 = -\ln \lambda_1 \quad \Rightarrow \quad \varepsilon_2 = -\varepsilon_1 \quad (4.37)$$

If  $\varepsilon_2$  is plotted as function of  $\varepsilon_1$ , a straight line appears, suggesting proportional deformation. This is typically what is presented in a forming limit diagram, where proportional deformation is commonly assumed. The current analysis demonstrates that proportionality cannot be determined from a graph of the deformation path in the forming limit diagram.

In Section 4.2 the texture evolution and stress–strain curves for pure shear and simple shear were presented. It was shown that a similar deformation texture develops. When the orientation of a single crystallite is followed, it is observed that in the pure shear case, the orientation changes towards a stable situation. In the simple shear case no stable situations exist, only stagnation areas, where the rate of rotation is low. After a relatively long time in a stagnation area, the rate of rotation increases until the following stagnation area. This behaviour seems to be typical for the viscoplastic formulation (see also Rollet and Wright, 1998; Kocks, 1998).

The effect of texture evolution on the flow curves was considered with reference to Figures 4.6(e) and 4.6(f). It was shown that in pure shear deformation, the magnitude of  $-\sigma_x$  starts deviating from  $\sigma_y$  after a while, and that in simple shear normal stresses  $\sigma_x$  and  $\sigma_y$  develop. Yet, in this work, the simple shear test is used to determine the pure shear stress



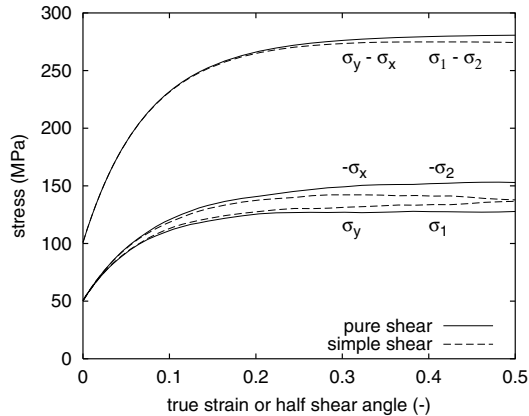


Figure 4.9: Pure shear and simple shear principal stresses.

points for the Vegter yield function.

In Figure 4.9, the stresses of a pure shear simulation are compared with the principal stresses of a simple shear simulation. In both cases the lattice orientations are updated during the simulation. As can be seen, the evolution of normal stresses in the pure shear case and principal stresses in the simple shear case are similar up to a true strain of about 0.2 or a shear angle of 0.4. The difference between maximum and minimum principal stress,  $\sigma_1 - \sigma_2$ , remains similar for even larger strains. Figure 4.6(f) shows that the stress in the  $x$ -direction, which cannot be measured in the simple shear test, is negligible up to a shear angle of 0.4. Based on the analysis of texture evolution, the simple shear test can be used to determine pure shear stresses up to a shear angle of 0.4. For validation it is useful to measure the stress in the  $y$ -direction accurately. Influences other than texture evolution are ignored and therefore the results should still be used with care.

## 4.4 Closure

In this chapter, the extension from small strain to general large plastic strain analysis was considered. The section on continuum mechanics introduced equations that can readily be used in finite element codes. In these codes, yield functions are typically used with constant shape yield surfaces. Large deformations then mainly involve a ‘correct’ rotation of the stresses and the material axes.

The same continuum equations can also be used at a lower abstraction level, where a single grain is considered. The ‘plastic spin’ has a clear meaning at this level and the complementary lattice rotation can easily be calculated. The lattice rotation of all crystallites in a polycrystal determines the texture evolution. The connection between plastic spin and texture evolution led to the conclusion that for practical sheet forming simulations, where a constant shape yield surface is used, the Jaumann rate is sufficient and the material axes can be updated with the continuum spin. If the material spin starts deviating from the continuum spin, the change in shape must also be included in the analysis.

The influence of the deformation texture on yield loci and flow curves was demonstrated. Some influence could be found for strains that are actually very large for sheet forming processes. For the prediction of the general strain distribution, *e.g.* to predict thickness distributions, the influence is not expected to be high. For localisation predictions, however, this is still an open question.

Finally, proportionality of deformation was defined. Three factors were developed that can be used in a finite element analysis. This is useful if the validity of some post-processing values depends on the proportionality of the strain path. The difference between pure shear and simple shear was used as an example. It was argued that the simple shear test can be used up to a shear angle of 0.4 to determine pure shear flow stresses.

# 5. Tensile Instabilities and Forming Limits

An important type of failure in sheet forming processes is fracture. Fracture of ductile metals is often preceded by strong local thinning. This phenomenon is called *necking*. Necking is a deviation from locally uniform deformation due to a tensile instability. Instability occurs if the load carrying capacity decreases, because work hardening of the material cannot compensate for the reduction in cross section. Necking limits the formability of sheet material. Two important material parameters that influence the forming limits are the work hardening and the shape of the yield locus.

In Section 5.1 some terminology is introduced. Furthermore, the flow curve of the investigated aluminium alloy is recalled. The hardening model used to describe the flow curve will show to have a significant effect on predicted forming limits in subsequent sections. In Section 5.2 analytical relations for diffuse necking will be derived. Relations for localised necking are presented in Section 5.3. These are derived partly analytically and partly numerically. The numerical approach is used to predict the influence of several model parameters on forming limit curves. The results are presented in Section 5.4. Finally, in Section 5.5, finite element calculations are presented showing the capabilities of FEM models to predict necking.

## 5.1 Preliminaries

In this section the terminology that is used in this chapter is introduced. Also, experimental data for the investigated aluminium alloy is presented. Two different hardening models are fitted to the flow curve as a preparation for later sections.

### Diffuse and Local Necking

Two types of necking are generally distinguished: diffuse and local necking (see *e.g.* Dodd and Bai, 1987). Examples of diffuse and local necking are presented in Figure 5.1. The size of a diffuse neck is of the order of the width of the specimen. The size of a local neck is of the order of the sheet thickness. The occurrence of diffuse and local necking is determined by the boundary conditions. A diffuse neck changes the in-plane displacements on the boundary, whereas a local neck does not. Consequently, if the boundary conditions prevent in-plane displacements perpendicular to the boundary, then diffuse necking cannot occur and the forming limit is determined by local necking. In deep drawing this is often the case, since the in-plane displacements are largely determined by the tool displacements. In Sections 5.2 and 5.3 conditions for diffuse and local necking are derived.

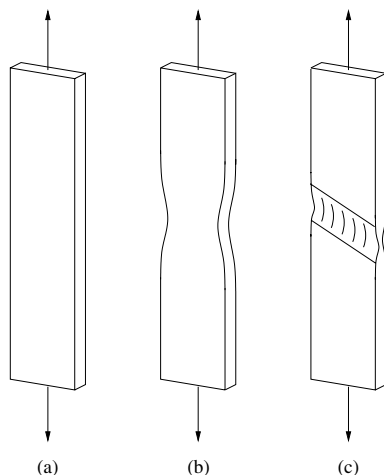


Figure 5.1: Sheet forming instabilities: (a) uniform deformation, (b) diffuse necking and (c) local necking.

### Forming Limit Diagrams

The deformation of a number of points in a sheet product can graphically be presented in a forming limit diagram<sup>1</sup> (FLD). In an FLD the major strain (maximum in-plane principal true strain) is represented vertically and the minor strain horizontally. All states in which the deformation becomes unstable can be connected graphically and then form a forming limit curve (FLC). The FLC gives an impression of the formability of a sheet material. Calculated strains, *e.g.* from FEM analysis, can be compared with an FLC to determine the feasibility of the analysed sheet forming process.

In Figure 5.2 an FLC is presented for the AA 5754-O alloy that is considered in this thesis. The FLC was determined with Nakazima tests. In a Nakazima test, sheets are deformed with a hemispherical punch until visible necking (see *e.g.* Pearce, 1991). The strain just before necking is considered to be a limit strain. By varying the sheet width, relative to the punch diameter, deformations from almost uniaxial stress to equi-biaxial strain can be obtained.

The stability of a deformation path depends on the material and on the complete deformation history. Forming limit curves are mostly presented for proportional deformation paths which will also be the case in this thesis. For proportional deformation paths, some analytical relations will be derived in the following sections.

### Work Hardening

The strain at which necking starts is largely affected by the work hardening. Later in this chapter, diffuse and local necking is analysed with the Nadai and the Voce hardening

<sup>1</sup>Also known as Keeler–Goodwin diagram.

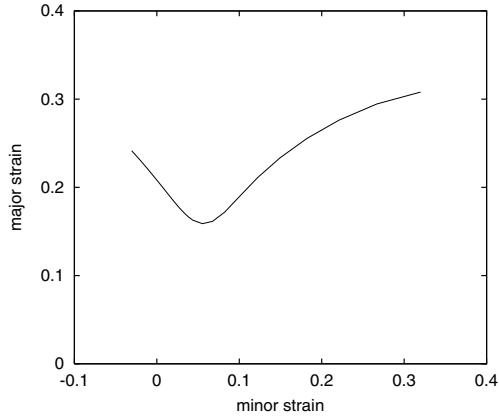


Figure 5.2: FLC for AA 5754-O, derived with Nakazima tests (courtesy Corus RD&T).

Table 5.1: Hardening parameters for the investigated AA 5754-O alloy.

$C$	Nadai		$\sigma_{y0}$	Voce	
	$n$	$\varepsilon_0$		$\Delta\sigma$	$\varepsilon_0$
446.3 MPa	0.292	0.0039	106.4 MPa	181.8 MPa	0.0824

models. In this work, we focus on one particular Al–Mg sheet. To compare the influence of the hardening function, the flow curve for the investigated AA 5754-O sheet at room temperature and with  $\dot{\varepsilon} = 0.02 \text{ s}^{-1}$  is modelled with a Nadai and with a Voce equation according to (3.48) and (3.50) respectively. Experimental stresses lower than the yield stress and strains larger than the uniform strain were not considered in the fitting process. A least squares fit of the parameters resulted in the values presented in Table 5.1.

In Figure 5.3 the experimental data and the fitted Nadai and Voce curves are plotted. Note that the Voce relation presents a better fit of the experimental flow curve than the Nadai relation. Especially at high strains, just before necking, the Nadai relation predicts too much hardening. In the following sections the fitted parameter values for Nadai and Voce hardening will be used for reference. It will be shown that small differences in the flow curves result in large differences in predicted forming limits.

## 5.2 Diffuse Necking

One of the criteria for diffuse necking is the maximum force criterion (MFC).<sup>2</sup> According to the maximum force criterion, diffuse necking starts if the maximum force on a plate

<sup>2</sup>The maximum force criterion is often attributed to Swift (1952), but the Swift criterion is only equivalent for the uniaxial, plane strain and equi-biaxial stress states.

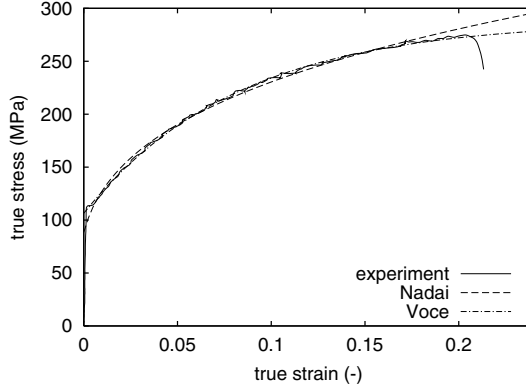


Figure 5.3: Uniaxial flow curve and best Nadai and Voce fits for AA 5754-O.

does not increase upon further stretching. For a given material model and a proportional deformation path, the point of necking can often be determined analytically.

For the analysis of diffuse necking, the elastic deformation is neglected and plastic deformation is assumed to be incompressible. To determine an analytical relation for diffuse necking, consider a biaxially loaded square plate and a proportional loading path. For isotropic hardening, proportional loading in stress will also result in proportional deformation:

$$\sigma_2 = \alpha \sigma_1, \quad \sigma_3 = 0 \quad (5.1)$$

$$d\varepsilon_2 = \beta d\varepsilon_1 \Rightarrow d\varepsilon_3 = -(1 + \beta) d\varepsilon_1 \quad (5.2)$$

The total loads in the 1- and 2-directions are

$$P_1 = A_1 \sigma_1, \quad P_2 = A_2 \sigma_2 \quad (5.3)$$

where  $A_1$  and  $A_2$  are the areas of the cross sections perpendicular to the 1- and 2-directions respectively. If  $l_1$  and  $l_2$  are the lengths of the plate in the 1- and 2-directions, the incompressibility constraint requires that  $A_1 l_1$  and  $A_2 l_2$  be constant, hence

$$dA_i l_i + A_i dl_i = 0 \Rightarrow d\varepsilon_i = \frac{dl_i}{l_i} = -\frac{dA_i}{A_i} \quad i = 1, 2 \text{ no sum} \quad (5.4)$$

The change in force in direction  $i$  is determined by writing (5.3) in a differential format:

$$dP_i = d\sigma_i A_i + \sigma_i dA_i \quad i = 1, 2 \text{ no sum} \quad (5.5)$$

As long as  $dP_1 > 0$  and  $dP_2 > 0$  upon further tensile deformation, the maximum force criterion predicts stable deformation. Combining (5.4) and (5.5), the condition for stable deformation becomes

$$\frac{d\sigma_i}{\sigma_i} > -\frac{dA_i}{A_i} = d\varepsilon_i \quad \forall i \in \{1, 2\} \text{ no sum} \quad (5.6)$$

For proportional loading  $d\sigma_1/\sigma_1 = d\sigma_2/\sigma_2$ . If  $\varepsilon_1$  is the major strain ( $\varepsilon_1 > \varepsilon_2$ ) then only the criterion with  $i = 1$  needs to be considered. This condition is commonly presented in a form in which the rate of hardening can be recognised:

$$\frac{d\sigma_1}{d\varepsilon_1} > \sigma_1 \quad (5.7)$$

If isotropic hardening based on plastic work  $w^p$  is assumed, this relation can be worked out further. In this case, the yield function can be written as a stress tensor part and a hardening part as in (3.52). For the biaxial stress state in the loaded plate this becomes

$$\phi(\sigma_1, \sigma_2, w^p) = \varphi(\sigma_1, \sigma_2) - F(w^p) \quad (5.8)$$

On plastic deformation  $\phi \equiv 0$ , hence

$$\frac{\partial \varphi}{\partial \sigma_1} d\sigma_1 + \frac{\partial \varphi}{\partial \sigma_2} d\sigma_2 = F'(w^p) dw^p \quad (5.9)$$

The change in plastic dissipation for the biaxially loaded plate can be written as

$$dw^p = \sigma_1 d\varepsilon_1 + \sigma_2 d\varepsilon_2 = (1 + \alpha\beta)\sigma_1 d\varepsilon_1 = \sigma_{eq} d\varepsilon_{eq} \quad (5.10)$$

and based on the normality principle:

$$\frac{d\varepsilon_2}{d\varepsilon_1} = \frac{\frac{\partial \varphi}{\partial \sigma_2}}{\frac{\partial \varphi}{\partial \sigma_1}} = \beta \quad (5.11)$$

Substituting (5.1), (5.10) and (5.11) in (5.9) and using (5.7), the condition for stable deformation becomes

$$F'(w^p) = \frac{\frac{\partial \varphi}{\partial \sigma_1} d\sigma_1 + \frac{\partial \varphi}{\partial \sigma_2} d\sigma_2}{\sigma_1 d\varepsilon_1 + \sigma_2 d\varepsilon_2} = \frac{\frac{\partial \varphi}{\partial \sigma_1} d\sigma_1}{\sigma_1 d\varepsilon_1} > \frac{\partial \varphi}{\partial \sigma_1} \quad (5.12)$$

The value  $\varepsilon_1^*$  at which diffuse necking starts is called the *uniform strain*. It is the solution of the equation  $F'(w^p) = \partial \varphi / \partial \sigma_1$ .  $F'(w^p)$  is completely determined by the hardening function and  $\partial \varphi / \partial \sigma_1$  by the shape of the yield locus.

In Appendix B.3 Equation (5.12) is elaborated for the planar isotropic Hill '48 model (3.33) and basic Nadai hardening  $\sigma = C\varepsilon^n$ . For this particular combination, it is shown that the uniform strain is independent of the strain ratio and the  $R$ -value:  $\varepsilon_1^* = n$ . For the Voce hardening model and a planar isotropic Hill '48 yield function the stability condition is checked numerically. Results are presented in Figure 5.4. In this figure the lines 'MFC/Nadai' and 'MFC/Voce' represent the diffuse necking criterion. It can be seen that for the Voce hardening model the results *do* depend on the yield function and the strain ratio  $\beta$ . The Voce hardening model results in a much lower uniform strain than the Nadai hardening model, although the parameters were fitted to the same experimental flow curve.

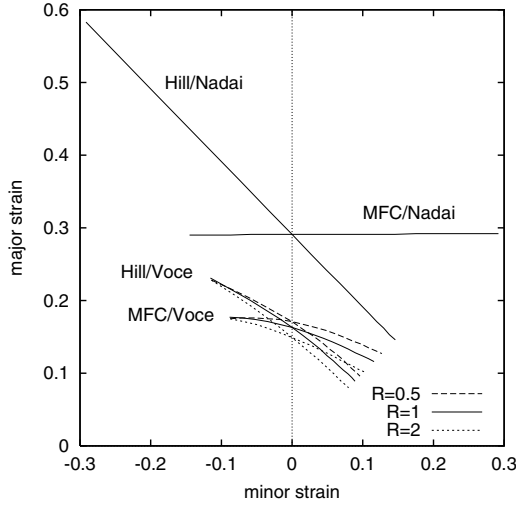


Figure 5.4: Diffuse and local necking predictions according to the maximum force criterion and the Hill criterion.

### 5.3 Localised Necking

In sheet forming processes in-plane deformations are often more or less kinematically determined by the tool displacements. In such cases, diffuse necks cannot develop since diffuse necking changes the in-plane deformation. Local necking does not directly influence the in-plane deformation. These necks typically have a neck size of the order of the sheet thickness and rapidly lead to fracture.

If FLC's are determined theoretically, local necking is usually assumed to be the determining factor. A distinction is made between the left part of the FLC (the drawing region) and the right part of the FLC (the stretching region). For the drawing region a simple stability analysis is sufficient, but for the stretching region an imperfection must be included in the analysis. These regions are treated separately in the subsequent sections.

#### 5.3.1 Localisation in the Drawing Region

First the localised necking criterion by Hill (1952) is reviewed. For this purpose again a biaxially loaded sheet and a proportional deformation process is considered. The proportionality relations (5.1) and (5.2) also apply here. Instead of the total load in the  $i$ -direction,  $P_i$ , now the force per unit sheet length  $T_i$  is considered:

$$T_1 = t\sigma_1, \quad T_2 = t\sigma_2 \quad (5.13)$$

where  $t$  is the sheet thickness. Local necking is assumed to start if  $dT = 0$ . Due to the proportional deformation, this will occur for  $T_1$  and  $T_2$  simultaneously. The necking



condition for the 1-direction yields

$$\begin{aligned} dT_1 &= dt \sigma_1 + t d\sigma_1 = t(\sigma_1 d\varepsilon_3 + d\sigma_1) = t[-\sigma_1(1 + \beta) d\varepsilon_1 + d\sigma_1] = 0 \\ \Rightarrow \quad \frac{d\sigma_1}{d\varepsilon_1} &= (1 + \beta)\sigma_1 \end{aligned} \quad (5.14)$$

If the hardening of the material can be described by the basic Nadai function it is demonstrated in Appendix B.2 that for proportional deformation and isotropic hardening the relation  $\sigma_1 = C'\varepsilon_1^n$  holds. In this case the localised necking condition (5.14) becomes

$$nC'\varepsilon_1^{n-1} = \frac{n\sigma_1}{\varepsilon_1} = (1 + \beta)\sigma_1 \quad (5.15)$$

Therefore the major and minor strain at maximum  $T_1$  are

$$\varepsilon_1^* = n/(1 + \beta) \quad \varepsilon_2^* = \beta n/(1 + \beta) \quad \Rightarrow \quad \varepsilon_1^* + \varepsilon_2^* = n \quad (5.16)$$

In a forming limit diagram this condition can be represented by a straight line through the point where the major strain is  $n$  and the minor strain is 0, parallel to the line  $y = -x$ . For the Nadai hardening function, the limit strains are independent of the yield function. This is not the case for the Voce hardening function.

The results for the maximum force criterion and Hill localisation analysis are presented in Figure 5.4 for the range  $-0.5 \leq \beta \leq 1$ . In the necking analysis a planar isotropic Hill '48 yield function was used with hardening parameters according to Table 5.1. Equations (5.7) and (5.14) determine that for  $\beta < 0$  the diffuse necking criterion (MFC) is reached before the local necking criterion (Hill) and for  $\beta > 0$  *vice versa*. For the Nadai hardening relation, the limit strains are nearly independent of the used  $R$ -value, even with  $\varepsilon_0 \neq 0$ , and only  $R = 1$  is presented. The limit strain for a Voce hardening model *does* depend on the  $R$ -value. Note that for  $R \neq 1$ , the strain ratio  $\beta = -0.5$  does not describe a uniaxial stress state.

The differences between the predicted limit strains for the Nadai and the Voce hardening models are considerable. This is the case for the maximum force criterion as well as the Hill analysis. Following the importance of the hardening ratio in both criteria, the difference is attributed to the overestimated hardening rate at large strain for the Nadai model, as shown in Figure 5.3. Figure 5.4 also clearly shows that the straight line  $\varepsilon_1^* + \varepsilon_2^* = n$  for local necking with the Nadai hardening model does not transfer to the Voce hardening model.

### Strain Incompatibility

If necking takes place as described by the Hill criterion, a localisation band emerges at a specific angle to the major strain direction (Figure 5.5). The strain rate in the band accelerates, while the strain outside the band remains constant (neglecting elastic spring-back). However, the displacements inside and outside the band must remain compatible. Therefore, the strain in the direction along the band must be zero. Since the deformation is proportional up to the localisation strain, the band will develop in the direction in which the strain is zero. The relation between the strain  $\varepsilon_{tt}$  in a direction at angle  $\theta$  to the major strain direction and the principal strains  $\varepsilon_1$  and  $\varepsilon_2$  is given by

$$\varepsilon_{tt} = \frac{1}{2}(\varepsilon_1 + \varepsilon_2) + \frac{1}{2}(\varepsilon_1 - \varepsilon_2) \cos 2\theta \quad (5.17)$$

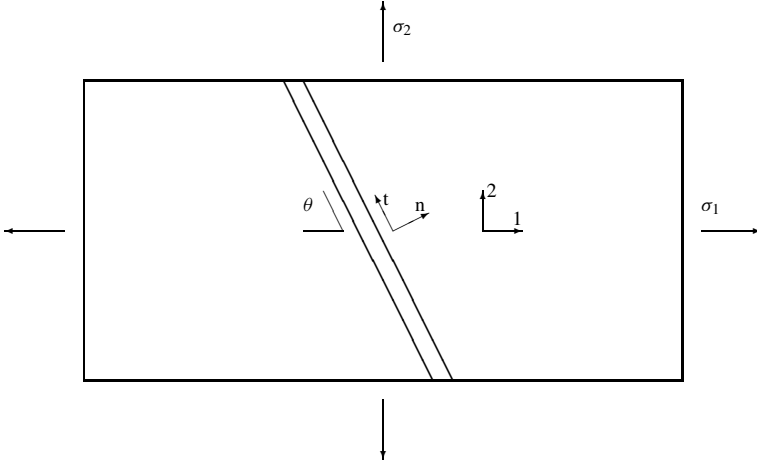


Figure 5.5: Localisation band in a uniformly strained region.

The direction of the localisation band can now be determined from the condition  $\varepsilon_{tt} = 0$ , leading to

$$\cos 2\theta = -\frac{\varepsilon_1 + \varepsilon_2}{\varepsilon_1 - \varepsilon_2} = -\frac{1 + \beta}{1 - \beta} \quad (5.18)$$

From this result it can be concluded that for values  $\beta > 0$  no solution for  $\theta$  exists. Therefore, the localisation criterion according to Hill is only valid for the drawing region, which is represented by the left side of the FLD.

The above derivations assume that the deformation in the localisation band is not hindered by the boundary conditions. If *e.g.* the part to the left of the band is not free to move vertically with respect to the part to the right of the band, the inclination angle and localisation strain can differ.

### 5.3.2 Localisation in the Stretching Region

It was shown that under proportional biaxial extension ( $\varepsilon_1 > 0$  and  $\varepsilon_2 > 0$ ) localised necking within a sheet is impossible. However, due to inhomogeneities, the local rate of deformation can rotate to a plane strain state, facilitating localised necking. Marciniak and Kuczynski (1967) introduced an analysis used for the determination of localised necking in biaxial extension. In this analysis a sheet is considered with an initial groove with reduced thickness, as presented in Figure 5.6(a). Quantities referring to the groove are given an index *B* and quantities referring to the rest of the sheet are given an index *A*. The initial thickness of the groove is  $t_{B,0}$  and outside the groove  $t_{A,0}$ . In practice, in the stretching regime a neck is observed perpendicular to the direction of the major strain. Therefore, the initial groove is aligned with the minor strain in the Marciniak–Kuczynski (M–K) analysis. For planar anisotropic material models, the orientation of the groove should be varied, in order to determine the lowest localisation strain. The M–K analysis is reviewed here briefly. A more comprehensive description is given by Marciniak and Duncan (1992).

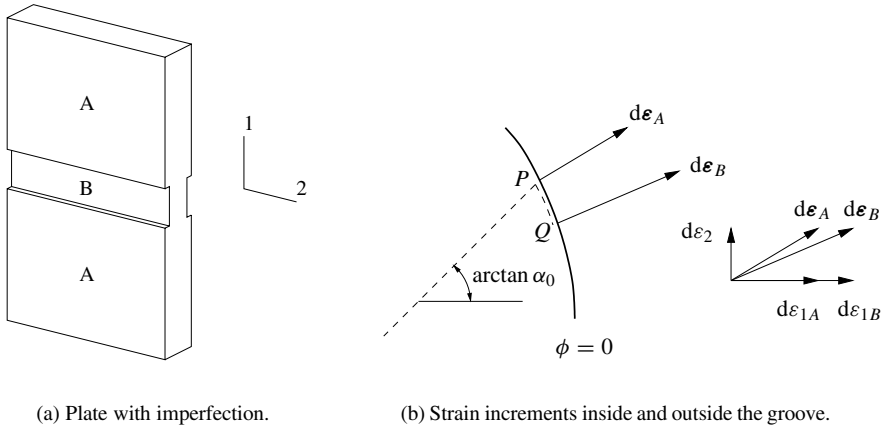


Figure 5.6: Principle of the Marciniak–Kuczynski analysis.

### Marciniak–Kuczynski Analysis

Outside the groove a proportional deformation path is assumed. According to (5.1) and (5.2) this is described by

$$\sigma_{2A} = \alpha_0 \sigma_{1A} \quad \sigma_{3A} = 0 \quad (5.19)$$

$$\varepsilon_{2A} = \beta_0 \varepsilon_{1A} \quad \varepsilon_{3A} = -(1 + \beta_0) \varepsilon_{1A} \quad (5.20)$$

Compatibility between the uniform part *A* and the groove *B* requires that

$$d\varepsilon_{2A} = d\varepsilon_{2B} \quad (5.21)$$

The force per unit sheet length in direction 1 must be transmitted through the groove, hence

$$T_1 = \sigma_{1A} t_A = \sigma_{1B} t_B \quad \Rightarrow \quad \sigma_{1B} = \sigma_{1A} / f \quad (5.22)$$

Where  $f = t_B/t_A$  is the current thickness ratio. As long as  $f \approx 1$ , the stress ratio  $\alpha_0$  approximately holds for both regions *A* and *B*. Since the stress  $\sigma_{1B}$  in the groove is larger than  $\sigma_{1A}$  in the uniform part, the material in the groove reaches the yield surface first. In Figure 5.6(b) this is approximately at position *P*. Because of the constraint equation (5.21) no yielding takes place, since the uniform region is still fully elastic. The stress state in region *B* will move along the yield locus to position *Q*, until also region *A* reaches the yield locus at position *P*. This situation is depicted in Figure 5.6(b). In that period  $\sigma_{1B}$  has increased and  $\sigma_{2B}$  has decreased, hence the stress ratio  $\alpha$  has decreased and proportional deformation is not possible in the groove.

With the stress state in *A* and *B* at two different positions on the yield locus, the normal to the yield surface is different and because of the constraint (5.21), the strain perpendicular to the neck must be larger in the neck than in the uniform part. This is presented in the

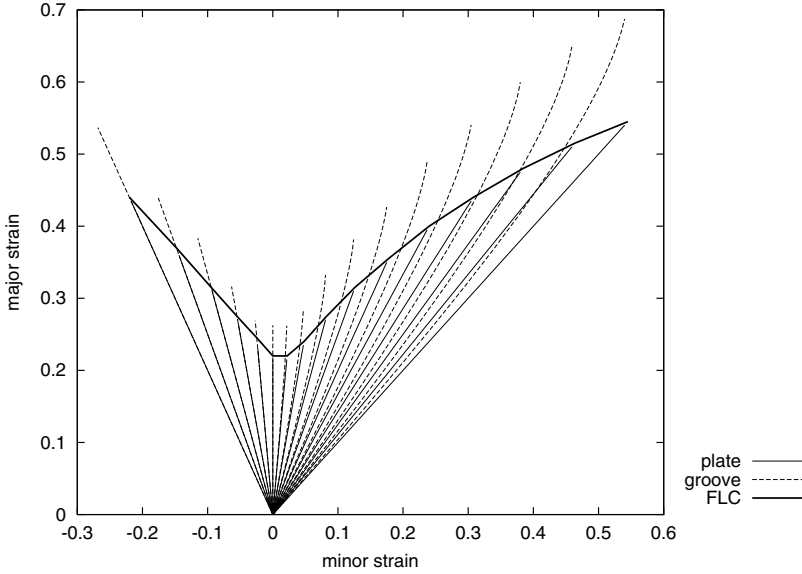


Figure 5.7: The strain-paths inside and outside the groove in a Marciniak–Kuczynski analysis.

vector plot in Figure 5.6(b). As a consequence, the hardening in region *B* will be larger and the two stress situations can no longer be projected on the same yield locus. With an equal strain increment in the 2-direction and a larger strain in the 1-direction, the thickness strain in the neck will be more negative than in the uniform part, decreasing the thickness ratio ( $f < f_0$ ).

The analysis of the deformation can be further developed numerically. The drawing region can be included in the analysis by assuming an inclined groove. For planar isotropic material the inclination angle can be determined beforehand by (5.18). Strain increments  $\Delta \boldsymbol{\varepsilon}_A$  are prescribed on region *A*, respecting the proportionality ratio  $\beta_0$ . For every increment  $\Delta \boldsymbol{\varepsilon}_A$  a strain increment  $\Delta \boldsymbol{\varepsilon}_B$  is calculated iteratively, such that the plate forces normal and tangential to the groove in region *A* and *B* are in equilibrium. The plate forces (per unit length) can be calculated from the stresses and the local thickness as

$$\mathbf{T} = \begin{pmatrix} T_{nn} \\ T_{nt} \end{pmatrix} = t \begin{pmatrix} \sigma_{nn} \\ \sigma_{nt} \end{pmatrix} \quad (5.23)$$

in which the normal and tangential directions *n* and *t* refer to the directions as indicated in Figure 5.5. The sheet is considered to have failed if the strain increment in the groove is larger than a prescribed multiple of the strain increment in the uniform part. The strain in the uniform region at the time of failure is considered to be the limiting strain for that particular strain ratio  $\beta_0$ .

In Figure 5.7 the strain paths in the plate (region *A*) and in the groove (region *B*) are presented in a forming limit diagram. An initial thickness ratio  $f_0 = 0.99$  was used. The failure criterion stopped the increments when the strain increment in the groove was more

than 10 times the strain increment in the uniform region. A Von Mises yield locus was used with a Nadai hardening model with parameters as given in Table 5.1.

In the drawing region of the FLD, the strains inside the groove in the directions 1 and 2 have the same ratio as in the uniform region. The limit strain follows a line at an angle of  $45^\circ$  with respect to the major strain axis, as predicted by the Hill analysis. The limit strain for the plane strain path is lower than the corresponding  $n$ -value of 0.292 because of the initial thickness ratio of 0.99. In the stretching region, the strains inside and outside the groove are no longer in the same direction. It can be seen that the strain ratio  $\varepsilon_{1B}/\varepsilon_{1A}$  keeps increasing until the rate of deformation in the groove approaches a plane strain situation. For a fixed strain increment in part A, the strain increment in the groove becomes very large and localisation is detected.

## 5.4 Forming Limit Curves

To investigate the influence of several parameters on the predicted FLC, a number of M–K analyses were performed with a planar isotropic Hill '48 yield function. The FLC for an isotropic yield function ( $R = 1$ ) and a Nadai hardening curve were selected as reference curves. The hardening parameters of Table 5.1 were used and a thickness ratio of  $f_0 = 0.99$ . In Figure 5.8, FLC's are presented with varying initial thickness ratio, hardening parameter  $n$  and Lankford  $R$ -value. Also, the difference between isotropic and kinematic hardening and between the Nadai and Voce hardening laws are presented, as well as the influence of strain rate sensitivity. Figure 5.9 presents FLC's for the Tresca and polycrystal yield models.

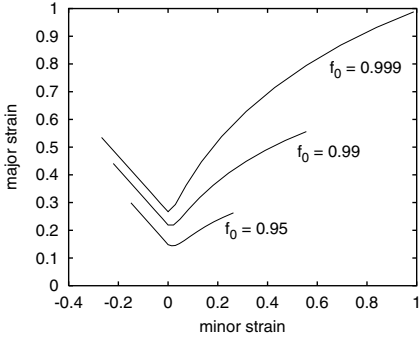
Before discussing the influence of the model parameters, it is observed that for all calculations with the Nadai hardening model, the drawing region shows a relation  $\varepsilon_1^* + \varepsilon_2^* = c$  as predicted with the Hill local necking criterion.

### Initial Thickness Ratio

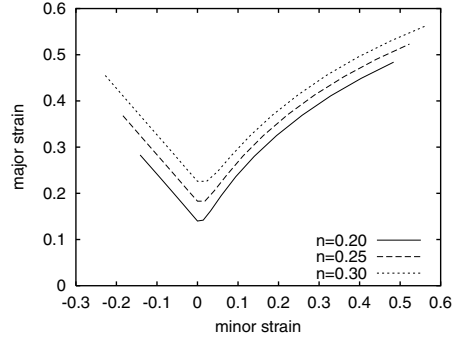
The direction of the FLC in the drawing region conforms the Hill local necking criterion, but the height of the curve is below the theoretical values. In the plane strain situation ( $\varepsilon_{\text{minor}} = 0$ ) the major strain should equal the work hardening exponent  $n = 0.292$ . In Figure 5.8(a) the influence of the initial thickness ratio  $f_0$  is presented. It shows that with decreasing groove depth ( $f_0$  approaching 1), the plane strain limit strain approaches the theoretical value. However, with decreasing groove depth, the limit strains in the stretching region increase to unrealistically large values, compared with Figure 5.2.

### Hardening Exponent

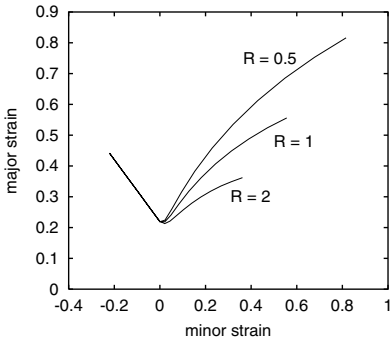
The hardening exponent  $n$  is often used as a technological parameter that determines the formability of sheet metal. The relevance of  $n$  is demonstrated in Figure 5.8(b). As already predicted by the Hill local necking criterion for the drawing region, the FLC translates to higher values for increasing hardening exponents. Also for the stretching region, the change leads to more or less equidistant FLC's.



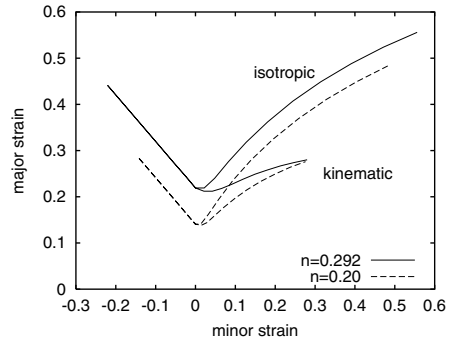
(a) influence of  $f_0$



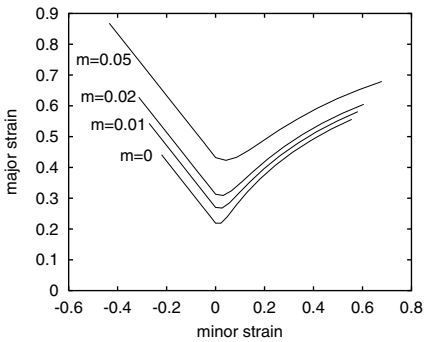
(b) influence of  $n$



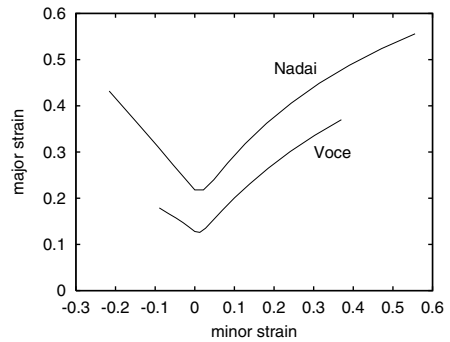
(c) influence of  $R$



(d) influence of hardening type



(e) strain rate dependence



(f) hardening law dependence

Figure 5.8: Influence of the model and material parameters on a Marciniak–Kuczynski analysis.

### Lankford $R$ -value

It was demonstrated in Section 5.3 that, with Nadai hardening, the local necking criterion according to Hill was independent of the yield function. In Figure 5.8(c) it is shown that this is well represented by the M–K analysis; the FLC is independent of the  $R$ -value in the drawing region. In the stretching region, however, a large influence is seen. This can be explained by the larger curvature of the yield locus for  $R = 2$  and the lower curvature for  $R = 0.5$ . In the stretching region, the rate of deformation must rotate from the initial value  $\beta_0$  to a plane strain state (see Figure 5.6(b)). It can be expected from Figure 3.6 that the plane strain state is reached earlier for higher  $R$ -values, since the distance in stress space is lower.

### Isotropic and Kinematic Hardening

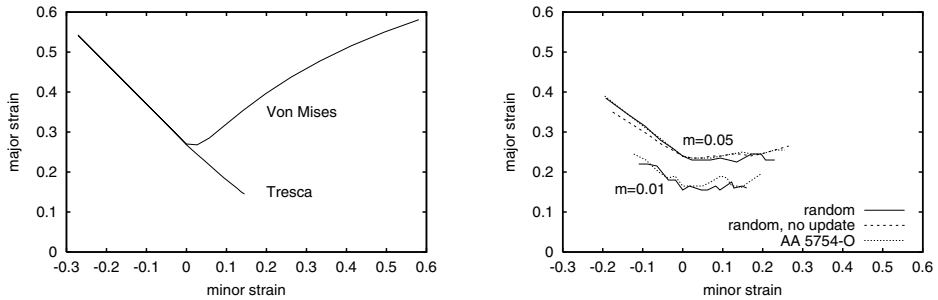
In Figure 5.8(d) FLC's are presented for isotropic and kinematic hardening for 2 different  $n$ -values each. It is shown that isotropic or kinematic hardening again, does not influence the drawing part. With isotropic hardening, the yield locus grows and therefore the curvature decreases. As with low  $R$ -values, this increases the limit strains. For kinematic hardening, the curvature remains constant and the limit strains are below the values for isotropic hardening. The difference is larger for higher hardening exponents.

### Strain Rate Dependent Material

In material with a positive strain rate sensitivity, localisation is delayed. In the groove the strain rate increases to compensate a decreasing thickness ratio. With strain rate dependent material, the stress increases because of hardening *and* because of the increasing strain rate. Hence, the strain rate increase is less than without strain rate sensitivity. In Figure 5.8(e) results are presented for a hardening law according to (3.58) with  $\dot{\epsilon}_0 = 0.01 \text{ s}^{-1}$  and a strain rate in the uniform region of  $\dot{\epsilon}_{1A} = 0.01 \text{ s}^{-1}$ . It is observed that the limit strains increase significantly, already for a low value of  $m = 0.01$ . In the drawing region the FLC shifts to higher strain values. In the stretching region, the limit strain increases slightly less. For  $m = 0.05$  this results in a slightly decreased steepness of the FLC.

### Nadai and Voce Hardening

Figure 5.8(f) presents the results of an M–K analysis with Nadai and Voce hardening models. The parameters for both models were fitted to experimental data and the resulting flow curves are shown in Figure 5.3. The analysis with the Voce hardening model shows a less steep curve in the drawing region, in agreement with the Hill local necking prediction, presented in Figure 5.4. The main importance of this picture is the overall much lower value for the Voce law, compared to Nadai. This difference is attributed to the deviation of the Nadai model for strains near the localisation strain. It clearly indicates that a 'best fit', based on the complete flow curve does not give a good prediction of the FLC, but that for this purpose the high-strain range should be fitted with more precision. For the material under consideration, the Voce hardening law is more appropriate.



(a) Von Mises and Tresca yield locus

(b) Crystal plasticity models

Figure 5.9: Influence of the yield locus on a Marciniak–Kuczynski analysis.

### Tresca Yield Criterion

In the discussion of the Hill local necking criterion, it was concluded that in the stretching region necking cannot occur in proportional loading, because no plane strain direction can be found. The influence of  $R$ -values and isotropic and kinematic hardening showed that, indeed, the curvature of the yield locus in the area between the proportional path and the plane strain deformation determines whether the limit strain will be relatively high or low. In the Tresca criterion the curvature between any stretching deformation and plane strain is infinite (see Figure 3.7). Directly at the point where the Hill local necking criterion predicts local necking, the strain rate can change to plane strain. An M–K analysis with the Tresca criterion and a strain rate dependent Nadai relation with  $m = 0.01$ , presented in Figure 5.9(a), confirms that the Hill necking criterion is now also valid in the stretching region. A comparison with a Von Mises yield locus and the same hardening function shows again that necking in the drawing region is independent of the yield locus.

### Crystal Plasticity Models

In an M–K analysis only two material points are considered, one in the uniform region and one in the groove. In this case it is feasible to use the crystal plasticity model described in Section 3.2 and Section 4.2 directly. The crystal plasticity models, described in this thesis, are viscoplastic models and therefore strain rate dependent.

In Figure 5.9(b), calculated FLC's are presented for strain rate sensitivities of  $m = 0.05$  and  $m = 0.01$ . A full constraints Taylor model was used with 500 crystals; one random set and one set corresponding to the measured texture of the AA 5754-O sheet. The influence of  $m$  was already discussed with reference to Figure 5.8(e) and from that figure it can be expected that the rate independent FLC would be somewhat lower than the FLC for  $m = 0.01$ . For the hardening of the critical resolved shear stress, a Voce relation is used, fitted to the uniaxial tensile test. In the drawing region, the slope of the FLC compares well with the slope for the Voce relation in Figure 5.8(f). For  $m = 0.05$  and a random texture,



calculations are performed with and without updating the lattice orientations. It can be seen in Figure 5.9(b) that the texture development has a minor influence on the resulting FLC. The calculations show hardly any increasing limit strain near the equi-biaxial point. This can be due to poor convergence, especially for the  $m = 0.01$  case. For the random texture the relatively low equi-biaxial point was also found by Zhou and Neale (1995). Results with rate independent crystal plasticity models were recently presented by Knockaert *et al.* (2002). They show a more realistic prediction in the stretching area. Hiwatashi *et al.* (1998) presented calculated FLC's, in which the plastic deformation was based on a 6th order Taylor expansion of the plastic dissipation function and measured texture. This method, where the texture information is used indirectly, seems to be more robust and more efficient than the direct use of crystal plasticity models. In the stretching region a more realistic FLC is found. This method is comparable with the use of Vegter's yield function in Section 5.5.

### Alternative Yield Loci

It is very clear from all calculated FLC's that the shape of the yield locus has a distinct influence on the stretching region of the forming limit diagram, but not on the drawing region. Apart from the Hill '48 model, the Tresca model and polycrystal models, many other models exist. Recent publications have shown the influence of the shape of the yield locus on FLC predictions. In Vegter *et al.* (1998, 1999) the Hill '90, Hill '93, Barlat and Vegter models are compared and the influence of the equi-biaxial stress of the FLC is demonstrated. Kuroda and Tvergaard (2000) showed results for the Hill '48, Hill '90, Gotoh '77 and Barlat–Lian '89 yield loci. They also demonstrated the influence of boundary conditions and the inclination of the groove for planar anisotropic models. Banabic and Dannemann (2001) reviewed the Hill '93 model using an M–K analysis and the Swift diffuse necking criterion.

The Barlat and Vegter models are able to describe the yield locus accurately enough to make proper FLC predictions. FLC predictions with the Vegter model are performed in the next section using a finite element approach.

## 5.5 Finite Element Analysis

In this section a comparison is made between the Marciniak–Kuczynski analysis and a finite element analysis with membrane elements. In membrane and shell element models, the change in thickness between different positions in the plate is not coupled, just like in an M–K analysis. It therefore seems justified to expect that a finite element model of a grooved plate will give comparable results. This expectation is supported by the work of Kelder (2001) who investigated the stability of tube hydroforming. Another type of analysis is the simulation of the plane strain tensile test. In this analysis, the instability is not introduced by an initial groove, but by the natural inhomogeneity at the edges of the specimen.

### 5.5.1 Grooved Plate

A biaxially loaded grooved plate is simulated with a finite element model as presented in Figure 5.10(a). On the left and lower edges, no displacements perpendicular to the edge are allowed and on the right and upper edge, displacements perpendicular to the edges

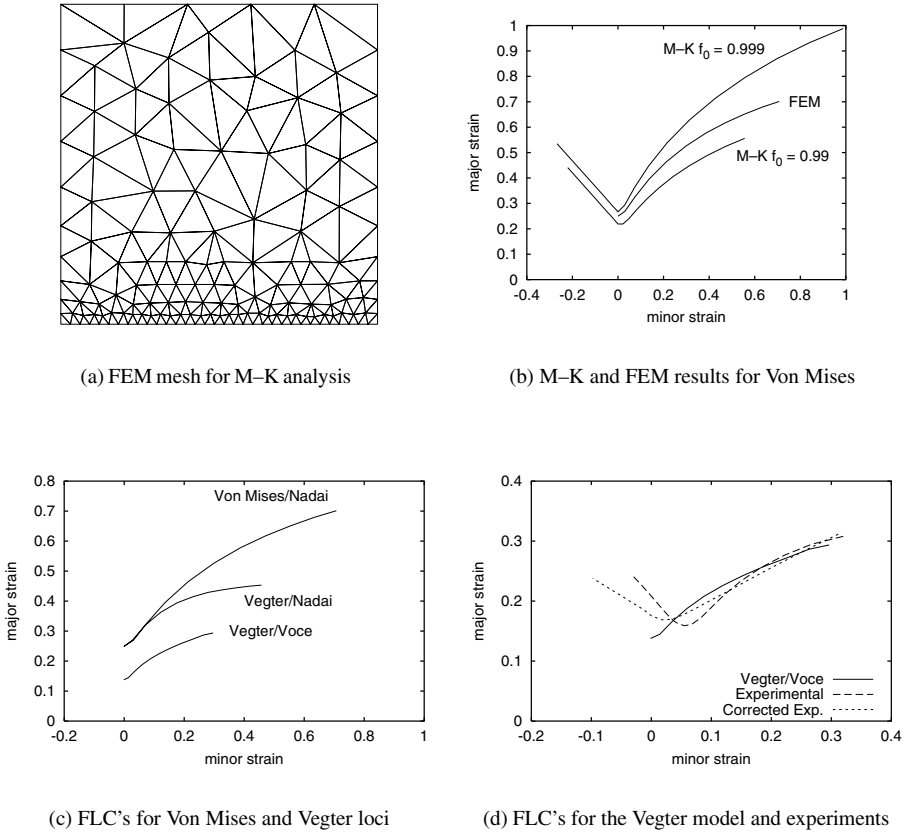


Figure 5.10: FLC's, based on a FEM model of a Marciniak–Kuczynski analysis.

are prescribed. The ratio of displacements in the  $x$ - and  $y$ -directions is constant within every simulation and is comparable with the strain-ratio  $\beta$  in the M–K analysis. The initial nominal thickness of the plate is 1.2 mm but at the nodes on the lower boundary the plate is 1% thinner. The interpolation of nodal thickness to the integration points of the elements results in a thickness of the lower row of elements of about 0.995 times the nominal thickness. With the groove perpendicular to the major strain, only the stretching region of an FLC can be compared with an M–K analysis.

The loading of the model differs somewhat from the M–K analysis. In the FEM model the strain increments perpendicular to the groove in the uniform region decrease upon localisation. In the M–K analysis, the strain increments remain constant. This means that in the FEM analysis the strain ratio  $\beta$  changes when the strain localises in the groove: the strain perpendicular to the groove decreases to zero and in the direction of the groove it remains constant. The analysis is stopped if the strain increment in an element at the lower

edge is larger than 5 times the strain increment in an element in the centre of the plate. Upon failure, the total strain in the element in the upper right corner is used to determine a point on the FLC.

For comparison, an analysis is first performed with a Von Mises yield criterion and Nadai hardening, as in the previous section. The results are presented in Figure 5.10(b). The FLC from the FEM analysis falls nicely between the curves for  $f_0 = 0.99$  and  $f_0 = 0.999$  in the M–K analysis, in spite of the different boundary conditions. This validates the FEM analysis for the determination of an FLC, comparable with the M–K analysis.

In Figure 5.10(c) the predicted FLC's for the Von Mises and Vegter yield functions are compared. The parameters for the Vegter model are set for the investigated AA 5754-O sheet. The curvature of the yield locus between equi-biaxial stress and plane strain states is now much larger than with the Von Mises model and it is seen immediately that the limit strains in the stretching region decrease. By using a Voce hardening law instead of Nadai hardening, the limit strains decrease further. From uniaxial and biaxial tests, the Vegter yield function with Voce type hardening was already selected as an appropriate continuum model for the investigated alloy. The FLC that is predicted in this way resembles the experimentally obtained FLC quite well. In Figure 5.10(d) the experimental FLC and a corrected experimental FLC are depicted. The correction, performed by Vegter (2002), accounts for the difference between the strain on the mid-surface and on the outer surface and for an equi-biaxial pre-strain in the Nakazima tests. The most notable difference between the corrected proportional deformation and the Nakazima strain path is that the lowest point of the FLC shifts in the direction of the plane strain point. For the correction the Vegter yield function was used, therefore the validation of the calculated FLC with the corrected experimental curve is not completely independent. However, the parameters for the Vegter model with Voce hardening were obtained solely from uniaxial and biaxial tensile tests. The similarity between the Vegter/Voce model and the raw and corrected experimental data is satisfactory, especially compared to all other simulations with the Hill '48 yield function or with the Nadai hardening model.

### 5.5.2 Plane Strain Test

In the plane strain tension experiments, described in Section 2.3, the strain distribution is not completely uniform. Near the edges of the specimen a uniaxial stress-state prevails and near the centre a plane strain state. In the experiments it was observed that necking starts in the centre of the specimen, while the edges are still relatively uniform. This behaviour can be explained with the Hill local necking criterion described in Section 5.3.1. A uniaxial deformation has a higher uniform strain than a plane strain deformation.

In the simulation of a completely uniform plate, an initial imperfection is necessary to trigger necking instability. Since the plane strain test is not completely uniform, we investigated numerically how the strain distribution localises, with no further imperfection.

The finite element mesh is presented in Figure 5.11. A quarter of the deformation zone is modelled. Symmetry conditions are applied at the bottom and the right-hand boundary of the mesh. The left-hand boundary is free and a vertical displacement is prescribed at the top boundary where horizontal displacements are suppressed. The initial thickness is set to 1.2 mm with no imperfection. The strain in the vertical direction is followed for the

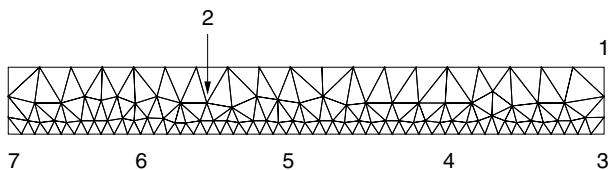


Figure 5.11: FEM mesh of a quarter of the plane strain tensile specimen.

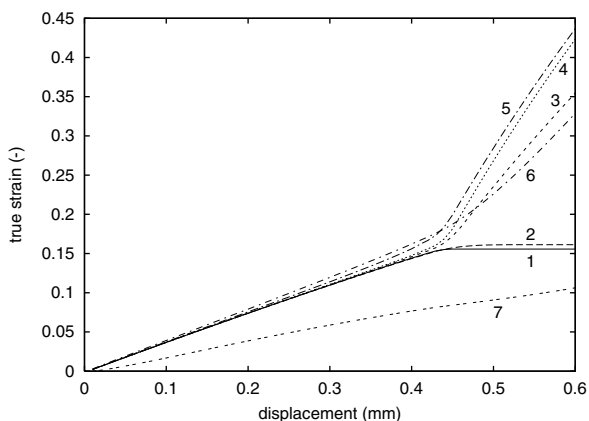


Figure 5.12: Strain evolution in the plane strain test.

numbered positions.

In Figure 5.12, the true strain  $\varepsilon_y$  is presented as a function of the vertical displacement of the upper edge. It can be seen that at positions 3–5 strain localisation starts at a top displacement of 0.43 mm and at position 6 a little later. This shows that necking starts at the centre of the specimen and grows towards the outer edges, corresponding to the experiments. Before the onset of necking, positions 5 and 6 show a slightly larger strain than locations 1–4. The magnitude of the strain at positions 3–6, after localisation, is mesh dependent and cannot be used quantitatively. The ‘uniform strain’ at positions 1 and 2 is 0.156 and 0.161, respectively. This fits the experimentally determined force maximum in the plane strain test, that appears at a strain of 0.16–0.18. It is noted that the strain at the free edge (position 7) is lower than in the rest of the specimen, and it increases uniformly for the presented displacement range. The edge part of the specimen can still bear increasing loads while the centre part is already necking. If, in an experiment, the strain is calculated from measured displacements on either side of a local neck, apparent high strains are ‘measured’, comparable to locations 3 and 4. The measured force at this ‘high strain’ is still relatively high because of the load that is transmitted in the edge areas. This explains the relatively high apparent maximum strains for the plane strain tests in Figure 2.7.

The results for the onset of localisation in a dominating plane strain situation are realistic, even without an initial groove in the model. It suggests that, apart from ‘ideal’ uniform situ-

ations, local necking will be triggered by FEM models with membrane and shell elements, without special model adaptations.

## 5.6 Conclusion

In this chapter the relation between the material model and forming limits was discussed. It was demonstrated that the drawing region of an FLC is mainly determined by the hardening function. In the stretching region, however, the shape of the yield function influences the FLC significantly. For this region, the relevant part of the yield locus is the relatively small part between plane strain and equi-biaxial stress states. For aluminium alloys, this part of the locus is poorly represented by the Hill '48 yield function. Therefore, an FLC predicted with the Hill '48 model does not reproduce the experimentally determined FLC for this material in the stretching region. The Vegter yield function performs much better. It is important that the stress and hardening rate are predicted accurately in the range where necking is expected. Parameters for the Nadai and the Voce hardening models were obtained by least square fits of data from a uniaxial tensile test. The Nadai model gave a reasonable reproduction of the flow curve, but at high strains the deviation in hardening rate increased. The Voce model showed good agreement for the complete strain range. The resulting difference in predicted FLC's is large and the prediction with the Voce model is much more realistic.

Finite element models with membrane and shell elements can spot the onset of local necking. For models with uniform strain distributions an initial imperfection is necessary to trigger strain localisation. This is comparable to the Marciniak–Kuczynski analysis. In such cases the determined forming limit strains are similar. In situations where the strain is not uniformly distributed, an imperfection is not necessary. This even holds for the weak non-uniformity of the plane strain test. In many industrial forming simulations the strain or thickness distribution can therefore be used directly, to view potential necking zones. In large uniform areas, there is a risk that the deformation will follow an unstable path, without strain localisation in the model. In that case, a comparison of strains with an FLC is useful.

FEM models have the additional benefit that boundary conditions, non-proportional deformation and *e.g.* friction with the tools are completely included. For a correct localisation prediction, however, the accuracy of the material model is critical. After localisation, the numerical results become mesh dependent and the results should be interpreted with great care.



## 6. Efficient Finite Element Simulations

In the previous chapters the focus was on an accurate description of the material model. For the simulation of industrial sheet forming processes, the geometrical discretisation and time discretisation are two other important factors that determine the accuracy and efficiency of the algorithm. For relatively small models, the implicit time integration method is preferred, because of its inherent equilibrium check. For large models, however, the computation time becomes prohibitively large and, in practice, often explicit methods are used. In this chapter a strategy is presented that enables the application of implicit finite element simulations for large scale sheet forming analysis.

In the first two sections, the basic finite element formulations are reviewed and the thermo-mechanical continuum problem is discretised. The discretisation leads to huge linear sets of equations, resulting in large computation times for implicit methods. In Section 6.3 the implicit and explicit time integration algorithms are compared. In Section 6.4 it is shown that iterative solvers can reduce the calculation time considerably. Section 6.5 demonstrates the influence of model parameters and dynamics contributions on the efficiency of iterative solvers.

### 6.1 Problem Definition

In this section the basic equations for implicit and explicit methods are reviewed. The common basis for the two methods is the conservation of mass, linear momentum, angular momentum and energy. These principles lead to the following equations, respectively:

$$\dot{\rho} + \rho \nabla \cdot \mathbf{v} = 0 \quad (6.1a)$$

$$\rho \dot{\mathbf{v}} = \nabla \cdot \boldsymbol{\sigma} + \rho \mathbf{b} \quad (6.1b)$$

$$\boldsymbol{\sigma} = \boldsymbol{\sigma}^T \quad (6.1c)$$

$$\rho \dot{u}_{\text{int}} = \boldsymbol{\sigma} : \mathbf{D} - \nabla \cdot \mathbf{q} + \rho r \quad (6.1d)$$

where  $\rho$  is the mass density,  $\mathbf{v}$  the velocity,  $\boldsymbol{\sigma}$  the Cauchy stress,  $\mathbf{b}$  the body force per unit mass,  $u_{\text{int}}$  the internal energy per unit mass,  $\mathbf{D}$  the rate of deformation,  $\mathbf{q}$  the heat flux and  $r$  the heat production per unit mass. A superposed dot denotes a material time derivative, hence  $\dot{\mathbf{v}}$  is the acceleration.

It is assumed that we have constitutive equations that give the stress  $\boldsymbol{\sigma}$  as a result of the strain and strain history and the heat flux  $\mathbf{q}$  as a function of the temperature gradient. The strain measure is determined by the displacement field.

The thermo-mechanical problem to be solved can be phrased as: find a displacement field  $\mathbf{u}(\mathbf{x})$  and temperature field  $T(\mathbf{x})$  such that the balance equations are fulfilled, subject to the initial conditions

$$\mathbf{u}(\mathbf{x}, t_0) = \mathbf{u}_0(\mathbf{x}), \quad \mathbf{v}(\mathbf{x}, t_0) = \mathbf{v}_0(\mathbf{x}), \quad T(\mathbf{x}, t_0) = T_0(\mathbf{x}) \quad \forall \mathbf{x} \in \Omega \quad (6.2)$$

the essential boundary conditions

$$\mathbf{u} = \bar{\mathbf{u}} \quad \text{on } \Gamma_u \quad T = \bar{T} \quad \text{on } \Gamma_T \quad (6.3)$$

and the natural boundary conditions

$$\boldsymbol{\sigma} \cdot \mathbf{n} = \bar{\mathbf{t}} \quad \text{on } \Gamma_t \quad \mathbf{q} \cdot \mathbf{n} = -\bar{h} \quad \text{on } \Gamma_h \quad (6.4)$$

where  $\Omega$  is the deformed domain of the analysed body,  $\Gamma_u$  is that part of the boundary on which the displacements  $\bar{\mathbf{u}}$  are prescribed,  $\Gamma_T$  the part where the temperature  $\bar{T}$  is prescribed,  $\Gamma_t$  the part where the traction  $\bar{\mathbf{t}}$  is prescribed and  $\Gamma_h$  the part where the heat flux  $\bar{h}$  into the body is prescribed.

Using the weighted residual method, integration by parts and the divergence theorem, the weak form of the momentum equation becomes

$$\int_{\Omega} \mathbf{w}_u \cdot \rho \dot{\mathbf{v}} \, d\Omega + \int_{\Omega} \nabla \mathbf{w}_u : \boldsymbol{\sigma} \, d\Omega = \int_{\Omega} \mathbf{w}_u \cdot \rho \mathbf{b} \, d\Omega + \int_{\Gamma_t} \mathbf{w}_u \cdot \bar{\mathbf{t}} \, d\Gamma \quad \forall \mathbf{w}_u \in \mathcal{V} \quad (6.5)$$

where  $\mathcal{V}$  contains all  $C_0$  vector functions with a value of 0 on  $\Gamma_u$ . The weak form of the energy equation reads

$$\int_{\Omega} w_T (\rho \dot{u} - \boldsymbol{\sigma} : \mathbf{D}) \, d\Omega - \int_{\Omega} \nabla w_T \cdot \mathbf{q} \, d\Omega = \int_{\Omega} w_T \rho r \, d\Omega + \int_{\Gamma_h} w_T \bar{h} \, d\Gamma \quad \forall w_T \in \mathcal{T} \quad (6.6)$$

where  $\mathcal{T}$  contains all  $C_0$  functions with a value of 0 on  $\Gamma_T$ . For metal forming processes, the rate of internal energy is approximated by  $\dot{u} = c\dot{T}$ , neglecting contributions to  $u$  from the elastic deformation and evolution of micro-structure.

A finite element discretisation is used to discretise the space dimension, usually by a Galerkin method. The nodal displacements and temperatures are the degrees of freedom, assembled in a vector  $\mathbf{d}$ . In the first integral of (6.5)  $\dot{\mathbf{v}}$  relates directly to the second time derivative of the nodal displacements. The contribution can be written as  $\mathbf{w}^T \mathbf{M} \ddot{\mathbf{d}}$ , where  $\mathbf{M}$  is the *mass matrix* and  $\mathbf{w}$  the vector with discrete weighting factors, contributing to  $\mathbf{w}_u$  and  $w_T$ . In the first integral of (6.6)  $\dot{u}$  and  $\mathbf{D}$  relate directly to the first time derivative of the nodal temperatures and displacements respectively. This contribution can be written as  $\mathbf{w}^T \mathbf{C} \dot{\mathbf{d}}$ , where  $\mathbf{C}$  would be called the *capacity matrix* for pure thermal problems. In thermo-mechanical problems the contribution for mechanical work is included. The second integrals in both (6.5) and (6.6) depend on the current stress and heat flux. Their contribution is given by  $\mathbf{w}^T \mathbf{f}_{\text{int}}$ , with the internal (generalised) load vector  $\mathbf{f}_{\text{int}}$ . The right-hand side of both equations are related to externally applied loads. Their contribution is given by  $\mathbf{w}^T \mathbf{f}_{\text{ext}}$  with the external (generalised) load vector  $\mathbf{f}_{\text{ext}}$ . Under the condition that the discretised momentum and energy balance equations are fulfilled for every admissible weighting vector  $\mathbf{w}$ , the semi-discrete equations in matrix format become

$$\mathbf{M} \ddot{\mathbf{d}} + \mathbf{C} \dot{\mathbf{d}} + \mathbf{f}_{\text{int}} - \mathbf{f}_{\text{ext}} = \mathbf{0} \quad (6.7)$$



The internal load vector, and in the case of *e.g.* a pressure load also the external load vector, depend on the displacements and temperatures and in some cases on their time derivatives. Hence, (6.7) is nonlinear in displacements and temperatures. A time integration algorithm must be selected that can cope with this nonlinearity.

### 6.1.1 Time Integration Methods

An incremental-iterative strategy is followed as solution method for the nonlinear semi-discrete equations. A Newton–Raphson method is used for the iterative part. For the time integration procedure at the level of the system equations a Newmark algorithm is chosen. By particular choices for the Newmark parameters some other familiar algorithms can be derived. The total increment in the displacement vector is defined by

$$\mathbf{d}_{n+1} = \mathbf{d}_n + \Delta \mathbf{d} \quad (6.8)$$

and the iterative increment by

$$\Delta \mathbf{d}^{k+1} = \Delta \mathbf{d}^k + \delta \mathbf{d}^k \quad (6.9)$$

where the subscript  $n$  denotes the increment number and the superscript  $k$  denotes the iteration number. Writing (6.7) for time  $t_{n+1}$  in a residual form, omitting the index  $n + 1$  for brevity, gives

$$\mathbf{M}\ddot{\mathbf{d}} + \mathbf{C}\dot{\mathbf{d}} + \mathbf{f}_{\text{int}} - \mathbf{f}_{\text{ext}} = \mathbf{r}(\Delta \mathbf{d}) \quad (6.10)$$

in which the residual  $\mathbf{r}$  must iteratively be brought to zero to conform to equation (6.7). This leads to the Newton–Raphson iteration relation for  $\delta \mathbf{d}^k$ :

$$\left( \frac{\partial \mathbf{r}}{\partial \Delta \mathbf{d}} \right)^k \delta \mathbf{d}^k = -\mathbf{r}^k \quad (6.11)$$

The matrix with derivatives is called the Jacobian matrix and can be written as

$$\frac{\partial \mathbf{r}}{\partial \Delta \mathbf{d}} = \mathbf{M} \frac{\partial \ddot{\mathbf{d}}}{\partial \Delta \mathbf{d}} + \mathbf{C} \frac{\partial \dot{\mathbf{d}}}{\partial \Delta \mathbf{d}} + \left( \frac{\partial \mathbf{f}_{\text{int}}}{\partial \Delta \mathbf{d}} - \frac{\partial \mathbf{f}_{\text{ext}}}{\partial \Delta \mathbf{d}} \right) \quad (6.12)$$

If  $\mathbf{M}$  or  $\mathbf{C}$  depend on  $\mathbf{d}$  their derivatives should also be included in the Jacobian matrix, but this is neglected for clarity. The derivatives  $\partial \ddot{\mathbf{d}}/\partial \Delta \mathbf{d}$  and  $\partial \dot{\mathbf{d}}/\partial \Delta \mathbf{d}$  depend on the selected time integration algorithm. If the internal or external load vector depends explicitly on the velocity or temperature rate, the derivatives of that part could be included in the  $\mathbf{C}$ -matrix. However, the damping that is caused by dissipation in the constitutive equations, *e.g.* plasticity, is most often calculated as a function of the strain increments and will hence be accounted for in the last term of (6.12). The last term is known as the stiffness and conduction matrix  $\mathbf{K}$ .

### Newmark Integration Method

The Newmark integration method is a one-step integration method, using only the current state and the state to be calculated (Zienkiewicz and Taylor, 2000a; Belytschko *et al.*, 2000).

The basic assumptions in the Newmark method are

$$\mathbf{d}_{n+1} = \mathbf{d}_n + \Delta t \dot{\mathbf{d}}_n + \Delta t^2 [(\frac{1}{2} - \beta) \ddot{\mathbf{d}}_n + \beta \ddot{\mathbf{d}}_{n+1}] \quad (6.13)$$

$$\dot{\mathbf{d}}_{n+1} = \dot{\mathbf{d}}_n + \Delta t [(1 - \gamma) \ddot{\mathbf{d}}_n + \gamma \ddot{\mathbf{d}}_{n+1}] \quad (6.14)$$

All values at time  $n$  are fixed and the derivatives  $\partial \ddot{\mathbf{d}} / \partial \Delta \mathbf{d}$  and  $\partial \dot{\mathbf{d}} / \partial \Delta \mathbf{d}$  can now be determined. Equation (6.12) yields an equivalent stiffness matrix

$$\mathbf{K}^* = \frac{\partial \mathbf{r}}{\partial \Delta \mathbf{d}} = \frac{1}{\beta \Delta t^2} \mathbf{M} + \frac{\gamma}{\beta \Delta t} \mathbf{C} + \mathbf{K} \quad (6.15)$$

where the parameters  $\beta$  and  $\gamma$  can be chosen freely. In the linear case, the Newmark integration method is unconditionally stable for  $2\beta \geq \gamma \geq \frac{1}{2}$ . It is second order accurate for  $\gamma = \frac{1}{2}$  and first order accurate for other cases. However, the scheme can lose stability in the nonlinear case (Kuhl and Crisfield, 1999).

The most widely used scheme is the  $\beta = \frac{1}{4}$  and  $\gamma = \frac{1}{2}$  scheme. For  $\gamma > \frac{1}{2}$  the algorithm is dissipative and so-called numerical damping is introduced. To maintain dissipation at high frequencies,  $\beta = \frac{1}{4}(\gamma + \frac{1}{2})^2$  must be used (Hughes, 1987). The accuracy of the time integration is now only first order. If the dynamical contribution in the system is important an integration scheme should be used that is more appropriate for nonlinear transient analysis, *e.g.* the Hilber–Hughes–Taylor  $\alpha$ -method (Hilber *et al.*, 1977).

An Euler backward integration scheme is achieved by choosing  $\beta = \gamma = 1$ . This scheme does not seem to be attractive, because a lot of numerical damping is added. It reduces the accuracy of the algorithm, but on the other hand it is an unconditionally stable, easily implemented and robust algorithm and it is consistent with the usual integration of constitutive equations at the material point level. However, the lack of control over the damping remains a disadvantage.

A completely different result is obtained when we choose  $\beta = 0$  and  $\gamma = \frac{1}{2}$ . If (6.13) is written out for  $\mathbf{d}_{n+1}$  and  $\mathbf{d}_{n+2}$  then  $\ddot{\mathbf{d}}_n$  and  $\ddot{\mathbf{d}}_{n+1}$  can be solved. By substitution of the results into (6.14) it shows that for this choice of parameters the scheme is equivalent to the central difference scheme. A more direct way to describe this scheme for constant time increments  $\Delta t$  is

$$\mathbf{M} \ddot{\mathbf{d}}_n + \mathbf{C} \dot{\mathbf{d}}_n = \mathbf{f}_{\text{ext},n} - \mathbf{f}_{\text{int},n} \quad (6.16)$$

$$\dot{\mathbf{d}}_n = \dot{\mathbf{d}}_{n-1/2} + \frac{1}{2} \Delta t \ddot{\mathbf{d}}_n \quad (6.17)$$

$$\mathbf{d}_{n+1} = 2\mathbf{d}_n - \mathbf{d}_{n-1} + \Delta t^2 \ddot{\mathbf{d}}_n \quad (6.18)$$

Clearly,  $\mathbf{d}_{n+1}$  can be calculated explicitly, and no iterations are needed. The central difference scheme is conditionally stable and the time increment  $\Delta t$  must be less than the critical time increment  $\Delta t_{\text{crit}} = 2/\omega_{\text{max}}$ , where  $\omega_{\text{max}}$  is the maximum eigenfrequency of the linearised system (Hughes, 1987; Belytschko *et al.*, 2000). For linear continuum elements,  $\Delta t_{\text{crit}}$  can be approximated by the smallest time needed for a wave to cross one element. The big advantage of the central difference scheme is that the mass matrix and capacity matrix can be diagonalised and in that case the solution of  $\ddot{\mathbf{d}}$  from (6.16) is trivial. Note, however, that the coupling part in  $\mathbf{C}$  cannot be diagonalised and a staggered scheme must be used in order to avoid the necessity for matrix inversion.

## 6.2 Elements

The weak form of conservation of momentum and energy (6.5) and (6.6) form the basis of the finite element discretisation. With an assumed displacement and temperature field within an element that only depends on the nodal degrees of freedom from that element, the integrals that appear in the weak form can be evaluated element by element. The nodal d.o.f. typically represent displacements and temperatures and—for shell elements—rotations. The d.o.f. for an element are represented by  $\mathbf{d}_e$ , which is a subvector of  $\mathbf{d}$ . The interpolation of displacements and temperatures from nodal values to any interior location can symbolically be represented with interpolation matrices:

$$\mathbf{u} = \mathbf{N}_u \mathbf{d}_e \quad (6.19)$$

$$T = \mathbf{N}_T \mathbf{d}_e \quad (6.20)$$

By virtue of the Galerkin method, the interpolation of the weighting functions  $\mathbf{w}_u$  and  $w_T$  is carried out with the same interpolation matrices  $\mathbf{N}_u$  and  $\mathbf{N}_T$ .

Before the evaluation of the weak formulation at element level, it is noted that the rate of deformation can be written as

$$\mathbf{D} = \frac{1}{2}(\nabla \mathbf{v} + (\nabla \mathbf{v})^T) = \mathbf{B}_u \dot{\mathbf{d}}_e \quad (6.21)$$

where  $\mathbf{B}_u$  can be considered as a vector of second order tensors containing gradients of  $\mathbf{N}_u$ , although the usual implementation uses a vector representation of the strain and then  $\mathbf{B}_u$  is a matrix. Because of the symmetry of the stress tensor  $\boldsymbol{\sigma}$ , the contraction  $\nabla \mathbf{w}_u : \boldsymbol{\sigma}$  can also be written in matrix-vector format as  $\mathbf{w}^T \mathbf{B}_u^T \boldsymbol{\sigma}$ .

Element mass and capacity/damping matrices and internal and external load vectors can be derived from the element contributions to the integrals in (6.5) and (6.6), leading to

$$\mathbf{M}_e = \int_{\Omega_e} \rho \mathbf{N}_u^T \mathbf{N}_u \, d\Omega \quad (6.22a)$$

$$\mathbf{C}_e = \int_{\Omega_e} \rho c \mathbf{N}_T^T \mathbf{N}_T \, d\Omega - \int_{\Omega_e} \mathbf{N}_T^T (\boldsymbol{\sigma}^T \mathbf{B}_u) \, d\Omega \quad (6.22b)$$

$$\mathbf{f}_{\text{int},e} = \int_{\Omega_e} \mathbf{B}_u^T \boldsymbol{\sigma} \, d\Omega - \int_{\Omega_e} \nabla \mathbf{N}_T^T \mathbf{q} \, d\Omega \quad (6.22c)$$

$$\mathbf{f}_{\text{ext},e} = \int_{\Omega_e} \mathbf{N}_u^T \rho \mathbf{b} \, d\Omega + \int_{\Gamma_{le}} \mathbf{N}_u^T \bar{\mathbf{t}} \, d\Gamma + \int_{\Omega_e} \mathbf{N}_T^T \rho r \, d\Omega + \int_{\Gamma_{he}} \mathbf{N}_T^T \bar{h} \, d\Gamma \quad (6.22d)$$

Coupling between thermal and displacement/rotation degrees of freedom occurs in the capacity/damping matrix (6.22b), where the second part represents the dissipation of mechanical work. Further coupling exists in the internal force vector (6.22c), where a change of temperature influences the stress by thermal expansion and change of material behaviour and where the displacements may influence the thermal conduction.

In this work the thermal part of the equations is kept linear, except from displacement-dependent heat transfer in contact elements. The heat capacity per volume  $\rho c$  is considered constant and for thermal conduction the Fourier law is adopted:

$$\mathbf{q} = -\boldsymbol{\lambda} \cdot \nabla T = -\lambda_{\text{iso}} \nabla T \quad (6.23)$$

where  $\lambda$  is a 2nd order conduction tensor for general conduction. The second form with scalar  $\lambda_{\text{iso}}$  is for isotropic conduction. Because of the large heat capacity of the tools, the temperature distribution in the aluminium sheet is almost completely determined by the tool temperature. Therefore, the heat production due to plastic dissipation and friction is completely ignored.

### 6.2.1 Continuum Elements

For some simple geometries, sheet forming can be modelled with continuum elements. *E.g.* for bending of a rectangular plate, plane strain elements can be applied and for deep drawing of a cylindrical cup with planar isotropic material, axisymmetric elements can be applied. The continuum elements used in this thesis are only of the quadrilateral type. Each node has two displacement d.o.f. and, for thermo-mechanical elements, additionally one temperature d.o.f. The displacement and temperature fields within an element are interpolated with the same interpolation functions, that can be described as

$$\phi = \alpha_1 + \alpha_2\xi + \alpha_3\eta + \alpha_4\xi\eta \quad (6.24)$$

where  $\xi$  and  $\eta$  are the natural coordinates and  $\phi$  can be the  $x$ - or  $y$ -displacements or the temperature. The element matrices and vectors can be derived from the integrals (6.22a)–(6.22d) in a straightforward manner. They are evaluated using a  $2 \times 2$  Gauss integration scheme. To avoid volume locking, the dilatational part of the deformation is assumed constant over the element, leading to the so-called B-bar method (Nagtegaal *et al.*, 1974; Simo *et al.*, 1985). The temperature and displacements are interpolated with the same interpolation functions, but the thermal expansion is assumed constant, corresponding to the B-bar approach.

### 6.2.2 Shell Elements

Simulation of industrial sheet forming processes with continuum elements is not feasible, due to the enormous CPU time and memory consumption required. Shell elements are suitable for this purpose, because only the plane of the sheet is discretised with elements and the thickness direction is completely evaluated within one element. In the plane, larger elements can be allowed than would be justified with continuum elements. In standard formulations, the displacements in the element are now interpolated from nodal displacements *and* rotations. In this thesis two kinds of three-node triangular shell elements are used: discrete Kirchhoff elements (Batoz *et al.*, 1980) and discrete shear elements (Batoz and Lardeur, 1989). Both elements have 3 translational and 3 rotational d.o.f. in each node as indicated in Figure 6.1.

In both formulations, the in-plane displacements of the neutral plane are only determined by the in-plane nodal displacements. The interpolation function can be described as

$$\phi = L_1\phi_1 + L_2\phi_2 + L_3\phi_3 \quad (6.25)$$

where  $L_i$  is the area coordinate corresponding to node  $i$  and  $\phi_i$  is the value of  $\phi$  in node  $i$ . For both element types, the out-of-plane displacement is only defined along the element edges, on which a cubic polynomial is assumed. The parameters are determined by the

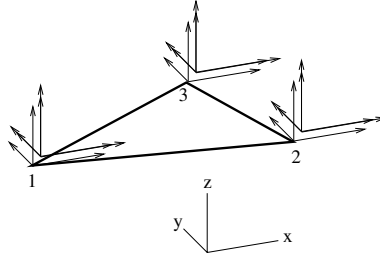


Figure 6.1: Three-node triangular shell element in the  $xy$ -plane with 18 d.o.f.

nodal displacements and rotations and constraint conditions at discrete points. Note that at the mid-point of the element edges, for the discrete Kirchhoff element the shear force is zero and for the discrete shear element the shear force and shear angle are related by the material model.

Preliminary analyses showed that the temperature distribution is almost constant in the thickness direction, therefore the elements were extended with a linear in-plane temperature interpolation as in (6.25) and no variation was assumed in the thickness direction. One temperature d.o.f. was added at each node. The element integrals are numerically integrated with 3 integration points in the plane and 2 to 7 in the thickness direction. For the thermal part, the creation of element matrices and vectors is straightforward. For the mechanical part, the problem arises that the displacements are not explicitly defined over the complete element. This means that a consistent interpolation matrix  $\mathbf{N}_u$  cannot be defined. The matrix  $\mathbf{B}_u$  is composed of the contribution from the mid-plane deformation and the curvature as described by Carleer (1997). Two additional points of attention are discussed next.

### Stiffness Matrix

The rotational d.o.f. along the normal of the element does not contribute to any deformation in the element. Hence, this so-called drilling d.o.f. gives no contribution to the mass or stiffness matrices. Without further measures, the equivalent stiffness matrix  $\mathbf{K}^*$  will be singular and thus will break down any solution procedure. One way to avoid this is to add a small stiffness to the diagonal element that represents this d.o.f. (Hughes, 1987). If a direct solver is used, this approach leads to good results. However, the very small diagonal terms lead to ill-conditioned matrices that are detrimental for iterative solvers. The approach described by Zienkiewicz and Taylor (2000b) may therefore be beneficial in combination with iterative solvers. Here, a coupling between all drilling d.o.f.  $\phi_{zi}$  is achieved by a stiffness relation between drilling moments  $M_{zi}$  and rotations  $\phi_{zi}$ :

$$\begin{Bmatrix} M_{z1} \\ M_{z2} \\ M_{z3} \end{Bmatrix} = \alpha \begin{bmatrix} 2 & -1 & -1 \\ -1 & 2 & -1 \\ -1 & -1 & 2 \end{bmatrix} \begin{Bmatrix} \phi_{z1} \\ \phi_{z2} \\ \phi_{z3} \end{Bmatrix} \quad (6.26)$$

where  $\alpha$  is a factor that scales with the stiffness of the element. This relation contributes to the stiffness matrix. In the examples,  $\alpha$  is 0.1 times the average of the other rotational

stiffness diagonal terms. The results are not influenced much by this contribution, but the condition number of the matrix improves considerably.

### Mass Matrix

For efficient use in an explicit central difference algorithm the mass matrix must be diagonalised. This can be done in several ways *e.g.* row-sum techniques, proportional scaling or nodal integration (Hughes, 1987; Zienkiewicz and Taylor, 2000a). For higher order elements—and that includes shell elements—row-sum and nodal integration can lead to negative values on the diagonal. For a shell element this is easily understood, since by moving all mass to the nodes, the moment of inertia becomes larger than with a distributed mass and the contribution of the rotational d.o.f. has to become negative in order to compensate for this effect. With proportional scaling, the diagonal terms are scaled in such a way that the sum of all components of the mass matrix is equal to the sum of the diagonal terms in the lumped matrix. In this way, the total mass is retained for continuum elements, but for shell elements the contributions from translational and rotational d.o.f. are mixed up and a physical justification fails.

For a three-node triangular shell element with a lumped mass matrix, all the nodes get one third of the mass on the translational d.o.f. An option for implicit methods is to ignore the rotational part altogether and apply only the translational inertia to the nodes. For explicit methods this is no option, because it would lead to a division by zero. Therefore, in explicit methods a value is assigned to the rotational d.o.f., scaled in such a way that the critical time step is not influenced by the rotational d.o.f. (Belytschko *et al.*, 2000).

For Kirchhoff elements a lumped mass matrix was developed based on equivalent acceleration moments or ‘mass moments of inertia’ (Meinders *et al.*, 2002). The total virtual work due to rotational acceleration for an element along one of its edges is approximated by

$$\delta W = \delta \omega I_m \ddot{\omega} \approx \delta \omega \rho h I \ddot{\omega} \approx \delta \omega \rho h \frac{1}{12} b h^3 \ddot{\omega} \approx \delta \omega \rho h \frac{1}{3} A^2 \ddot{\omega} = \delta \omega \frac{1}{3} m A \ddot{\omega} \quad (6.27)$$

with  $m$  the element mass and  $A$  the element area. The resulting diagonal mass matrix becomes

$$\mathbf{M} = \frac{1}{3} m \text{diag} \left[ 1 \quad 1 \quad 1 \quad \frac{1}{3} A \quad \frac{1}{3} A \quad \frac{1}{3} A \quad \dots (\times 3) \dots \right] \quad (6.28)$$

The rotational part of this matrix is not correct, but at least it has correct dimensions and scales properly on mesh refinement.

For discrete shear elements a lumped mass matrix was developed based on row-sum lumping for the mass matrix of a Mindlin element. Here the rotational d.o.f. only result in in-plane shear deformation which gives a small contribution to the acceleration. This results in a value of  $m/3$  on the rows that represent a displacement and a value of  $mh^2/36$  on the rows that represent a rotation. This diagonal matrix cannot be used in an explicit algorithm, because of the zeros in the drilling d.o.f. positions. Usually, a value equal to the other rotational d.o.f. is applied for the drilling mass also, leading to

$$\mathbf{M} = \frac{1}{3} m \text{diag} \left[ 1 \quad 1 \quad 1 \quad \frac{1}{12} h^2 \quad \frac{1}{12} h^2 \quad \frac{1}{12} h^2 \quad \dots (\times 3) \dots \right] \quad (6.29)$$

Both methods give satisfactory results in a simple dynamic beam bending test. In Section 6.5.1 the influence of the drilling stiffness and mass matrix on the performance of iterative solvers is investigated.

### 6.2.3 Contact Elements

In this work, contact is modelled using contact elements. A penalty method is used, that can be considered as a distributed spring that is stiff if penetration is detected and relaxed if not. For a 2-dimensional analysis, a contact element is connected to one side of a continuum element. For 3-dimensional shell element models one side of a contact element is connected to the shell element, with an offset of half the shell thickness from the neutral plane. In both cases, the other side of the contact element is projected onto a rigid tool surface. The projection is updated at each increment.

The integrals (6.22a)–(6.22d) can also be used for contact elements if matrix  $\mathbf{B}_u$  interpolates from nodal displacements to displacement differences between upper and lower contact faces and  $\sigma$  is substituted by the contact traction. In a thermo-mechanical contact element the conductivity will be a function of the separation of two contact faces. Usually, the conductivity will be set to a high value if contact occurs and to a low value if the element is open. A variational derivation for the matrix and vector representation of thermo-mechanical contact elements is given by Van der Lugt (1988) and Rietman (1999).

## 6.3 Comparison Between Implicit and Explicit Methods

The two main solution procedures for the simulation of sheet forming processes are the dynamic explicit and the static implicit algorithms. The dynamic explicit method is frequently used in simulations of sheet forming processes, since it reduces the computation time drastically compared to implicit methods, using a diagonal mass matrix to solve the equations of motion (Mattiasson *et al.*, 1991; Mercer *et al.*, 1995; Yang *et al.*, 1995). A disadvantage of this method is the conditional stability, necessitating extremely small time steps or artificial adaptations to the model. Equilibrium is not fulfilled after each time step, which can result in erroneous stress distributions and unrealistic product shapes (Gelin *et al.*, 2000).

The static implicit method is unconditionally stable. Equilibrium is satisfied at the end of each time step and thus will lead to more reliable results. The main drawback of this method, however, is that a linear set of equations must be solved repeatedly. For 2D or planar 3D finite element models and uniform refinement, the computation time increases quadratically with the size of the model, when using a direct solver. Another drawback is that sometimes convergence is hard to reach.

In large scale implicit finite element simulations the computation time for a direct solution of linear sets of equations is the bottle-neck. The linear sets of equations arise from the implicit solution method by a linearisation, *e.g.* the Newton–Raphson method. A way to alleviate this problem is to use iterative solvers instead of direct solvers, to solve the linear sets of equations. The use of iterative solvers (including multi-grid solvers) in quasi-static elasto-plastic simulations was reported by Kacou and Parsons (1993); Mahnken (1995); Jefferson and Thomas (1997); Van den Boogaard *et al.* (1998); Ferencz and Hughes (1998); Demarco and Dvorkin (2001); Mocellin *et al.* (2001). These papers concerned mainly the convergence behaviour of the iterative solver and the parallel implementation. For transient linear dynamic analysis with a Newmark integration scheme a study was presented by Fish and Chen (1999). In 3D solid analysis the time-saving compared to direct solvers is impress-

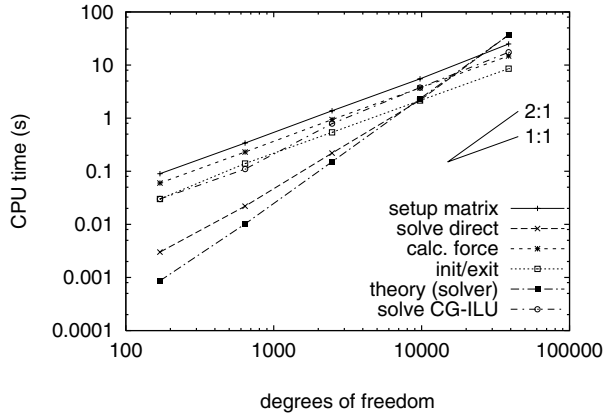


Figure 6.2: CPU usage for different parts of an implicit algorithm.

ive. For shell-element models, however, the condition of the matrix is poor and the reduction in computation time, if any, is less dramatic. Current research in this field is mainly focused on the improvement of preconditioners for this type of problem (Saint-Georges *et al.*, 1996, 1999; Benzi *et al.*, 2001; Gee *et al.*, 2001).

In this section the strengths and weaknesses of the implicit and explicit methods are assessed. The results from this assessment will be used to improve the efficiency of implicit methods.

### 6.3.1 Implicit Methods

Most sheet forming processes can be considered quasi-statically. In this case it is customary to ignore the mass term in (6.7) altogether and iterate on equilibrium ( $\mathbf{f}_{\text{int}} = \mathbf{f}_{\text{ext}}$ ). The (rate dependent) dissipation is usually incorporated in the constitutive equations, hence there is no explicit  $\mathbf{C}$ -matrix and the iterations in (6.11) are performed with the stiffness matrix  $\mathbf{K}$  only. The implicit methods of practical relevance are unconditionally stable. This means that the time increment can be selected based on the required accuracy or convergence behaviour.<sup>1</sup> The determination of iterative increments  $\delta \mathbf{d}^k$  requires the solution of a linear set of equations.

In an implicit algorithm, the computation time for one iteration and the number of iterations largely determines the total analysis time. One full Newton–Raphson iteration can broadly be split into 3 parts: the calculation of the tangential stiffness matrix, the calculation of the incremental displacement vector and the calculation of the internal force vector. Furthermore some initialisation and closure of each increment takes time, independently of the number of Newton–Raphson iterations. In Figure 6.2 the relative CPU-times for tension test simulations (see Section 6.4.4) are presented for increasing numbers of d.o.f.

<sup>1</sup>Note that the implicit *time integration algorithm* is unconditionally stable. That does not imply, however, that the (Newton–Raphson) *equilibrium iterations* within a time increment are also stable. And, conversely, the explicit time integration is conditionally stable, but since no equilibrium iterations are performed the solution for one time increment is very robust.



It can be seen that the setup of the matrix, the calculation of the internal force vector and the initialisation and closure of an increment are linear in time (note the logarithmic scale). As could be expected from the theory, the time complexity for a direct solver tends to be quadratic in the number of d.o.f. for a 2D analysis. Up to about 10000 d.o.f., the time required for the solver is negligible compared to the setup of the matrix and internal force vector. Above approximately 40000 d.o.f. (in this example) the solver takes more than half of the solution time. In Figure 6.2 also a preconditioned Conjugate Gradient (iterative) solver is presented. Although initially this solver takes much more time than a direct solver, the time complexity is only slightly more than linear in the number of d.o.f. Within the presented range the CG solver takes less time than the generation of the matrix. In this example, the CG solver is faster than the direct solver for systems with more than 20000 d.o.f. From the directions in the logarithmic graph it can be seen that the advantage increases rapidly if the number of d.o.f. increase.

Two serious disadvantages of implicit methods are the (lack of) stability of the Newton–Raphson iteration process and the rapid increase in computation time when direct solvers are used. Iterative solvers can decrease the computation time for large systems, but this depends heavily on the condition of the matrix. Typically for shell structures the condition number of the matrix is very high, and as a consequence iterative solvers converge very slowly or not at all.

### 6.3.2 Explicit Methods

Compared to the implicit methods, the explicit methods are very easy and straightforward. For reasons of accuracy, only the central difference scheme is used in practice, apart from small deviations in the case of a change of time step. As indicated in Section 6.1.1 an explicit method is derived from the central difference scheme only if the mass matrix  $\mathbf{M}$  and the capacity/damping matrix  $\mathbf{C}$  are diagonalised.

In an explicit method no stiffness matrix needs to be generated, avoiding a lot of triple matrix products and sometimes tedious derivation of consistent stiffness matrices. The memory requirement for the (diagonal) mass matrix is marginal and since no iterations are required on the material level, no separate start- and end-of-increment data need to be stored. No ‘unbalance’ force exists, since the difference between external and internal forces determine the acceleration at the start of the same time increment. In this way an explicit method will never suffer from convergence problems within a time increment.

The most significant drawback of the central difference method is its conditional stability. With an elastic wave speed in steel of about  $\sqrt{E/\rho} \approx 5$  km/s and a typical element length of 5 mm, the critical time step is about 1  $\mu$ s. For a sheet forming process the time lapse is of the order of 1–10 seconds (the higher values *e.g.* for hydroforming). The maximum allowable time increment then becomes prohibitively small, leading to a minimum of  $10^6$ – $10^7$  increments.

To reduce the computation time for processes that are not completed within milliseconds, mass scaling is often applied. The mass density of the material is then artificially increased, thus decreasing the wave speed and increasing the critical time step. Another approach is to increase the actual velocities in the process, *e.g.* the punch speed in deep drawing. If no rate dependent material behaviour is used, dividing  $\Delta t^2$  or multiplying  $\mathbf{M}$  by the same

factor is completely equivalent. To reach acceptable computation times for processes like deep-drawing, mass scaling with a factor of 100 to 10000 is not uncommon.

The critical time step also holds for the almost linear elastic springback phase of the analysis. It is reported in the literature that with explicit methods, the analysis of the springback phase often takes the same or even more computation time as the complete forming phase (Mercer *et al.*, 1995; Rojek *et al.*, 1998). With implicit codes the springback phase (with only some minor geometrical nonlinearities) can be performed within a few increments. In explicit finite element codes for forming, therefore, often an implicit code is incorporated for the springback analysis (Lee *et al.*, 1999).

It is interesting to note the similarity between the explicit method and one of the simplest iterative linear equation solvers *viz.* the Jacobi iteration. Decomposing the matrix  $\mathbf{A}$  in a diagonal part  $\mathbf{D}$  and an off-diagonal part  $\mathbf{F}$ , the Jacobi iteration method to solve  $\mathbf{Ax} = \mathbf{b}$  can be presented as (Golub and Van Loan, 1989)

$$\mathbf{D}\mathbf{x}^{k+1} = -\mathbf{F}\mathbf{x}^k + \mathbf{b} \quad (6.30)$$

If we use an implicit method with an initial continuation prediction, the initial estimate for the displacement is  $\mathbf{d}_{n+1}^0 = 2\mathbf{d}_n - \mathbf{d}_{n-1}$ . In the next Newton–Raphson iteration, the displacement becomes  $\mathbf{d}_{n+1}^1 = 2\mathbf{d}_n - \mathbf{d}_{n-1} - \mathbf{K}^{*-1}\mathbf{r}$ . If this set of equations is solved by a Jacobi iteration method, setting  $\mathbf{A} = \mathbf{K}^*$  and  $\mathbf{b} = -\mathbf{r}$ , the first iteration of the Jacobi solver (starting with  $\mathbf{x}^0 = \mathbf{0}$ ) yields  $\mathbf{d}_{n+1}^1 = 2\mathbf{d}_n - \mathbf{d}_{n-1} + \mathbf{D}^{-1}\mathbf{b}$ . If the diagonal of the iteration matrix is dominated by  $\mathbf{M}/\Delta t^2$  (*e.g.* by choosing  $\beta = 1$  in the Newmark scheme and using a lumped mass matrix) then, by comparison with (6.16) and (6.17) it shows that one increment in the explicit method performs like one Jacobi iteration.

It should be noted that the diagonalised matrix is not consistent with the spatial discretisation. Different strategies exist to derive a diagonalised mass matrix, but none of them seems to be attractive for higher order elements. This also involves ‘linear’ plate and shell elements, where translational and rotational d.o.f. are mixed.

In conclusion: the explicit time integration method is fast and robust. However, the nodal lumping of the mixed interpolation of translations and rotations in the mass matrix of shell elements lacks mathematical rigour. Mass scaling for slow processes *can* introduce non-physical effects and equilibrium is not checked during the process. Therefore, the accuracy relies, to a larger extent than for implicit methods, on the expertise of the analyst.

### 6.3.3 An Efficient Strategy for Implicit Methods

Regarding the previous discussion on implicit and explicit methods the analysis strategy based on implicit methods can be optimised. It is clear that the use of direct solvers is not a feasible option for large systems. Iterative solvers do not perform very well for shell models, but at the other hand it was noted that the explicit method can be regarded as one of the simplest iterative solvers. Clearly the dominance of the mass terms in an explicit method is essential. This implies that the strategy should be to retain inertial effects in the implicit finite element code in combination with the use of iterative solvers. When the mass and capacity matrix are diagonalised and added to the stiffness matrix, the diagonal terms of the system matrix will increase and the condition of the matrix improves, which makes an effective use of iterative solvers possible. Another advantage of introducing dynamics

contributions into an implicit finite element code is that it stabilises the Newton–Raphson iterations. Problems that are under-constrained, *e.g.* when closing a doubly curved blank holder, benefit from this stabilising effect. This strategy is extensively described by Van den Boogaard *et al.* (2003).

## 6.4 Linear Equation Solvers

As was shown in Figure 6.2, the computation time needed for the solution of a linear set of equations dominates the total computation time of implicit methods for large models. The chosen analysis strategy advocates the use of iterative solvers for this part. In this section some properties of direct and iterative solvers are discussed.

### 6.4.1 Direct Solvers

Direct solvers are generally based on use some form of Gaussian elimination process. The types that are used in finite element codes typically take advantage of symmetry and the bandedness or skyline-profile. Bandwidth optimisation algorithms are used to reduce the bandwidth and thus the required computation time. In all the examples in this thesis, the solution time for the direct solvers is optimised by a bandwidth optimisation algorithm according to Sloan (1989). More recent direct sparse matrix solvers even optimise on a reduced fill-in during the elimination process. The computational complexity of direct solvers is proportional to  $n_{\text{eq}}n_{\text{bw}}^2$ , where  $n_{\text{eq}}$  is the number of equations and  $n_{\text{bw}}$  the (mean) bandwidth. In sheet forming simulations (a curved plane in 3D) a uniform decrease in element size results in a quadratic increase in the number of equations and a linear increase in the bandwidth, so finally a fourth order increase in the computation time (or quadratic in the number of d.o.f.). The storage requirements are proportional to the number of d.o.f. and the mean bandwidth. For a planar model this scales with  $n_{\text{eq}}^{3/2}$ .

The advantage of direct solvers is that they give a solution within a predetermined number of operations up to a high accuracy. The accuracy depends on the condition number of the matrix but is usually high enough to be used within the Newton–Raphson iterations. Pivoting is not often used because it destroys the band structure and would lead to excessive computation times.

### 6.4.2 Iterative Solvers

The solution of a linear set of equations can be approximated in an iterative way. Several examples can be found in Golub and Van Loan (1989); Hackbush (1994); Barret *et al.* (1994). These solvers become interesting if they produce an acceptable iterative displacement vector  $\delta \mathbf{d}^k$  in a shorter time and using less memory than a direct solver. The memory requirements are very clear. Usually only the non-zero components of a matrix have to be stored. With uniform mesh refinement in 2 directions, the typical connectivity remains the same and therefore the number of non-zeros per row remains equal. Hence, iterative solvers need memory proportional to  $n_{\text{eq}}$ .

The time requirements for iterative solvers are not so clear. For every local iteration, the time depends linearly on the number of d.o.f. but the number of iterations is not fixed.

The number of iterations depends on the local convergence criterion (see Section 6.4.3) and the condition of the matrix. For conjugate-gradient-like solvers the ratio between the largest and smallest eigenvalues determines the convergence rate. Typically the convergence deteriorates due to high stiffness ratios (stiff contact elements, multi-physics or shell elements), due to decreasing material stiffness (plasticity) and due to singularities (constant volume constraints). Preconditioning of the matrix can significantly improve the convergence characteristics.

Several iterative solvers have been compared in the examples presented in Section 6.4.4 and more extensively in Van den Boogaard *et al.* (1998). The iterative solvers used are: Symmetric Successive Over Relaxation (SSOR), Conjugate Gradient (CG), Generalised Minimum Residual (GMRES), Quasi-Minimal Residual (QMR) and BiConjugate Gradient Stabilised (Bi-CGSTAB). With the exception of the SSOR solver, all solvers are used without preconditioner and with Jacobi, SSOR and Incomplete Cholesky (IC) preconditioning. The CG solver is derived for symmetric positive definite matrices and the others for non-symmetric and indefinite matrices.

### 6.4.3 Convergence Criterion

In the nonlinear solution process the linear set of equations (6.11) must be solved repeatedly to obtain the iterative displacement increments  $\delta \mathbf{d}^k$ .

With (6.15) we write the residual force vector as the last known value at iteration  $k$ , a linearised increment  $\mathbf{K}^{*k} \delta \mathbf{d}^k$  and an error  $\mathbf{e}^{k+1}$ :

$$\mathbf{r}(\Delta \mathbf{d}^{k+1}) = \mathbf{r}(\Delta \mathbf{d}^k) + \mathbf{K}^{*k} \delta \mathbf{d}^k + \mathbf{e}^{k+1} \quad (6.31)$$

Here the first and second terms on the right-hand side are the constant and linear terms of a Taylor series expansion and the error term  $\mathbf{e}$  represents all higher order terms.

In the Newton–Raphson process the increment  $\delta \mathbf{d}^k$  is calculated, using (6.11), from

$$\mathbf{K}^{*k} \delta \mathbf{d}^k = -\mathbf{r}^k \quad (6.32)$$

Substituting (6.32) into (6.31) makes clear that  $\mathbf{r}^{k+1}$  equals  $\mathbf{e}^{k+1}$ .

The iterations are stopped if the Euclidean norm of  $\mathbf{r}$  is less than  $\varepsilon$  times the Euclidean norm of  $\mathbf{f}_{\text{int}}$ . The actual ratio in iteration  $k$  is designated as  $\varepsilon^k$ :

$$\frac{\|\mathbf{r}^k\|}{\|\mathbf{f}_{\text{int}}\|} = \varepsilon^k \leq \varepsilon \quad (6.33)$$

We now consider an iterative solution process for the linear system of equations, described by (6.32). With an iterative solver  $\delta \mathbf{d}^k$  is not calculated exactly, but it is approximated by  $\hat{\delta \mathbf{d}}^k$  so that an error  $\boldsymbol{\epsilon}$  remains according to

$$\mathbf{K}^{*k} \hat{\delta \mathbf{d}}^k = -\mathbf{r}^k + \boldsymbol{\epsilon} \quad (6.34)$$

The iterative process will be terminated if the Euclidean norm of the error vector  $\boldsymbol{\epsilon}$  is less than  $\delta_{\text{it}}$  times the Euclidean norm of  $\mathbf{r}^k$ :

$$\|\boldsymbol{\epsilon}\| \leq \delta_{\text{it}} \|\mathbf{r}^k\| \quad (6.35)$$

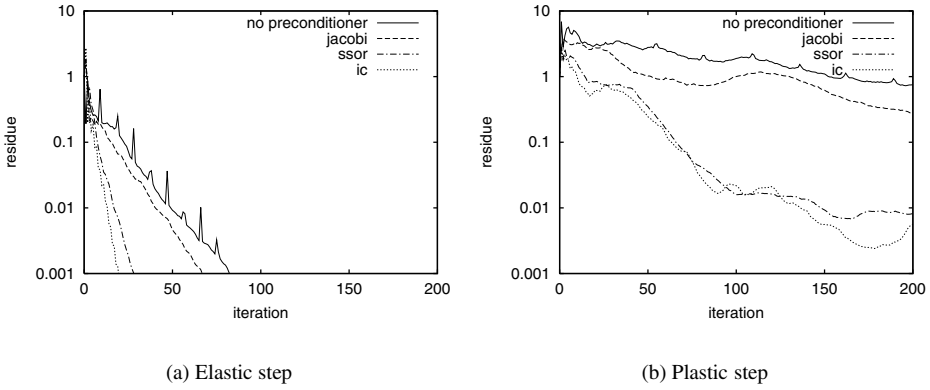


Figure 6.3: Convergence behaviour of the CG solver with different preconditioners.

Relating the convergence to  $\mathbf{r}^k$  instead of directly to  $\mathbf{f}_{\text{int}}$  facilitates the use of ‘of the shelf’ solvers as is done in this work.

In Figure 6.3 the norm  $\|\boldsymbol{\epsilon}\|$  is plotted against the iteration number for an elastic and a fully plastic step of the deep drawing example presented in Section 6.4.4. In this case a CG solver is used without preconditioner and with Jacobi, SSOR and Incomplete Cholesky preconditioner. From these graphs it is clear that good preconditioning is essential, especially in the fully plastic case and that a solution within ‘machine accuracy’ cannot be reached. An important issue for the application of iterative solvers in forming processes is, therefore, the selection of the required accuracy in the solution of the linear set of equations.

It is arguable that the value of  $\delta_{\text{it}}$  should be related to the required accuracy  $\varepsilon$  of the global Newton–Raphson process. If we use the approximated vector  $\delta\hat{\mathbf{d}}$  instead of  $\delta\mathbf{d}$  in (6.31) we obtain, using (6.34),

$$\mathbf{r}(\Delta\hat{\mathbf{d}}^{k+1}) = \mathbf{r}(\Delta\mathbf{d}^k) + \mathbf{K}^{*k} \delta\hat{\mathbf{d}}^k + \hat{\mathbf{e}}^{k+1} = \boldsymbol{\epsilon} + \hat{\mathbf{e}}^{k+1} = \mathbf{r}^{k+1} \quad (6.36)$$

The norm of  $\mathbf{r}^{k+1}$  is bounded by

$$\|\mathbf{r}^{k+1}\| = \|\hat{\mathbf{e}}^{k+1} + \boldsymbol{\epsilon}\| \leq \|\hat{\mathbf{e}}^{k+1}\| + \|\boldsymbol{\epsilon}\| \quad (6.37)$$

Here  $\hat{\mathbf{e}}$  represents an error due to nonlinearity in the system (second and higher order terms) and  $\boldsymbol{\epsilon}$  represents an error in the linear solver, which is linear in the displacement.

We require that  $\|\boldsymbol{\epsilon}\| \leq \delta_{\text{it}}\|\mathbf{r}^k\|$ . The global convergence norm is then:

$$\frac{\|\mathbf{r}^{k+1}\|}{\|\mathbf{f}_{\text{int}}\|} = \varepsilon^{k+1} \leq \frac{\|\hat{\mathbf{e}}^{k+1}\|}{\|\mathbf{f}_{\text{int}}\|} + \delta_{\text{it}} \cdot \varepsilon^k \quad (6.38)$$

Although  $\hat{\mathbf{e}}^{k+1}$  is not equal to  $\mathbf{e}^{k+1}$  they are both due to nonlinearity in the system. If the right-hand side is smaller than  $\varepsilon$  the Newton–Raphson process is considered to be converged. If we achieve that  $\delta_{\text{it}} \cdot \varepsilon^k$  is much smaller than  $\varepsilon$  the global process receives only a small

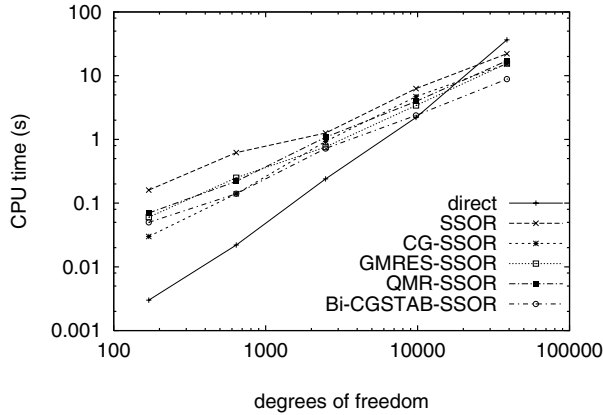


Figure 6.4: CPU usage for one solve step in the necking stage of a tensile test.

additional contribution to the residue. We can conclude that if  $\delta_{it}$  is set to the value of

$$\delta_{it} = \eta \cdot \frac{\varepsilon}{\varepsilon^k} \quad (6.39)$$

with a small  $\eta$ , the global iteration process is only marginally influenced by the linear iteration process. A rigorous proof of convergence for some plasticity algorithms and the Von Mises yield function for  $\delta_{it} < 1$  was given by Blaheta and Axelsson (1997); Blaheta (1997). For practical situations, several authors have advocated a value of  $\delta_{it} = 0.1$  or  $\eta = 0.1$  (Kacou and Parsons, 1993; Jefferson and Thomas, 1997; Blaheta and Axelsson, 1997), based however on different definitions of the convergence norms. The criterion can be less strict in the first iteration of every increment, if convergence is not expected in the first iteration (Mahnken, 1995). In Section 6.4.4 the influence of  $\eta$  on the global convergence will be demonstrated.

#### 6.4.4 Examples

The solvers that were used in the following examples were taken from the public domain (Skalický, 1996), and are also described by Barret *et al.* (1994). The cited direct solvers did not use pivoting and the GMRES solver was restarted after every 20 iterations.

##### Tensile Test

First a simple tension test problem was used to assess the rate of convergence in the case of large plastic deformations and the influence of uniform mesh refinement. All types of non-stationary iterative solvers performed best with an SSOR preconditioner. In Figure 6.4 the results for an increment in the necking stage are presented for different mesh densities. The coarsest mesh has 5 elements in the radial direction and 15 in the axial direction. The finer meshes are obtained by doubling the number of elements in both directions. This leads to  $80 \times 240$  elements in the finest mesh. A Nadai hardening curve with exponent 0.13 was

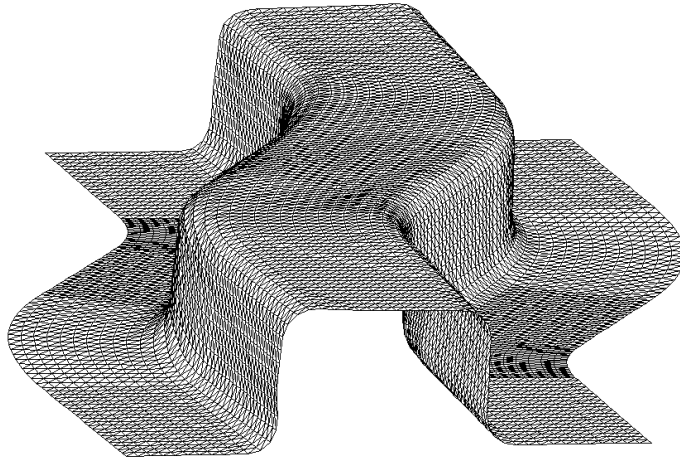


Figure 6.5: S-Rail final geometry.

taken in an elastoplastic material model. The CPU time was measured on a slow machine, compared to current standards (spec fp92 = 170).

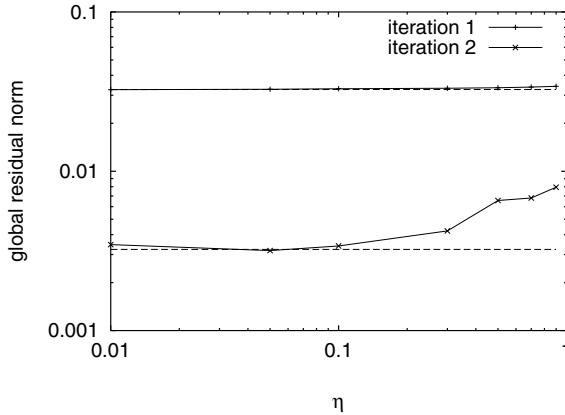
It can be seen that for the finer meshes—where iterative solvers are faster than direct solvers—the Bi-CGSTAB solver with SSOR preconditioning is the fastest of the examined solvers. The time complexity of all iterative solvers is almost linear.

### Deep Drawing

In the second example the deep drawing of an S-shaped rail is simulated. This example originates from the NumiSheet '96 conference (Lee *et al.*, 1996) and was run on a HP 8000 workstation (spec fp95 = 62.7). The presented model contains 12000 triangular shell elements and a total of 36968 d.o.f. In the stiffness matrix only the symmetric contribution of the contact elements was used. In 72 increments a flat sheet metal blank was deformed into the end geometry as shown in Figure 6.5. With the direct solver, every iteration took about 45 s of which 16 s were used for the direct solver. The same simulation was carried out with a CG solver with SSOR preconditioning for different values of  $\eta$  (see Eq. 6.39).

In Figure 6.6 the convergence of the global residual norm in step number 10 is presented. The first iteration is always performed with a local criterion  $\delta_{it} = 0.01$  and should be independent of  $\eta$ . In the figure the horizontal dashed lines represent the convergence characteristics with the direct solver. For the second iteration  $\delta_{it}$  depends on the achieved convergence in the previous iteration and on  $\eta$ . The global criterion was set to  $\varepsilon = 0.01$ . It can be seen that for  $\eta \rightarrow 1$  the global criterion tends to this norm. For this particular model and this particular step, global convergence is always achieved in the second iteration, even with  $\eta = 0.9$  but in general it can be seen from Figure 6.6 that for  $\eta > 0.1$  the global convergence can deteriorate.

In Table 6.1 the number of Newton–Raphson iterations, solver iterations and the CPU time necessary to perform the first 10 steps with different values of  $\eta$  and with the direct solver

Figure 6.6: Global convergence at different  $\eta$ .Table 6.1: Influence of  $\eta$  on convergence and time for 10 steps.

$\eta$	N-R	local	CPU time (s)
direct	20	-	843
0.01	20	1389	691
0.05	20	961	639
0.1	20	769	625
0.3	20	626	608
0.5	20	607	605
0.7	20	582	594
0.9	21	560	612

are presented. For small values of  $\eta$  the CPU time increases because more local iterations must be performed in the iterative solver. For larger values of  $\eta$  at some point more global Newton–Raphson iterations must be performed. The optimum for this particular example is about  $\eta = 0.7$ . Since not much more time is needed, and with reference to Figure 6.6,  $\eta = 0.1$  or  $0.3$  seems to be a robust and efficient choice.

With the direct solver the simulation of all 72 steps took 7560 s for 154 Newton–Raphson iterations. Using an iterative solver with  $\eta = 0.1$ , the simulation time reduced to 6977 s for 149 iterations. Although this is not a dramatic improvement, the improvement in the solver is significant. The total time used by the direct solver was 2334 s and by the iterative solver 1841 s. For larger models the difference between direct and iterative solvers will increase rapidly. In the next section, methods are investigated to improve the performance of iterative solvers.



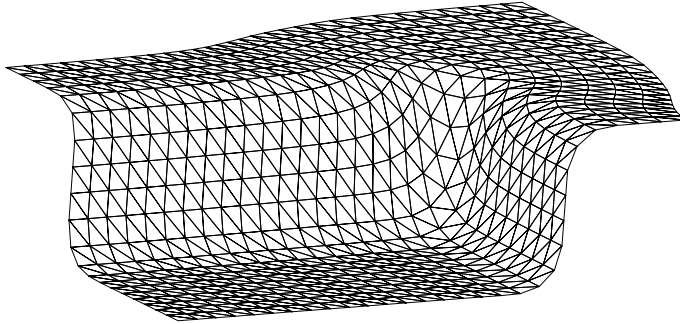


Figure 6.7: Finite element mesh for a quarter section of a rectangular product.

## 6.5 Stabilisation by Dynamics Contributions

In this section the influence of dynamics contributions on the simulation of deep drawing is investigated. The main goal of the dynamics contributions is to stabilise the calculation and improve the convergence of iterative solvers. First a relatively small model is used to investigate the influence of drilling stiffness, time integration scheme and punch velocity. Then the impact on computation time in a large scale analysis is presented.

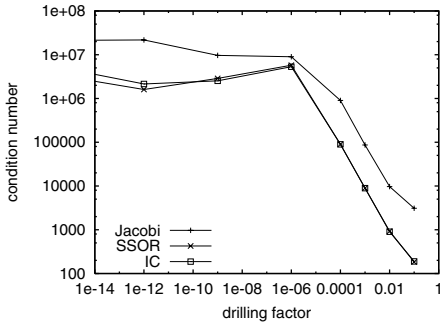
### 6.5.1 Deep Drawing of a Rectangular Product

In this section a relatively small model for the deep drawing of a rectangular product is used to determine the influence of several model parameters. The results from the backward difference scheme are used as reference values. The difference with the Newmark scheme and the influence of the drilling stiffness and punch velocity are presented. A lumped mass matrix approach is used.

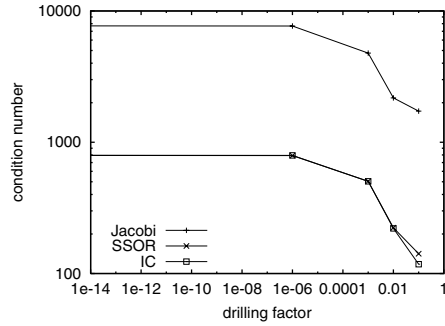
In Figure 6.7 the final shape, at a depth of 100 mm, is presented for a quarter section of the product. The initial dimensions of the blank are 313 mm by 221 mm, with a thickness of 1 mm. The unbalance criterion of the global Newton–Raphson iterations ( $\varepsilon$  in (6.33)) is set at 0.01.

The influence of several parameters on the condition number of the matrix and on the required number of iterations is determined. To this end, for every parameter set 40 increments with 0.5 mm punch displacement per increment were taken, using a direct solver. After 20 mm displacement a large part of the blank is plastic, while some parts in the flange are still elastic. This results in large stiffness ratios that are usually detrimental for iterative solvers. The matrix and right-hand side vector that were assembled in the first iteration of the 40-th step were exported to an external file. The condition number for this matrix and the solution for this set of equations was subsequently derived with one direct and several iterative solvers. The set of equations was solved by a CG and a Bi-CGSTAB method with Jacobi, SSOR and IC preconditioning with a local convergence criterion  $\delta_{it} = 10^{-5}$  according to (6.35). Without preconditioning, the solution was often not obtained within a prescribed maximum of 500 iterations and these results are not presented.

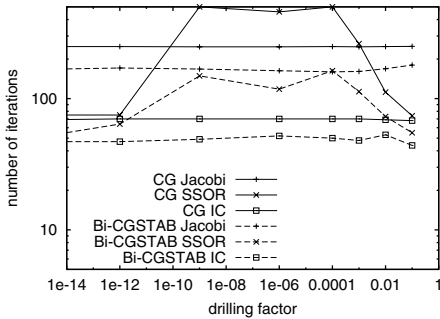
The influence of the artificial drilling mode stiffness ( $\alpha$  in (6.26)) is presented in Fig-



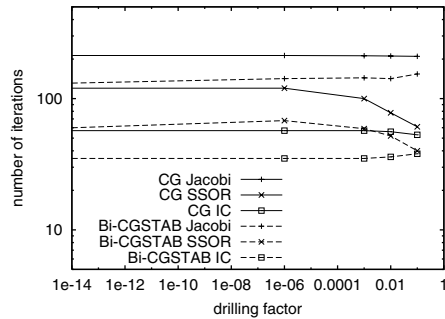
(a) Condition numbers, static



(b) Condition numbers,  $v = 10$  m/s



(c) Number of iterations, static

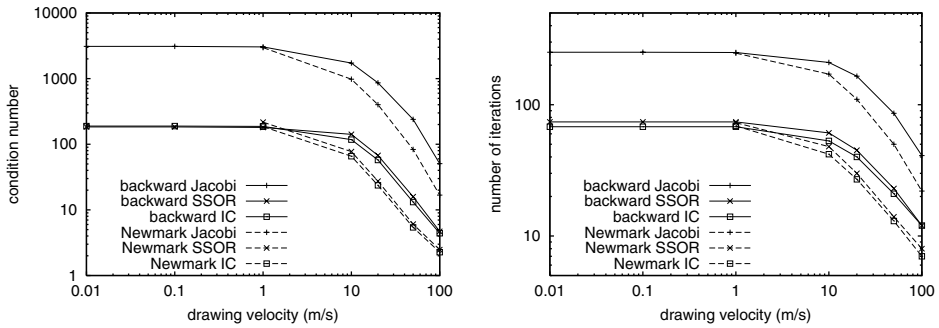


(d) Number of iterations,  $v = 10$  m/s

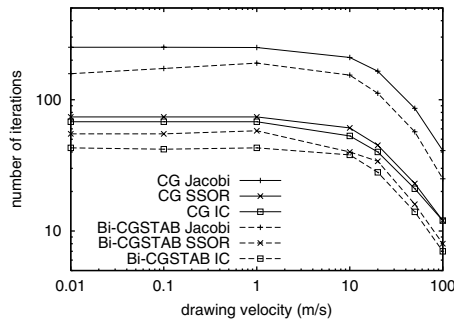
Figure 6.8: Influence of the drilling stiffness factor  $\alpha$ .

ure 6.8. It can be seen in Figure 6.8(a) that, in a static analysis, the condition numbers are very high for a low  $\alpha$  and start to decrease rapidly for  $\alpha > 10^{-6}$ . At a punch speed of 10 m/s, Figure 6.8(b), the mass terms regularise the matrix, but still an improvement of the condition number is achieved for  $\alpha > 10^{-6}$ . Looking at Figure 6.8(c) and Figure 6.8(d) (note the logarithmic scale) it is evident that the condition number of the matrix is not the only relevant parameter. For Jacobi and IC preconditioned methods, the decay in condition number for  $\alpha > 10^{-6}$  does not influence the number of required iterations much. However, for the SSOR preconditioned methods in the static analysis, an anomalous increase of required iterations is seen for  $10^{-12} < \alpha < 0.1$ . This may be due to the particular spectrum of eigenvalues, which is known to influence the convergence behaviour (Hackbush, 1994). This detrimental effect does not appear in the dynamic analysis, and some beneficial effect can be observed for the SSOR preconditioner for  $\alpha > 10^{-3}$ .

In this particular example, the factor  $\alpha = 0.1$  did not influence the convergence of global Newton–Raphson iterations and, given the results as presented in Figure 6.8, this value was



(a) Condition numbers; backward vs. Newmark (b) Convergence; backward vs. Newmark integration with CG solver



(c) Convergence; CG vs. Bi-CGSTAB solver

Figure 6.9: Influence of the velocity on condition number and convergence.

used for all subsequent analyses.

In Figure 6.9, the influence of the punch velocity on the condition numbers and the required number of iterations for the iterative solvers is presented. Since no rate dependent material is used, an increase in punch velocity is equivalent to a quadratic increase in mass density (mass scaling). It can be seen in Figure 6.9(a) that the condition number decreases for velocities higher than 1 m/s. The number of iterations for the CG solver needed to achieve a residue of  $10^{-5}$  are presented in Figure 6.9(b). The condition number and number of iterations scale very well. It can also be seen from these graphs that the Newmark method results in a lower condition number and number of iterations, compared to the backward difference method. This can be explained by the stronger weighting of the mass matrix in (6.15). In this case  $\beta = 0.3$  and  $\gamma = 0.6$  was used, in order to add some numerical damping. In Figure 6.9(c) the difference between the CG and Bi-CGSTAB iterative solvers are presented. In all circumstances, the Bi-CGSTAB solver converged within less iterations

than the CG solver. But, because one CG iteration is faster than one Bi-CGSTAB iteration, the CG solver was always faster. Because the IC preconditioning is more time-consuming than SSOR, the CG solver with SSOR preconditioning was in almost all circumstances the fastest of the applied iterative solvers. With only 3754 d.o.f. in the matrix, this is a relatively small model and the direct symmetric skyline solver was faster than the iterative solvers for punch velocities below 50 m/s. The CPU times for the solvers depend on the exact implementation details and the machine architecture and are therefore not compared here.

The inertial effect also influences the convergence behaviour of the Newton-Raphson procedure. The simulation without dynamics contributions needs 586 iterations for the entire simulation of 200 increments. The simulation of a dynamic process with a punch velocity of 50 m/s, using the backward difference method, needs 502 iterations for the entire simulation. Hence, a reduction of 14 % in the number of iterations is achieved by the stabilising effect of inertia. Both simulations were performed using a direct skyline matrix solver in order to separate this effect from possible effects of iterative solvers as seen in Figure 6.6.

The thickness strain distribution in the product for a static and a dynamic simulation was presented by Meinders *et al.* (2002). It was observed that the inertial terms *do* influence the thickness strain distribution for a punch velocity of 50 m/s. A simulation performed with a drawing speed of 20 m/s showed hardly any difference between the results for the static and dynamic simulations. Already at this speed, the iterative solvers benefit a lot from the added inertia.

### 6.5.2 Front Door Panel

In this section, the forming of an AUDI front door panel is discussed. This product served as a benchmark for the NumiSheet '99 conference (Gelin and Picart, 1999). The blank holder is doubly curved which gives rise to numerical instabilities while closing the blank holder if dynamics contributions are not taken into account. This automotive product will be used to investigate the performance of the improved implicit code with respect to the conventional implicit code.

Two simulations were performed. For both simulations, the dynamics contributions were switched on, gravity loads were applied and automatic refinement used. The deep drawing velocity was set to 10 m/s. One simulation was performed in which the Bi-CGSTAB iterative solver with SSOR preconditioning was used, and one simulation was performed with a direct solver (Cholesky decomposition).

The results of the simulation using the iterative solver are discussed first. During the first 90 steps, the blank holder is closed. Then the punch moves downwards, until the desired deep drawing depth is reached in step 191. The final deformed mesh is presented in Figure 6.10.

During deep drawing, the mesh is refined in areas with high curvatures (Meinders, 2000). The initial mesh contains 17244 d.o.f., whereas the mesh ends up with 79344 d.o.f. The generation of new elements during the simulation is graphically represented in Figure 6.11(a). The total computation time for the entire simulation took 5.5 hours on a HP8000 workstation. This is similar to the computation time of explicit codes for this simulation (Gelin and Picart, 1999).

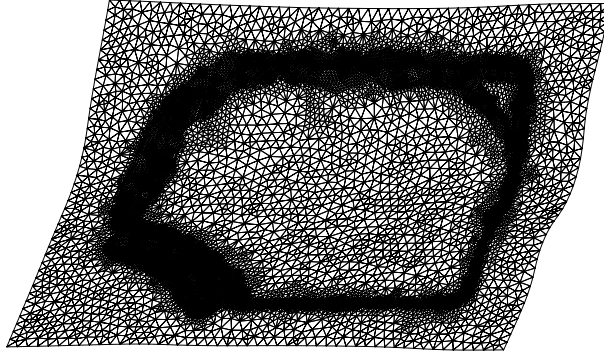


Figure 6.10: Final shape of front door panel.

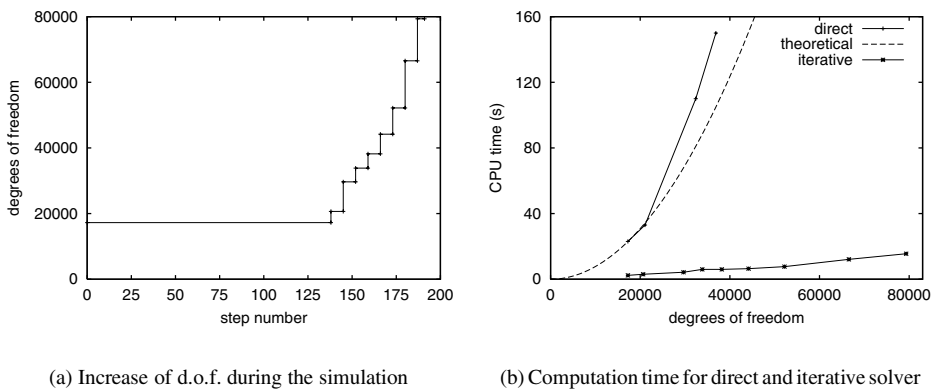


Figure 6.11: Evolution of d.o.f. and solver time in front door panel simulation.

Next, a simulation was started using a direct solver. At increment 166 the mesh contained 36876 d.o.f. and another mesh refinement was required. At this moment the simulation could not proceed due to insufficient internal memory on that particular computer. The computation time for one iteration strongly depends on the number of d.o.f. see Figure 6.11(b). This figure shows the computation time for one linear solution with the iterative and the direct solvers, during the simulation. The theoretical increase in computation time for the direct solver, based on uniform refinement proportional to  $n_{eq}^2$ , is also included. The figure clearly shows that the iterative solver is significantly faster than the direct solver. For 17244 d.o.f. the iterative solver is 10 times faster than the direct solver while this factor increases up to 25 for 36876 d.o.f. The time for the direct solver increases more than quadratically, which is due to the non-uniformity of the refined mesh. The computation time of the iterative solver increases slightly more than linearly. If the theoretical approach is taken as a lower bound for the prediction of the computation time for the direct solver in the case of 79344 d.o.f., the computation time will increase by at least a factor 40 with respect to the iterative solver.

With the iterative solver the total calculation time is no longer dominated by the solver and other parts of the code should be scrutinised for optimisation.

## 6.6 Conclusion

The convergence of iterative solvers for sets of equations derived from elasto-plastic shell element models is usually slow. It was shown, however, that in quasi-static sheet forming simulations, by balancing the global Newton–Raphson convergence criterion and the iterative solver convergence criterion, iterative solvers can reduce the computation time compared to direct solvers.

To improve the convergence of iterative solvers, inertial effects can be included in the algorithm. In this way the matrix becomes more diagonally dominant and the condition number of the matrix improves, which is advantageous for iterative solvers. Special attention should be given to the drilling d.o.f. in shell elements. Without (rotational) mass contribution, the presented artificial stiffness largely influences the performance of the iterative solver with SSOR preconditioning. If (artificial) rotational mass is added to this d.o.f., the influence of the drilling stiffness is reduced.

Under realistic deep drawing conditions, the contribution of the mass matrix is not enough to improve the behaviour of iterative solvers. If mass scaling or reduced process times are used, comparable to that used in explicit methods, the reduction in computation time can be tremendous.

Another advantage of using dynamics contributions in the implicit finite element code is that it stabilises the Newton–Raphson iterations. This is especially important when the problem is under-constrained *e.g.* in the stage where the blank is not yet fully clamped by a doubly curved blank holder.

It is shown that significant time and memory savings can be achieved by using iterative solvers with appropriate preconditioners. In the large deep drawing examples, the linear solution stage no longer dominates the total solution process. This means that for these particular examples a further significant reduction of the analysis time cannot be achieved from the linear solver alone. Optimisation should also focus on the creation of the matrix, the calculation of the internal force vector and the contact search algorithm. In this chapter only isothermal calculations were presented. The performance of the method for thermo-mechanical models is equally good. This will be demonstrated in the next chapter.

## 7. Applications

During the past 25 years, a large amount of literature has been published about warm forming of aluminium. Almost all papers describe experimental results. Some include a model for observed material behaviour. Only a few simulations of aluminium warm forming have been presented recently. Keum *et al.* (2001) presented 3D FEM simulations of cylindrical cup deep drawing with an AA 5042-H32 alloy. They used the Barlat yield function and a phenomenological work hardening relation similar to (3.58). A fifth order polynomial was used for the temperature dependent hardening parameters instead of Equations (3.60a)–(3.60c) in this thesis. The anisotropy parameters for the Barlat yield function were made temperature dependent, in order to obtain an isotropic model at the solidus temperature. They presented accurate thickness predictions, compared to experiments. The punch force–displacement curve, however, was not presented.

Takuda *et al.* (2002) used a 2D axisymmetric FEM model for the simulation of cylindrical cup deep drawing with an AA 5182-O alloy. They concentrated on the calculation of the temperature distribution. A rigid-plastic material model was used with a Nadai hardening model, equivalent to (3.47). The hardening constant  $C$  and exponent  $n$  were made temperature dependent. Rate sensitivity was *not* included in the material model. They claim that the accurate analysis of temperatures, including the heat transfer resistance between tool and workpiece, is important for the prediction of the limiting drawing ratio. We believe, however, that their results are unreliable, because of the absence of strain rate sensitivity.

In this chapter, two deformation processes are presented to demonstrate the applicability of the material models and solution strategies presented in this thesis. First, some of the uniaxial tensile tests that were used to determine the material parameters are simulated. The simulations include the geometry of the specimens. It is investigated whether simulations for strains beyond the uniform strain yield realistic predictions. In the second application, deep drawing of a cylindrical cup is simulated. The results are compared with experimentally obtained punch force–displacement curves and thickness distributions. Simulations with 2D axisymmetric models as well as with 3D shell element models are presented.

### 7.1 Tensile Test

The first process to be simulated was the uniaxial tensile test. The material parameters were derived from uniaxial tensile tests. Only measurements before reaching the maximum tensile force were used in the fitting process, because at higher strains the deformation becomes non-uniform. Therefore, it is to be expected that the experimental flow curves will be represented accurately by the simulation, up to the uniform strain (maximum tensile

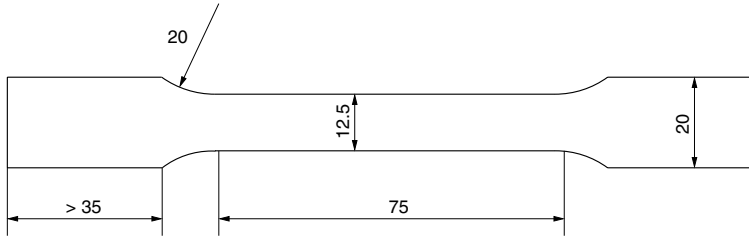


Figure 7.1: Geometry of the tensile test specimen (dimensions in mm).

force). For tensile test experiments at elevated temperatures, local necking occurs (far) beyond the uniform strain. With the simulations it is investigated whether the FEM model can predict the necking strain at different temperatures and strain rates.

The dimensions of the tensile test specimen are presented in Figure 7.1. The thickness of the specimen is 1.2 mm. For the simulations, the Vegter yield function and the Bergström hardening model were used, fitted to the investigated AA 5754-O sheet. In experiments at room temperature, a neck developed at an angle to the lateral direction. This was also predicted by the Hill necking criterion, according to Equation (5.18). At elevated temperatures the necking was approximately perpendicular to the tensile direction.

In a first analysis, under room temperature conditions, no use was made of symmetry to see whether a neck would develop along an angle. The simulations included the geometry of the specimen in the clamping area. This results in a slightly non-uniform strain distribution and strain localisation occurs, without initial imperfection. However, with no imperfection, significant diffuse necking starts first and due to the constraint imposed by the material outside the neck, the plane strain direction in the neck then rotates until it is perpendicular to the tensile direction. As a result, the numerically observed neck does not show the typical inclination angle. If one edge-node is given a smaller thickness, and the mesh is fine enough, an inclined neck is also found numerically, starting at the thinner node. Since at elevated temperatures the tensile specimens did neck perpendicular to the tensile direction, and because the arbitrary size of an imperfection in the model affects the results, the simulations were performed without imperfection and the numerical neck was then symmetric. Therefore, finally, the experiments were simulated with only a quarter section of the specimen modelled, applying symmetry conditions.

### 7.1.1 Influence of Element Size

To investigate the influence of mesh density, three different meshes were used. A coarse mesh and a medium sized mesh with uniform mesh density and a refined mesh, with the mesh refined in the centre area. The undeformed meshes are presented in Figures 7.2(a,c,e). On the left and bottom boundaries, symmetry conditions are prescribed. On the top boundary, the displacements are prescribed in the tensile direction and suppressed in the transverse direction. It is assumed that this represents the clamping of the real specimen. The model consists of linear triangular membrane elements with one integration point. The out-of-plane displacement is completely suppressed and the temperature is prescribed at all nodes.



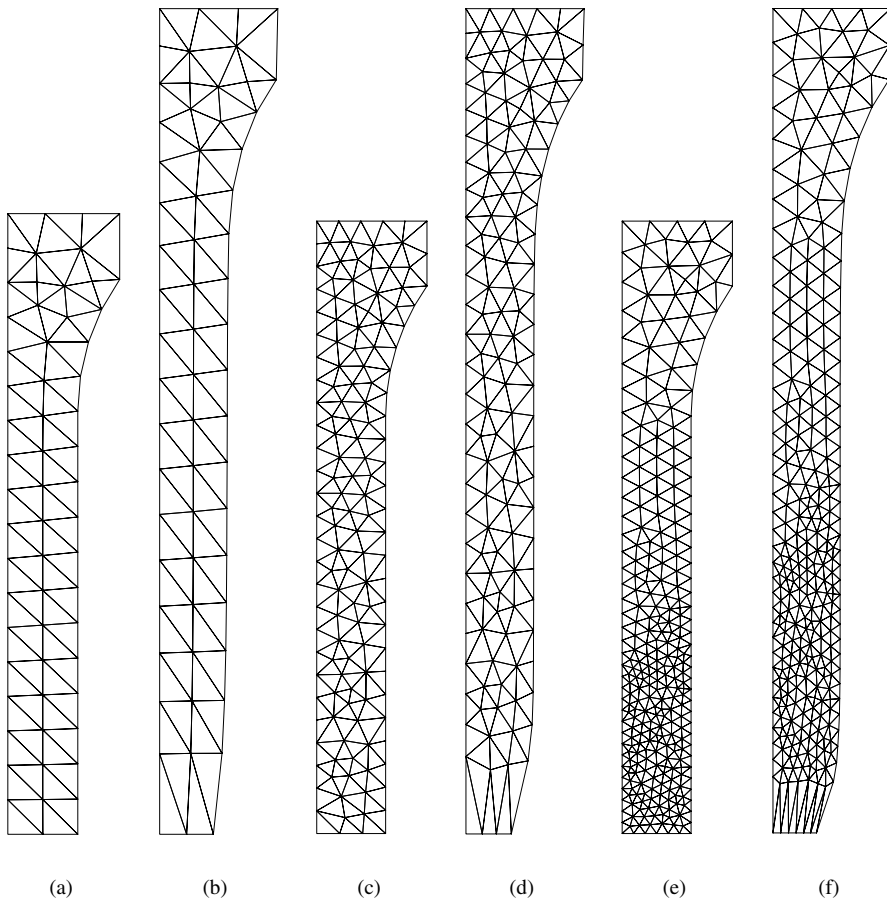


Figure 7.2: Three undeformed finite element meshes of a quarter of the tensile test specimen (a,c,e) and the corresponding deformed meshes at a gauge length elongation of 40% at 25 °C (b,d,f).

In the finest mesh, the smallest element edges have a size of approximately 1 mm. This is of the same order as the sheet thickness. Further refinement in the plane would not be consistent with the assumptions of the membrane element, *viz.* the plane stress condition and negligible out-of-plane shear strain.

Often, these types of tests are modelled with a mesh covering only the uniform part of the specimen and a small initial imperfection to trigger strain localisation. In order to study the influence of an initial imperfection, simulations were performed with and without imperfection. The imperfection consists of an initial groove, comparable to the M–K analysis. In these cases the nodes at the bottom of the model were given a thickness of 1.15, *i.e.* 96% of the nominal thickness. Because of the modelling of the clamping area

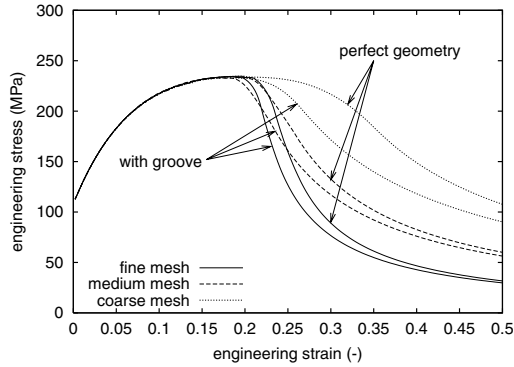


Figure 7.3: Flow curves for meshes with and without initial imperfection at 25 °C.

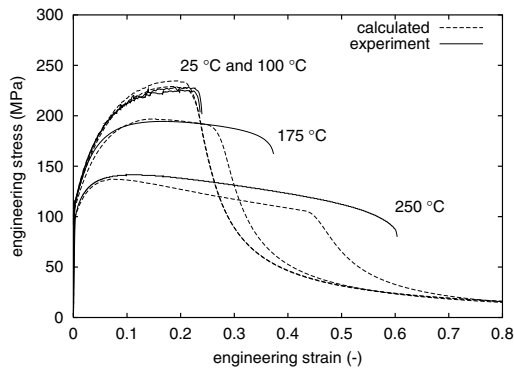


Figure 7.4: Flow curves for experiments and fine meshes for  $\dot{\epsilon} = 0.02 \text{ s}^{-1}$ .

and the applied boundary conditions, even the models without imperfection localised in the centre of the specimen. For a temperature of 25 °C and a strain rate of  $0.02 \text{ s}^{-1}$ , the resulting geometries are presented in Figures 7.2(b,d,f). The corresponding flow curves are presented in Figure 7.3. In Figure 7.4 the numerical results are compared with experiments. The experimental and numerical flow curves were determined for a gauge length of 50 mm.

The material parameters were determined by fitting to the experimental data up to the maximum tensile force for four temperatures and two strain rates simultaneously. Therefore, the flow curves of the simulations and the experiments agree well in the range that was used for fitting. After the load maximum, the results from the coarse mesh only show a gradual decrease in load and it is not obvious from the flow curves that localisation has started. The medium and refined meshes show a clear, sudden load drop, indicating localisation. The localisation is also very clear in plots of the deformed mesh (Figures 7.2(d,f)). After the onset of localisation, the results become mesh dependent and cannot be used quantitatively. The meshes with imperfection localise at lower strains than the meshes with perfect geometry.

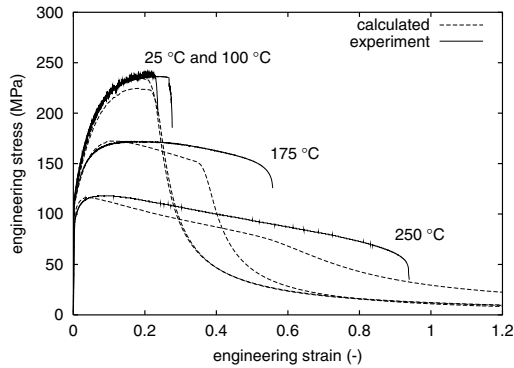


Figure 7.5: Flow curves for experiments and fine meshes for  $\dot{\epsilon} = 0.002 \text{ s}^{-1}$ .

This is consistent with the results for the Marciniak–Kuczynski analysis in Chapter 5. The models with imperfection generally show necking at too low strains. Therefore, comparisons for different temperatures are made for element models without an initial groove.

### 7.1.2 Influence of Temperature and Strain Rate

In Figures 7.4 and 7.5 experimental and numerical flow curves are presented for strain rates of  $0.02 \text{ s}^{-1}$  and  $0.002 \text{ s}^{-1}$  and several temperatures. At  $25^\circ\text{C}$  and  $100^\circ\text{C}$  the strain at localisation is in agreement with the experiments. At these temperatures, the stress hardly depends on the strain rate at all and the specimen necks when the maximum engineering stress is reached. At temperatures above  $130^\circ\text{C}$ , the deformation remains reasonably stable, even beyond the uniform strain. This is attributed to the stabilising effect of strain rate sensitivity. At a strain rate of  $0.02 \text{ s}^{-1}$  and temperature of  $175^\circ\text{C}$ , the calculated stress–strain curve follows the experimentally obtained curve well beyond the maximum stress. Yet, numerical localisation starts earlier than observed in the experiments. At a temperature of  $250^\circ\text{C}$ , the numerical curve already deviates before the maximum stress is reached. Still, the slope of the curve at higher strains resembles the experimental one quite well. Again, final localisation is numerically predicted before the experimental necking strain. Note, however, that for determination of the material parameters, only strains up to the maximum stress were used. At  $250^\circ\text{C}$ , the calculated localisation strain is four times higher.

At a strain rate of  $0.002 \text{ s}^{-1}$ , the results are similar. The predicted stress–strain curves are good up to the maximum stress and necking is predicted correctly at  $25^\circ\text{C}$  and  $100^\circ\text{C}$ . At this strain rate, the strain rate sensitivity is higher than at high strain rates. Indeed, at  $175^\circ\text{C}$  and  $250^\circ\text{C}$ , necking is postponed compared to a strain rate of  $0.02 \text{ s}^{-1}$ . Again, the final necking strain is underestimated. For the simulation at  $250^\circ\text{C}$  and  $\dot{\epsilon} = 0.002 \text{ s}^{-1}$ , localisation did not occur in the centre area but halfway between the centre and the fillet area. This leads to a more diffuse neck and the localisation cannot clearly be identified in the stress–strain curve. In a deformation plot, however, localisation can easily be seen. The softening slope before necking in the  $250^\circ\text{C}$  experiment and in the numerical prediction

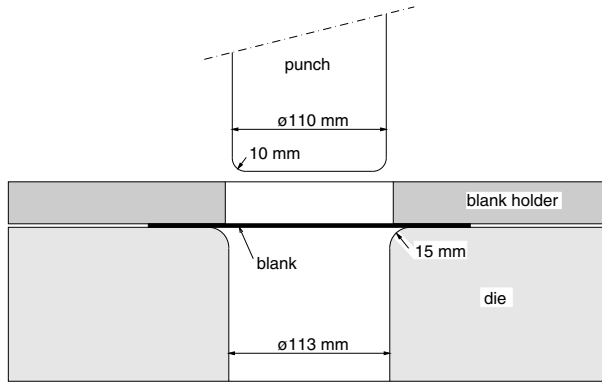


Figure 7.6: Dimensions of the tools for cylindrical deep drawing.

agree well, although the stress level is too low.

The trends that are important for warm forming can be predicted with the current material model. Stress–strain curves up to the maximum stress are predicted accurately because the experiments were used to fit the material parameters. Beyond the maximum stress the predicted curves depend on the modelling of the strain rate sensitivity. The calculated strains at elevated temperatures are much higher than the strains on which the material parameters were fitted. Furthermore, the experimentally observed necking strain shows a variability of 5–10% of their mean values. Regarding this, the predictions are found to be in reasonable agreement with experiments. Improvements can be expected from a more accurate modelling of the strain rate sensitivity of the material.

## 7.2 Cylindrical Cup Deep Drawing

In this section, experiments and simulations are presented for deep drawing of cylindrical cups. Three experiments with the die and blank holder at room temperature and at elevated temperatures were analysed numerically. The punch was kept at room temperature. An illustration of the maximum achieved cups heights for drawing with the flange at room temperature and 250 °C, was already presented in Figure 1.1. There, the drawing ratio was increased to 2.6 for the 250 °C case. In the simulated experiments, the drawing ratio was fixed at 2.09. For this ratio, cups could be drawn at all temperatures, without failure, and the influence of the flange temperature on the punch force and wall thickness can be compared.

First the experimental setup is described, followed by simulations with an axisymmetric model. Finally, simulations with a shell element model are presented.

### 7.2.1 Experiments

Experiments were performed with a tool set of which the dimensions are given in Figure 7.6. All experiments were performed with blanks of 230 mm diameter that were taken from the AA 5754-O sheet of 1.2 mm thickness that is used throughout this thesis. In the experiments,

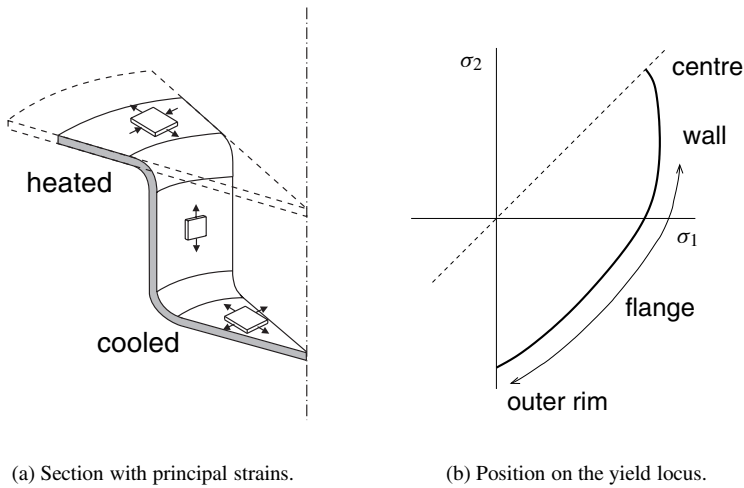


Figure 7.7: Stress states in deep drawing of a cylindrical cup.

the effective punch stroke was 80 mm and the punch velocity 2 mm/s. The die and the blank holder were given a temperature of 25 °C, 175 °C and 250 °C, while the punch was kept at 25 °C. The die and blank holder were heated with internal heat rods, and the punch was cooled with water through internal channels. Thermocouples were used to measure the temperatures of the punch and die. The blank holder force was 25.5 kN, equivalent to an initial pressure of 1.0 MPa on the contact area. The sheet was lubricated with a water based lubricating paste, which still gave sufficient lubrication at 250 °C. With this configuration, cups could be drawn without failure at all three temperatures.

The friction between tool and workpiece is one of the least known factors in the simulations. For this combination of materials and lubricant, a friction coefficient of 0.06 was measured experimentally at room temperature. At temperatures above 150 °C, the friction coefficients varied between 0.12 and 0.18 in different experiments. In the deep drawing process, the contact and friction conditions can be different than in the friction test, due to a locally different geometry and normal pressure.

During deep drawing, the force–displacement curve of the punch was recorded. After the experiments, the cups were removed and the thickness distribution from the centre to the outer diameter in the rolling direction was measured. The force–displacement curve and the thickness data will be used to validate the simulations.

The directions of the principal strain rates during the deep drawing process are schematically given in Figure 7.7(a). Three deformation zones can be distinguished: the flange, the wall and the bottom of the cup. In the flange we see extension in the radial direction and compression in the circumferential direction. This is typically represented by the left-hand side of an FLD. At the outer blank radius, the stress state is uniaxially compressive in the circumferential direction. Towards the die hole, this changes through pure shear and uni-

axial tension in the radial direction to plane strain deformation. In the wall a plane strain situation exists, because the radius of the cylindrical part is constant. In the bottom of the cup, the deformation is in biaxial extension, which is typically represented by the right-hand side of an FLD. Because of symmetry the deformation in the bottom is mainly equi-biaxial, with only a deviation due to planar anisotropy. In Figure 7.7(b), the corresponding positions on the yield locus are denoted in the principal stress space.

In order to draw the material into the die, the material in the flange must deform heavily. The force that is necessary to deform the material is exerted by the punch on the bottom of the cup, mainly near the punch radius. The force is transmitted through the cup wall to the flange. Failure often occurs near the punch radius, when the material cannot withstand the punch force. The resistance to deformation in the flange area decreases by increasing the temperature. As a result, the punch force will decrease. In the potential failure area, near the punch radius, the blank is cooled and is therefore relatively stronger. This is the reason why the deepest cups can be made by heating the die and blank holder, and cooling the punch. Heating of the complete blank would reduce the drawing force, but would also decrease the strength in the critical area.

### 7.2.2 Axisymmetric Simulations

Since the geometry and loading are axisymmetric, and the material is nearly planar isotropic, a first series of simulations was performed with axisymmetric continuum elements. With this two-dimensional model a relatively quick analysis is possible. This has the advantage that many simulations can be performed to investigate the influence of several parameters. A drawback is that the Vegter yield function cannot be used, because it is defined in the plane stress space. Therefore, in this section, a Von Mises yield function is applied. In Section 7.2.3 shell elements are used and a comparison between the results with Von Mises and Vegter yield functions will be made.

The experiments are simulated with the extended Nadai and the Bergström hardening models, described in Section 3.4. A model with 4 node constant dilatation axisymmetric continuum elements is used for the simulation of the deep drawing experiments. The sheets of 1.2 mm thickness are modelled with 2 elements in the thickness direction and an initial element size of 1 mm in the radial direction. In Figure 7.8 the undeformed mesh and the deformed mesh after 20, 40, 60 and 80 mm punch displacement are plotted. A temperature dependent friction coefficient was used. Unless stated otherwise, the value of the friction coefficient was 0.06 below 90 °C, 0.12 above 110 °C and linearly interpolated in between.

A preliminary analysis was performed with the FEM program MSC.MARC, with the extended Nadai material model implemented as a user routine. In this model a part of the punch, die and blank holder was also modelled, including the heat rods and cooling channels. These analyses showed that the sheet in contact with the punch or the die and blank holder acquires the temperature of that tool very rapidly. The die shoulder and punch radius showed only a small cooling and heating respectively, during the analysis. Subsequent analyses were therefore performed with rigid tools, with a prescribed temperature. Only the deformable blank was modelled with finite elements. The simulations were performed with the in-house code DIEKA.

In Figures 7.9 and 7.10, the force–displacement diagrams of the punch and the thick-

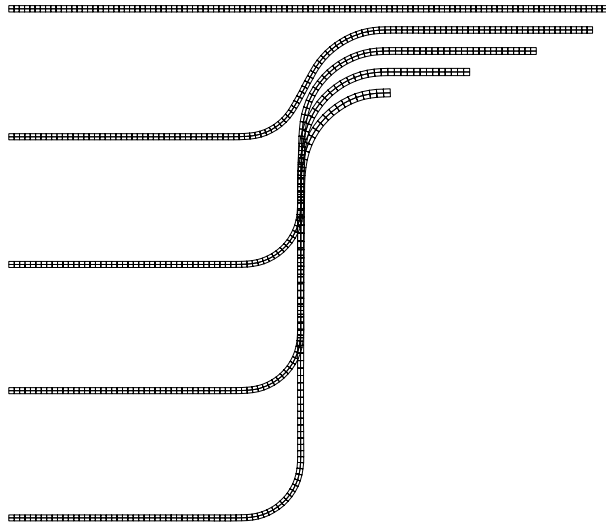


Figure 7.8: Initial and deformed mesh with axisymmetric elements, after 20, 40, 60 and 80 mm punch displacement (shifted 4 mm each, to view the draw-in of the flange).

ness distributions of the cup at a depth of 80 mm are plotted for the experiments and the simulations with the extended Nadai and Bergström models, respectively.

In the extended Nadai model the flow stress depends directly on the equivalent strain, strain rate and temperature. In the Bergström model an evolution equation for the dislocation density is solved. As a result, the Nadai model shows a stress jump upon a strain rate change, while the Bergström model will reach the flow curve of the new strain rate only after some additional strain. The same arguments hold for a change in temperature. In the simulation of the deep drawing experiments the strain rate and temperature are not constant. It is therefore expected that this difference will influence the results.

Comparing the different punch force–displacement curves, it can be seen that both numerical models underestimate the maximum punch force. The underestimation is more severe with the Bergström model than with the extended Nadai model. The direct influence of strain rate changes in the extended Nadai model leads to a less stable analysis. The wiggles in the numerical curves of the Nadai model are due to not fully converged increments. The trends with changing temperature are predicted well, but the difference between 25 °C and 175 °C is overestimated with the extended Nadai model. The relatively small difference in punch force between 25 °C and 175 °C is due to the increasing friction coefficient around 100 °C.

The influence of the temperature on the thickness after the 80 mm punch stroke is most pronounced in the bottom of the cup. In the simulations, the thickness reduction in the bottom of the cup is too high with both hardening models. The Bergström model performs better than the extended Nadai model. This can be related to the lower punch force prediction of the Bergström model.

In the deep drawing experiments the friction between tool and workpiece is difficult

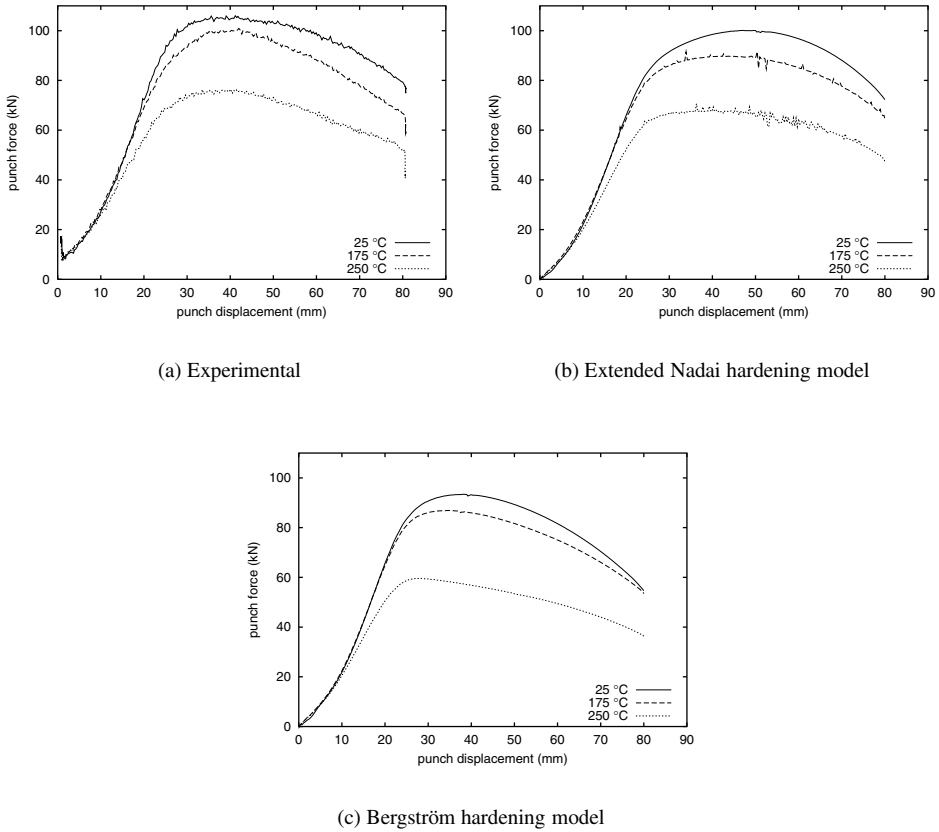


Figure 7.9: Punch force–displacement curves.

to assess. Friction tests at room temperature showed a friction coefficient of 0.06, which is lower than the value of 0.12, that is commonly used based on simulation experience. Experiments at high temperatures showed values varying between 0.12 and 0.18, both for a temperature of 175 °C and 250 °C. To investigate the influence of the friction on the force–displacement curve and the thickness prediction, a parameter study was performed for a flange temperature of 175 °C. In Figure 7.11 the influence of friction on the punch force is shown for an analysis with the Bergström model. In three analyses, the friction coefficient below 90 °C,  $\mu_l$ , was kept at 0.06, but the friction coefficient above 110 °C was subsequently set to 0.06, 0.12 and 0.18. A linear interpolation was used between these temperatures. With a friction coefficient of 0.18 the calculated punch force–displacement diagram resembles the experimental one quite well. As a result of the increased friction, however, the predicted thickness strain deteriorates even more (see Figure 7.12).

As an alternative parameter set, the friction coefficient for all tool blank contact was set



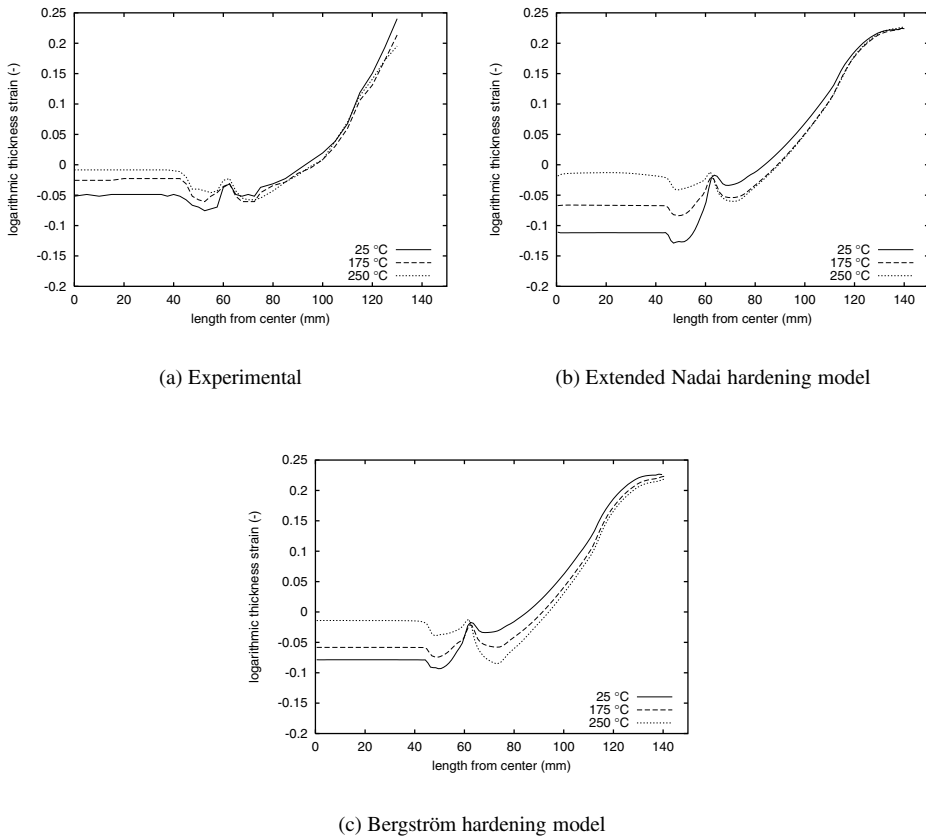


Figure 7.10: Thickness distributions.

at 0.12. This is compared with the original set with a friction coefficient of 0.12 between die and blank and blank holder and blank and a friction coefficient of 0.06 between punch and blank. Interestingly, increasing the punch–blank friction has almost no effect on the punch force–displacement curve. The predicted thickness of the bottom area, however, improves considerably, while the predicted thickness in wall and flange hardly changes. This shows that the friction conditions are significant parameters in the simulation and the current uncertainties should be resolved.

Another reason for the overestimation of the thickness strain may be the adoption of an isotropic Von Mises yield surface. The yield surface of aluminium in the principal stress space has a much more corner-like shape in the equi-biaxial area. In the next section a 3D shell element model is used to investigate the influence of the yield function.

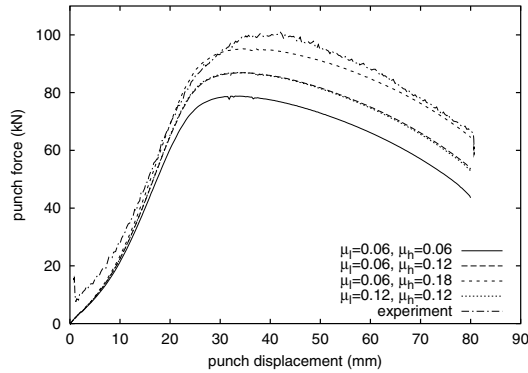


Figure 7.11: Punch force–displacement curves for different friction coefficients.

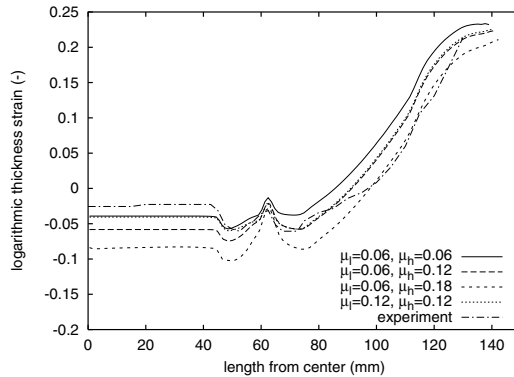


Figure 7.12: Thickness distributions for different friction coefficients.

### 7.2.3 Shell Element Simulations

Only few industrial applications can be modelled with axisymmetric elements—in general 3D models are required. For sheet forming, large scale analysis is currently only feasible with shell elements. To compare the results from shell element simulations with axisymmetric simulations, the deep drawing of cylindrical cups is now modelled with shell elements.

Orthotropic symmetry was assumed for the material model. A quarter of the blank was modelled and boundary conditions were applied on the displacement and rotation degrees of freedom to represent the symmetry. Two finite element meshes were used: a coarse mesh with 934 discrete Kirchhoff triangular shell elements and a fine mesh with 3716 elements. The size of a typical element edge is 5 mm in the coarse model and 2.5 mm in the fine model. First, the coarse mesh was used to investigate the influence of the yield locus on the deformation at room temperature. Then, with the coarse mesh, the same simulations were performed as with the axisymmetric model at elevated temperatures. Finally, the fine mesh

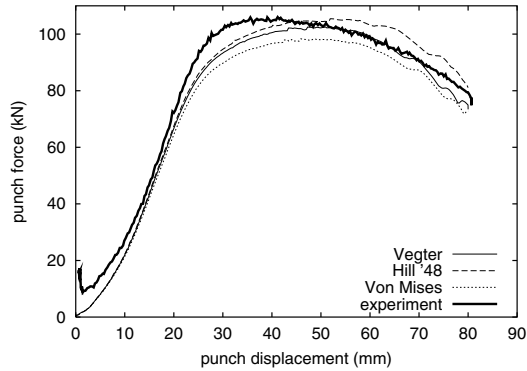


Figure 7.13: Punch force–displacement diagrams at 25 °C with shell elements.

was used to check the results of the coarse analysis upon mesh refinement and to apply the solution strategy with iterative solvers presented in Section 6.5 to a thermo-mechanically coupled analysis.

### Influence of the Yield Locus

To investigate the influence of the yield locus on the analysis results, simulations were performed with three different yield loci. To exclude the influence of temperature and rate dependent material behaviour, a simple rate independent Nadai hardening model was used, representing the room temperature stress–strain curve. With the coarse mesh, an analysis was run with a Von Mises, Hill '48 and Vegter material model. The same  $R$ -values were used for the Hill '48 and the Vegter models. For the friction coefficient a fixed value of 0.06 was used.

In Figure 7.13 it can be seen that the punch force–displacement curve for the Von Mises model is lower than for both other material models. This is attributed to the lower shear factor as presented in Table 3.2. The material deformation takes place mainly in the flange area, and in this area shear deformation dominates. Hence a lower shear factor will result in a lower punch force.

In Figure 7.14, the prediction of the wall thickness is presented. On the horizontal axis, the arc-length is given starting at the outer radius in the transverse direction, going to the centre, continuing to the outer radius in the rolling direction and returning to the transverse direction along the outer radius. All simulations predict too much thinning at the bottom of the cup, but the Hill '48 model performs notably badly. This can be attributed to the poor representation of the equi-biaxial stress by the Hill '48 model. Experiments show an equi-biaxial factor of 1.02, but the Hill '48 model predicts a factor of 0.927. This is a result of the low  $R$ -values for aluminium and the basic shape of the Hill '48 yield locus.

At the bottom of the cup an equi-biaxial stress state dominates, as shown in Figure 7.7. Hence, a too low equi-biaxial flow stress will result in too much plastic strain at the bottom and therefore too thin a product. The Von Mises model and the Vegter model (with the same  $R$ -values as the Hill '48 model) perform better. The remaining difference with the

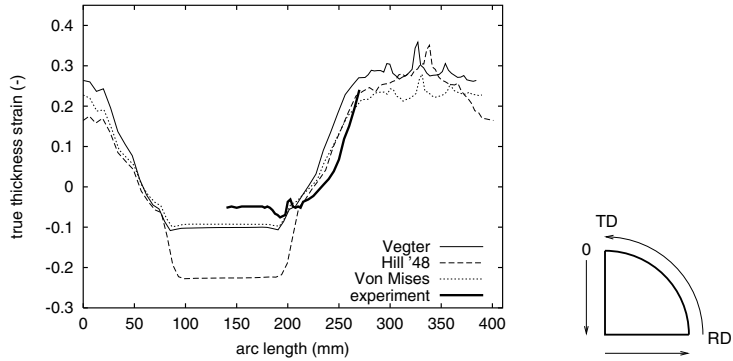


Figure 7.14: Thickness distributions at 25 °C with shell elements.

measured thickness is still quite large and should be investigated further.

It should be noted here that *not* just the anisotropy, but specifically the *shape* of the yield locus is important. This is the origin of the so-called anomalous behaviour of aluminium. The stress in the bottom is mainly determined by the force needed to deform the flange area. In the flange area, the stress state can be characterised by the pure shear yield stress. Therefore, the ratio between equi-biaxial yield stress and pure shear yield stress is a better indicator for deep drawability than the commonly used  $R$ -value. If the yield locus is reasonably well described by the Hill '48 model—as for steel—the  $R$ -value and the equi-biaxial/pure shear yield stress ratio correlate quite well, but for aluminium this is not the case. Unfortunately, the equi-biaxial yield stress and pure shear yield stress are much more difficult to determine experimentally than the  $R$ -values.

In the flange, at an arc length of between 250 mm and 380 mm, some wrinkles develop between the die and the blank holder. This results in extreme local thickness variations with all material models. The wrinkles are, however, initiated numerically by the relatively large elements sliding over the die radius. In the simulation with the refined mesh they disappear.

### Comparison between Axisymmetric and Shell Element Analysis

In Figures 7.15 and 7.16, the predicted force–displacement curves and thickness distributions from the axisymmetric and the shell element meshes are compared. In the axisymmetric models a Von Mises yield function is used and in the shell element models a Vegter yield function is used. For both sets of simulations, the temperature and rate dependent Bergström hardening model is used. The differences between the axisymmetric model and shell element model are relatively small. The thickness strains in the bottom of the cup are similar, but a thicker flange and cylindrical part is predicted with the shell model than with the axisymmetric model. A possible explanation is that the blank holder force leads to a compressive normal stress in the model with axisymmetric continuum elements, whereas in the shell element model the normal stress remains zero by definition. Although the normal stress is small (order of 1 MPa) this may lead to an additional thickness reduction that is

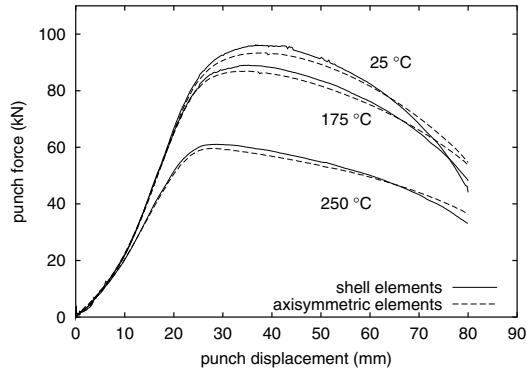


Figure 7.15: Punch force–displacement diagrams with axisymmetric and shell elements.

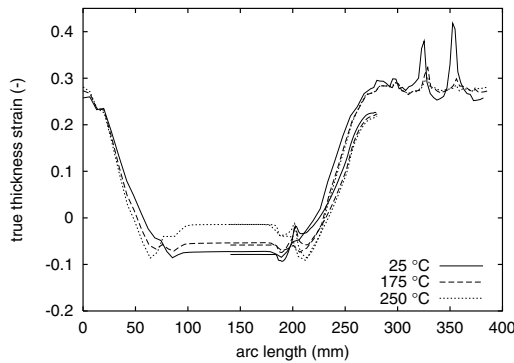


Figure 7.16: Thickness distributions with axisymmetric and shell elements (axisymmetric results start at 140 mm).

not represented in the shell element model. For all temperatures, two numerically induced wrinkles appear at the same positions in the flange, leading to locally increased thickness when they are compressed between the die and the blank holder.

### Dynamic Regularisation

The simulations with the coarse mesh were repeated with a fine mesh. With the fine mesh, convergence on mesh refinement can be checked as well as the effectiveness of dynamic regularisation—as presented in Section 6.5—for thermo-mechanical analyses. The fine mesh contains 3716 shell elements and 7432 contact elements, resulting in 13311 independent degrees of freedom. The global convergence criterion was set to 0.5% relative unbalance force. In the simulations displacement increments of 0.1 mm were used, after a start-up phase with smaller increments. Convergence could only be reached by adding inertial forces to the simulation. A mass scaling factor of  $2.6 \cdot 10^7$  was used. This extremely

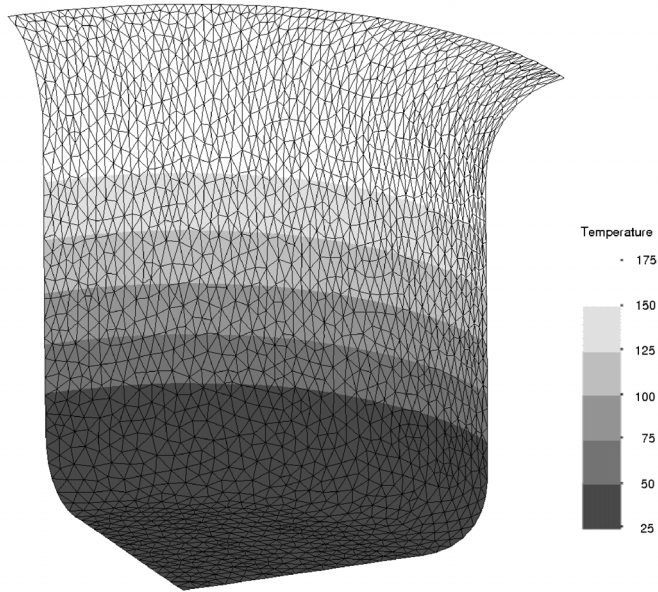


Figure 7.17: Calculated temperature distribution for a fine mesh and die temperature of 175 °C.

large factor is a consequence of the very low punch velocity of 2 mm/s. Compared to the simulations presented in the previous chapter, the mass scaling is equivalent to increasing the punch velocity to 10 m/s, which did not show much influence on the results. Because the material behaviour is strain rate dependent in the current simulation, the mass is scaled and not the velocity. Mass scaling is only applied to the dynamic contribution and not to the thermal capacity. As explained in Chapter 6, the goal of mass scaling is to improve the efficiency of iterative solvers. The final mesh geometry and temperature distribution is plotted in Figure 7.17.

In Figure 7.18 force–displacement curves for the fine and coarse meshes are compared. The coarse mesh was analysed without dynamics contribution and the fine mesh with dynamics and a large mass scaling. Apart from some instabilities in the solution process for the fine mesh, no significant difference is observed between results for the coarse and the fine meshes. In Figure 7.19 the predicted thickness distribution for the fine mesh is presented. It should be compared with Figure 7.16. In the coarse mesh, the punch radius is discretised with approximately three element edges and in the fine mesh with six. The thickness variation near the punch radius is therefore predicted more smoothly with the fine mesh. In the 25 °C analysis, the fine mesh predicts a slightly thinner cup bottom than the coarse mesh. At 175 °C and 250 °C, the bottom thickness hardly differs between the two meshes. The predicted thickness in the flange does not show the two peaks that were apparent in Figure 7.16. The nominal thickness prediction in the flange is similar to the results of the coarse mesh, but because of a smoother discretisation in the die radius region ‘numerical’ wrinkles are no longer induced. For a general prediction of punch force and wall thickness,

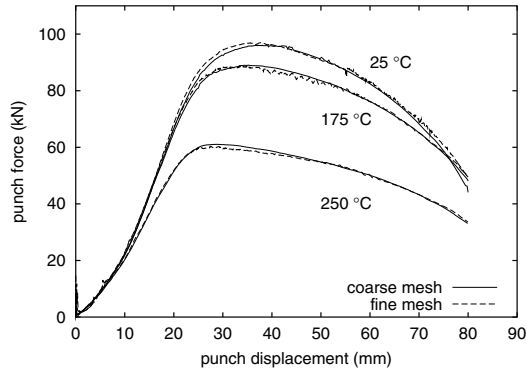


Figure 7.18: Punch force–displacement diagrams for coarse and fine shell element meshes.

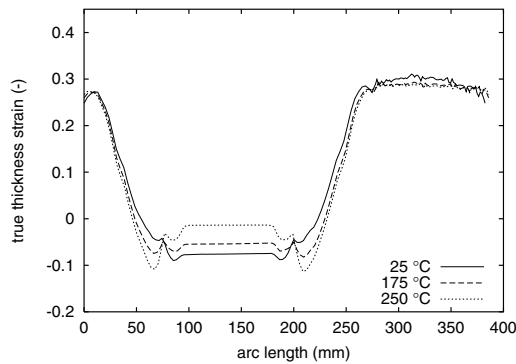


Figure 7.19: Thickness distributions for a fine shell element meshes after 80 mm punch displacement.

the coarse mesh seems to be accurate enough.

The BiCGSTAB solver with SSOR preconditioner typically needed 30 to 70 iterations to determine the iterative displacements within the Newton–Raphson process. On a Compaq-alpha processor that took 2–5 s. The solution by a direct skyline solver on the same machine took 55 s. We thus conclude that the efficient solution strategy presented in Section 6.5 for isothermal calculations is also applicable to the warm forming process. The mechanical and thermal part of the equations are not strongly coupled and, since no out-of-plane gradients are considered, the thermal part is effectively a 2D analysis. Apart from the initial heating phase, the mechanical unbalance forces determine the global convergence. Evidently, the BiCGSTAB solver with SSOR preconditioner is able to solve the coupled mechanical and thermal equations efficiently. As demonstrated in the previous chapter this is a prerequisite for a large scale analysis of sheet forming processes with implicit finite element solution algorithms.

### 7.3 Conclusion

The simulations of the uniaxial tensile tests show that the initiation of strain localisation can be predicted with a shell element model. At room temperature the predicted failure strain corresponds to the experimental ultimate strain. With a perfect specimen, a numerical neck develops, perpendicular to the tensile direction, while in the experiments an inclined neck appears. When a small numerical imperfection is added, the simulations also show an inclined neck.

At elevated temperatures, the material model is less accurate than at room temperature. This has a large effect on the predicted localisation strain. Regarding the accuracy of the material model, the predicted localisation strain agrees reasonably well with the experiments.

From the presented simulations of the cylindrical cup deep drawing, it can be concluded that the shape of the yield locus has an important effect on the calculated punch force–displacement curve and most notably on the predicted thickness distribution. The anisotropy in the material, modelled with the  $R$ -values, is less important than the ratios between equibiaxial, plane strain, uniaxial and pure shear yield stresses. This was demonstrated by the large difference between the results for the Hill '48 and the Vegter models, that both used the same  $R$ -values.

Even with a 'correct' description of the yield locus using the Vegter model, the calculated thickness reduction at the bottom of the cup is too high. The results can be improved by adapting the friction coefficients. However, the coefficients used were obtained by friction tests, and a pragmatic adaptation in order to obtain better correspondence with some measured results is not very satisfactory. We recommend that the friction be investigated in more detail.



## 8. Conclusions and Recommendations

In this thesis, the numerical modelling of warm forming of aluminium sheet is presented. The most important aspects for simulation of the warm forming process are the material model, the thermo-mechanical finite element model, the prediction of necking and an efficient solution of the resulting equations. In this chapter, conclusions from the research are drawn and recommendations are presented for future research.

### Material Modelling

An important difference between room temperature forming and warm forming is caused by the strain rate sensitivity of aluminium at temperatures above 100 °C. For high-temperature processes, such as hot-rolling and extrusion, the strain rate determines the stress response and work hardening can be ignored. At low temperatures, work hardening is the determining factor and strain rate sensitivity can be ignored. For warm forming, work hardening and strain rate sensitivity must both be included. Hence, material models for warm sheet forming are more complex than for cold forming or hot forming.

In classical plasticity algorithms, the material model comprises two separate parts: the definition of the yield surface and the work hardening. For simulation of forming processes, the shape of the yield surface determines the resulting strain distribution. For example in deep drawing, often areas with prevailing shear, plane strain and equi-biaxial deformations can be denoted. The ratios between yield stress in shear, plane strain and equi-biaxial deformation determine the mode of deformation. It was demonstrated that the widely used quadratic Hill yield function cannot properly describe the yield surface of aluminium. In the simulation of the deep drawing of a cylindrical cup this resulted in too much thinning of the bottom area. Experiments in simple shear, uniaxial stress, plane strain and equi-biaxial stress indicate a more corner-like plane stress yield locus than the quadratic Hill locus. The shape can also be derived, based on crystal plasticity theory. The experimentally determined yield stresses, supplemented with data from crystal plasticity analysis can readily be used in the Vegter yield function. Using the Vegter model, the thickness distribution from a finite element analysis of cylindrical cup drawing improves considerably, compared to the quadratic Hill model.

The hardening model affects a forming simulation in two ways. Firstly, the tool forces, *e.g.* punch force, are directly influenced by the flow stress. Secondly, in the warm forming process, the ratio between flow stress in the flange and in the product wall determines the strain distribution in the sheet. For an accurate analysis of warm forming, the hardening model must include work hardening, the influence of temperature and strain rate sensitivity.

Two hardening models were used in this thesis, a completely phenomenological model—the extended Nadai model—and a physically based model that considers the evolution of dislocation density—the Bergström model. For constant temperature and strain rate, the Bergström model reduces to the Voce model. The extended Nadai and Bergström models were fitted to the experimental flow curves at different temperatures and strain rates with reasonable success. The Bergström model can describe the experimental curves better than the extended Nadai model.

Large differences between the two hardening models appear when strain rate jumps are modelled. The Bergström model predicts a gradually changing stress along the curve that corresponds to the new strain rate. The extended Nadai model predicts a stress jump. Experimental observations showed a response in between both models when the strain rate was increased. On a strain rate reduction, the stress in the experiments dropped very fast. This is represented better with the extended Nadai model than with the Bergström model. In forming processes, strain rates will usually not be constant, therefore it is recommended to further investigate the modelling of material behaviour at changing strain rates.

The initial yield stress hardly changes up to temperatures of 175 °C and is also independent of strain rate at these temperatures. Above 175 °C the initial yield stress drops and becomes strain rate dependent. This behaviour is contrary to commonly applied relations. Therefore, an instantaneous contribution of strain rate to the stress—the dynamic stress component—is not used in this thesis. The poor prediction of stress–strain curves by the Bergström model for 250 °C and low strain rates is caused by the inaccurate modelling of the initial yield stress. We recommend that the model be improved for the prediction of the initial yield stress.

Some dynamic strain ageing effects can be seen in the experimental results. At 100 °C, a low strain rate yields higher stresses than a high strain rate. This phenomenon is not covered by the current model. In the investigated alloy, this effect is only small, but it can be larger in alloys with a higher magnesium content. Slight improvements in forming simulations may be possible if this effect were incorporated. However, the earlier two recommendations should have a higher priority.

### **Finite Element Modelling**

The warm forming of aluminium sheet necessitates the solution of a thermo-mechanically coupled set of equations. The high conduction coefficient of aluminium and low sheet thickness ensures that the temperature is almost constant across the thickness. Hence, shell elements can be used with only one thermal d.o.f. per node. The gradient in the thickness direction need not be modelled. Because of the large heat capacity of the tools, the temperature of the tools is not much affected by the blank. The stiffness of the tools is also much greater than that of the blank. It is therefore justified to model the tools as rigid contours with prescribed temperatures.

Apart from the temperature dependent material behaviour, the friction also depends on the temperature. If the contact between the tools and the blank is modelled with contact elements, this is readily implemented. Experimental determination of the friction coefficient at elevated temperatures did not give consistent results. A forming simulation will only benefit from improving material models if the modelling of the friction is equally accurate.

We recommend investigating the friction behaviour for sheet forming processes at elevated temperatures.

### Necking

A forming analysis is often used to predict the manufacturability of a product. The prediction of the onset of necking must then be included. Currently, analysis results are often compared with forming limit curves for the material, in order to determine the feasibility of the calculated strains. For warm forming the forming limits clearly depend on the temperature and strain rate and probably also the history of strain, temperature and strain rate. Therefore, the calculated strains cannot be compared with just one FLC.

Failure by necking is a geometric instability. If a proper material model is used, necking can be modelled by a finite element model with shell elements. The material model is absolutely critical. It was shown that small deviations in the hardening model can result in large differences in predicted forming limits. For the investigated Al–Mg alloy, the experimental flow curve can accurately be described by the Bergström hardening model. For low temperature applications the Voce hardening model can be used. In the drawing regime (negative minor strain), the instability point is mainly a function of the hardening rate. In the stretching region (positive minor strain) the instability point depends very much also on the shape of the yield locus.

The advantage of a FEM model is that the boundary conditions are completely incorporated and that the analysis is not restricted to proportional strain paths. The accuracy for non-proportional strain paths depends on the accuracy of the material model for such deformation histories. Currently, the capabilities of material models for non-proportional loading are limited.

In sheet forming simulations, the combination of the Vegter yield function and the Bergström hardening model can give a valuable contribution to the process design. Process forces and strain distributions can be predicted, as well as the onset of necking. For more accurate analyses, the material model should be improved for varying strain rate deformation and non-proportional loading paths.

### Efficiency

For large scale sheet forming simulations explicit time integration schemes are nowadays preferred in industry because of their speed. Implicit schemes with direct solvers require solution times that increase quadratically with the number of nodes for shell element models. Until recently, iterative linear solvers were considered unsuitable for shell element models. It was demonstrated in Chapter 6 that by *not* neglecting dynamic effects, shell element models can be used efficiently with implicit time integration schemes. For large finite element models the analysis time could be reduced by a factor of 10. For quasi-static forming processes, mass scaling or increased punch velocities are required to benefit from this approach. This is also common practice for explicit methods.

Mass scaling can influence the analysis results. It is necessary to determine criteria for allowable scaling factors. Much can be learned from explicit methods. However, the application in implicit methods is more flexible because the time increment can be chosen freely. It is not restricted to a critical time step.



# A. Selected Topics from Tensor Algebra

In this appendix some topics of tensor algebra are discussed that are used in the main text. First tensor functions and specifically the exponential and logarithmic tensor functions are defined and slightly elaborated. Then some examples from continuum mechanics are worked out in Cartesian components. A detailed introduction on tensor algebra and its application in mechanics can be found *e.g.* in Malvern (1969); Crisfield (1997); Bonet and Wood (1997).

## A.1 Functions of a 2nd Order Tensor

Analytical functions that are defined for a real valued scalar can be extended to the domain of 2nd order tensors by using an equivalent Taylor series expansion. For a scalar function  $f(x)$  *e.g.*, this yields

$$f(x) = \sum_{k=0}^{\infty} a_k x^k \quad \text{with} \quad a_k = \frac{1}{k!} \frac{d^k f}{dx^k}(0) \quad (\text{A.1})$$

The corresponding tensor function  $f(\mathbf{A})$  is then defined as

$$f(\mathbf{A}) = \sum_{k=0}^{\infty} a_k \mathbf{A}^k \quad (\text{A.2})$$

where  $\mathbf{A}^k$  is recursively defined by

$$\mathbf{A}^k = \mathbf{A}^{k-1} \cdot \mathbf{A} = \mathbf{A} \cdot \mathbf{A}^{k-1} \quad \text{and} \quad \mathbf{A}^0 = \mathbf{1} \quad (\text{A.3})$$

In components, the power of a tensor is represented by the power of the components matrix  $[\mathbf{A}^k] = [\mathbf{A}]^k$ . If, *e.g.* by a rotation of the coordinate system, the components of the tensor in matrix format are written as  $[\mathbf{A}]' = [\mathbf{Q}]^T [\mathbf{A}] [\mathbf{Q}]$ , with  $\mathbf{Q}$  an orthogonal tensor such that  $\mathbf{Q} \cdot \mathbf{Q}^T = \mathbf{1}$ , it follows that

$$[\mathbf{A}^k]' = [\mathbf{A}]'^k = ([\mathbf{Q}]^T [\mathbf{A}] [\mathbf{Q}])^k = [\mathbf{Q}]^T [\mathbf{A}]^k [\mathbf{Q}] = [\mathbf{Q}]^T [\mathbf{A}^k] [\mathbf{Q}] \quad (\text{A.4})$$

Hence,  $\mathbf{A}^k$ , and therefore also the series expansion  $f(\mathbf{A})$ , have tensor character.

Functions of a symmetric 2nd order tensor can be evaluated in a simplified manner by writing the tensor in a normal representation. A symmetric 2nd order tensor  $\mathbf{S}$  has three real

eigenvalues,  $\lambda_\alpha$ , and three orthogonal eigenvectors  $\mathbf{n}_\alpha$ , and can be written as

$$\mathbf{S} = \sum_{\alpha=1}^3 \lambda_\alpha \mathbf{n}_\alpha \mathbf{n}_\alpha \quad (\text{A.5})$$

Because of the orthogonality of the vectors  $\mathbf{n}_\alpha$  the power of a symmetric tensor simply becomes

$$\mathbf{S}^k = \sum_{\alpha=1}^3 \lambda_\alpha^k \mathbf{n}_\alpha \mathbf{n}_\alpha \quad (\text{A.6})$$

The Taylor series expansion of a scalar function can now be applied directly to the eigenvalues of the symmetric tensor, yielding

$$f(\mathbf{S}) = \sum_{k=0}^{\infty} \left( a_k \sum_{\alpha=1}^3 \lambda_\alpha^k \mathbf{n}_\alpha \mathbf{n}_\alpha \right) = \sum_{\alpha=1}^3 f(\lambda_\alpha) \mathbf{n}_\alpha \mathbf{n}_\alpha \quad (\text{A.7})$$

### The Exponential Function

With the procedure as explained above, the exponential function  $\exp(\mathbf{A})$  can be defined as

$$\exp(\mathbf{A}) = \sum_{k=0}^{\infty} \frac{\mathbf{A}^k}{k!} \quad (\text{A.8})$$

The derivative with respect to time of a function  $\exp(\mathbf{A}t)$ , with time-independent tensor  $\mathbf{A}$  then follows from

$$\frac{d}{dt} \exp(\mathbf{A}t) = \sum_{k=1}^{\infty} \frac{\mathbf{A}^k t^{k-1}}{k-1!} = \mathbf{A} \cdot \left( \sum_{k=0}^{\infty} \frac{\mathbf{A}^k t^k}{k!} \right) = \left( \sum_{k=0}^{\infty} \frac{\mathbf{A}^k t^k}{k!} \right) \cdot \mathbf{A}$$

hence

$$\frac{d}{dt} \exp(\mathbf{A}t) = \mathbf{A} \cdot \exp(\mathbf{A}t) = \exp(\mathbf{A}t) \cdot \mathbf{A} \quad (\text{A.9})$$

It is now easily verified by substitution that the solution of the ordinary differential equation  $\dot{\mathbf{X}} = \mathbf{A} \cdot \mathbf{X}$  is given by

$$\mathbf{X}(t) = \exp(\mathbf{A}t) \cdot \mathbf{X}(0) \quad (\text{A.10})$$

and the solution of  $\dot{\mathbf{X}} = \mathbf{A} \cdot \mathbf{X} + \mathbf{X} \cdot \mathbf{B}$  is given by

$$\mathbf{X}(t) = \exp(\mathbf{A}t) \cdot \mathbf{X}(0) \cdot \exp(\mathbf{B}t) \quad (\text{A.11})$$

The relation between the rotation tensor  $\mathbf{R}$  and the (skew-symmetric) spin tensor  $\mathbf{W}$  can give a geometrical interpretation to (A.10) and thereby suggest alternative ways to calculate  $\exp(\mathbf{W})$  (Crisfield, 1997). For example, if  $\mathbf{W}$  is a constant, skew-symmetric tensor:

$$\exp(\mathbf{W}t) = \mathbf{R}(t) = \mathbf{1} + \frac{\sin \theta}{\theta} \mathbf{W}t + \frac{1 - \cos \theta}{\theta^2} \mathbf{W}t \cdot \mathbf{W}t \quad (\text{A.12})$$

where  $\theta = \frac{1}{2} \|\mathbf{W}\|$ .

### The Logarithmic Function

The logarithmic tensor function is of particular importance for the definition of the logarithmic strain  $\ln \mathbf{U}$ . With (A.7) the logarithm of  $\mathbf{U}$  is defined by

$$\ln \mathbf{U} = \sum_{\alpha=1}^3 \ln \lambda_{\alpha} \mathbf{n}_{\alpha} \mathbf{n}_{\alpha} \quad (\text{A.13})$$

The derivative of  $\ln \mathbf{U}$  with respect to  $\mathbf{U}$  now follows from

$$\frac{\partial \ln \mathbf{U}}{\partial \mathbf{U}} = \sum_{\alpha=1}^3 \frac{d \ln \lambda_{\alpha}}{d \lambda_{\alpha}} \mathbf{n}_{\alpha} \mathbf{n}_{\alpha} \mathbf{n}_{\alpha} \mathbf{n}_{\alpha} = \sum_{\alpha=1}^3 \lambda_{\alpha}^{-1} \mathbf{n}_{\alpha} \mathbf{n}_{\alpha} \mathbf{n}_{\alpha} \mathbf{n}_{\alpha} \quad (\text{A.14})$$

If, and only if, the tensors  $\mathbf{U}$  and  $\dot{\mathbf{U}}$  commute, the derivative with respect to time can be written as

$$\frac{d \ln \mathbf{U}}{dt} = \frac{\partial \ln \mathbf{U}}{\partial \mathbf{U}} : \dot{\mathbf{U}} = \sum_{\alpha=1}^3 \lambda_{\alpha}^{-1} \mathbf{n}_{\alpha} \mathbf{n}_{\alpha} \mathbf{n}_{\alpha} \mathbf{n}_{\alpha} : \sum_{\beta=1}^3 \dot{\lambda}_{\beta} \mathbf{n}_{\beta} \mathbf{n}_{\beta} = \sum_{\alpha=1}^3 \frac{\dot{\lambda}_{\alpha}}{\lambda_{\alpha}} \mathbf{n}_{\alpha} \mathbf{n}_{\alpha} \quad (\text{A.15})$$

It is easily seen that for commuting tensors this result is also represented by the single contraction of  $\mathbf{U}^{-1}$  and  $\dot{\mathbf{U}}$ , hence

$$\frac{d \ln \mathbf{U}}{dt} = \mathbf{U}^{-1} \cdot \dot{\mathbf{U}} = \dot{\mathbf{U}} \cdot \mathbf{U}^{-1} \quad (\text{A.16})$$

The rate of deformation  $\mathbf{D}$  is defined as  $\frac{1}{2}(\mathbf{L} + \mathbf{L}^T)$ . With  $\mathbf{L} = \dot{\mathbf{F}} \cdot \mathbf{F}^{-1}$  and  $\mathbf{F} = \mathbf{R} \cdot \mathbf{U}$ , the rate of deformation follows from

$$\mathbf{D} = \mathbf{R} \cdot \frac{1}{2}(\dot{\mathbf{U}} \cdot \mathbf{U}^{-1} + \mathbf{U}^{-1} \cdot \dot{\mathbf{U}}) \cdot \mathbf{R}^T \quad (\text{A.17})$$

Combining (A.16) and (A.17) shows that, for commuting  $\mathbf{U}$  and  $\dot{\mathbf{U}}$ , the rate of the logarithmic strain  $\ln \mathbf{U}$  is equal to the co-rotational rate of deformation  $\hat{\mathbf{D}}$ :

$$\frac{d \ln \mathbf{U}}{dt} = \mathbf{R}^T \cdot \mathbf{D} \cdot \mathbf{R} = \hat{\mathbf{D}} \quad (\text{A.18})$$

## A.2 2D Polar Decomposition

The deformation gradient  $\mathbf{F}$  can be decomposed into a proper orthogonal tensor  $\mathbf{R}$  and a (symmetric) right stretch tensor  $\mathbf{U}$ :

$$\mathbf{F} = \mathbf{R} \cdot \mathbf{U} \quad (\text{A.19})$$

In two dimensions, the components of  $\mathbf{R}$  and  $\mathbf{U}$  can be calculated explicitly. The tensor  $\mathbf{R}$  represents a rotation with an angle  $\alpha$  along the  $z$ -axis. For a fixed Cartesian coordinate system, the components of  $\mathbf{R}$  and  $\mathbf{F}$  can be represented in matrix format as

$$[\mathbf{R}] = \begin{bmatrix} \cos \alpha & -\sin \alpha \\ \sin \alpha & \cos \alpha \end{bmatrix} \quad [\mathbf{F}] = \begin{bmatrix} F_{11} & F_{12} \\ F_{21} & F_{22} \end{bmatrix} \quad (\text{A.20})$$

$\mathbf{U}$  is calculated using  $\mathbf{U} = \mathbf{R}^T \cdot \mathbf{F}$ :

$$[\mathbf{U}] = \begin{bmatrix} \cos \alpha & -\sin \alpha \\ \sin \alpha & \cos \alpha \end{bmatrix} \begin{bmatrix} F_{11} & F_{12} \\ F_{21} & F_{22} \end{bmatrix} = \begin{bmatrix} U_{11} & U_{12} \\ U_{21} & U_{22} \end{bmatrix} \quad (\text{A.21})$$

With the condition that  $\mathbf{U}$  is symmetric, the angle  $\alpha$  can be determined from  $U_{12} = U_{21}$ :

$$F_{12} \cos \alpha - F_{22} \sin \alpha = F_{11} \sin \alpha + F_{21} \cos \alpha \quad (\text{A.22})$$

Division by  $\cos \alpha$  leads to

$$\frac{\sin \alpha}{\cos \alpha} = \tan \alpha = \frac{F_{12} - F_{21}}{F_{22} + F_{11}} \quad (\text{A.23})$$

$\sin \alpha$  and  $\cos \alpha$  can then directly be found as

$$\begin{aligned} \sin \alpha &= \frac{F_{12} - F_{21}}{\sqrt{(F_{12} - F_{21})^2 + (F_{22} + F_{11})^2}} \\ \cos \alpha &= \frac{F_{22} + F_{11}}{\sqrt{(F_{12} - F_{21})^2 + (F_{22} + F_{11})^2}} \end{aligned} \quad (\text{A.24})$$

There is no need to calculate  $\alpha$  explicitly. After the calculation of  $\mathbf{R}$  the components of the right stretch tensor  $\mathbf{U}$  are given by

$$\begin{aligned} U_{11} &= F_{11} \cos \alpha - F_{21} \sin \alpha \\ U_{12} &= F_{12} \cos \alpha - F_{22} \sin \alpha \\ U_{22} &= F_{12} \sin \alpha + F_{22} \cos \alpha \end{aligned} \quad (\text{A.25})$$

### A.3 Simple Shear

For comparison between simple shear and pure shear deformation, the relation between the simple shear deformation  $\gamma$  and the principal stretches  $\lambda_1$  and  $\lambda_2$  are derived. Simple shear is considered in a 2-dimensional plane, with deformation gradient components

$$[\mathbf{F}] = \begin{bmatrix} 1 & \gamma \\ 0 & 1 \end{bmatrix} \quad (\text{A.26})$$

With (A.24) we then find

$$\sin \alpha = \frac{\gamma}{\sqrt{\gamma^2 + 4}} \quad \cos \alpha = \frac{2}{\sqrt{\gamma^2 + 4}} \quad (\text{A.27})$$

and with (A.25)

$$[\mathbf{U}] = \begin{bmatrix} \frac{2}{\sqrt{\gamma^2 + 4}} & \frac{\gamma}{\sqrt{\gamma^2 + 4}} \\ \frac{\gamma}{\sqrt{\gamma^2 + 4}} & \frac{\gamma^2 + 2}{\sqrt{\gamma^2 + 4}} \end{bmatrix} \quad (\text{A.28})$$



The eigenvalues of  $\mathbf{U}$  represent the principal stretches, they are derived from the characteristic equation

$$\left(\frac{2}{\sqrt{\gamma^2 + 4}} - \lambda\right) \left(\frac{\gamma^2 + 2}{\sqrt{\gamma^2 + 4}} - \lambda\right) - \frac{\gamma^2}{\gamma^2 + 4} = 0 \quad (\text{A.29})$$

or, after some elaboration

$$\lambda^2 - \lambda\sqrt{\gamma^2 + 4} + 1 = 0 \quad (\text{A.30})$$

Solving this equation for  $\lambda$  yields

$$\lambda_{1,2} = \frac{1}{2} \left( \sqrt{\gamma^2 + 4} \pm \gamma \right) \quad (\text{A.31})$$

and solving for  $\gamma$  yields

$$\gamma = \pm \left( \lambda - \frac{1}{\lambda} \right) \quad (\text{A.32})$$

Note that  $\lambda_1\lambda_2 = 1$  or, alternatively,  $\lambda_1 = 1/\lambda_2$ .



## B. Proportional Deformation

### B.1 Proportionality Factors

In this section, a proportional deformation path is defined with respect to the right stretch tensor. One total and two instantaneous proportionality factors are defined.

**Definition B.1** *A deformation path  $\mathbf{F}(t)$  is called proportional if for any time  $t$ , the logarithm of the right stretch tensor  $\mathbf{U}$ , derived from the polar decomposition of the deformation gradient  $\mathbf{F} = \mathbf{R} \cdot \mathbf{U}$ , can be written as  $\ln \mathbf{U}(t) = \alpha(t) \ln \mathbf{U}^*$ .*

If an incremental path is followed in the ‘logarithmic strain space’, every increment

$$\Delta \ln \mathbf{U}_i = \ln \mathbf{U}_i - \ln \mathbf{U}_{i-1} \quad (\text{B.1})$$

can be decomposed into a part in the direction of  $\ln \mathbf{U}^*$  and a part perpendicular to it:

$$\Delta \ln \mathbf{U}_i^{\parallel} = \Delta \beta_i \ln \mathbf{U}^* \quad (\text{B.2a})$$

$$\Delta \ln \mathbf{U}_i^{\perp} = \Delta \ln \mathbf{U}_i - \Delta \beta_i \ln \mathbf{U}^* \quad (\text{B.2b})$$

where

$$\Delta \beta_i = \frac{\Delta \ln \mathbf{U}_i : \ln \mathbf{U}^*}{\|\ln \mathbf{U}^*\|} \quad (\text{B.2c})$$

This leads to the relation for the norm of the increment of  $\ln \mathbf{U}$ :

$$\|\Delta \ln \mathbf{U}_i\|^2 = \|\Delta \ln \mathbf{U}_i^{\parallel}\|^2 + \|\Delta \ln \mathbf{U}_i^{\perp}\|^2 = \Delta \beta_i^2 \|\ln \mathbf{U}^*\|^2 + \|\Delta \ln \mathbf{U}_i^{\perp}\|^2 \quad (\text{B.3})$$

or

$$|\Delta \beta_i| \|\ln \mathbf{U}^*\| = \sqrt{\|\Delta \ln \mathbf{U}_i\|^2 - \|\Delta \ln \mathbf{U}_i^{\perp}\|^2} \quad (\text{B.4})$$

In the case of proportional deformation,  $\Delta \beta_i$  equals  $\alpha(t_i) - \alpha(t_{i-1})$ , and from (B.4):  $\|\Delta \ln \mathbf{U}_i\| = |\Delta \beta_i| \|\ln \mathbf{U}^*\|$ . If the deformation is also monotonic ( $\alpha(t)$  monotonically increasing, and therefore  $\Delta \beta_i$  always positive) then

$$\sum_{i=1}^n |\Delta \beta_i| \|\ln \mathbf{U}^*\| = \alpha(t_n) \|\ln \mathbf{U}^*\| = \|\ln \mathbf{U}(t_n)\| \quad (\text{B.5})$$

Combining (B.4) and (B.5) yields

$$\|\ln \mathbf{U}(t_n)\| = \sum_{i=1}^n \sqrt{\|\Delta \ln \mathbf{U}_i\|^2 - \|\Delta \ln \mathbf{U}_i^\perp\|^2} \quad (\text{B.6})$$

Hence,  $\|\ln \mathbf{U}(t_n)\|$  is equal to  $\sum_{i=1}^n \|\Delta \ln \mathbf{U}\|$  for a proportional deformation path. If the deformation path becomes non-proportional, the norm of the logarithmic strain grows less than the sum of the norm of the logarithmic strain increments. Scaling the difference with the ‘length’ of the strain path  $\sum_{i=1}^n \|\Delta \ln \mathbf{U}\|$  gives a measure for the proportionality of the total deformation path

$$\Lambda_{\text{prop}} = \frac{\|\ln \mathbf{U}(t_n)\|}{\sum_{i=1}^n \|\Delta \ln \mathbf{U}_i\|} \quad (\text{B.7})$$

The proportionality factor  $\Lambda_{\text{prop}}$  equals 1 for a proportional deformation and tends to 0 for a highly non-proportional or non-monotonic deformation.  $\Lambda_{\text{prop}}$  can be interpreted as the ratio between the distance from the starting and the end point and the path length of the deformation in the  $\ln \mathbf{U}$  space. The advantage of this definition of  $\Lambda_{\text{prop}}$  above other obvious choices is that it can be calculated incrementally, without prior knowledge of the final direction of  $\ln \mathbf{U}(t_n)$ .

The current deviation from a proportional path can be defined by the cosine of the angle between the current deformation direction and the current value of  $\ln \mathbf{U}$ :

$$\lambda_{\text{prop},1} = \cos(\Delta \ln \mathbf{U}, \ln \mathbf{U}) = \frac{\Delta \ln \mathbf{U} : \ln \mathbf{U}}{\|\Delta \ln \mathbf{U}\| \|\ln \mathbf{U}\|} \quad (\text{B.8})$$

Another value stems from the idea that, if the current deformation direction had been along a proportional deformation path, then the time derivative of  $\ln \mathbf{U}$  would be the corotational rate of deformation  $\hat{\mathbf{D}} = \mathbf{R}^T \cdot \mathbf{D} \cdot \mathbf{R}$ . The deviation of proportionality can then be defined as

$$\lambda_{\text{prop},2} = \cos(\hat{\mathbf{D}}, \ln \mathbf{U}) = \frac{\hat{\mathbf{D}} : \ln \mathbf{U}}{\|\hat{\mathbf{D}}\| \|\ln \mathbf{U}\|} \quad (\text{B.9})$$

Both  $\lambda_{\text{prop},1}$  and  $\lambda_{\text{prop},2}$  are equal to +1 if the current deformation direction is proportional to the total deformation and equal to –1 on proportional reversal of deformation.

## B.2 Hardening Relations

If a deformation path is proportional and monotonically increasing, total stress–strain relations can be derived for evolution laws. A typical use is the derivation of total stress–strain relations for plastic deformation.

The direction of plastic deformation is perpendicular to the yield surface. Neglecting elastic deformation, the plastic deformation itself must be proportional, hence the position of the current stress at the yield surface must have the same normal direction all the time. For isotropic hardening and a strictly convex yield function this means that the stress path is proportional also. Note that this is not true for Prager-type kinematic hardening.

For proportional deformation paths and isotropic hardening, the ratio between components in the stress tensor and the ratio between components in the strain tensor remain constant:

$$\boldsymbol{\sigma}(t) = \alpha_1(t)\boldsymbol{\sigma}^* \quad (\text{B.10})$$

$$\boldsymbol{\varepsilon}(t) = \alpha_2(t)\boldsymbol{\varepsilon}^* \quad (\text{B.11})$$

For large deformations the logarithmic strain  $\ln \mathbf{U}$  must be used as the strain measure  $\boldsymbol{\varepsilon}$ .

Proper definitions for the equivalent stress and strain must necessarily be first degree homogeneous functions of the stress and strain tensor respectively, therefore

$$\sigma_{\text{eq}}(t) = \alpha_1(t)\sigma_{\text{eq}}^* \quad (\text{B.12})$$

$$\varepsilon_{\text{eq}}(t) = \alpha_2(t)\varepsilon_{\text{eq}}^* \quad (\text{B.13})$$

Any component of  $\boldsymbol{\sigma}^*$  can be related to the reference equivalent stress by  $\sigma_{ij}^* = \xi_{ij}\sigma_{\text{eq}}^*$ , and likewise for the components of the strain tensor  $\varepsilon_{ij}^* = \zeta_{ij}\varepsilon_{\text{eq}}^*$ . For proportional deformation, the factors  $\xi_{ij}$  and  $\zeta_{ij}$  are constant and therefore also (omitting an explicit reference to the time  $t$ )

$$\sigma_{ij} = \xi_{ij}\sigma_{\text{eq}} \quad (\text{B.14})$$

$$\varepsilon_{ij} = \zeta_{ij}\varepsilon_{\text{eq}} \quad (\text{B.15})$$

The values of  $\xi_{ij}$  and  $\zeta_{ij}$  depend on the particular yield function.

Work hardening is commonly defined as a relation between equivalent stress and equivalent strain. With (B.14) and (B.15) the hardening relation can be rephrased for any component of the stress and strain tensors, in case of proportional loading:

$$\sigma_{\text{eq}} = Y(\varepsilon_{\text{eq}}) \quad \Rightarrow \quad \sigma_{ij} = \xi_{ij}Y(\varepsilon_{ij}/\zeta_{ij}) \quad (\text{no summation}) \quad (\text{B.16})$$

For the basic Nadai hardening function this results in a simple relation:

$$\sigma_{\text{eq}} = C\varepsilon_{\text{eq}}^n \quad \Rightarrow \quad \sigma_{ij} = C'\varepsilon_{ij}^n \quad (\text{B.17})$$

where

$$C' = \frac{C\xi_{ij}}{\zeta_{ij}^n} \quad (\text{no summation}) \quad (\text{B.18})$$

For proportional and monotonic deformation, the basic Nadai relation can be applied to any component of the stress and strain tensor. The exponent  $n$  is equal for all components, only the multiplier  $C'$  depends on the direction of deformation and the shape of the yield surface.

### B.3 Diffuse Necking with the Hill '48 Yield Locus and Nadai Hardening model

In this section the diffuse necking criterion (5.12) is elaborated for the planar isotropic Hill '48 yield function according to (3.33) and a Nadai hardening model.

In the formulation of (5.8) the yield function is split in a part  $\varphi$  and  $F$  such that

$$\varphi = \sigma_1^2 + \sigma_2^2 - \frac{2R}{R+1}\sigma_1\sigma_2, \quad \frac{\partial\varphi}{\partial\sigma_1} = 2\sigma_1 - \frac{2R}{R+1}\sigma_2 \quad \text{and} \quad F = \sigma_f^2 \quad (\text{B.19})$$

Substitution of  $\sigma_2 = \alpha\sigma_1$  yields

$$\varphi = \sigma_1^2 \left( 1 + \alpha^2 - \frac{2R}{R+1}\alpha \right), \quad \frac{\partial\varphi}{\partial\sigma_1} = 2\sigma_1 \left( 1 - \frac{R}{R+1}\alpha \right) \quad (\text{B.20})$$

On plastic deformation, the flow stress is equal to the equivalent stress and the plastic work is  $dw^p = \sigma_{\text{eq}} d\varepsilon_{\text{eq}}$ . With the hardening rate  $h = d\sigma_f/d\varepsilon_{\text{eq}}$ , the derivative of  $F$  as function of  $w^p$  becomes

$$F' = 2\sigma_f \frac{d\sigma_f}{dw^p} = 2\sigma_f \frac{d\sigma_f}{d\varepsilon_{\text{eq}}} \frac{1}{\frac{dw^p}{d\varepsilon_{\text{eq}}}} = 2\sigma_f h \frac{1}{\sigma_{\text{eq}}} = 2h \quad (\text{B.21})$$

and the relation between  $\sigma_1$  and  $\sigma_{\text{eq}}$  reads

$$\sigma_f = \sigma_{\text{eq}} = \sqrt{\varphi} = \sigma_1 \sqrt{1 + \alpha^2 - \frac{2R}{R+1}\alpha} \quad (\text{B.22})$$

The condition for instability follows from substitution of (B.21) in (5.12):

$$\frac{h}{\sigma_f} \leq \frac{1 - \frac{R}{R+1}\alpha}{\sqrt{1 + \alpha^2 - \frac{2R}{R+1}\alpha}} \quad (\text{B.23})$$

With (5.10) and for proportional loading, the strain in direction 1 can be written as function of the equivalent strain:

$$\varepsilon_1 = \varepsilon_{\text{eq}} \frac{\sigma_{\text{eq}}}{\sigma_1} \frac{1}{1 + \alpha\beta} = \varepsilon_{\text{eq}} \frac{1}{1 + \alpha\beta} \sqrt{1 + \alpha^2 - \frac{2R}{R+1}\alpha} \quad (\text{B.24})$$

For the Nadai hardening function  $\sigma_{\text{eq}} = C\varepsilon_{\text{eq}}^n$  and the hardening relation becomes  $h = nC\varepsilon_{\text{eq}}^{n-1}$ . The left-hand side of (B.23) becomes  $h/\sigma_f = n/\varepsilon_{\text{eq}}$  and the condition for diffuse necking reads

$$\varepsilon_{\text{eq}} \geq n \frac{\sqrt{1 + \alpha^2 - \frac{2R}{R+1}\alpha}}{1 - \frac{R}{R+1}\alpha} \quad (\text{B.25})$$

For the selected yield function, the ratio  $\beta$  can be expressed in  $\alpha$ :

$$\beta = \frac{\frac{\partial\varphi}{\partial\sigma_2}}{\frac{\partial\varphi}{\partial\sigma_1}} = \frac{2\sigma_1 \left( \alpha - \frac{R}{R+1} \right)}{2\sigma_1 \left( 1 - \frac{R}{R+1}\alpha \right)} = \frac{\alpha - \frac{R}{R+1}}{1 - \frac{R}{R+1}\alpha} \quad (\text{B.26})$$

hence

$$1 + \alpha\beta = 1 + \frac{\alpha^2 - \frac{R}{R+1}\alpha}{1 - \frac{R}{R+1}\alpha} = \frac{1 + \alpha^2 - \frac{2R}{R+1}\alpha}{1 - \frac{R}{R+1}\alpha} \quad (\text{B.27})$$

Substitution of this result in (B.24) and subsequently in (B.25) yields that deformation is unstable for

$$\varepsilon_1 \geq n \quad (\text{B.28})$$

## C. Yield Locus Parameters

In this appendix, characteristic values for the determination of the yield locus are presented. The main characteristics are the ratios between the yield stress for an equi-biaxial, plane strain or pure shear test and a uniaxial test ( $f_{bi}$ ,  $f_{ps}$  and  $f_{sh}$ ). These values are determined for the tensile direction inclined at  $0^\circ$ ,  $45^\circ$  and  $90^\circ$  with respect to the rolling direction. The ratio between the uniaxial yield stress in the  $45^\circ$  direction or  $90^\circ$  direction and the  $0^\circ$  direction, and the ratio between the stress in the tensile direction and the stress in the transverse direction in a plane strain test are two other characteristic values. Three strain ratios determine the direction of the yield locus. The ratio between strain in the width and thickness directions is given by the  $R$ -value. The ratio between the transverse strain and the main tensile strain in a pure shear test and an equi-biaxial test are given by  $(\varepsilon_2/\varepsilon_1)_{sh}$  and  $(\varepsilon_2/\varepsilon_1)_{bi}$ . For a specimen with orthorhombic symmetry—as is usually assumed for a rolled sheet—the mechanical behaviour in the  $-45^\circ$  direction should be equal to that in the  $+45^\circ$  direction.

### Experiments

The experimentally determined values were obtained by uniaxial, plane strain, simple shear and normal compression tests. The stress ratios were derived by fitting the first 5% strain of the stress–strain curve to each other. In this way, no difference is found with respect to the tensile direction.  $R$ -values and equi-biaxial strain ratios were measured directly on the specimens. The experimental values are presented in Table C.1. With the experimental setup applied here, the plane strain stress ratio and the pure shear strain ratio cannot be determined.

### Polycrystal Calculations

The stress and strain ratios can also be calculated. For this purpose, a viscoplastic full constraints Taylor model was used with a strain rate sensitivity  $m = 0.05$ . A set with 2000 randomly oriented grains was used to test the analysis program and for comparison. For a random texture, the results must be independent from the tensile direction. The plane strain stress ratio should be 0.5, the  $R$ -value and equi-biaxial strain ratio should be 1.0 and the pure shear strain ratio should be  $-1.0$ . From the results in Table C.2, it can be concluded that the strain ratios in the uniaxial and equi-biaxial situation deviate considerably. This is attributed to the high curvature of the yield locus at those points.

Another set of 2000 orientations was derived from the orientation distribution function

of the applied AA 5754-O sheet. The results are presented in Table C.3. Note that the results for the  $+45^\circ$  and  $-45^\circ$  direction are not equal, especially for the  $R$ -value and equi-biaxial strain ratio. For an orthorhombic symmetry, the equi-biaxial strain ratio should be 1.0 in the  $45^\circ$  direction. Clearly, the values that showed to be very sensitive to the local curvature of the yield locus in the isotropic (random texture) case, also show the largest deviations here.

Table C.1: Measured stress and strain ratios for the AA 5754-O sheet.

angle with RD	$0^\circ$	$45^\circ$	$90^\circ$
$(\sigma_1/\sigma_1^{\text{RD}})_{\text{un}}$	1	1	1
$f_{\text{bi}}$	1.02	1.02	1.02
$f_{\text{ps}}$	1.15	1.15	1.15
$f_{\text{sh}}$	0.605	0.605	0.605
$R$ -value	0.85	0.67	0.70
$(\varepsilon_2/\varepsilon_1)_{\text{bi}}$	1.17		0.855

Table C.2: Calculated stress and strain ratios for a random texture.

angle with RD	$0^\circ$	$45^\circ$	$90^\circ$	$-45^\circ$
$(\sigma_1/\sigma_1^{\text{RD}})_{\text{un}}$	1	0.9981	1.0021	1.0036
$f_{\text{bi}}$	0.9997	1.0016	0.9976	0.9961
$f_{\text{ps}}$	1.0934	1.0908	1.0968	1.0970
$f_{\text{sh}}$	0.5481	0.5494	0.5470	0.5464
$(\sigma_2/\sigma_1)_{\text{ps}}$	0.4920	0.4862	0.4969	0.4912
$R$ -value	1.0165	0.9439	1.0102	1.0211
$(\varepsilon_2/\varepsilon_1)_{\text{sh}}$	-1.0001	-1.0005	-1.0000	-0.9995
$(\varepsilon_2/\varepsilon_1)_{\text{bi}}$	0.9756	0.8962	1.0250	1.1159

Table C.3: Calculated stress and strain ratios for the AA 5754-O sheet.

angle with RD	$0^\circ$	$45^\circ$	$90^\circ$	$-45^\circ$
$(\sigma_1/\sigma_1^{\text{RD}})_{\text{un}}$	1	1.0275	0.9617	0.9868
$f_{\text{ps}}$	1.1035	1.0624	1.0772	1.0451
$f_{\text{sh}}$	0.5555	0.5782	0.5776	0.6020
$f_{\text{bi}}$	0.9661	0.9403	1.0046	0.9790
$(\sigma_2/\sigma_1)_{\text{ps}}$	0.4863	0.4675	0.5170	0.4795
$R$ -value	0.9008	0.5269	0.6033	0.3365
$(\varepsilon_2/\varepsilon_1)_{\text{sh}}$	-1.0070	-1.0050	-0.9934	-0.9952
$(\varepsilon_2/\varepsilon_1)_{\text{bi}}$	1.5215	1.5835	0.6573	0.6315



# Bibliography

- Asaro, R. J. and A. Needleman (1985), Texture development and strain hardening in rate dependent polycrystals, *Acta Metallurgica*, vol. 33, pp. 923–953.
- Banabic, D. and E. Dannenmann (2001), Prediction of the influence of yield locus on the limit strains in sheet metals, *Journal of Materials Processing Technology*, vol. 109, pp. 9–12.
- Barret, R., M. Berry, T. F. Chan, J. Demmel, J. Donato, J. Dongarra, V. Eijkhout, R. Pozo, C. Romine and H. van der Vorst (1994), *Templates for the Solution of Linear Systems: Building Blocks for Iterative Methods*, SIAM, Philadelphia, PA, URL <http://www.netlib.org/templates/Templates.html>.
- Bathe, K.-J. (1982), *Finite Element Procedures in Engineering Analysis*, Prentice-Hall.
- Batoz, J. L., K. J. Bathe and L. W. Ho (1980), A study of three-node triangular plate bending elements, *International Journal for Numerical Methods in Engineering*, vol. 15, pp. 1771–1812.
- Batoz, J. L. and P. Lardeur (1989), A discrete shear triangular nine d.o.f. element for the analysis of thick to very thin plates, *International Journal for Numerical Methods in Engineering*, vol. 28, pp. 533–560.
- Beaudoin, A. J., P. R. Dawson, K. K. Mathur, U. F. Kocks and D. A. Korzekwa (1994), Application of polycrystal plasticity to sheet forming, *Computer Methods in Applied Mechanics and Engineering*, vol. 117, pp. 49–70.
- Becker, E. and W. Bürger (1975), *Kontinuumsmechanik*, Teubner, Stuttgart.
- Belytschko, T., W. K. Liu and B. Moran (2000), *Nonlinear Finite Elements for Continua and Structures*, Wiley, Chichester.
- Benzi, M., R. Kouhia and M. Tüma (2001), Stabilized and block approximate inverse preconditioners for problems in solid and structural mechanics, *Computer Methods in Applied Mechanics and Engineering*, vol. 190, pp. 6533–6554.
- Bergström, Y. (1969), Dislocation model for the stress-strain behaviour of polycrystalline  $\alpha$ -Fe with special emphasis on the variation of the densities of mobile and immobile dislocations, *Materials Science and Engineering*, vol. 5, pp. 193–200.
- Bergström, Y. (1983), The plastic deformation of metals—a dislocation model and its applicability, *Reviews on Powder Metallurgy and Physical Ceramics*, vol. 2, pp. 105–115.
- Betten, J. (1993), *Kontinuumsmechanik- Elasto-, Plasto- und Kriechmechanik*, Springer Verlag Heidelberg, Berlin.
- Blaheta, R. (1997), Convergence of Newton-type methods in incremental return mapping analysis of elasto-plastic problems, *Computer Methods in Applied Mechanics and Engineering*, vol. 147, pp. 167–185.

- Blaheta, R. and O. Axelsson (1997), Convergence of inexact Newton-like iterations in incremental finite element analysis of elasto-plastic problems, *Computer Methods in Applied Mechanics and Engineering*, vol. 141, pp. 281–295.
- Bolt, P. J., N. A. P. M. Lamboo and P. J. C. M. Rozier (2001), Feasibility of warm drawing of aluminium products, *Journal of Materials Processing Technology*, vol. 115, pp. 118–121.
- Bolt, P. J., N. A. P. M. Lamboo, J. F. C. van Leeuwen and R. J. Werkhoven (2000), Warm drawing of aluminium components, in: *Proceedings of the 7th Saxon Conference on Forming Technology, Lightweight Construction by Forming Technology*, pp. 101–118, Chemnitz.
- Bonet, J. and R. D. Wood (1997), *Nonlinear continuum mechanics for finite element analysis*, Cambridge University Press.
- Bronkhorst, C. A., S. R. Kalidindi and L. Anand (1992), Polycrystalline plasticity and the evolution of crystallographic texture in FCC metals, *Philosophical Transactions of the Royal Society of London; A*, vol. 341, pp. 443–477.
- Carle, D. and G. Blount (1999), The suitability of aluminium as an alternative material for car bodies, *Materials and Design*, vol. 20, pp. 267–272.
- Carleer, B. (1997), *Finite element analysis of deep drawing*, Ph.D. thesis, University of Twente.
- Chaboche, J. L. (1986), Time-independent constitutive theories for cyclic plasticity, *International Journal of Plasticity*, vol. 2, pp. 149–188.
- Chadwick, P. (1976), *Continuum Mechanics, Concise Theory and Problems*, George Allen & Unwin Ltd., London.
- Crisfield, M. A. (1991), *Non-linear Finite Element Analysis of Solids and Structures, volume 1: Essentials*, John Wiley & Sons.
- Crisfield, M. A. (1997), *Non-linear Finite Element Analysis of Solids and Structures, volume 2: Advanced Topics*, John Wiley & Sons.
- De Borst, R. (1987), Integration of plasticity equations for singular yield functions, *Computers and Structures*, vol. 26, pp. 823–829.
- De Borst, R. and P. H. Feenstra (1990), Studies in anisotropic plasticity with reference to the Hill criterion, *International Journal for Numerical Methods in Engineering*, vol. 29, pp. 315–336.
- Demarco, D. and E. N. Dvorkin (2001), Modeling of metal forming processes: implementation of an iterative solver in the flow formulation, *Computers and Structures*, vol. 79, pp. 1933–1942.
- Dienes, K. (1979), On the analysis of rotation and stress rate in deforming bodies, *Acta Mechanica*, vol. 32, pp. 217–232.
- Dodd, B. and Y. Bai (1987), *Ductile Fracture and Ductility—With Applications to Metalworking*, Academic Press, London.
- Estrin, Y. (1996), Dislocation-density-related constitutive modeling, in: A. S. Krausz and K. Krausz (eds.), *Unified Constitutive Laws of Plastic Deformation*, pp. 69–104, Academic Press, San Diego.
- Eterovic, A. L. and K.-J. Bathe (1990), A hyperelastic-based large strain elasto-plastic constitutive formulation with combined isotropic-kinematic hardening using the logarithmic stress and strain measures, *International Journal for Numerical Methods in Engineering*, vol. 30, pp. 1099–1114.

- Ferencz, R. M. and T. J. R. Hughes (1998), Iterative finite element solutions in nonlinear solid mechanics, in: P. G. Ciarlet and J. L. Lions (eds.), *Handbook of numerical analysis*, vol. 6, North-Holland, Amsterdam.
- Fish, J. and W. Chen (1999), On accuracy, stability and efficiency of the Newmark method with incomplete solution by multilevel methods, *International Journal for Numerical Methods in Engineering*, vol. 46, pp. 253–273.
- Gabriel, G. and K. J. Bathe (1995), Some computational issues in large strain elasto-plastic analysis, *Computers and Structures*, vol. 56, pp. 249–267.
- Gee, M., W. A. Wall and E. Ramm (2001), Parallel iterative solvers in nonlinear shell analysis, *Zeitschrift für angewandte Mathematik und Mechanik*, vol. 81, pp. 389–390.
- Gelin, J. C., B. Liu and C. Labergere (2000), Stable and accurate algorithms for the simulation of deep drawing and tube hydroforming processes, in: E. Oñate (ed.), *European Congress on Computational Methods in Applied Sciences and Engineering*, CIMNE Publishing, Barcelona, on cd-rom.
- Gelin, J. C. and P. Picart (Eds.) (1999), *Numisheet'99, Numerical Simulation of 3D Sheet Forming Processes*, vol. 2, Burs Edition, Besançon.
- Goerdeler, M. and G. Gottstein (2001), A microstructural work hardening model based on three internal state variables, *Materials Science and Engineering A*, vol. 309–310, pp. 377–381.
- Golub, G. H. and C. F. Van Loan (1989), *Matrix Computations*, The Johns Hopkins University Press, 2nd edn.
- Green, A. E. and P. M. Naghdi (1965), A general theory of an elastic-plastic continuum, *Archive for Rational Mechanics and Analysis*, vol. 18, pp. 251–281.
- Hackbush, W. (1994), *Iterative Solution of Large Sparse Systems of Equations*, no. 95 in Applied Mathematical Sciences, Springer.
- Hähner, P. (1996a), On the physics of the Portevin–Le Châtelier effect part 1: The statistics of dynamic strain ageing, *Materials Science and Engineering A*, vol. 207, pp. 208–215.
- Hähner, P. (1996b), On the physics of the Portevin–Le Châtelier effect part 2: microscopic to macroscopic behaviour, *Materials Science and Engineering A*, vol. 207, pp. 216–223.
- Hilber, H. M., T. J. R. Hughes and R. L. Taylor (1977), Improved numerical dissipation for time integration algorithms in structural dynamics, *Earthquake Engineering and Structural Dynamics*, vol. 5, pp. 283–292.
- Hill, R. (1948), A theory of the yielding and plastic flow of anisotropic metals, *Proceedings of the Royal Society of London; Series A*, vol. 193, pp. 281–297.
- Hill, R. (1950), *The mathematical theory of plasticity*, Clarendon Press, Oxford.
- Hill, R. (1952), On discontinuous plastic states, with special reference to localized necking in thin sheets, *Journal of the Mechanics and Physics of Solids*, vol. 1, pp. 19–30.
- Hiwatashi, S., A. van Bael, P. van Houtte and C. Teodosiu (1998), Prediction of forming limit strains under strain-path changes: application of an anisotropic model based on texture and dislocation structure, *International Journal of Plasticity*, vol. 14, pp. 647–669.
- Hughes, T. J. R. (1987), *The Finite Element Method: Linear Static and Dynamic Analysis*, Prentice-Hall, Englewood-Cliffs.
- Hutchinson, J. W. and K. W. Neale (1985), Wrinkling of curved thin sheet metal, in: J. Salencon (ed.), *Plastic Instability*, pp. 71–78, Press Ponts et Chaussées.
- Jefferson, A. D. and H. R. Thomas (1997), Convergence criteria for iterative solvers ap-

- plied to nonlinear plasticity problems, in: *Computational Plasticity, Fundamentals and Applications*, pp. 441–446.
- Kacou, S. and I. D. Parsons (1993), A parallel multigrid method for history-dependent elastoplasticity computations, *Computer Methods in Applied Mechanics and Engineering*, vol. 108, pp. 1–21.
- Kelder, M. H. (2001), *Quantifying the hydroformability of tubes*, Master's thesis, University of Twente.
- Keum, Y. T., B. Y. Ghoo and R. H. Wagoner (2001), 3-dimensional finite element analysis of non-isothermal forming processes for non-ferrous sheets, in: K.-I. Mori (ed.), *Simulation of Materials Processing: Theory, Methods and Applications*, pp. 813 – 818, A.A. Balkema, Lisse.
- Knockaert, R., Y. Chastel and E. Massoni (2000), Rate-independent crystalline and polycrystalline plasticity, application to FCC materials, *International Journal of Plasticity*, vol. 16, pp. 179–198.
- Knockaert, R., Y. Chastel and E. Massoni (2002), Forming limit prediction using rate-independent polycrystalline plasticity, *International Journal of Plasticity*, vol. 18, pp. 231–247.
- Kocks, U. F. (1976), Laws for work-hardening and low-temperature creep, *Journal of Engineering Materials and Technology*, vol. 98, pp. 76–85.
- Kocks, U. F. (1998), Kinematics and kinetics of plasticity, in: U. F. Kocks, C. N. Tomé and H.-R. Wenk (eds.), *Texture and Anisotropy, Preferred Orientations in Polycrystals and their Effect on Materials Properties*, chap. 8, pp. 326–389, Cambridge University Press, Cambridge.
- Koiter, W. T. (1953), Stress–strain relations, uniqueness and variational theorems for elastic-plastic materials with a singular yield surface, *Quarterly of Applied Mathematics*, vol. 11, pp. 350–354.
- Kok, S., A. J. Beaudoin and D. A. Tortorelli (2001), Numerical integration of lattice rotation in polycrystal plasticity, *International Journal for Numerical Methods in Engineering*, vol. 52, pp. 1487–1500.
- Kok, S., A. J. Beaudoin and D. A. Tortorelli (2002), A polycrystal plasticity model based on the mechanical threshold, *International Journal of Plasticity*, vol. 18, pp. 715–741.
- Krabiell, A. and W. Dahl (1981), Zum Einfluss von Temperatur und Dehngeschwindigkeit auf die Streckgrenze von Baustählen unterschiedlicher Festigkeit, *Archiv für das Eisenhüttenwesen*, vol. 52, pp. 429–436.
- Krausz, A. S. and K. Krausz (Eds.) (1996), *Unified Constitutive Laws of Plastic Deformation*, Academic Press, San Diego.
- Kuhl, D. and M. A. Crisfield (1999), Energy-conserving and decaying algorithms in non-linear structural dynamics, *International Journal for Numerical Methods in Engineering*, vol. 45, pp. 569–599.
- Kuroda, M. and V. Tvergaard (2000), Forming limit diagrams for anisotropic metal sheets with different yield criteria, *International Journal of Solids and Structures*, vol. 37, pp. 5037–5059.
- Kuwabara, T., M. Kuroda, V. Tvergaard and K. Nomura (2000), Use of abrupt strain path change for determining subsequent yield surface: experimental study with metal sheets, *Acta Materialia*, vol. 48, pp. 2071–2079.

- Lebyodkin, M., L. Dunin-Barkowskii, Y. Bréchet, Y. Estrin and L. P. Kubin (2000), Spatio-temporal dynamics of the Portevin–Le Chatelier effect: experiment and modelling, *Acta Materialia*, vol. 48, pp. 2529–2541.
- Lee, E. H. (1969), Elastic-plastic deformation at finite strains, *Journal of Applied Mechanics, ASME*, vol. 36, pp. 1–6.
- Lee, J. K., G. L. Kinzel and R. H. Wagoner (Eds.) (1996), *Proceedings of the 3rd International Conference: Numisheet '96*, The Ohio State University.
- Lee, S. W., J. W. Yoon and D. Y. Yang (1999), Comparative investigation into the dynamic explicit and the static implicit method for springback of sheet metal stamping, *Engineering Computations*, vol. 16, pp. 347–373.
- Mahnken, R. (1995), A Newton-multigrid algorithm for elasto-plastic/viscoplastic problems, *Computational Mechanics*, vol. 15, pp. 408–425.
- Malvern, L. E. (1969), *Introduction to the mechanics of a continuous medium*, Prentice-Hall Inc., Englewood Cliffs, New Jersey.
- Mandel, J. (1973), Equations constitutives et directeurs dans les milieux plastiques et viscoplastiques, *International Journal of Solids and Structures*, vol. 9, pp. 725–740.
- Marciniak, Z. and J. L. Duncan (1992), *Mechanics of Sheet Metal Forming*, Edward Arnold, London.
- Marciniak, Z. and K. Kuczynski (1967), Limit strains in processing of stretch forming sheet metal, *International Journal of Mechanical Sciences*, vol. 9, pp. 609–620.
- Mattiasson, K., L. Bernspång, A. Honecker, E. Schedin, T. Hamman and A. Melander (1991), On the use of explicit time integration in finite element simulation of industrial sheet metal forming processes, in: *Numerical simulations of 3D Sheet Forming Processes*, pp. 479–498, VDI-Berichte, VDI Verlag GmbH, Dusseldorf.
- Mecking, H. and U. F. Kocks (1981), Kinetics of flow and strain-hardening, *Acta Metallurgica*, vol. 29, pp. 1865–1877.
- Meinders, T. (2000), *Developments in numerical simulations of the real-life deep drawing process*, Ph.D. thesis, University of Twente.
- Meinders, T., A. H. van den Boogaard and J. Huétink (2002), Improvement of implicit finite element code performance in deep drawing simulations by dynamics contributions, *Journal of Materials Processing Technology*, accepted.
- Mercer, C. D., J. D. Nagtegaal and N. Rebelo (1995), Effective application of different solvers to forming simulations, in: S.-F. Shen and P. R. Dawson (eds.), *Simulation of Materials Processing: Theory, Methods and Applications*, pp. 469–474, Balkema, Rotterdam.
- Meyers, M. A. (1999), Dynamic deformation and failure, in: M. A. Meyers, R. W. Armstrong and H. O. K. Kirchner (eds.), *Mechanics and Materials; Fundamentals and Linkages*, pp. 489–594, John Wiley & Sons, Inc., New York etc.
- Miehe, C. and J. Schröder (2001), A comparative study of stress update algorithms for rate-independent and rate-dependent crystal plasticity, *International Journal for Numerical Methods in Engineering*, vol. 50, pp. 273–298.
- Miller, W. S., L. Zhuang, J. Bottema, A. J. Wittebrood, P. de Smet, A. Haszler and A. Vieregge (2000), Recent developments in aluminium alloys for the automotive industry, *Materials Science and Engineering A*, vol. 280, pp. 37–49.
- Mocellin, K., L. Fourment, T. Coupez and J. L. Chenot (2001), Toward large scale F.E. computation of hot forging process using iterative solvers, parallel computation and mul-

- tigrid algorithms, *International Journal for Numerical Methods in Engineering*, vol. 52, pp. 473–488.
- Moon, Y. H., Y. K. Kang, J. W. Park and S. R. Gong (2001), Tool temperature control to increase the deep drawability of aluminum 1050 sheet, *Machine Tools and Manufacture*, vol. 41, pp. 1283–1294.
- Nagtegaal, J. C. and J. E. de Jong (1981), Some computational aspects of elastic-plastic, large strain analysis, *International Journal for Numerical Methods in Engineering*, vol. 12, pp. 15–41.
- Nagtegaal, J. C., D. M. Parks and J. R. Rice (1974), On numerically accurate finite element solutions in the fully plastic range, *Computer Methods in Applied Mechanics and Engineering*, vol. 4, pp. 153–177.
- Naka, T. and F. Yoshida (1999), Deep drawability of type 5083 aluminium-magnesium alloy sheet under various conditions of temperature and forming speed, *Journal of Materials Processing Technology*, vol. 89–90, pp. 19–23.
- Nes, E. (1998), Modelling of work hardening and stress saturation in FCC metals, *Progress in Materials Science*, vol. 41, pp. 129–193.
- Pearce, R. (1991), *Sheet Metal Forming*, IOP Publishing Ltd, Bristol.
- Peeters, B., E. Hoferlin, P. van Houtte and E. Aernoudt (2001), Assessment of crystal plasticity based calculation of the lattice spin of polycrystalline metals for FE implementation, *International Journal of Plasticity*, vol. 17, pp. 819–836.
- Pijlman, H. H. (2001), *Sheet material characterisation by multi-axial experiments*, Ph.D. thesis, University of Twente.
- Rietman, A. D. (1999), *Numerical Analysis of Inhomogeneous Deformation in Plane Strain Compression*, Ph.D. thesis, University of Twente.
- Rojek, J., E. Oñate and E. Postek (1998), Application of explicit FE codes to simulation of sheet and bulk metal forming processes, *Journal of Materials Processing Technology*, vol. 80–81, pp. 620–627.
- Rollet, A. D. and S. I. Wright (1998), Typical textures in metals, in: U. F. Kocks, C. N. Tomé and H.-R. Wenk (eds.), *Texture and Anisotropy, Preferred Orientations in Polycrystals and their Effect on Materials Properties*, chap. 5, pp. 178–239, Cambridge University Press, Cambridge.
- Roters, F., D. Raabe and G. Gottstein (2000), Work hardening in heterogeneous alloys—a microstructural approach based on three internal state variables, *Acta Materialia*, vol. 48, pp. 4181–4189.
- Saint-Georges, P., G. Warzee, R. Beauwens and Y. Notay (1996), High-performance PCG solvers for FEM structural analysis, *International Journal for Numerical Methods in Engineering*, vol. 39, pp. 1313–1340.
- Saint-Georges, P., G. Warzee, Y. Notay and R. Beauwens (1999), Problem-dependent preconditioners for iterative solvers in FE elastostatics, *Computers and Structures*, vol. 73, pp. 33–43.
- Schieck, B. and H. Stumpf (1995), The appropriate corotational rate, exact formula for the plastic spin and constitutive model for finite elastoplasticity, *International Journal of Solids and Structures*, vol. 32, pp. 3643–3667.
- Schmoeckel, D. and C. Heller (1988), Umformen von Aluminiumblechen bei erhöhten Temperaturen, Teil 1, EFB-Forschungsbericht 34, Europäische Forschungsgesellschaft

- für Blechverarbeitung E.V., Hannover.
- Schmoeckel, D., B. C. Liebler and F.-D. Speck (1995a), Temperaturgeführter Stofffluß beim Tiefziehen von Al-Blech – Grundlagen und Modellversuche, *Bänder Bleche Rohre*, vol. 36, pp. 14–21.
- Schmoeckel, D., B. C. Liebler and F.-D. Speck (1995b), Temperaturgeführter Stofffluß beim Tiefziehen von Al-Blech – Realversuche, *Bänder Bleche Rohre*, vol. 36, pp. 24–27.
- Selman, A., T. Meinders, A. H. van den Boogaard and J. Huétink (2002), Numerical analysis of wrinkling in sheet metal forming, *International Journal of Forming Processes*, accepted.
- Shehata, F., M. J. Painter and R. Pearce (1978), Warm forming of aluminium/magnesium alloy sheet, *Journal of Mechanical Working Technology*, vol. 2, pp. 279–291.
- Simo, J. C. (1988a), A framework for finite strain elastoplasticity based on maximum plastic dissipation and the multiplicative decomposition: Part I. Continuum formulation, *Computer Methods in Applied Mechanics and Engineering*, vol. 66, pp. 199–219.
- Simo, J. C. (1988b), A framework for finite strain elastoplasticity based on maximum plastic dissipation and the multiplicative decomposition: Part II. Computational aspects, *Computer Methods in Applied Mechanics and Engineering*, vol. 68, pp. 1–31.
- Simo, J. C. and T. J. R. Hughes (1998), *Computational Inelasticity*, Interdisciplinary Applied Mathematics, Springer-Verlag, New York etc.
- Simo, J. C., J. G. Kennedy and S. Govindjee (1988), Non-smooth multisurface plasticity and viscoplasticity. Loading/unloading conditions and numerical algorithms, *International Journal for Numerical Methods in Engineering*, vol. 26, pp. 2161–2185.
- Simo, J. C. and M. Ortiz (1985), A unified approach to finite deformation elastoplasticity based on the use of hyperelastic constitutive equations, *Computer Methods in Applied Mechanics and Engineering*, vol. 49, pp. 221–245.
- Simo, J. C., R. L. Taylor and K. S. Pister (1985), Variational and projection methods for the volume constraint in finite deformation plasticity, *Computer Methods in Applied Mechanics and Engineering*, vol. 51, pp. 177–208.
- Skalický, T. (1996), *LASPack Reference Manual*, Dresden University of Technology, 1.12.3 edn., URL <http://www.tu-dresden.de/mwism/skalicky/laspack/laspack.html>.
- Sloan, S. W. (1989), A fortran program for profile and wavefront reduction, *International Journal for Numerical Methods in Engineering*, vol. 28, pp. 2651–2679.
- Stiomak/tht (1978), *Materiaalkeuze in de werktuigbouwkunde*, Stam Technische Boeken, Culemborg.
- Swift, H. W. (1952), Plastic instability under plane stress, *Journal of the Mechanics and Physics of Solids*, vol. 1, pp. 1–18.
- Takuda, H., K. Mori, I. Masuda, Y. Abe and M. Matsuo (2002), Finite element simulation of warm deep drawing of aluminium alloy sheet when accounting for heat conduction, *Journal of Materials Processing Technology*, vol. 120, pp. 412–418.
- Taylor, G. I. (1938), Plastic strain in metals, *Journal of the Institute of Metals*, vol. 62, pp. 307–324.
- Tóth, L. and P. van Houtte (1992), Discretization techniques for orientation distribution functions, *Textures and Microstructures*, vol. 19, pp. 229–244.
- Vadon, A. (1986), Graphic representation of texture data, in: H. J. Bunge and C. Esling (eds.), *Quantitative Texture Analysis*, chap. 9, pp. 235–258, DMG, Oberursel, Germany.

- Van den Boogaard, A. H., P. J. Bolt and R. J. Werkhoven (2001a), Aluminum sheet forming at elevated temperatures, in: K.-I. Mori (ed.), *Simulation of Materials Processing: Theory, Methods and Applications*, pp. 819–824, A.A. Balkema, Lisse.
- Van den Boogaard, A. H., P. J. Bolt and R. J. Werkhoven (2001b), Modeling of AlMg sheet forming at elevated temperatures, *International Journal of Forming Processes*, vol. 4, pp. 361–375.
- Van den Boogaard, A. H., T. Meinders and J. Huétink (2003), Efficient implicit finite element analysis of sheet forming processes, *International Journal for Numerical Methods in Engineering*, vol. 56, in press.
- Van den Boogaard, A. H., A. D. Rietman and J. Huétink (1998), Iterative solvers in forming process simulations, in: J. Huétink and F. P. T. Baaijens (eds.), *Simulation of Materials Processing: Theory, Methods and Applications*, pp. 219–224, Balkema, Rotterdam.
- Van der Lugt, J. (1988), *A finite element method for the simulation of thermo-mechanical contact problems in forming processes*, Ph.D. thesis, University of Twente.
- Van Horn, K. R. (Ed.) (1967), *Aluminum—Volume I. Properties, Physical Metallurgy and Phase Diagrams*, American Society for Metals, Metals Park, Ohio.
- Van Houtte, P., L. Delannay and S. R. Kalidindi (2002), Comparison of two grain interaction models for polycrystal plasticity and deformation texture prediction, *International Journal of Plasticity*, vol. 18, pp. 359–377.
- Van Liempt, P. (1994), Workhardening and substructural geometry of metals, *Journal of Materials Processing Technology*, vol. 45, pp. 459–464.
- Vegter, H. (1991), *On the plastic behaviour of steel during sheet forming*, Ph.D. thesis, University of Twente.
- Vegter, H. (2002), private communication.
- Vegter, H., Y. An, H. H. Pijlman, B. D. Carleer and J. Huétink (1998), Advanced material models in simulation of sheet forming processes and prediction of forming limits, in: *First ESAFORM Conference on Material Forming*, pp. 499–502.
- Vegter, H., Y. An, H. H. Pijlman and J. Huétink (1999), Different approaches to describe the plastic material behaviour of steel and aluminium-alloys in sheet forming, in: J. A. Covas (ed.), *Proceedings of the 2nd ESAFORM Conference on Material Forming*, pp. 127–132, Guimarães.
- Vegter, H., P. Drent and J. Huétink (1995), A planar isotropic yield criterion based on mechanical testing at multi-axial stress states, in: S.-F. Shen and P. R. Dawson (eds.), *Simulation of Materials Processing: Theory, Methods and Applications*, pp. 345–350, Balkema, Rotterdam.
- Verdier, M., Y. Bréchet and P. Guyot (1999), Recovery of AlMg alloys: flow stress and strain-hardening properties, *Acta Materialia*, vol. 47, pp. 127–134.
- Vetter, R. and A. van den Beukel (1977), Dislocation production in cold worked copper, *Scripta Metallurgica*, vol. 11, pp. 143–146.
- Voce, E. (1948), The relation between stress and strain for homogeneous deformation, *Journal of the Institute of Metals*, vol. 74, pp. 537–562.
- Wagenhofer, M., M. Erickson-Natishan, R. W. Armstrong and F. J. Zerilli (1999), Influences of strain rate and grain size on yield and serrated flow in commercial Al-Mg alloy 5086, *Scripta Materialia*, vol. 41, pp. 1177–1184.
- Wilson, D. V. (1988), Aluminium versus steel in the family car—the formability factor,



- Journal of Mechanical Working Technology*, vol. 16, pp. 257–277.
- Woodthorpe, J. and R. Pearce (1970), The anomalous behaviour of aluminium sheet under balanced biaxial tension, *International Journal of Mechanical Sciences*, vol. 12, pp. 341–346.
- Wu, P. D., K. W. Neale and E. van der Giessen (1996), Simulation of the behaviour of fcc polycrystals during reversed torsion, *International Journal of Plasticity*, vol. 12, pp. 1199–1219.
- Yang, D. Y., D. W. Jung, I. S. Song, D. J. Yoo and J. H. Lee (1995), Comparative investigation into implicit, explicit, and iterative implicit/explicit schemes for the simulation of sheet-metal forming processes, *Journal of Materials Processing Technology*, vol. 50, pp. 39–53.
- Yao, X. and S. Zajac (2000), The strain-rate dependence of flow stress and work-hardening rate in three Al-Mg alloys, *Scandinavian Journal of Metallurgy*, vol. 29, pp. 101–107.
- Zener, C. and J. H. Hollomon (1944), Effect of strain rate upon plastic flow of steel, *Journal of Applied Physics*, vol. 15, p. 22.
- Zhou, Y. and K. W. Neale (1995), Predictions of forming limit diagrams using a rate-sensitive crystal plasticity model, *International Journal of Mechanical Sciences*, vol. 37, pp. 1–20.
- Zienkiewicz, O. C. and R. L. Taylor (2000a), *The Finite Element Method, volume 1: The Basis*, Butterworth–Heinemann, Oxford etc., 5th edn.
- Zienkiewicz, O. C. and R. L. Taylor (2000b), *The Finite Element Method, volume 2: Solid Mechanics*, Butterworth–Heinemann, Oxford etc., 5th edn.



# Curriculum Vitae

Antonius Henricus (Ton) van den Boogaard, geboren 28 mei 1961 te Haarlem

- 1973–1979 Atheneum-B, Pius X-College, Beverwijk
- 1979–1981 Werktuigbouwkunde, Hogere Technische School, Haarlem (eerste twee jaar)
- 1981–1988 Werktuigbouwkunde, Technische Hogeschool Twente, later Universiteit Twente, Enschede
- 1986 Beklimming top ‘Rakaposhi’, 7788 m, Pakistan
- 1988–1989 Vervulling militaire dienstplicht als luitenant-logistiek bij de staf en stafcompagnie van 101 genie-gevechtsgroep, Wezep
- 1989–1995 Wetenschappelijk medewerker bij de afdeling Numerieke Mechanica van TNO Bouw, Rijswijk
- 1995–heden Universitair docent bij de faculteit Werktuigbouwkunde, thans Construerende Technische Wetenschappen, van de Universiteit Twente, Enschede



# Index

- anisotropy, 17, 23, 55
- annealing, 9
- anomalous behaviour of aluminium, 51, 130
  
- b.c.c. metals, 44
- back-stress, 22, 32, 53
- bandwidth optimisation, 105
- Bauschinger effect, 32
- Bergström, *see* hardening
- Bezier function, 37
- Burgers vector, 44
  
- capacity matrix, 94
- chemical composition, 7
- co-rotating reference frame, 55, 68, 141
- conditional stability, 101, 103
- conjugate gradient solver, 103, 106
- conservation principles, 93
- contact element, 101
- convergence criterion, 106–108
- critical resolved shear stress, 27, 28, 42
- critical time step, 96, 100, 103
- cross slip, 10
- crystal plasticity, *see* polycrystal plasticity
- cylindrical cup warm deep drawing, 122
  
- Debye frequency, 45
- deformation gradient, 54
- diagonalised matrix, 96–104
- discrete Kirchhoff element, 98–100, 128
- discrete shear element, 98–100
- dislocation, 9, 42
  - annihilation, 47
  - density, 44, 46–48
  - dynamic recovery, 47
  - glide, 25, 26, 28, 45
  - immobilisation, 42, 47
  - remobilisation, 47
  - structure, 28
- drilling d.o.f., 99
- Drucker's postulate, 22, 32, 37
- dynamic recovery, 46
- dynamic regularisation, 111, 131
- dynamic strain ageing, 9
- dynamic stress, 45
  
- earing, 24, 38
- equi-biaxial factor, 42, 149
- equivalent slip value, 29
- equivalent strain, 40–42
- equivalent stress, 40–42
- explicit time integration, 96, 100, 101, 103
- exponential function, 140
  
- f.c.c. metals, 25, 31, 44, 46
- finite element analysis
  - cylindrical cup, 124, 128
  - front door panel, 114
  - grooved plate, 87
  - plane strain test, 89
  - rectangular product, 111
  - S-rail, 109
  - tensile test, 117
- finite element formulation, 97–101
- formability, 1–3
- forming limit curve, 73, 74, 83–87
- forming limit diagram, 70, 74
- friction, 123–125
- friction stress, 45
- functions of a tensor, 139
  
- Galerkin method, 94, 97

- grain size, 7  
 Green–Naghdi rate, 57
- hardening, 38, 45, 74, 83, 135  
   Bergström, 47, 118, 124  
   extended Nadai, 44, 124  
   isotropic, 22, 28, 32, 42, 85, 146  
   kinematic, 22, 33, 58, 85, 146  
   latent, 28  
   Nadai, 40, 43, 74, 85  
   physically based, 46  
   Voce, 29, 40, 48, 74, 85
- heat treatments, 9  
 Hill '48, *see* yield function  
 Hill local necking criterion, 78  
 homogeneous function, 32  
 homologous temperature, 10
- implicit time integration, 101, 102, 104  
 instabilities  
   compressive, *see* wrinkling  
   tensile, *see* necking
- Jacobi iteration, 104  
 Jaumann rate, 58
- Kocks–Mecking models, 47
- Lankford  $R$ -value, 23, 65, 85, 149  
 large rotations, 53  
 latent hardening, 28  
 lattice rotation, 61  
 lattice spin, 26, 60  
 left stretch tensor, 54  
 linear set of equations  
   direct solvers, 105  
   iterative solvers, 105  
 logarithmic strain, 12, 53, 56, 141, 145  
 logarithmic tensor function, 141  
 lumped matrix, *see* diagonalised matrix
- Mandel spin, 58, 59  
 Marciniak–Kuczynski analysis, 80–89  
 mass matrix, 94, 100  
 mass scaling, 103, 104, 113, 131  
 material axes, 55, 57–59  
 maximum force criterion, 75
- mesh refinement, 114  
 micro-structure, 9, 15, 39, 44, 46, 67  
 micro-structure, 7  
 Mises, *see* yield function  
 multiplicative decomposition, 59
- Nadai, *see* hardening  
 Nakazima test, 74, 89  
 necking, 3, 6, 12, 23, 29, 31, 36, 52, 65,  
   73–91, 108, 118–122, 137  
   diffuse, 75–77, 118, 147–148  
   localised, 78–83  
 Newmark time integration, 95, 113  
 Newton–Raphson algorithm, 95, 101, 103,  
   107, 110  
 normal anisotropic, 24
- objectivity, 53  
 orientation distribution function, 7, 64  
 Orowan equation, 44
- planar anisotropic, 24  
 planar isotropic, 24  
 plane strain factor, 42, 149  
 plane stress condition, 29, 33  
 plastic spin, 26, 60  
 plastic work, 29, 41  
 polar decomposition, 54, 56, 141, 145  
 pole figure, 61  
 polycrystal plasticity, 25, 60, 149  
 Portevin–Le Chatelier effect, 9, 12  
 precipitation, 9  
 preconditioner, 102, 106, 107, 111  
 principal stress, 34  
 proportional deformation, 23, 57, 68–70,  
   74, 145  
 proportionality factor, 68, 146
- $R$ -value, *see* Lankford  $R$ -value  
 rate of deformation, 55  
 rate of rotation, 55  
 recovery, 9  
 recrystallisation, 9  
 right stretch tensor, 54, 145
- Schmid tensor, 26

- serrations, 9, 12
- shear factor, 42, 149
- slip
  - rate, 25, 27
  - system, 25–28
- solute atoms, 9
- specific stiffness, 1
- specific strength, 1
- spin tensor, 26, 55–61, 140
- springback, 21
- strain hardening, *see* hardening
- strain rate sensitivity, 9, 28, 43, 85, 121, 135
- stretcher lines, 3, 9, 12
- Swift criterion, 75
  
- Taylor equation, 46
- Taylor model, 29, 63, 65
- tensile test
  - equi-biaxial, 17, 36, 61, 65, 67, 149
  - plane strain, 18, 36, 63, 65, 67, 89, 149
  - pure shear, 36, 63, 65, 67, 142, 149
  - simple shear, 18, 63, 65, 67, 142
  - uniaxial, 23, 36, 63, 65, 67, 108, 149
    - constant strain rate, 10–15, 48, 117
    - strain rate jump, 15–17, 50
- texture, 7, 31
  - deformation, 61
  - evolution, 27, 29, 60–67
  - rolling, 23
- Tresca, *see* yield function
- true strain, *see* logarithmic strain
- true stress, 12
  
- uniform strain, 12, 77, 117
  
- Vegter, *see* yield function
- velocity gradient, 25, 54
- Voce, *see* hardening
- Von Mises, *see* yield function
  
- weighted residual method, 94
- work hardening, *see* hardening
- wrinkling, 3, 130
  
- yield function, 22, 41
  - Hill '48, 31, 77, 129
  - polycrystal based, 25, 86
  - Tresca, 35, 86
  - Vegter, 36, 89, 118, 129
  - Von Mises, 32, 41, 89, 124, 129
- yield locus, *see* yield surface
- yield point elongation, 39
- yield surface, 21–24, 27, 87, 149
  - polycrystal based, 29–31, 64
  
- Zener–Hollomon parameter, 43, 47